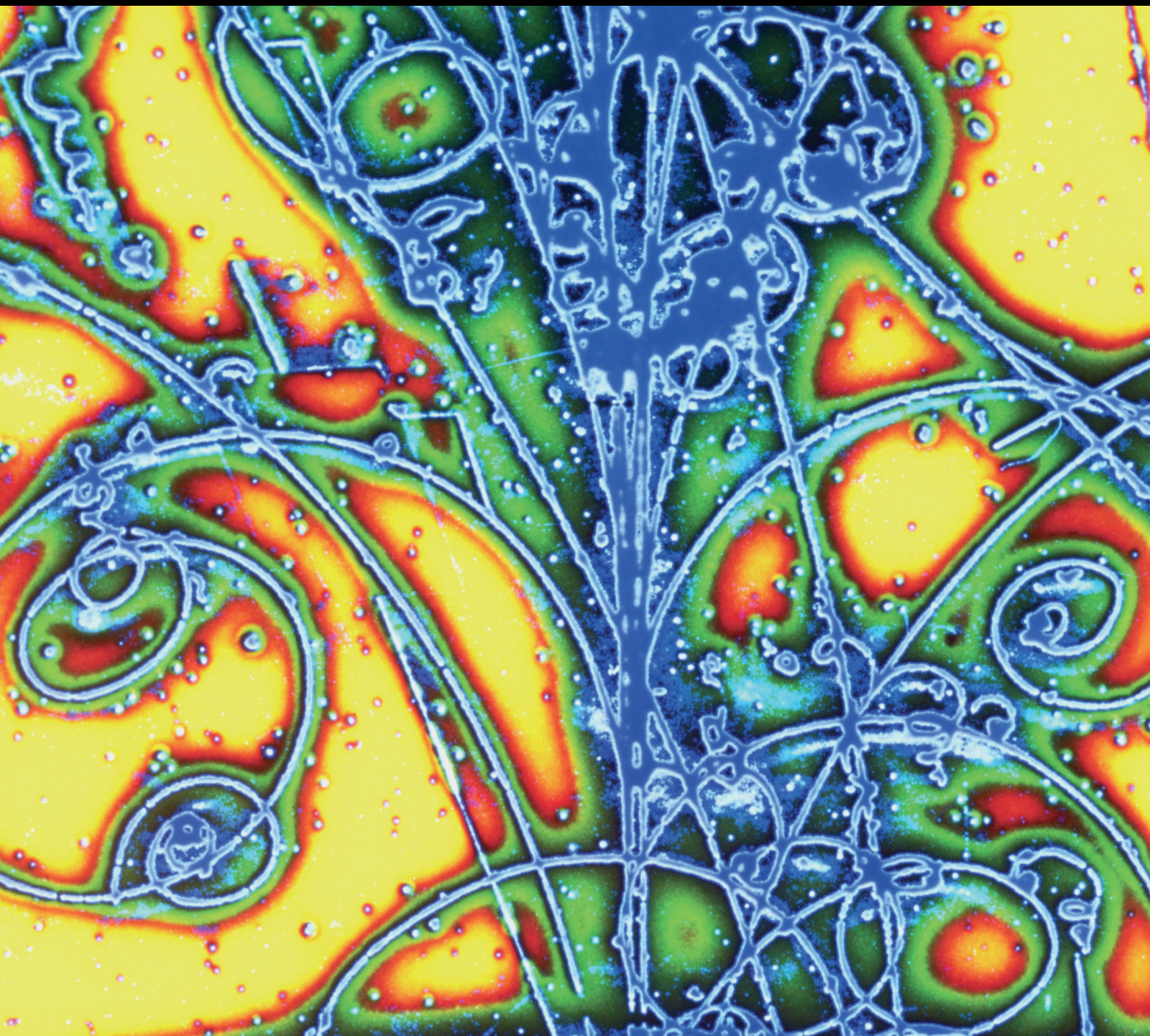


Advances in High Energy Physics

Quantum Gravitational Spectroscopy

Guest Editors: Valery V. Nesvizhevsky, Ignatios Antoniadis, Stefan Baessler,
and Guillaume Pignol





Quantum Gravitational Spectroscopy

Advances in High Energy Physics

Quantum Gravitational Spectroscopy

Guest Editors: Valery V. Nesvizhevsky, Ignatios Antoniadis,
Stefan Baessler, and Guillaume Pignol



Copyright © 2015 Hindawi Publishing Corporation. All rights reserved.

This is a special issue published in "Advances in High Energy Physics." All articles are open access articles distributed under the Creative Commons Attribution License, which permits unrestricted use, distribution, and reproduction in any medium, provided the original work is properly cited.

Editorial Board

Luis A. Anchordoqui, USA
T. Asselmeyer-Maluga, Germany
Marco Battaglia, Switzerland
Botio Betev, Switzerland
Emil Bjerrum-Bohr, Denmark
Rong-Gen Cai, China
Duncan L. Carlsmith, USA
Ashot Chilingarian, Armenia
Shi-Hai Dong, Mexico
Edmond C. Dukes, USA
Amir H. Fatollahi, Iran
Frank Filthaut, The Netherlands
Chao-Qiang Geng, Taiwan

Maria Giller, Poland
Xiaochun He, USA
Filipe R. Joaquim, Portugal
Kyung K. Joo, Korea
Michal Kreps, UK
Ming Liu, USA
Enrico Lunghi, USA
Piero Nicolini, Germany
Seog H. Oh, USA
Sergio Palomares-Ruiz, Spain
Anastasios Petkou, Greece
Alexey A. Petrov, USA
Thomas Rossler, Sweden

Juan José Sanz-Cillero, Spain
Reinhard Schlickeiser, Germany
Sally Seidel, USA
George Siopsis, USA
Luca Stanco, Italy
Satyendra Thoudam, The Netherlands
Smarajit Triambak, South Africa
Elias C. Vagenas, Kuwait
Nikos Varelas, USA
Kadayam S. Viswanathan, Canada
Yau W. Wah, USA

Contents

Quantum Gravitational Spectroscopy, Valery V. Nesvizhevsky, Ignatios Antoniadis, Stefan Baessler, and Guillaume Pignol
Volume 2015, Article ID 467409, 2 pages

Neutron Interferometry at the National Institute of Standards and Technology, D. A. Pushin, M. G. Huber, M. Arif, C. B. Shahi, J. Nsofini, C. J. Wood, D. Sarenac, and D. G. Cory
Volume 2015, Article ID 687480, 7 pages

Status of the GRANIT Facility, Damien Roulier, Francis Vezzu, Stefan Baeßler, Benoît Clément, Daniel Morton, Valery V. Nesvizhevsky, Guillaume Pignol, and Dominique Rebreyend
Volume 2015, Article ID 730437, 10 pages

Neutron Scattering on Impurity Nanoclusters in Gel Samples, V. B. Efimov, L. P. Mezhov-Deglin, C. D. Dewhurst, A. V. Lokhov, and V. V. Nesvizhevsky
Volume 2015, Article ID 808212, 4 pages

UCN Source at an External Beam of Thermal Neutrons, E. V. Lychagin, A. Yu. Muzychka, G. V. Nekhaev, V. V. Nesvizhevsky, E. I. Sharapov, and A. V. Strelkov
Volume 2015, Article ID 547620, 7 pages

Prospects for Studies of the Free Fall and Gravitational Quantum States of Antimatter, G. Dufour, D. B. Cassidy, P. Crivelli, P. Debu, A. Lambrecht, V. V. Nesvizhevsky, S. Reynaud, A. Yu. Voronin, and T. E. Wall
Volume 2015, Article ID 379642, 16 pages

Can We Observe the Gravitational Quantum States of Positronium?, P. Crivelli, V. V. Nesvizhevsky, and A. Yu. Voronin
Volume 2015, Article ID 173572, 7 pages

Regge Poles in Neutron Scattering by a Cylinder, K. V. Protasov and A. Y. Voronin
Volume 2014, Article ID 124592, 8 pages

Precision Measurement of the Position-Space Wave Functions of Gravitationally Bound Ultracold Neutrons, Y. Kamiya, G. Ichikawa, and S. Komamiya
Volume 2014, Article ID 859241, 7 pages

Error-Disturbance Uncertainty Relations in Neutron-Spin Measurements, Stephan Sponar, Georg Sulyok, Jaqueline Erhart, and Yuji Hasegawa
Volume 2014, Article ID 735398, 6 pages

Gravitational Resonance Spectroscopy with an Oscillating Magnetic Field Gradient in the GRANIT Flow through Arrangement, G. Pignol, S. Baeßler, V. V. Nesvizhevsky, K. Protasov, D. Rebreyend, and A. Voronin
Volume 2014, Article ID 628125, 7 pages



Rough Mirror as a Quantum State Selector: Analysis and Design, M. Escobar, F. Lamy, A. E. Meyerovich,
and V. V. Nesvizhevsky
Volume 2014, Article ID 764182, 11 pages

Quantized Ultracold Neutrons in Rough Waveguides: GRANIT Experiments and Beyond,
M. Escobar and A. E. Meyerovich
Volume 2014, Article ID 185414, 7 pages

In-Pile ^4He Source for UCN Production at the ESS, Esben Klinkby, Konstantin Batkov,
Ferenc Mezei, Eric Pitcher, Troels Schönfeldt, Alan Takibayev, and Luca Zanini
Volume 2014, Article ID 241639, 4 pages

Editorial

Quantum Gravitational Spectroscopy

Valery V. Nesvizhevsky,¹ Ignatios Antoniadis,² Stefan Baessler,^{3,4} and Guillaume Pignol⁵

¹*Institut Max von Laue-Paul Langevin, 38042 Grenoble, France*

²*The European Organization for Nuclear Research, 1211 Geneva, Switzerland*

³*Physics Department, University of Virginia, Charlottesville, VA 22904, USA*

⁴*Oak Ridge National Laboratory, Oak Ridge, TN 37831, USA*

⁵*Laboratoire de Physique Subatomique et de Cosmologie/IN2P3-UJF-INPG, 38000 Grenoble, France*

Correspondence should be addressed to Valery V. Nesvizhevsky; nesvizhevsky@ill.eu

Received 31 December 2014; Accepted 31 December 2014

Copyright © 2015 Valery V. Nesvizhevsky et al. This is an open access article distributed under the Creative Commons Attribution License, which permits unrestricted use, distribution, and reproduction in any medium, provided the original work is properly cited. The publication of this article was funded by SCOAP³.

Quantum gravitational spectroscopy with ultracold systems is an emerging field of particle physics based on recent major advances in related experimental and theoretical developments. The gravitational spectroscopy is profiting from its exceptional sensitivity due to extreme weakness of the gravitational interaction compared to other fundamental interactions; thus it provides us with access to the precision frontier in particle physics and other domains. Quantum gravitational spectroscopy is the ultimate limit of gravitational spectroscopy, which studies/measures fragile and thus sensitive quantum states of ultracold particles and systems. To provide observable phenomena with ultracold systems, like neutrons, atoms, or antiatoms, in gravitational quantum states, one has to produce them with sufficiently high phase-space density. Some of such studies in a gravitational field, like those with ultracold neutrons, have become reality; others with ultracold atoms and antiatoms are in preparation.

This subject is traditionally covered in a series of GRANIT Workshops (<http://lpsc.in2p3.fr/Indico/conferenceDisplay.py?confId=947>, <https://lpsc.in2p3.fr/Indico/conferenceDisplay.py?confId=371>, and <http://lpsc.in2p3.fr/congres/granit-06/index.php>) [1]. Quantum gravitational spectroscopy with ultracold systems plays an important interdisciplinary role on a crossroad of many scientific domains. We are particularly interested in contributions describing research to be done with the new GRANIT facility, including not only all aspects from the theoretical motivation and analysis of already measured results but also potentially new areas, methodical and instrumental developments, which could improve its

performance and universality, and finally analyzing priorities of these studies.

The topics include the following: (i) the GRANIT facility, measurements of gravitational quantum states of neutrons, including experimental results and theoretical developments, and also neutron interferometry in broad sense; (ii) novel instruments and methods for gravitational spectroscopy and interferometry, including those capable of improving the performance of GRANIT facility; (iii) fundamental interactions in near-surface quantum systems, including short-range forces, chameleon-like forces, noncommutative quantum mechanics, emerging gravity, and antimatter and gravity; (iv) precision fundamental measurements with ultracold systems, including gravity with atoms, molecules, neutrons, and antimatter, quantum reflection, and dissipation; (v) surface studies with the GRANIT facility, including materials with predefined properties, levitating nanoparticles, and whispering gallery effect.

Bound states of a system could be formed by interactions of different kind. Detailed studies of such states do not only serve to explore the system itself, but also are a good tool to better understand the interaction responsible for the binding force. The problem is that a gravitational force is very weak to form easily a quantum bound system. One could cite Brian Hatfield in “Feynman Lectures on Gravitation” published in 1995 by Addison-Wesley Publishing Company: “Let us consider another possibility, an atom held together by gravity alone. For example, we might have two neutrons in a bound state. When we calculate the Bohr radius of such an atom, we

find that it would be 10^8 light years, and that the atomic binding energy would be 10^{-70} Rydbergs. *There is then little hope of ever observing gravitational effects on systems which are simple enough to be calculable in quantum mechanics.*” However, gravitationally bound quantum states of neutrons were discovered in a quite special configuration of the potential.

For this observation, one used the fact that ultracold neutrons (UCNs) experience a neutron-optical potential (sometimes called Fermi potential) in matter of a size big enough that matter can totally reflect UCNs if their energy is sufficiently low. In fact, the term “ultracold neutron” is loosely defined as the neutrons which are totally reflected at all incidence angles by the matter used for the confining bottle for them. Here, we focus on UCNs with even lower energy, for which we can approximate the potential in matter as infinite. These neutrons bounce on a horizontal table essentially like ping-pong balls on a table. They are confined in a box formed by the infinite potential of the table and the linear gravitational potential. In order to detect effects of the quantization, one has to focus on neutrons in one of the lowest possible states in such a system.

General solutions of the corresponding one-dimensional Schrödinger equation are given in all major textbooks on quantum mechanics, for instance, in [2, 3]. In relation to the neutron, this problem was considered for the first time in [4]. Energies of the lowest quantum states are very small, a few peV, which can be compared with the upper energy limit for UCNs which is of the order of hundred neV. The size of the lowest quantum states is of the order of tens of micrometers.

The aim of previous experiments performed in the last decade was to discover these quantum states. For the discovery, a method was used that is essentially a measurement of the height and shape of wave functions [5–7]. The accuracy of such height measurement was not very high, $\sim 10^{-1}$. In order to improve it, efforts are currently undertaken by qBounce and Tokyo collaborations; the methods used are resonant transitions between quantum states induced by mechanical vibrations of the bottom mirror [8] and precision studies of wave functions of neutrons in gravitational quantum states [9]. Analysis of systematic effects and estimations of actual accuracy are in progress. The GRANIT collaboration is aiming at achieving an ultimate accuracy using long storage of UCNs in gravitational quantum states in a closed trap [10] with a dedicated UCN source [11] with high phase-space density to be put in reliable operation soon.

One of the main goals for improving the accuracy of quantum gravitational spectroscopy with neutrons is searches for extra short-range fundamental forces [12]. As usual, we discuss also any progress in all competing nonneutron methods as well as constraints at other characteristic distances. Among major methodical developments related to the phenomenon of gravitational quantum states are the detailed theoretical analysis and the planning experiments on observation of gravitational quantum states of antihydrogen atoms.

Acknowledgments

Over 50 participants from 12 countries in 4 continents attended the previous GRANIT-2014 Workshop. The organizers

would like to thank ILL, IN2P3/CNRS, and UJF/Grenoble for financial support of the Workshop as well as for their help in preparation of the Workshop.

Valery V. Nesvizhevsky
Ignatios Antoniadis
Stefan Baessler
Guillaume Pignol

References

- [1] I. Antoniadis, S. Baessler, O. Bertolami et al., “Workshop GRANIT-2010, 14-19 February 2010, Les Houches, France,” *Comptes Rendus Physique*, vol. 12, no. 8, pp. 703–706, 2011.
- [2] I. I. Goldman, V. D. Krivchenkov, V. I. Kogan, and V. M. Galitski, *Problems in Quantum Mechanics*, Academic Press, New York, NY, USA, 1960.
- [3] J. J. Sakurai, *Modern Quantum Mechanics*, Benjamin/Cummings, Menlo Park, Calif, USA, 1985.
- [4] V. I. Luschnikov and A. Frank, “Quantum effects occurring when ultracold neutrons are stored on a plane,” *JETP Letters*, vol. 28, pp. 559–561, 1978.
- [5] V. V. Nesvizhevsky, H. G. Börner, A. K. Petukhov et al., “Quantum states of neutrons in the Earth’s gravitational field,” *Nature*, vol. 415, no. 6869, pp. 297–299, 2002.
- [6] V. V. Nesvizhevsky, H. G. Börner, A. M. Gagarski et al., “Measurement of quantum states of neutrons in the Earth’s gravitational field,” *Physical Review D*, vol. 67, Article ID 102002, 2003.
- [7] V. V. Nesvizhevsky, A. K. Petukhov, H. G. Börner et al., “Study of the neutron quantum states in the gravity field,” *European Physical Journal C*, vol. 40, no. 4, pp. 479–491, 2005.
- [8] T. Jenke, P. Geltenbort, H. Lemmel, and H. Abele, “Realization of a gravity-resonance-spectroscopy technique,” *Nature Physics*, vol. 7, no. 6, pp. 468–472, 2011.
- [9] G. Ichikawa, S. Komamiya, Y. Kamiya et al., “Observation of the spatial distribution of gravitationally bound quantum states of ultracold neutrons and its derivation using the Wigner function,” *Physical Review Letters*, vol. 112, no. 7, Article ID 071101, 2014.
- [10] S. Baessler, M. Beau, M. Kreuz et al., “The GRANIT spectrometer,” *Comptes Rendus Physique*, vol. 12, pp. 707–728, 2011.
- [11] P. Schmidt-Wellenburg, K. H. Andersen, P. Courtois et al., “Ultracold-neutron infrastructure for the gravitational spectrometer GRANIT,” *Nuclear Instruments and Methods in Physics Research, Section A: Accelerators, Spectrometers, Detectors and Associated Equipment*, vol. 611, no. 2-3, pp. 267–271, 2009.
- [12] I. Antoniadis, S. Baessler, M. Büchner et al., “Short-range fundamental forces,” *Comptes Rendus Physique*, vol. 12, no. 8, pp. 755–778, 2011.

Research Article

Neutron Interferometry at the National Institute of Standards and Technology

**D. A. Pushin,^{1,2} M. G. Huber,³ M. Arif,³ C. B. Shahi,⁴ J. Nsofini,^{1,2} C. J. Wood,^{1,2}
D. Sarenac,^{1,2} and D. G. Cory^{1,5,6}**

¹*Institute for Quantum Computing, University of Waterloo, Waterloo, ON, Canada N2L 3G1*

²*Department of Physics and Astronomy, University of Waterloo, Waterloo, ON, Canada N2L 3G1*

³*National Institute of Standards and Technology, Gaithersburg, MD 20899, USA*

⁴*Physics and Engineering Physics Department, Tulane University, New Orleans, LA 70118, USA*

⁵*Department of Chemistry, University of Waterloo, Waterloo, ON, Canada N2L 3G1*

⁶*Perimeter Institute for Theoretical Physics, Waterloo, ON, Canada N2L 2Y5*

Correspondence should be addressed to D. A. Pushin; dmitry.pushin@uwaterloo.ca

Received 30 July 2014; Accepted 19 August 2014

Academic Editor: Guillaume Pignol

Copyright © 2015 D. A. Pushin et al. This is an open access article distributed under the Creative Commons Attribution License, which permits unrestricted use, distribution, and reproduction in any medium, provided the original work is properly cited. The publication of this article was funded by SCOAP³.

Neutron interferometry has proved to be a very precise technique for measuring the quantum mechanical phase of a neutron caused by a potential energy difference between two spatially separated neutron paths inside interferometer. The path length inside the interferometer can be many centimeters (and many centimeters apart) making it very practical to study a variety of samples, fields, potentials, and other macroscopic medium and quantum effects. The precision of neutron interferometry comes at a cost; neutron interferometers are very susceptible to environmental noise that is typically mitigated with large, active isolated enclosures. With recent advances in quantum information processing especially quantum error correction (QEC) codes we were able to demonstrate a neutron interferometer that is insensitive to vibrational noise. A facility at NIST's Center for Neutron Research (NCNR) has just been commissioned with higher neutron flux than the NCNR's older interferometer setup. This new facility is based on QEC neutron interferometer, thus improving the accessibility of neutron interferometry to the greater scientific community and expanding its applications to quantum computing, gravity, and material research.

1. Introduction

The first single crystal neutron interferometer of Mach-Zehnder type was demonstrated by Rauch et al. in 1974 [1]. A few months later Colella, Overhauser, and Werner studied the effects of gravity on a neutron by tilting the interferometer and observing a gravity induced phase shift [2]. In subsequent years the experiment was improved and repeated several times with thorough studies of systematic uncertainties (such as Sagnac effect and crystallographic stress [3–6]). In recent years there has been renewed interest in use of single crystal neutron interferometry to study gravity [7, 8] and also in proposals for searching for non-Newtonian gravity [9], dark energy [10, 11], and other forces [12].

2. Neutron Interferometer and Optics Facility at NIST

The Neutron Interferometer and Optics Facility (NIOF) at NIST was built during the construction of the guide hall with vibration isolation in mind. It is placed on a separate foundation from the guide hall floor and consists of two vibration isolation stages. The first stage is a 40,000 kg table suspended on air-springs and controlled via a computer with micrometer level position. For a more detailed description of the system see [13]. The second vibration isolation stage consists of a 1,000 kg table and is not currently in use. The facility also has sound dumping panels and a temperature controlled enclosure around interferometer. Temperature is

stabilized to 5 mK precision at room temperature in order to improve the phase stability of the system [14]. When the temperature is stabilized at this level the interferometer phase is stable within a couple of degrees over a one-month time scale. Neutrons are extracted from the cold guide and redirected to the interferometer enclosure via two sets of pyrolytic graphite (PG) crystal monochromators. The interferometer facility has access to a wide range of neutron wavelengths from 0.2 nm to 0.45 nm. Neutrons in this facility can be polarized via a V-shaped transmission supermirror polarizer with 93% polarization efficiency for 0.235 nm wavelength neutrons [15].

3. Equivalence of a Neutron Interferometer and Light Mach-Zehnder Interferometer

In the past years we have used several neutron interferometer designs that are equivalent to Mach-Zehnder optical interferometers (Figure 2). The first blade of the interferometer coherently splits the neutron beam into two paths (upper and lower) via Bragg diffraction, as illustrated in Figure 2(a). The middle blade(s) work as mirrors. They redirect and focus neutron paths into the third blade. At the third blade the neutron paths are recombined, and the resulting interference effects can be observed by ^3He -detectors placed in both paths behind interferometer. Each neutron inside the interferometer (satisfying the Bragg conditions) can be described as the superposition of the two paths (i.e., “upper” and “lower”):

$$\Psi = e^{i\phi_1} C_1 |\text{upper}\rangle + e^{i\phi_2} C_2 |\text{lower}\rangle, \quad (1)$$

where C_1 and C_2 are normalization coefficients that depend on the reflection and transmission coefficients of the interferometer blades and ϕ_1 and ϕ_2 are phases that the neutron acquires passing through different paths. An important point is that the reactor flux is so low that there will be only one neutron inside the interferometer at a time. Thus we only observe neutron self-interference, and neutron-neutron interferences can be neglected. Several high contrast (>75%) perfect Si crystal neutron interferometers are shown in Figure 2(b). They are on the order of 10 cm in size and so allow for the placement of an object (such as a sample, phase rotator, spin flipper, and neutron absorber) in one path without affecting the other path. This allows for the observation of interference effects due to neutrons passing through the interferometer with one path modified by this object [16]. This is why neutron interferometry is a clear example of macroscopic quantum coherence and a convenient test bed to study many aspects of quantum mechanics, neutron interactions, quantum information processing (QIP), and fundamental physics.

4. Coherence and QIP

The single crystal neutron interferometer is an ideal tool for the study of neutron coherence length. The clear way of changing the optical path length and shifting one path with respect to the other [14, 17–20] allows direct measurement of coherence lengths. The coherence length (l_c) often depends on the momentum distribution (δk) of neutrons entering the

interferometer, and it is limited by Heisenberg’s uncertainty relation

$$l_c = \frac{1}{2\delta k}. \quad (2)$$

To understand this limit in the measurement of the vertical coherence length we have engineered different momentum distributions using the focusing monochromator and set of slits as shown in Figure 3(a). By shielding some of the PG blades of the focusing monochromator we were able to create different vertical momentum distributions for the neutrons.

By measuring the contrast of the neutron interferometer we can directly map out the coherence function. In order to measure contrast we usually place fused silica flat (phase flag) in both neutron paths. By rotating this phase flag around vertical axis we modify the optical path length of neutrons traveling through different interferometer paths. This allows oscillations of neutron intensity (I) on the detectors behind the interferometer. The contrast is defined as the ratio:

$$\text{Contrast} = \frac{\max(I) - \min(I)}{\max(I) + \min(I)}. \quad (3)$$

The dependence of the contrast on the vertical path separation created by prisms inside neutron interferometer [14] with different initial momentum distributions is shown in Figure 3(b) (from top: 9 blades, 5 blades, and 1 blade of the focusing monochromator). The red dots are measured data while straight lines are obtained from the measured momentum distributions. Hence by shaping the momentum distribution we can, in principle, achieve a desired coherence length. In this measurement the neutron wavelength was 0.271 nm while the highest obtained vertical coherence length was 79 nm. Another important aspect to note is that the neutron path length is about 0.1×10^9 nm and is about 10^9 bigger than the neutron wavelength. That is why the neutron interferometer is an extremely sensitive device. It is also very sensitive to external disturbances such as vibrational noise, temperature instabilities and gradients, and sounds. Neutrons used for interferometry have velocities on the order 1000 m/s (which is relatively slow compared to the speed of light); that is why neutron interferometers are sensitive to low frequency vibrations. The setup shown in Figure 1 is designed to remove most of such disturbances and preserve long-time phase stability. However the massive vibration isolation stage keeps the interferometer further away from the source and makes it difficult to operate. As a result the facility has a low neutron fluency and is not particularly user friendly which is why neutron interferometers are rarely used for condensed matter applications.

To further help us deal with noise we can employ techniques from quantum information processing such as quantum error correction (QEC) schemes. One approach to passive QEC (well described by Lidar and Whaley in [21]) is a decoherence-free subspace (DFS), which corresponds to finding a subspace of a larger quantum system that is not affected by a noise process and then encoding our desired quantum state in this subspace. A DFS can be implemented in a neutron interferometer to make it insensitive to low

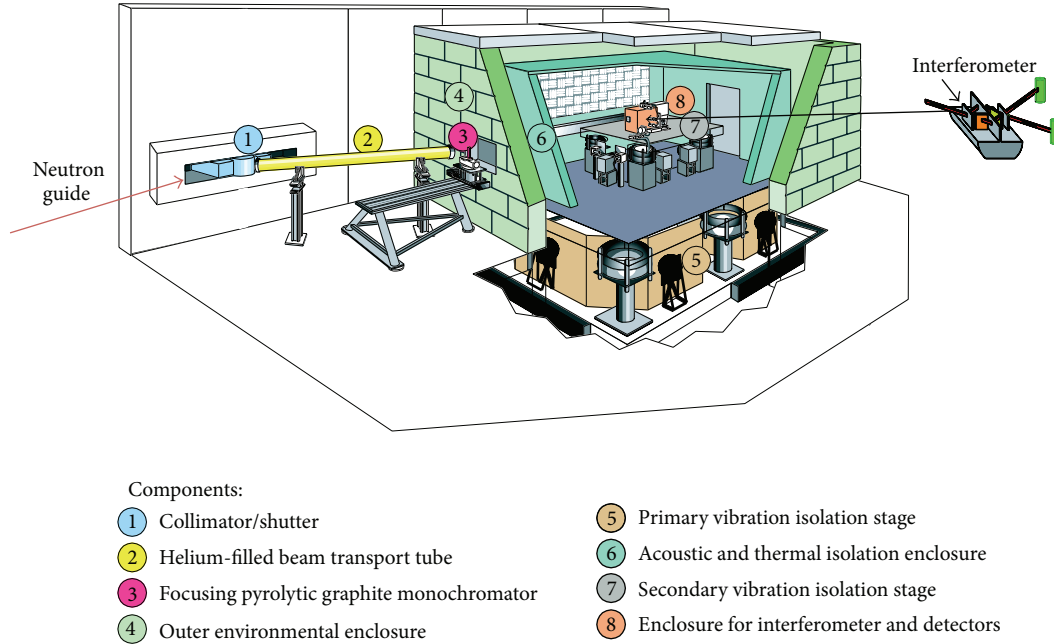


FIGURE 1: Schematic of the Neutron Interferometry and Optics Facility for Neutron Research at the National Institute of Standards and Technology. The isolated 40,000 kg room is supported by six air-springs. The system uses active vibration control to eliminate vibrations above 0.5 Hz. The temperature of the interferometer enclosure is stabilized to 5 mK precision to improve long-term phase stability (diagram also appeared in [16]).

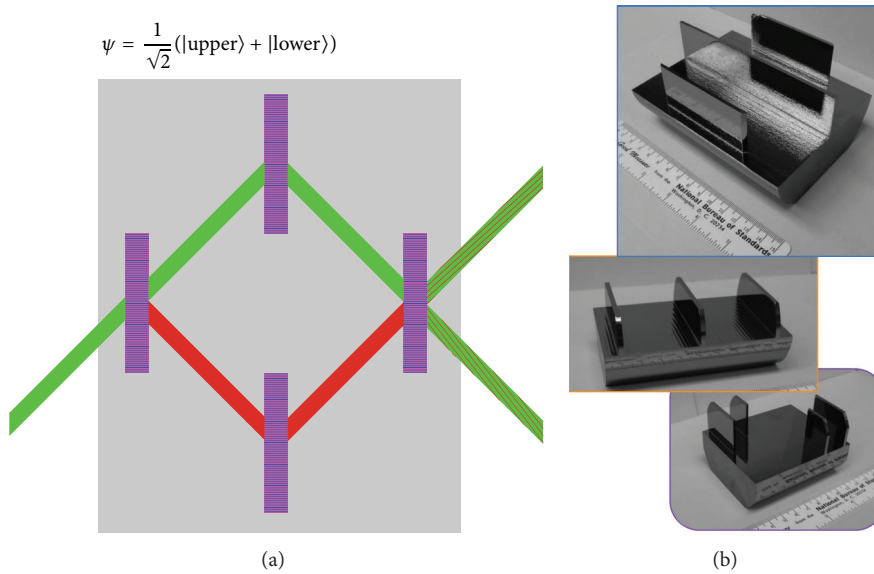


FIGURE 2: (a) Schematic diagram of the neutron paths in a perfect single crystal neutron interferometer. The neutron passing through the interferometer is coherently split into two paths (upper and lower) by the first interferometer blade, redirected by the middle blades (these blades represent mirrors of the light Mach-Zehnder interferometer and are recombined to observe interference effects by the last blade). The neutron’s wave function can be described as superposition of the paths inside the interferometer. (b) Pictures of NIST interferometers with high contrast (>75%).

frequency center-of-mass vibrations. The idea comes from using 2-qubit system shown in Figure 4(a), where each path represents a neutron basis state. In this system vibrational noise enters as the phase difference a neutron acquires by passing through different paths due to movement of the

interferometer. This noise can be represented in a form of σ_z Pauli operator. By removing the center blade (Figure 4(b)) we notice that the phase difference acquired by a neutron traveling through paths $|01\rangle$ and $|10\rangle$ due to the vibrational noise will be the same. Thus if we encode the state into logical

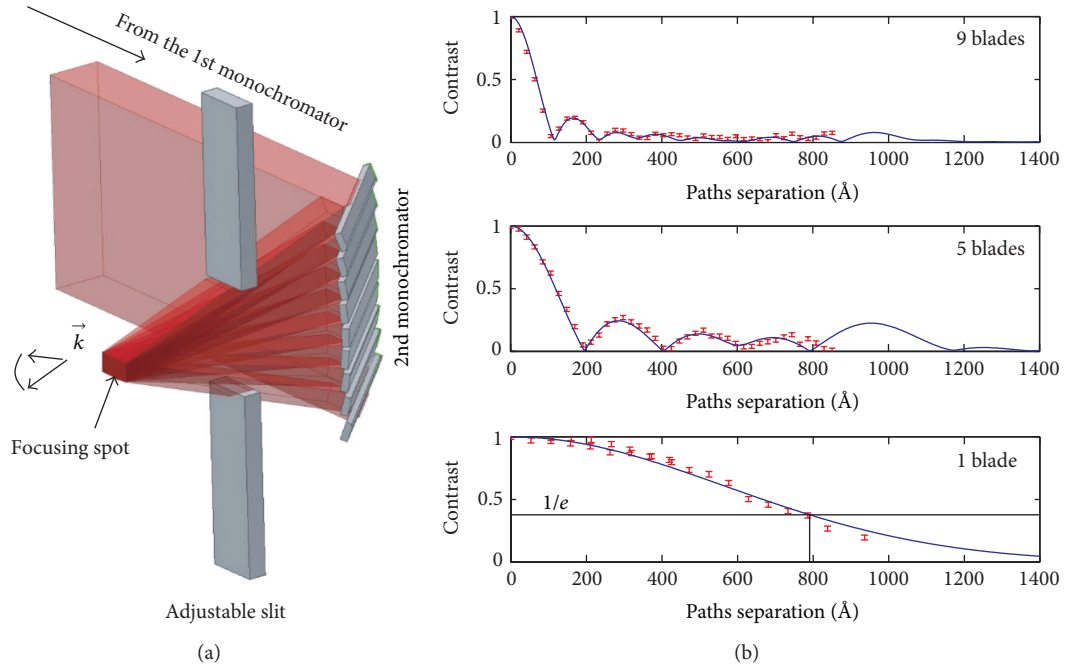


FIGURE 3: (a) Schematic of the second focusing PG monochromator for shaping the vertical momentum distribution of the neutron beam. By shielding some of the blades of the monochromator we can select different neutron momentum distributions. (b) Contrast versus path separations for different momentum distributions. The top figure is obtained when 9 blades of the 2nd monochromator are open, the middle figure when 5 middle blades are open, and the bottom figure when only one middle blade is open [14].

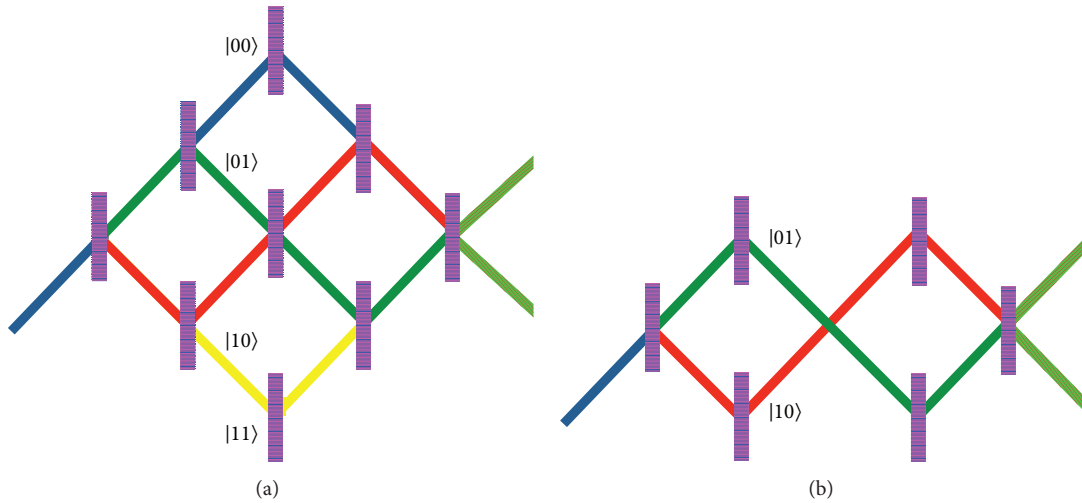


FIGURE 4: (a) Schematic of the 2-qubit (four paths) interferometer. (b) Schematic of the DFS interferometer.

states $|0_L\rangle = |01\rangle$ and $|1_L\rangle = |10\rangle$ then any state represented in this basis will be protected against this vibrational noise. As a result we came up with a DFS design for neutron interferometer shown in Figure 4(b).

To test our theory we built a 5-blade neutron interferometer [22] to accommodate both the Mach-Zehnder and DFS interferometer designs. This allows us to *in situ* change between these two designs without disturbing the facility and avoids discrepancies due to different crystal qualities.

Experimental results are shown in Figure 5(a). Here the top and bottom figures show data for the Mach-Zehnder and DFS interferometers, respectively. The red points give the interferogram without applied vibrations while blue points are when an 8 Hz vibration is applied to the interferometer. Figure 5(a) shows that 8 Hz vibrations are enough to destroy interference of the Mach-Zehnder interferometer while they do not have much effect on the contrast of the DFS interferometer. Figure 5(b) represents numerical simulation of the

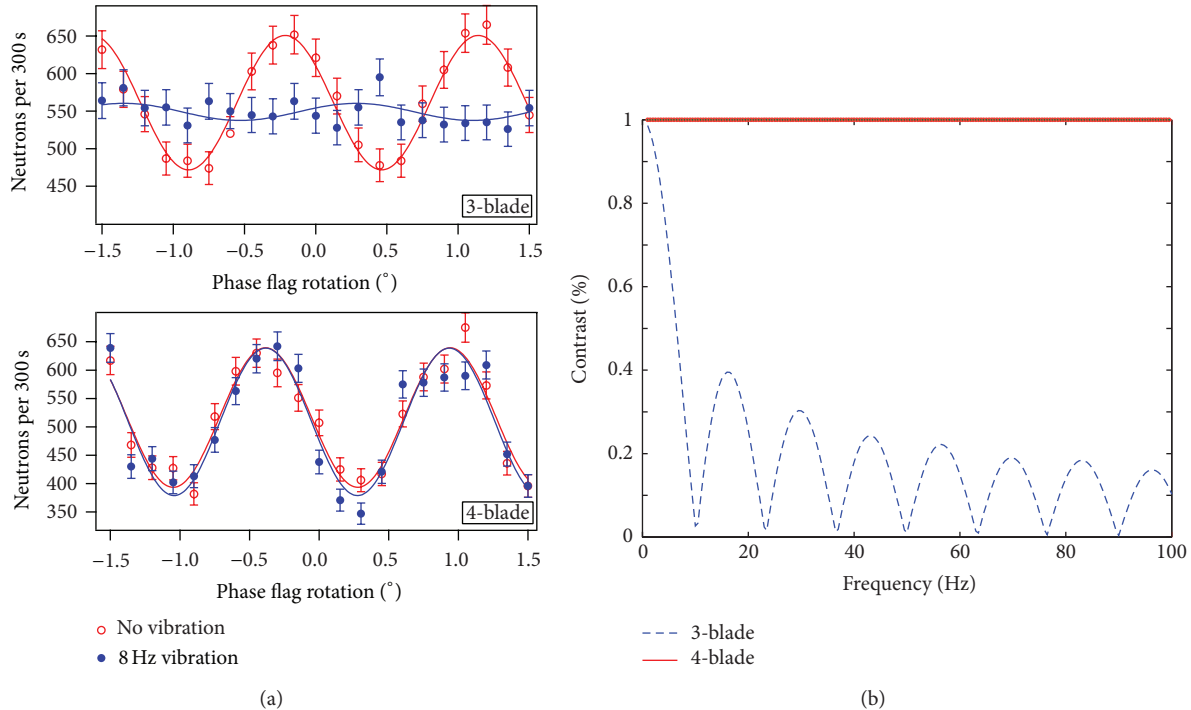


FIGURE 5: (a) Comparison data for standard (top) and DFS (bottom) interferometer designs without (red) vibrations and with (blue) 8 Hz applied vibrations. (b) Numerical simulation of standard interferometer (blue) and DFS (red) contrast versus rotational vibrations [22].

contrast for both the Mach-Zehnder (3-blade) and DFS (4-blade) setups versus frequency of applied vibrations [23]. These simulations clearly show the advantage of the DFS setup in the presence of vibrational noise.

Another aspect of noise in the neutron interferometer we investigated was the effect of random phase noise on the correlations between the neutron path and neutron spin. This type of noise can arise due to surface imperfections in the interferometer blades which introduce a random phase to neutrons traveling through interferometer, thus reducing the measured contrast of the interferometer when averaged over many neutrons. By entangling the path degree of freedom of the neutrons with the neutron spin we investigated how the phase noise behaves in the presence of a postselected spin measurement on the neutron beam. To quantify the correlations between the spin and path degree of freedom we compared quantum discord and entanglement. Quantum discord was originally proposed as a measure of the “quantumness” of correlations between two quantum systems that is more general than entanglement. It can be thought of as quantifying how much disturbance the measurement of one subsystem of a bipartite quantum system can induce on the other.

To investigate this effect we considered a configuration where we entangled the spin and path degrees of freedom of the neutron by placing a spin-rotator in one path of the interferometer and then observed the output path contrast and spin contrast with and without postselected spin measurements [24]. In the absence of spin measurements, our theoretical calculations found that strong phase noise caused

the entanglement to reduce to zero; however the quantum discord remained nonzero. This indicates that nonclassical correlations persist between the spin and path of the neutron and therefore must still be treated as a quantum system. Our calculations predicted, and our experimental results confirmed, that by measuring the Z-component of the neutron spin we could revive spin contrast even in the strong noise case where it would be zero in the absence of spin filtering. Our experimental setup consisted of thin permalloy films deposited on a Si substrate to implement the path-dependent spin rotation, and the spin measurements were implemented using an adiabatic coil to rotate the desired neutron spin state to the Z-basis where spin-up and spin-down neutrons were absorbed and transmitted, respectively, by either Heusler crystals or reflection-mode curved supermirrors.

5. A New Beam Line

Following our progress in understanding the effects of noise on the neutron interferometer and our advances in DFS interferometer design, we have decided to build a new beam line which utilizes the DFS interferometer. This beam line would have relaxed restrictions on the low frequency vibration isolation system. A typical optical table should be sufficient to operate a DFS interferometer beam line. This tremendously simplifies the beam line construction and, in principle, should improve neutron fluency with respect to the existing setup. Figure 6 shows a schematic of the existing beam line and outline for the new beam line.

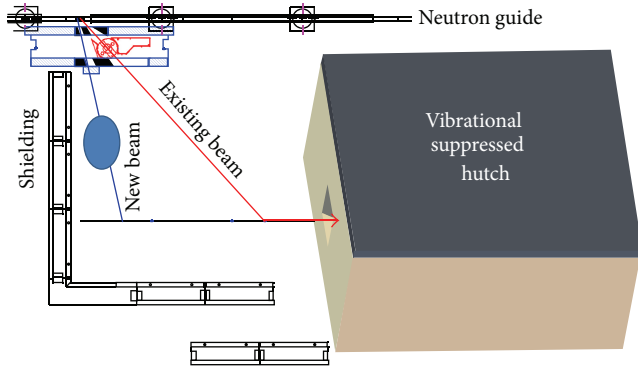


FIGURE 6: Schematic of the existing beam line setup with the hutch and a new beam line for the DFS interferometer.

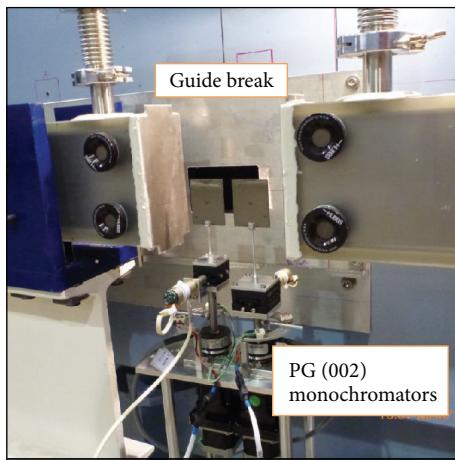


FIGURE 7: A picture of the monochromators for both beam lines inside the guide shielding of the NG7 guide. The crystals are PG crystals with 0.5° mosaic placed in the NG7 guide break.

We extract neutrons from the NG7 NIST NCNR cold beam guide by Bragg diffraction of PG crystal monochromators. Figure 7 shows the NG7 guide break with two new PG crystal monochromators: one is for the existing beam line and another is for the DFS interferometer beam line. This configuration will allow us to independently control the wavelength of the neutrons of both beam lines.

The current configuration shown in Figure 8 is configured for $\lambda = 0.44$ nm neutron wavelength and consists of an optical table (without vibration isolation), a pair of double-V cavity polarizer/analyzer (with greater than 98% polarization efficiency), and ^3He -detectors. Due to the high relative count rate at fractional wavelengths (λ/n , where $n = 2, 3, \dots$) we have installed a Be filter as shown in Figure 8. The beam line is currently under active construction and development.

Conflict of Interests

The authors declare that there is no conflict of interests regarding the publication of this paper.



FIGURE 8: A picture of the new beam line. It consists of a Be filter to remove $\lambda/2$ and $\lambda/3$ components, spin polarizer, spin analyzer, adiabatic spin flippers, temperature controlled enclosure for interferometer, and ^3He -detectors.

Acknowledgments

This work was supported in part by CREATE, Discovery, NSERC, Industry Canada, CERC, CIFAR, and Ministry of Research and Innovation, Province of Ontario, Canada. Support provided by NIST is also gratefully acknowledged. The authors are grateful to Sam Potts and University of Missouri-Columbia Physics Machine Shop for a wonderful job machining the interferometer and for discussions with D. L. Jacobson, T. Borneman, R. A. Barankov, P. Cappellaro, E. R. Sparks, and G. L. Greene.

References

- [1] H. Rauch, W. Treimer, and U. Bonse, "Test of a single crystal neutron interferometer," *Physics Letters A*, vol. 47, no. 5, pp. 369–371, 1974.
- [2] R. Colella, A. W. Overhauser, and S. A. Werner, "Observation of gravitationally induced quantum interference," *Physical Review Letters*, vol. 34, no. 23, pp. 1472–1474, 1975.
- [3] J.-L. Staudenmann, S. A. Werner, R. Colella, and A. W. Overhauser, "Gravity and inertia in quantum mechanics," *Physical Review A*, vol. 21, no. 5, pp. 1419–1438, 1980.
- [4] S. A. Werner, H. Kaiser, M. Arif, and R. Clothier, "Neutron interference induced by gravity: new results and interpretations," *Physica B+C*, vol. 151, no. 1-2, pp. 22–35, 1988.
- [5] D. L. Jacobson, S. A. Werner, and H. Rauch, "Spectral modulation and squeezing at high-order neutron interferences," *Physical Review A*, vol. 49, no. 5, pp. 3196–3200, 1994.
- [6] K. C. Littrell, B. E. Allman, and S. A. Werner, "Two-wavelength-difference measurement of gravitationally induced quantum interference phases," *Physical Review A*, vol. 56, no. 3, pp. 1767–1780, 1997.
- [7] H. Kaiser, N. L. Armstrong, F. E. Wietfeldt et al., "Gravitationally induced quantum interference using a coating interferometer crystal," *Physica B: Condensed Matter*, vol. 2, pp. 1384–1387, 2006.
- [8] M. Zawisky, J. Springer, and H. Lemmel, "High angular resolution neutron interferometry," *Nuclear Instruments and Methods in Physics Research, Section A: Accelerators, Spectrometers, Detectors and Associated Equipment*, vol. 634, Supplement 1, pp. S46–S49, 2011.

- [9] G. L. Greene and V. Gudkov, “Neutron interferometric method to provide improved constraints on non-Newtonian gravity at the nanometer scale,” *Physical Review C*, vol. 75, no. 1, Article ID 015501, 2007.
- [10] P. Brax, G. Pignol, and D. Roulier, “Probing strongly coupled chameleons with slow neutrons,” *Physical Review D: Particles, Fields, Gravitation and Cosmology*, vol. 88, no. 8, Article ID 083004, 2013.
- [11] Y. N. Pokotilovski, “Strongly coupled chameleon fields: possible test with a neutron Lloyd’s mirror interferometer,” *Physics Letters B*, vol. 719, no. 4-5, pp. 341–345, 2013.
- [12] A. P. Serebrov, P. Geltenbort, O. M. Zherebtsov et al., “Experimental search for long-range forces in neutron scattering via a gravitational spectrometer,” *Physical Review C*, vol. 89, no. 4, Article ID 044002, 2014.
- [13] M. Arif, D. E. Brown, G. L. Greene, R. Clothier, and K. Littrell, “Multistage position-stabilized vibration isolation system for neutron interferometry,” in *Vibration Monitoring and Control*, vol. 2264 of *Proceedings of SPIE*, pp. 20–26, San Diego, Calif, USA, 1994.
- [14] D. A. Pushin, M. Arif, M. G. Huber, and D. G. Cory, “Measurements of the vertical coherence length in neutron interferometry,” *Physical Review Letters*, vol. 100, no. 25, Article ID 250404, 2008.
- [15] M. G. Huber, M. Arif, T. C. Black et al., “Precision measurement of the n-He3 incoherent scattering length using neutron interferometry,” *Physical Review Letters*, vol. 102, no. 20, Article ID 200401, 2009.
- [16] H. Rauch and S. A. Werner, *Neutron Interferometry*, Oxford University Press, New York, NY, USA, 2000.
- [17] U. Bonse and H. Rauch, *Neutron Interferometry*, Oxford University Press, Oxford, UK, 1979.
- [18] H. Kaiser, S. A. Werner, and E. A. George, “Direct measurement of the longitudinal coherence length of a thermal neutron beam,” *Physical Review Letters*, vol. 50, no. 8, pp. 560–563, 1983.
- [19] H. Rauch, H. Wölwitsch, H. Kaiser, R. Clothier, and S. A. Werner, “Measurement and characterization of the three-dimensional coherence function in neutron interferometry,” *Physical Review A*, vol. 53, no. 2, pp. 902–908, 1996.
- [20] “Chapter 4, coherence properties,” in *Neutron Interferometry*, H. Rauch and S. A. Werner, Eds., Oxford University Press, Oxford, UK, 2000.
- [21] D. A. Lidar and K. B. Whaley, “Decoherence-free subspaces and subsystems,” in *Irreversible Quantum Dynamics*, F. Benatti and R. Floreanini, Eds., vol. 622 of *Lecture Notes in Physics*, pp. 83–120, Springer, Berlin, Germany, 2003.
- [22] D. A. Pushin, M. G. Huber, M. Arif, and D. G. Cory, “Experimental realization of decoherence-free subspace in neutron interferometry,” *Physical Review Letters*, vol. 107, no. 15, Article ID 150401, 2011.
- [23] D. A. Pushin, M. Arif, and D. G. Cory, “Decoherence-free neutron interferometry,” *Physical Review A*, vol. 79, no. 5, Article ID 053635, 2009.
- [24] C. J. Wood, M. O. Abutaleb, M. G. Huber, M. Arif, D. G. Cory, and D. A. Pushin, “Quantum correlations in a noisy neutron interferometer,” *Physical Review A*, vol. 90, no. 3, Article ID 032315, 2014.

Research Article

Status of the GRANIT Facility

Damien Roulier,^{1,2} Francis Vezzu,³ Stefan Baeßler,⁴ Benoît Clément,³ Daniel Morton,⁴ Valery V. Nesvizhevsky,² Guillaume Pignol,³ and Dominique Rebreyend³

¹Université Grenoble-Alpes, 38000 Grenoble, France

²Institut Max von Laue-Paul Langevin, 71 avenue des Martyrs, 38000 Grenoble, France

³LPSC Grenoble, Université Grenoble-Alpes, CNRS/IN2P3, 53 avenue des Martyrs, 38026 Grenoble Cedex, France

⁴Physics Department, University of Virginia, 382 McCormick Road, Charlottesville, VA 22904, USA

Correspondence should be addressed to Damien Roulier; roulier@ill.fr

Received 6 June 2014; Accepted 6 August 2014

Academic Editor: Ignatios Antoniadis

Copyright © 2015 Damien Roulier et al. This is an open access article distributed under the Creative Commons Attribution License, which permits unrestricted use, distribution, and reproduction in any medium, provided the original work is properly cited. The publication of this article was funded by SCOAP³.

The GRANIT facility is a follow-up project, which is motivated by the recent discovery of gravitational quantum states of ultracold neutrons. The goal of the project is to approach the ultimate accuracy in measuring parameters of such quantum states and also to apply this phenomenon and related experimental techniques to a broad range of applications in particle physics as well as in surface and nanoscience studies. We overview the current status of this facility, the recent test measurements, and the nearest prospects.

1. Introduction

The GRANIT facility [1, 2] is a follow-up project, which is motivated by the recent discovery of gravitational quantum states of ultracold neutrons (UCNs) [3–5]. The main goal of the project is to realize the resonance spectroscopy of those quantum states, with the prospect of achieving an unprecedented sensitivity. Such precision measurements would address in particular searches for extra short-range fundamental forces [6–9]. Also the phenomenon of gravitational quantum states and related experimental techniques could be applied to a broad range of other applications in particle physics as well as in surface and nanoscience studies [10].

GRANIT is located at the level C of the Institut Laue-Langevin (ILL) in Grenoble, at the H172A beamline as shown in Figure 1. The instrument comprises an ultracold neutron source based on the production of UCNs in superfluid helium and a spectrometer installed in an ISO 5 class clean room, pictured in Figure 2. A monochromatic neutron beam (0.89 nm wavelength) is extracted from a white cold neutron beam with a monochromator [11] and guided towards the

superfluid helium bath where UCNs are produced [2, 12, 13]. An extraction guide allows us then to transfer those UCNs to the spectrometer.

In the spectrometer, UCNs are first stored in an intermediate storage volume. To exit this volume, neutrons must go through an extraction slit of height $\approx 100 \mu\text{m}$, a compromise between the total UCN flux and the UCN phase-space density. Then neutrons will bounce over high quality mirrors very close to the surface and the method of resonance spectroscopy [14] will be applied. The resonance can be induced by a vibration of the bottom mirror, as used by the QBounce collaboration [15] or an oscillating magnetic field gradient as in the GRANIT spectrometer [16].

In 2013 we have performed extensive tests of the various components of the facility and connected for the first time the source to the spectrometer. In this paper we will present the characterization of the whole UCN chain: the 0.89 nm neutron beam, the cryogenic production volume, the extraction guides, and the mirror assembly. We also present a confrontation of the measurements to Monte-Carlo simulations. Finally we present the first UCN flux measurement in the GRANIT spectrometer.

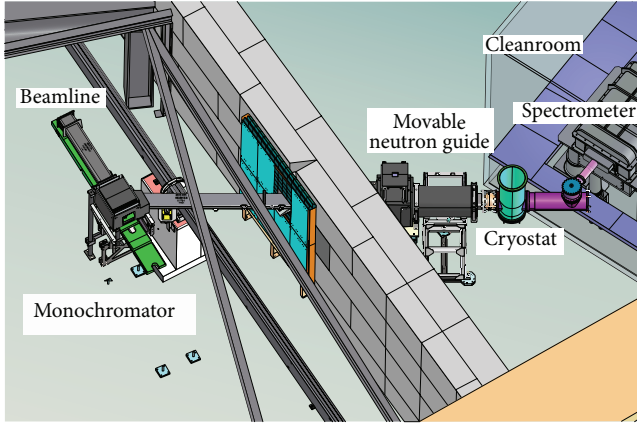


FIGURE 1: The GRANIT instrument at Level C of ILL, Grenoble.

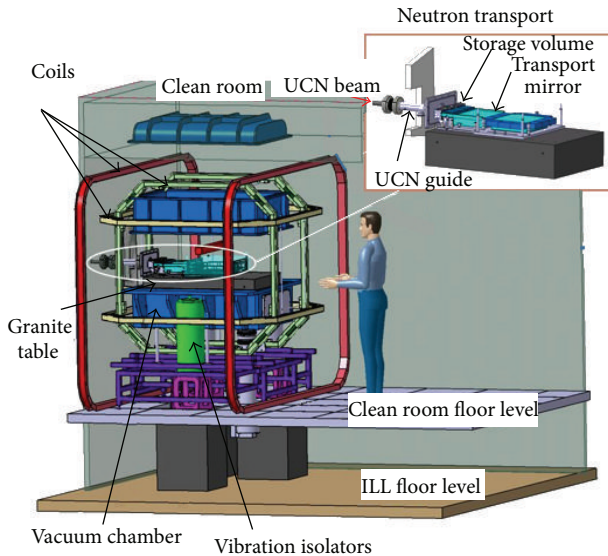


FIGURE 2: The spectrometer in the cleanroom. Measurement and control instruments are installed on a flat massive granite table with the mass of 550 kg, all inside a welded aluminum vacuum chamber with passivated wall surfaces. All this is placed in a clean controlled area (ISO 5) in order to protect the delicate optical elements.

2. 0.89 nm Neutrons Beam

In superfluid helium, cold neutrons with the wavelength of $\lambda = 0.89$ nm can be converted into UCNs through resonant phonon excitation [17]. Therefore, the UCN production rate in the source will depend directly on the neutron flux at this precise wavelength $(d\Phi/d\lambda)|_{0.89 \text{ nm}}$.

2.1. Monochromator Adjustment. The monochromator [11] is composed of 18 intercalated stage-2 KC_{24} crystals, with a lattice constant of $d = 8.74$ Å. According to the Bragg formula for the first order reflection, $2d \sin \theta = \lambda$, the outgoing beamline angle corresponding to $\lambda = 0.89$ nm is found to be $2\theta = 61.2$ degrees, defining the geometry of the installation downstream.

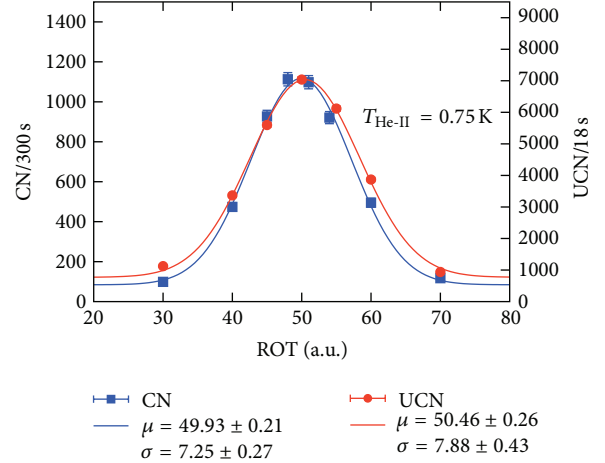


FIGURE 3: Neutron rate as a function of the monochromator rotation angle, for UCNs (dots) and cold neutrons (squares).

The position and orientation of the monochromator can be adjusted remotely with five parameters: rotation, two tilt angles, and two translation axes. These parameters are optimized by maximizing the UCN flux out of the source. The most critical parameter is the rotation of the monochromator, for which the neutron count rate varies by 80% of maximum a few degrees away from the optimal position. For the other parameters, within their whole range, the count rate varies at most by 40%. The result of the scan is shown in Figure 3. We checked that maximum UCN flux coincides with the maximum cold neutron flux, indicating that the setup is aligned correctly.

2.2. Differential Neutron Flux. We have characterized the wavelength distribution in the beam using the time of flight (TOF) technique. Two measurements were performed: the first over a flight length of 78 ± 1 cm, the second over 28 ± 1 cm. The spectrum of the first measurement is presented in Figure 4, together with a fit of the peaks. We obtained for the first order peak the central wavelength $\lambda = 0.879(11)$ nm. The uncertainty is dominated by the error on the flight length, which is itself defined by the uncertainty of knowledge of the position in the gaseous detector where the reaction occurred. The width of the peak, $\sigma = 0.022$ nm, is compatible with the expected TOF resolution.

The relative intensities of the peak shown in Figure 4 do not reflect the relative intensities of the corresponding neutron fluxes due to at least three important effects. First, the detector efficiency is proportional to λ according to the $1/v$ law. Second, losses in air, estimated to be 13% for 0.89 nm neutrons, are also proportional to λ . Finally, since different wavelength components of the beam have different angular divergencies, the geometrical acceptance of the setup is also wavelength dependent. To suppress the latter, a second TOF measurement with a shorter flight length of 28 ± 1 cm was performed.

We show in Figure 5 the TOF spectrum recorded at the short distance. After correcting for the detector efficiency, we

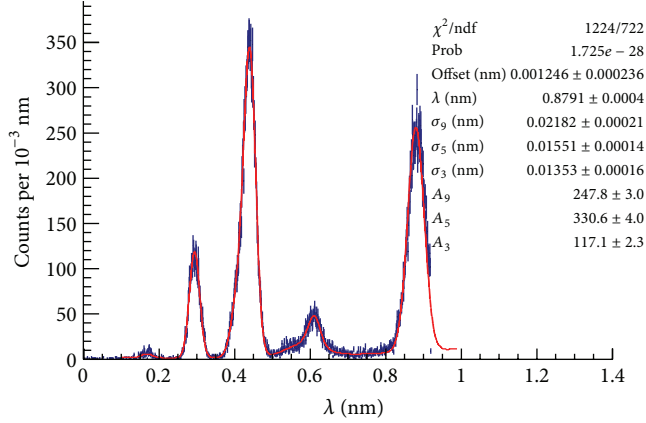


FIGURE 4: Long-distance (78 cm) TOF spectrum. It is assumed that the three main peaks arise from the three first orders of Bragg diffraction which fixes the wavelengths $\lambda/2$ and $\lambda/3$ for the second and third order peaks. There are 21 other free parameters to account for the offset of the X-axis, the amplitudes and width of the Gaussian peaks, as well as ad hoc background description.

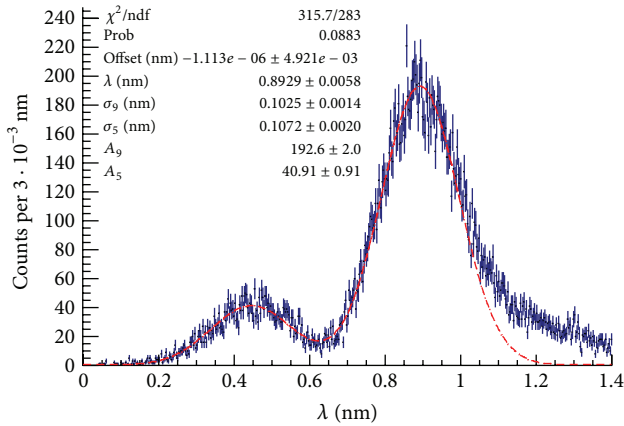


FIGURE 5: Short-distance (28 cm) TOF spectrum. The analysis is similar to that for Figure 4. The dashed line is here to guide the eye, and the corresponding data points were not included in the fit.

determined the relative contribution of the first and second order diffraction peaks to the total flux as

$$p_{0.89} = 0.74, \quad p_{0.445} = 0.26. \quad (1)$$

2.3. Integral Neutron Flux. To determine the integral neutron flux of the H172A beamline, we have used the standard gold foil activation technique that allows us to measure the capture flux density defined by

$$\Phi_{\text{gold}} = \int \frac{d\phi}{d\lambda} \frac{\lambda}{\lambda_{\text{th}}} d\lambda, \quad (2)$$

where $\lambda_{\text{th}} = 0.18$ nm is the wavelength of thermal neutrons. In July 2012 with a reactor power of 48 MW, we have obtained the following capture flux density:

$$\Phi_{\text{gold}} = 6.5 \times 10^8 \text{ cm}^{-2} \text{ s}^{-1}. \quad (3)$$

Knowing the proportion of each diffracted peak p_{λ} , neutron flux in the 0.89 nm peak can be calculated:

$$\Phi_{[0.89 \text{ nm}]} = \Phi_{\text{gold}} \times \frac{0.18 \text{ nm}}{0.89 \text{ nm}} \times \left(\sum_{\lambda \in \text{peaks}} \frac{p_{\lambda}}{p_{0.89}} \times \frac{\lambda}{0.89 \text{ nm}} \right)^{-1}. \quad (4)$$

From the differential neutron flux results (equation (1)), we estimate $\Phi_{[0.89 \text{ nm}]} = (1.1 \pm 0.1) \times 10^8 \text{ cm}^{-2} \text{ s}^{-1}$. Although the intrinsic width of the peak is unknown, it cannot be larger than the measured TOF width $\sigma = 0.02$ nm. Assuming a Gaussian shape for $d\Phi/d\lambda$, we deduce a worst case scenario estimate (with our limit on σ) of the differential neutron flux at 0.89 nm:

$$\left. \frac{d\Phi}{d\lambda} \right|_{0.89 \text{ nm}} = \Phi_{[0.89 \text{ nm}]} \times \frac{1}{\sigma \sqrt{2\pi}}. \quad (5)$$

The actual flux inside the UCN conversion volume is further reduced by two effects. First, the walls of the conversion volume (0.85 mm thick aluminum and 1 mm thick beryllium) attenuates the beam by a factor of 0.895. Then, because of the angular divergence of the beam of 30 mrad, the fraction of the cold beam interacting with the source is 0.72 (estimated with a Monte-Carlo simulation).

Thus, the effective 0.89 nm differential flux inside the source is

$$\left. \frac{d\Phi}{d\lambda} \right|_{0.89 \text{ nm}}^{\text{eff}} = (1.3 \pm 0.2) \times 10^9 \text{ cm}^{-2} \text{ s}^{-1} \text{ nm}^{-1} \quad (6)$$

with the reactor power of 48 MW. As the conversion rate in BeO vessel can be estimated [2], the volumic production rate is

$$P = (4.97 \pm 0.38) \times 10^{-9} \text{ nm} \cdot \text{cm}^{-1} \times \left. \frac{d\Phi}{d\lambda} \right|_{0.89 \text{ nm}}^{\text{eff}}. \quad (7)$$

We deduce that we produce $P \times V = 32000$ UCN/s in our 5-liter vessel with the reactor power of 48 MW.

3. UCN Source

The GRANIT superthermal UCN source is an evolution of the SUN1 apparatus [12, 13]. The UCN conversion volume consists of a vessel made out of BeO/Be filled in with superfluid ^4He , where 0.89 nm neutrons are downscattered to the UCN energy range by resonant phonon excitation. This rectangular volume of the size $7 \times 7 \times 100 \text{ cm}^3$ is placed in continuity with the neutron guide, which is also of squared section ($7 \times 7 \text{ cm}^2$). The conversion volume is encased in a cryostat that allows cooling the volume down to below 0.8 K. A first commissioning of SUN1 at its definitive position was reported in [12, 13], where a large diameter extraction guide from the source to a UCN detector was installed. In order to avoid diluting of UCNs in the phase-space density, a more elaborate extraction guide assembly, with smaller diameter in particular, was designed and built. In the following we report the necessary modifications to the source as well as the current performances.

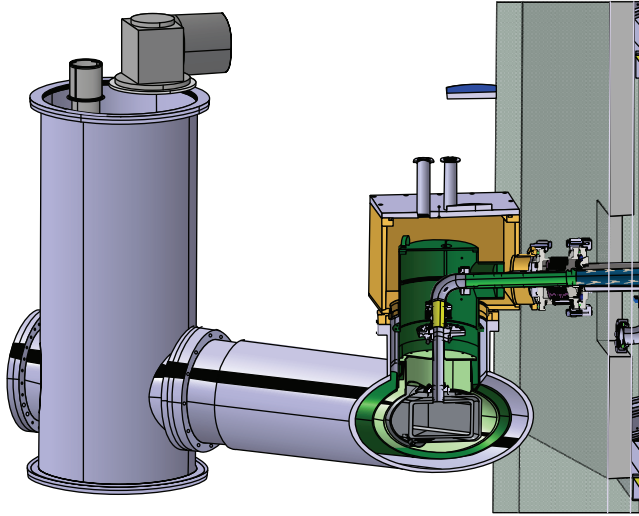


FIGURE 6: Extraction guides from the source to the spectrometer. The extraction guides are composed of several tubular elements, which are thin foils of stainless steel inserted inside tubes. The design of the guides allows compensating for the misalignment between the source and the spectrometer.

To determine these performances, a temporary set-up was installed. A box (filled in with Argon to reduce the UCN losses) was connected to the UCN extraction guide outside the clean room. That set-up allowed us to perform our first measurements with UCNs.

3.1. Cryostat. With the assembly of the new extraction presented in Figure 6, which connects the coldest part to the ambient temperature, first tests showed a loss of cryogenic power. In the first configuration it was not possible to cool down the UCN volume below the temperature of 1 K; thus we had to increase the cryogenic power of the refrigerator. A first temporary set-up using a LN_2 cooling system for the thermal screens (around the inner parts of the extraction) was installed in order to validate that increasing power could solve the problem. This set-up permitted us to reach the temperature of 0.74 K. In the second configuration this LN_2 cooling system was replaced with a Sumitomo cold head 150 W @ 77 K. The outlet box of the cryostat and some thermal screens were also replaced. The current cryogenic system is now adapted for our configuration. Figure 7 shows a cool down and filling of the conversion volume.

3.2. Separation Windows. In several occurrences, we need to physically separate volumes at different pressures keeping UCN-transparency. This is the case for any gaseous UCN detector. Also, the spectrometer vacuum has to be separated from the extraction vacuum to avoid reheating in case of spectrometer openings. Any material separation is a cause of extra UCN losses due to quantum reflection and absorption.

The first choice for a material was aluminum that has both low optical potential (54 neV, corresponding to a critical velocity of 3.2 m/s) and small neutronic absorption cross-section (~ 102 barn for 5 m/s neutrons). However, soft UCNs

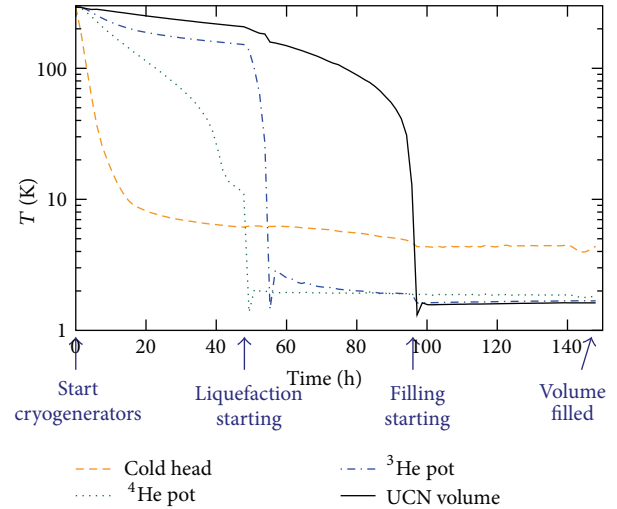


FIGURE 7: A successful cooldown in 100 hours. The temperature of several areas of the cryostat is constantly monitored. It takes 48 hours from the beginning to start ^4He liquefaction, which helps cooling the conversion volume. 48 hours later, the conversion volume is cold enough for keeping liquid ^4He . 52 additional hours are needed to fill in this volume. Then, He-II can be cooled down to the temperature of 0.74 K.

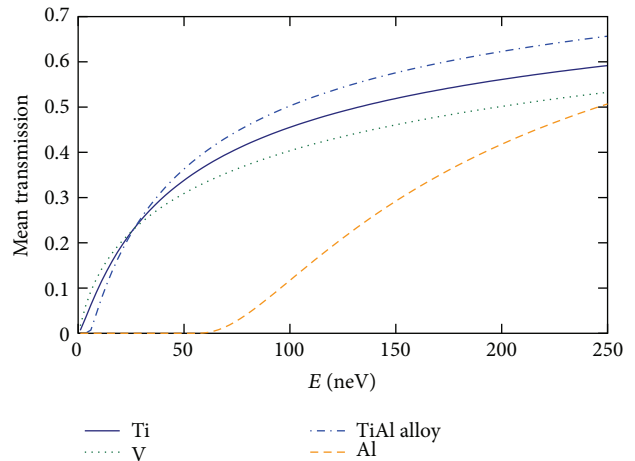


FIGURE 8: An analytical calculation of the probability of transmission of UCNs through two foils ($15\ \mu\text{m}$ each for Ti, V, and TiAl alloy, $30\ \mu\text{m}$ each for Al) for an isotropic UCN gas as a function of UCN energy.

(with the velocity lower than 3.2 m/s) are supposed to represent a nonnegligible fraction of UCNs extractable out of the source. A simple calculation of the transmission through two windows (one in the extraction and one for the gaseous detector) considering an isotropic angular distribution of UCNs, illustrated in Figure 8, shows that better materials exist for our application.

We conclude that titanium would be better-suited as long as soft UCNs are available, and pure titanium windows are quite easy to set up. However, the thickness of the windows is far more critical for titanium than for aluminum (because of



FIGURE 9: Vacuum-separating window in the extraction guides. The foil must guarantee the vacuum tightness but also it should resist to an overpressure of 1.5 bar max in both directions in case of eventual fast heating of the source. Such overpressure is limited using two safety valves. The window is made with 2 aluminum half pieces milled by electrocutting reinforced by letting ribs 0.25 mm thick. Between these two parts a titanium foil 0.015 mm thick and 2 o-rings are inserted. The assembly is bolted. The window assembly had been tested with success under vacuum and under 5 bar pressure.

the absorption cross-section for neutrons). Thus, depending on mechanical constraints, the windows should be as thin as possible. Figure 9 shows the extraction window between the extraction and the spectrometer that was designed for GRANIT.

3.3. UCN Count Rate versus Temperature. A measurement of the UCN count rate as a function of He-II temperature was realized with a ^3He counter. The extraction window was made of a $30\ \mu\text{m}$ aluminum foil, as well as the detector entrance window. The result is presented in Figure 10.

Two regimes appear. When $T \geq 1.2\ \text{K}$, the UCN flux is highly dependent on temperature because of the upscattering of UCNs in He-II. At lower temperature ($T \leq 0.9\ \text{K}$), the UCN flux saturates, because the main losses are caused by absorption of UCNs in the beryllium walls of the conversion volume. If this effect was an order of magnitude smaller, the transition would occur at a lower temperature and the saturation UCN density would be nearly an order of magnitude higher.

When the UCN valve of the source is open, radiative heat on He-II causes an important increase in temperature ($0.045\ \text{K}/\text{min}$). For this reason, the valve should not be opened for longer than 10–15 seconds in order to have a reliable and stable measurement, as well as to be able to cool back down He-II ($\sim 10\ \text{min}$). Thus, the source can operate in a pulsed regime at a temperature below $0.9\ \text{K}$ (stable as long as the opening time of the valve is short), or in a continuous mode at a higher but always stable temperature ($\sim 1.3\ \text{K}$), but with a smaller UCN flux.

3.4. Source and Extraction Characteristic Times. We define two characteristic times for this system. The emptying time τ_{emptying} is the average time necessary to extract UCNs from the apparatus. The storage time τ_{storage} is the average lifetime of UCNs in the isolated source.

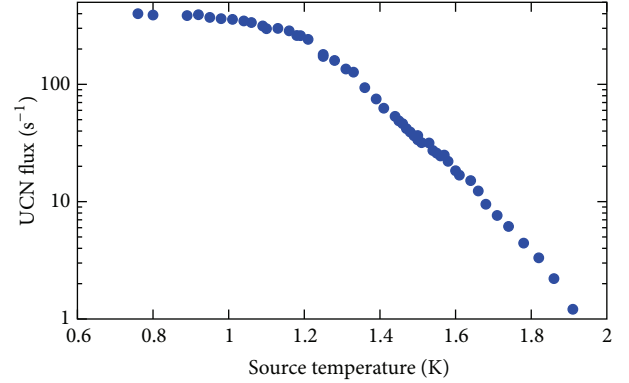


FIGURE 10: UCN count rate versus the temperature of He-II. The cold neutron beam constantly passes through the source and the UCN valve is opened periodically.

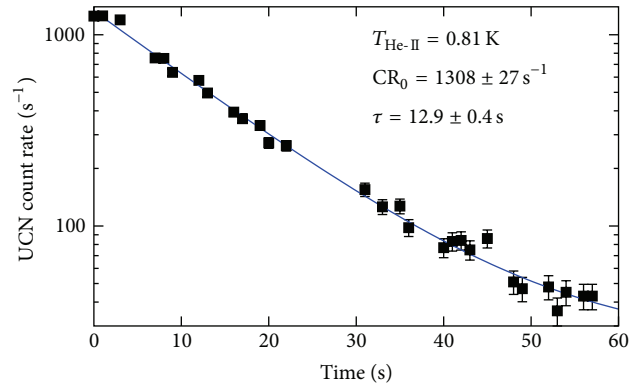


FIGURE 11: Emptying time of UCNs in the source and extraction with Ti windows.

TABLE 1: Emptying time of UCNs in the source and extraction with two titanium windows for several waiting times.

Waiting time (s)	τ_{emptying} (s)
0	12.9 ± 0.4
50	18.6 ± 0.6
100	23.8 ± 1.4

The emptying time is measured by accumulating UCNs in the source during 2 min, then closing the cold beam shutter and waiting for a few seconds. The UCNs are then released through the extraction to a UCN detector, with a differential UCN count measurement. The data are fitted with a single exponential as illustrated in Figure 11. The results for different waiting times are summarized in Table 1. One can notice that the longer the waiting time, the longer the emptying time. We conclude that the softer UCNs are stored longer in the source, and that a sufficiently long time must be chosen to integrate the number of neutrons extracted without introducing a bias between measurements with different waiting times.

The storage time is measured in a similar way, but the total number of extracted neutrons is counted, and the procedure

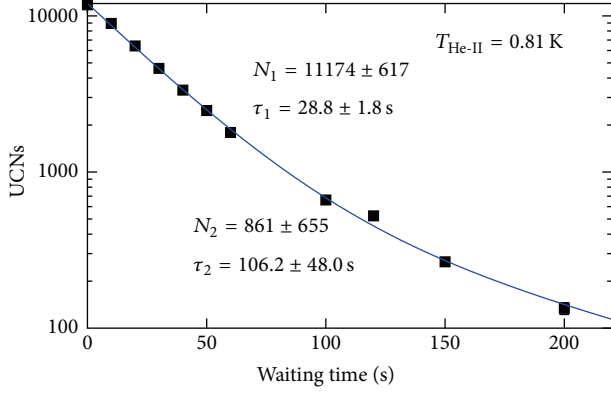


FIGURE 12: Storage time of UCNs in the source with Ti windows.

TABLE 2: Storage time in different configurations.

Extraction	Detector	τ_{storage} (s) @ 0.81 K
Al	Al	21.0 ± 0.4
Ti	Al	21.3 ± 0.4
Ti	Ti	30.4 ± 0.7

is repeated for different waiting times. This time is obtained by fitting the data with a double exponential, as shown in Figure 12, and calculating the weighted geometric mean of the two decay constants. The two exponentials allow accounting for several UCN populations with different velocities and storage times where a single exponential is not sufficient.

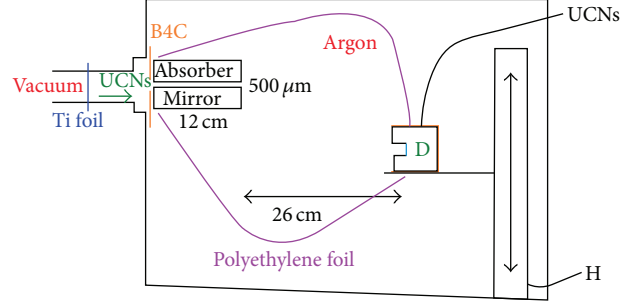
The storage time measurement was performed for several combinations of extraction and detector windows materials. The results are summarized in Table 2. Having at least one aluminum window cuts out the soft UCNs, resulting in similar storage times for Al-Al and Ti-Al configurations. Using only titanium allows recovering the soft UCNs. The noticeable increase of the storage time is expected as slower UCNs have less collisions on the source walls. The choice of titanium windows is therefore justified and gives us access to a nonnegligible fraction of the UCN velocity spectrum.

The results show that $\tau_{\text{emptying}} < \tau_{\text{storage}}$: the source can work in an accumulation mode where UCNs are accumulated in the source and then released all at the same time towards the spectrometer.

3.5. UCN Velocity Spectrum. The velocity distribution of UCNs can be determined with a free fall experiment, as described in Figure 13. The height of free fall for a UCN with a defined horizontal velocity is

$$h = \frac{g}{2} \left(\frac{d_{\text{freefall}}}{v_{\text{UCN}}} \right)^2. \quad (8)$$

Assuming we have spatially isotropic distribution of UCNs within our collimation system (this assumption is valid with high accuracy for any broad angular distribution of UCNs in the extraction system), the measurement of

FIGURE 13: Set-up for free fall measurement: in an argon-filled box, the UCN beam is collimated with a 12 cm long absorber-mirror system forming a slit of height $500 \mu\text{m}$. A detector with a $15 \mu\text{m}$ thick titanium window is placed at the distance of 26 cm from the slit, and record the neutron count as a function of the fixed free fall height.

horizontal velocity of the collimated UCNs is representative of the velocity distribution of the UCNs in the extraction.

The recorded UCNs counts as a function of the free fall height are shown in Figure 14. In order to obtain a velocity spectrum for this measurement, we make a Monte-Carlo simulation of the experiment to fit the initial velocity spectra to the data. Two shapes were assumed for the initial spectrum: a Gaussian distribution and an asymmetric triangular distribution. Both fitted correctly the data, and the obtained results for the mean and RMS of the distribution are

$$\begin{aligned} \mu_{\text{Gauss}} &= 5.1 \text{ m} \cdot \text{s}^{-1}, & \sigma_{\text{Gauss}} &= 1.6 \text{ m} \cdot \text{s}^{-1}, \\ \mu_{\text{Triangle}} &= 5.3 \text{ m} \cdot \text{s}^{-1}, & \sigma_{\text{Triangle}} &= 1.4 \text{ m} \cdot \text{s}^{-1}. \end{aligned} \quad (9)$$

The asymmetric triangular distribution is zero below 2.2 m/s, maximum at 4.5 m/s, and zero above 9.0 m/s. In both cases, we obtain a coarse UCN velocity spectrum and notice a quite wide distribution around the mean value.

Because of the low statistics (some hundreds of UCNs counted for 30 minutes), the valve was always open (thus the temperature was 1.35 K). In this configuration, there is no accumulation of soft UCNs in the source, thus a higher mean velocity than what we could have. This method of measurement for the velocity spectrum of UCNs, though lacking in precision, was successful. The precision could be improved by designing a UCN detector with a dedicated geometry or a large position-sensitive detector and a vacuum-tight environment. The result itself is in agreement with what we expected and confirms that the source/extraction system we use is well-suited for the GRANIT spectrometer.

4. Spectrometer

4.1. Description. UCNs are transported through the extraction guide from the He-II source to the spectrometer as shown in Figure 6. The extraction guides and the extraction window are the same as the previous configuration. The guides connect the source to an intermediate storage volume depicted in Figure 15. Optical elements, at the heart of the spectrometer, are connected at the exit of the storage volume. They are sets of silica pieces with different coatings

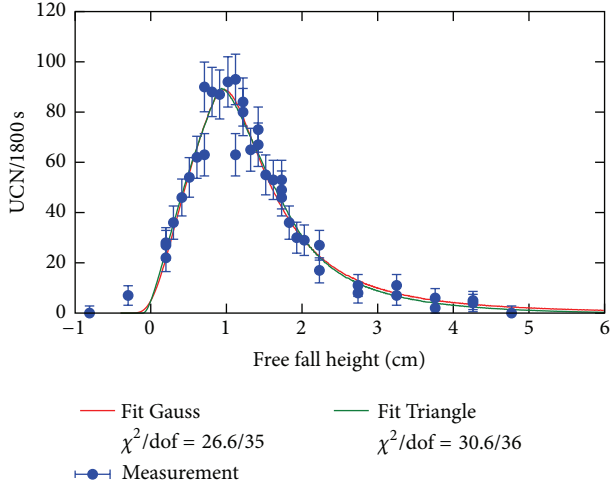


FIGURE 14: Number of UCNs detected for 30 min versus the free fall height. During the measurement, the temperature of He-II was 1.35 K. Since the UCN spectrum is defined by the storage and transmission properties of the whole system, and the temperature of He-II affects only the total count rates, the exact value of the temperature is of no importance. This measurement was fitted with a Monte-Carlo simulation, assuming an initial triangular or Gaussian spectrum.

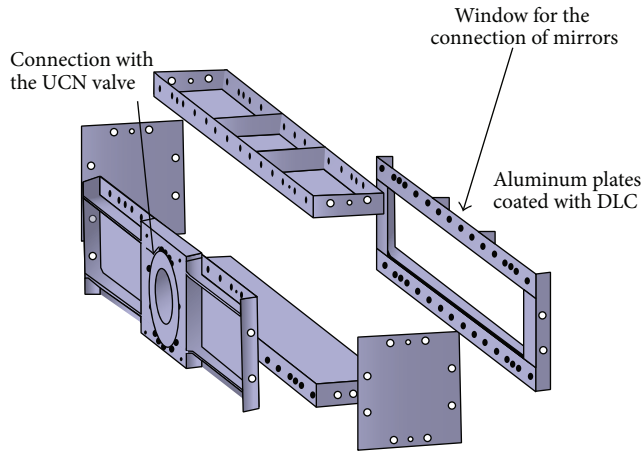


FIGURE 15: The DLC-coated storage volume. The inner sizes are $40 \times 40 \times 340 \text{ mm}^3$.

and roughness states, providing different conditions to the transport of UCNs. They are described in Figures 16 and 17. All these parts have been provided by the SESO Company in Aix en Provence (France), and Diamond-Like Carbon (DLC) coatings were applied by Advanced Material Laboratory (IN2P3, France).

The intermediate storage volume, made of several aluminum parts coated with DLC, is designed to randomize the UCNs trajectories. In order to close the storage volume, a nickel-coated butterfly valve is used, preventing the UCNs from returning into the source. The exit of the intermediate storage volume is closed by the first optical elements of the spectrometer, forming a slit and allowing only UCNs

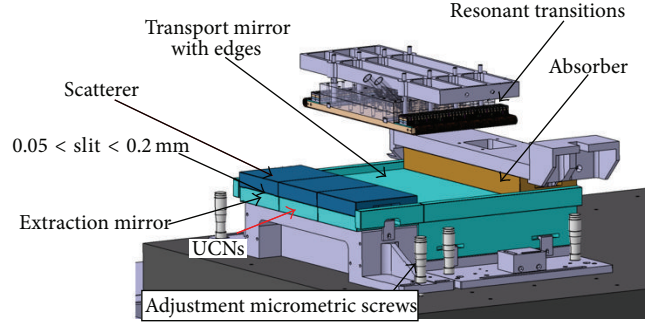


FIGURE 16: Schematics and pictures of the optical elements. The extraction mirror and the scatterer have the same sizes ($300 \times 100 \times 20 \text{ mm}^3$) and each consists of 3 pieces of $100 \times 100 \times 20 \text{ mm}^3$ glued together. The mean roughness of the extraction mirror (floor) is very low (0.5 nm) to allow for specular bouncing, whereas the mean roughness of the scatterer (ceiling) is intentionally high ($5.6 \mu\text{m}$) to allow UCNs with too high vertical velocity to be diffused back. The transport mirror ($300 \times 250 \times 70 \text{ mm}^3$) has a surface mean roughness of 0.5 nm and a planarity of 80 nm . The absorber mirror is $300 \times 90 \times 30 \text{ mm}^3$.

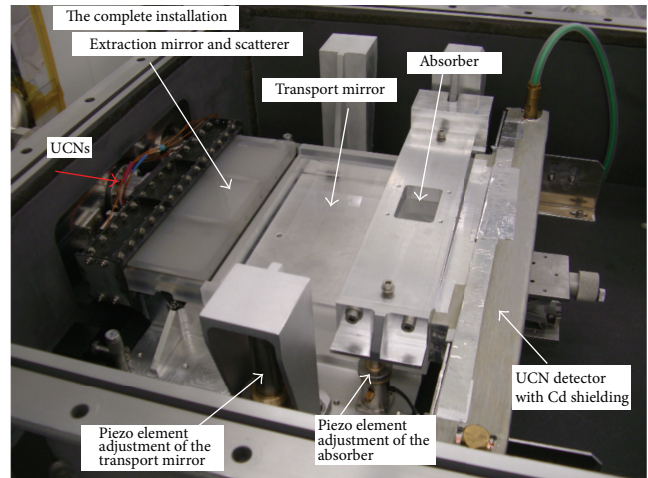


FIGURE 17: The optical elements on the granite table. The extraction mirrors assembly and the transport mirror are placed on two separate adjustable supports. Their adjustment could be done with $3 + 3$ micrometric screws. To adjust the height and the orientation of the surface of the transport mirror with a great accuracy, we use 3 piezo-electric elements. The distance between the absorber and the transport mirror is adjustable as well using 3 piezo-electric elements. The piezos are driven from the control computer with a Labview application.

with negligible vertical velocity to be transmitted. The slit is composed of an extraction mirror and a scatterer. The scatterer is placed above the extraction mirror at a height between 50 and $200 \mu\text{m}$. Both are coated with DLC in order to provide reflection of UCNs with a broad velocity range from the surfaces and thus to assure proper operation of the so-called semidiffusive slit [18, 19].

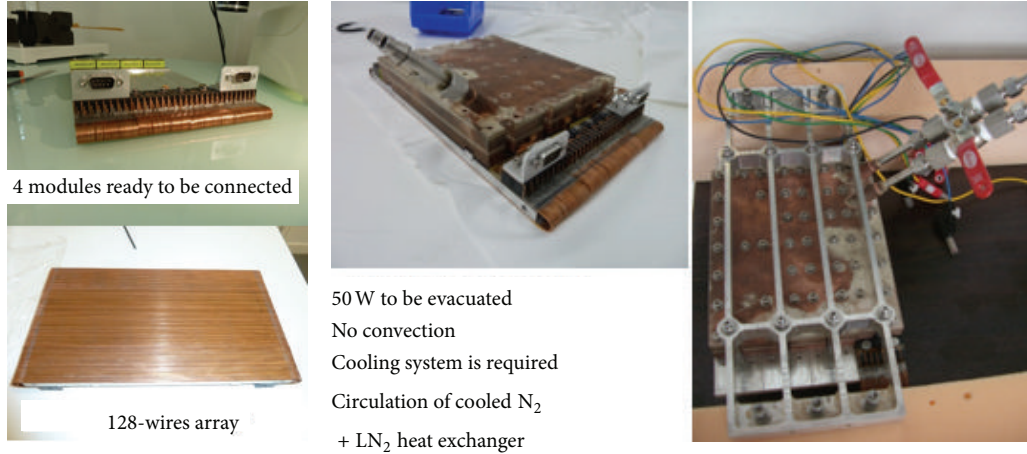


FIGURE 18: The magnetic excitation array is made of 4 modules of 32 wires each (1 mm^2) constituting a 128-wire array. The wires are spaced by 0.25 mm.

The second part of the spectrometer is a transport mirror, aligned with the slit (or positioned a few micrometers above/below the slit, allowing the selection of quantum states). The magnetic excitation array [16], described in Figure 18, can be placed above it. To induce resonant transitions between quantum states, a periodic magnetic field gradient will be produced with an array of wires located above the transport mirror. The third part of the spectrometer is an absorber, placed above and at the end of the transport mirror at an adjustable height to filter the quantum states.

4.2. Cooling of the Magnetic Excitation Array. The magnetic excitation array was built and tested before set-up. The current needed (5 A in average) to generate a sufficient magnetic field gradient produces 50 W of power that has to be dissipated without affecting too much the transport mirror. The wire system must be cooled down. Circulation of cooled gaseous N_2 will be used for that purpose. To test the cooling in conditions as close as in the experimental set-up, the magnetic excitation array was placed in a vacuum chamber and connected to a power supply (5 A, 8 V). The heat exchanger was placed in a LN_2 tank at a distance of 9 m from the magnetic excitation array, and a circulating N_2 circuit linked the heat exchanger to the magnetic excitation array. Results of that test were very good, and we could easily stabilize the temperature of the wires at 15°C during 12 h without human intervention. The magnetic excitation array equipped with the cooling system will be installed during autumn 2014.

4.3. Preliminary Results. In summer 2013, we conducted the first tests of the full extraction chain. During this cycle, the source temperature could not be cooled lower than 1.35 K. Removing the transport mirror and the absorber, and placing the detector at the exit of the extraction slit of height $127 \mu\text{m}$, we measured the first UCNs in the GRANIT spectrometer. The ^3He detector was equipped with a titanium window. In

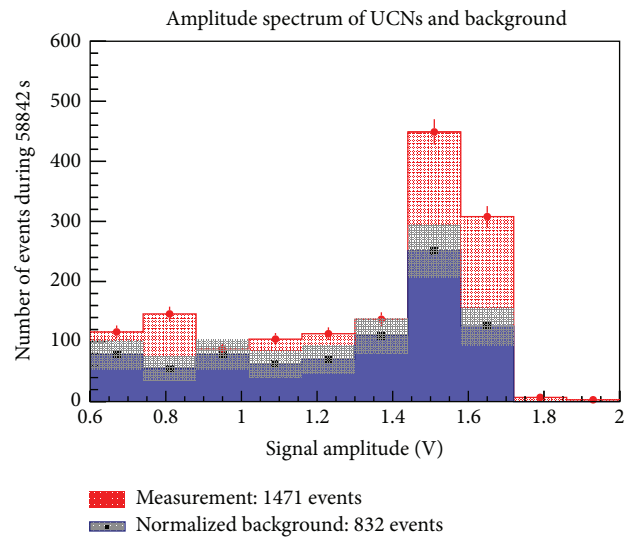


FIGURE 19: Amplitude spectrum of UCNs and background. The temperature of the source was 1.35 K.

this configuration, we measured $(10.9 \pm 1.5) \times 10^{-3}$ UCN/s as shown in Figure 19.

This count rate is one order of magnitude lower than expected in this configuration and two orders of magnitude lower than targeted. Potential explanations include (i) a defect in the extraction which, because of the modifications of the configuration, did not exist in the previous measurements, (ii) defects in the DLC-coated storage volume, which has not been characterized on its own due to its particular geometry, and (iii) the collection of impurities on a cold spot on the extraction window. This opens the way to further improvements and tests in the next cycles, which could not be done immediately because of the long reactor shutdown right after this measurement. In addition, the background, estimated to 14×10^{-3} events/s, is high compared to the signal because of background fast neutrons in the reactor building.

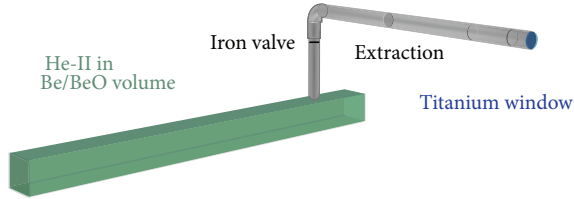


FIGURE 20: Geometry described and used in the simulation.

Extra-shielding will be added to the installation in order to reduce this background.

5. Simulation

STARucn (Simulation of Transmission, Absorption and Reflection of ultracold neutrons) is a public Monte-Carlo software designed to simulate experimental set-ups and guides for UCNs, developed at LPSC Grenoble [20]. It relies heavily on CERN's ROOT packages [21]. Its main features are modularity, easy configuration of geometry and simulation, propagation of UCNs, with or without gravity, interaction in volumes through effective lifetime, and interaction at surface (quantum reflection or transmission, surface losses due to absorption upon reflection, and specular and diffuse reflection). These features had been successfully benchmarked against analytical calculations and existing codes such as MCUCN of PSI and GEANT4UCN [22].

In STARucn, a material is described with its Fermi potential V_F , its fraction of diffuse reflections d , its loss factor η defined as the ratio of imaginary to real part of the Fermi potential, and its effective lifetime τ in the material.

Several measurements of the source characteristics can be used to estimate the unknown values of the parameters of the various materials. Our simulation (with geometries such as in Figure 20) shows that the build-up time within the source is only driven by the losses on the Be and BeO surfaces of the source. Using results from 2010 measurement [12, 13], we set $\eta_{\text{Be}} = 2.7 \times 10^{-4}$. In a similar way, the emptying time depends mostly on the reflective properties of the stainless steel extraction. Assuming this property is uniform in all the extraction, the best fit is found at $d_{\text{steel extraction}} = 3\%$. The parameter d_{Be} was arbitrarily set to 0.1 because the simulation showed that it had no significant influence on any measurement.

Assuming a production of 38000 UCN/s isotropically distributed in phase space in the source (corresponding to the reactor power of 56 MW), the expected number of UCNs detected in the simulation is around 5 times higher than what is measured. No satisfactory explanation was found: for instance, a 12 cm² hole in the extraction combined with a high $\eta_{\text{steel extraction}}$ would be needed. The most relevant figures are in Table 3.

Possible candidates to explain these losses are a larger angular divergency of the incoming beam of cold neutrons in the source than estimated, an eventual misalignment of the monochromator reducing the production rate, eventual

TABLE 3: Comparison of previous and recent measurements with simulations. The number of extractable UCNs corresponds to the number of UCNs available in the source after the UCN density has been saturated according to the simulation. The number of extracted UCNs corresponds to the number of UCNs detected during the experiments. The measured (resp., simulated) extraction efficiency is the ratio of the number of UCNs detected during the measurement (resp., the simulation) to the simulated number of extractable UCNs. The missing factor is calculated according to the discrepancy between these two efficiencies.

Configuration	2010 [12, 13]	2013
Storage time (meas.)	67 s	30 s
Extractible UCNs (sim.)	2.2×10^6	1.0×10^6
Extracted UCNs (meas.)	274000	21000
Extraction efficiency (meas.)	13%	2.1%
Extraction efficiency (sim.)	65–50%	15–5%
Missing factor	4–5	2.5–7

defects or losses in the extraction, and/or degradation of the BeO source volume. These options will be investigated during the next ILL reactor cycles.

Moreover, simulating the experiment of Section 4.3, with the corresponding count rate as measured in Section 2.1 and the spectrum as measured in Section 3.5, the number of neutrons measured is 10 times lower than simulated. However, no other measurement during this cycle can rule out a problem with the source or the extraction.

6. Improvements

These tests of all elements of the GRANIT experiment prompt us to modify some parts of the set-up. Some improvements are quite easy to perform. The cleanliness of the extraction guides could be easily improved, starting with a rigorous and defined production process, then having good procedures for washing, stoving, and packaging each part just before installation.

Moreover, due to the narrow UCN velocity range produced in the UCN source, DLC coating in extraction, mirrors, and intermediate storage volume is no longer crucial. For the next steps, we will replace the stainless steel foils of the extraction (that were due to be DLC-coated) by electropolished tubes. This will decrease the UCN losses due to the properties of the surface (mainly roughness and hydrogen adsorption) of these foils and will considerably help for the assembly of the guide, as well as for connecting source to spectrometer, thus diminishing risks of damage.

For the same reasons the intermediate storage volume will be replaced with a new one made of oxygen free high conductivity copper and in a cylindrical shape thus increasing the life time of UCNs in the volume and decreasing UCN losses. Another effort must be done to adjust the optical elements with more reliability without the contact of a probe. A solution using laser sensors is under study.

7. Conclusion

We have overviewed the current status of the GRANIT facility. First complete test of the GRANIT UCN source and spectrometer was performed during the last reactor cycle in 2013. Further improvements are identified based on the measured results, and they are being implemented.

Conflict of Interests

The authors declare that there is no conflict of interests regarding the publication of this paper.

Acknowledgments

The authors thank all the members of the GRANIT collaboration.

References

- [1] S. Baessler, M. Beau, M. Kreuz et al., “The GRANIT spectrometer,” *Comptes Rendus Physique*, vol. 12, no. 8, pp. 707–728, 2011.
- [2] P. Schmidt-Wellenburg, K. H. Andersen, P. Courtois et al., “Ultracold-neutron infrastructure for the gravitational spectrometer GRANIT,” *Nuclear Instruments and Methods in Physics Research Section A: Accelerators, Spectrometers, Detectors and Associated Equipment*, vol. 611, no. 2-3, pp. 267–271, 2009.
- [3] V. V. Nesvizhevsky, H. G. Börner, A. K. Petukhov et al., “Quantum states of neutrons in the Earth’s gravitational field,” *Nature*, vol. 415, no. 6869, pp. 297–299, 2002.
- [4] V. V. Nesvizhevsky, H. G. Boerner, A. M. Gagarsky et al., “Measurement of quantum states of neutrons in the Earth’s gravitational field,” *Physical Review D*, vol. 67, no. 10, Article ID 102002, 9 pages, 2003.
- [5] V. V. Nesvizhevsky, A. K. Petukhov, H. G. Börner et al., “Study of the neutron quantum states in the gravity field,” *The European Physical Journal C*, vol. 40, no. 4, pp. 479–491, 2005.
- [6] S. Baeßler, V. V. Nesvizhevsky, K. V. Protasov, and A. Y. Voronin, “Constraint on the coupling of axionlike particles to matter via an ultracold neutron gravitational experiment,” *Physical Review D—Particles, Fields, Gravitation and Cosmology*, vol. 75, no. 7, Article ID 075006, 2007.
- [7] V. V. Nesvizhevsky, G. Pignol, and K. V. Protasov, “Neutron scattering and extra-short-range interactions,” *Physical Review D*, vol. 77, no. 3, Article ID 034020, 8 pages, 2008.
- [8] I. Antoniadis, S. Baessler, M. Büchner et al., “Short-range fundamental forces,” *Comptes Rendus Physique*, vol. 12, no. 8, pp. 755–778, 2011.
- [9] P. Brax and G. Pignol, “Strongly coupled chameleons and the neutronic quantum bouncer,” *Physical Review Letters*, vol. 107, no. 11, Article ID 111301, 4 pages, 2011.
- [10] I. Antoniadis, S. Baessler, O. Bertolami et al., “Workshop GRANIT-2010, 14-19 February 2010, Les Houches, France,” *Comptes Rendus Physique*, vol. 12, no. 8, pp. 703–706, 2011.
- [11] P. Courtois, C. Menthonnex, R. Hehn et al., “Production and characterization of intercalated graphite crystals for cold neutron monochromators,” *Nuclear Instruments and Methods in Physics Research Section A: Accelerators, Spectrometers, Detectors and Associated Equipment*, vol. 634, no. 1, pp. S37–S40, 2011.
- [12] O. Zimmer, F. M. Piegsa, and S. N. Ivanov, “Superthermal source of ultracold neutrons for fundamental physics experiments,” *Physical Review Letters*, vol. 107, no. 13, Article ID 134801, 4 pages, 2011.
- [13] F. Piegsa, M. Fertl, S. N. Ivanov et al., “New source for ultracold neutrons at the Institut Laue-Langevin,” *Physical Review C*, vol. 90, no. 1, Article ID 015501, 10 pages, 2014.
- [14] V. V. Nesvizhevsky and K. V. Protasov, “Quantum states of neutrons in the Earth’s gravitational field: state of the art, applications, perspectives,” in *Trends in Quantum Gravity Research*, pp. 65–107, Nova Science, 2005.
- [15] T. Jenke, P. Geltenbort, H. Lemmel, and H. Abele, “Realization of a gravity-resonance-spectroscopy technique,” *Nature Physics*, vol. 7, no. 6, pp. 468–472, 2011.
- [16] G. Pignol, S. Baeßler, V. V. Nesvizhevsky, K. Protasov, D. Rebreyend, and A. Voronin, “Gravitational resonance spectroscopy with an oscillating magnetic field gradient in the GRANIT flow through arrangement,” *Advances in High Energy Physics*, vol. 2014, Article ID 628125, 7 pages, 2014.
- [17] R. Golub and J. M. Pendlebury, “The interaction of Ultra-Cold Neutrons (UCN) with liquid helium and a superthermal UCN source,” *Physics Letters A*, vol. 62, no. 5, pp. 337–339, 1977.
- [18] J. Barnard and V. Nesvizhevsky, “Analysis of a method for extracting angularly collimated UCNs from a volume without losing the density inside,” *Nuclear Instruments and Methods in Physics Research Section A: Accelerators, Spectrometers, Detectors and Associated Equipment*, vol. 591, no. 2, pp. 431–435, 2008.
- [19] P. Schmidt-Wellenburg, J. Barnard, P. Geltenbort et al., “Efficient extraction of a collimated ultra-cold neutron beam using diffusive channels,” *Nuclear Instruments and Methods in Physics Research A*, vol. 577, no. 3, pp. 623–625, 2007.
- [20] <http://sourceforge.net/projects/starucn/>.
- [21] R. Brun and F. Rademakers, “ROOT—an object oriented data analysis framework,” *Nuclear Instruments and Methods in Physics Research, Section A: Accelerators, Spectrometers, Detectors and Associated Equipment*, vol. 389, no. 1-2, pp. 81–86, 1997.
- [22] F. Atchison, T. Bryś, M. Daum et al., “The simulation of ultracold neutron experiments using GEANT4,” *Nuclear Instruments and Methods in Physics Research, Section A*, vol. 552, no. 3, pp. 513–521, 2005.

Research Article

Neutron Scattering on Impurity Nanoclusters in Gel Samples

V. B. Efimov,^{1,2} L. P. Mezhov-Deglin,² C. D. Dewhurst,³
A. V. Lokhov,² and V. V. Nesvizhevsky³

¹Physics Department, Lancaster University, Lancaster LA1 4YB, UK

²Laboratory of Quantum Crystals, Institute of Solid State Physics RAS, Chernogolovka, Moscow District 142432, Russia

³Institut Max von Laue-Paul Langevin, 71 Avenue des Martyrs, 38042 Grenoble, France

Correspondence should be addressed to V. B. Efimov; victor_efimov@yahoo.co.uk

Received 28 July 2014; Accepted 22 September 2014

Academic Editor: Guillaume Pignol

Copyright © 2015 V. B. Efimov et al. This is an open access article distributed under the Creative Commons Attribution License, which permits unrestricted use, distribution, and reproduction in any medium, provided the original work is properly cited. The publication of this article was funded by SCOAP³.

Results of recent SANS experiments with impurity-helium gel (IHG) samples in He-II are presented. We estimate the mean size of the impurity nanoparticles that form the frame of the IHG samples and discuss the possibility to use IHG samples for the production of ultracold neutrons (UCNs) in He-II cooled to the temperature of a few mK, as well as the reflection of UCNs at any temperature. Our results indicate that the most promising materials for these purposes might be the heavy water gel samples with the mean sizes of D₂O clusters of $d \sim 8$ nm and the heavy alcohol gel samples with the mean sizes of clusters of $d \sim 15$ nm.

1. Introduction

Many current investigations with ultracold neutrons (UCNs) are limited by available UCN densities [1–3]. Intense efforts are undertaken all over the world to increase the UCN densities. The most promising techniques are based on down-scattering of cold neutrons, mainly those with the wavelength of 8.9 Å, to the UCN energy due to phonon production in the bulk of superfluid He-II cooled below the temperature of 0.8 K or downscattering of neutrons with a broad initial energy spectrum in solid deuterium at the temperature of about 5 K [4].

Our primary goal in relation to the GRANIT project [5, 6] is to develop and model a new type of neutron moderator [7, 8] suitable for equilibrium cooling of UCNs in ultracold impurity-helium gel (IHG) matter. We will check the feasibility of the method based on equilibrium cooling of very cold neutrons (VCNs) in the process of their interaction with an IHG sample in superfluid He-II cooled below a temperature of a few mK. An IHG sample could play the role of a moderator for (very) cold neutrons and convert them into UCNs due to their quasielastic scattering by impurity clusters which are weakly connected with each other inside the gel frame (the dispersion matter) as well as with the surrounding

He-II (the dispersion medium of the gel), and in this manner, the energy could be transferred from VCNs to the dispersion medium. It should be noted that in this consideration we suppose that the wavelength of incident VCNs is comparable to characteristic sizes of the impurity nanoclusters.

The main goal of the SANS experiments discussed below was to study the structure of the IHG samples and to estimate the mean sizes of the impurity nanoclusters which form a firm skeleton (frame) of the sample in superfluid He-II. The IHG samples were prepared of the impurity nanoparticles weakly interacting with each other and weakly absorbing neutrons, like those prepared from molecular gases D₂ and O₂ or liquids like D₂O and C₂D₅OD [9–17].

Our preceding measurements of neutron transmission through a heavy water gel sample with the diameter of 2.5 cm in He-II at the temperature of $T = 1.5$ K have shown [18] that, with lowering the cold neutron velocity v from 160 m/s to 30 m/s, the angular distribution of the intensity of transmitted neutrons $I(\alpha)$ changed significantly: from near straightforward scattering at the velocities significantly larger than 60 m/s to preferred backscattering for velocities significantly smaller than 60 m/s (the corresponding transition neutron kinetic energy ≤ 0.2 K and the wavelength $\lambda \geq 6$ nm). In the case of transmission of a VCN beam through

a massive IHG sample, with increasing the sample diameter D from 2.5 cm to 25 cm, one might hope that the mechanism of transmission of VCNs with a velocity slightly above this transition velocity through the sample would change from straight forward to diffusion propagation (note that 25 cm is the inner diameter of the vessel in an industrial 10 l cryostat for storage of liquid helium). The total content of the impurity molecules could reach $\sim 10^{20} \text{ cm}^{-3}$, and supposing that about $\sim 1\%$ of the impurity molecules is contained in particles of small sizes (up to 100 molecules in a single cluster), one can estimate that the number density of small clusters in the IHG sample could reach $N \sim 10^{16} \text{ cm}^{-3}$. In the case of diffusion propagation of an VCN through a massive spherical sample with the diameter of $D = 25 \text{ cm}$, the effective length between two crossings of the neutron trajectory with walls of the vessel $L_{\text{eff}} \approx 1/3(D^2/L_N) \gg D$, while the distance between two elastic collisions of the neutron with nanoclusters in the bulk of the massive IHG sample $L_N \approx (1/\sigma N) \ll D$. Though the probability of inelastic scattering of VCNs on single nanoclusters with the diameter $d \leq 1 \text{ nm}$ is much smaller than the probability of elastic scattering and also could not be estimated reliably at this stage, the total number of collisions of the neutron with the impurity nanocluster particles in the volume of sample, proportional to the ratio D/L_n , could be large enough under certain conditions for effective cooling of neutrons to the bath temperature.

Thus, the primary focus of our participation in this GRANIT project includes a series of experiments relevant to the development of VCN moderators suitable for a new UCN source. We carried out a set of experiments to gain a better understanding of the properties and the behavior of IHG samples in He-II as a cold neutron moderator and UCN converter. The neutron studies are supported by X-ray investigations [19] of the structure and the phase transitions in the highly dispersed icy powder which are created following the decay of the water and ethanol gel samples on heating them above the temperature of 5 K in He gas atmosphere.

2. Experimental Technique and Results

The investigation was carried out using the SANS spectrometer D22. The range of neutron wavelengths λ was varied from 0.4 nm to 2.4 nm. The main measurements were performed at the wavelength of $\lambda \approx 0.6 \text{ nm}$. The spectrometer covers a total momentum transfer range q from 0.003 to 0.8 \AA^{-1} (see Figure 1).

For these measurements, we designed and tested a special optical cryostat [20]. Samples with the volume of a few cubic cm ($\sim 2.5 \text{ cm}$ in diameter) were prepared *in situ* in a quartz glass cell filled with superfluid He-II at the temperature of $T \sim 1.6 \text{ K}$. The process of sample preparation was controlled with a video camera installed outside the cryostat near the upper pairs of optical windows placed in the middle part of the cryostat. After preparation of a sample, the experimental cell was shifted down to the tail of the cryostat. All the pieces of the tail were produced from aluminum in order to decrease neutron scattering in the cryostat walls. The time of

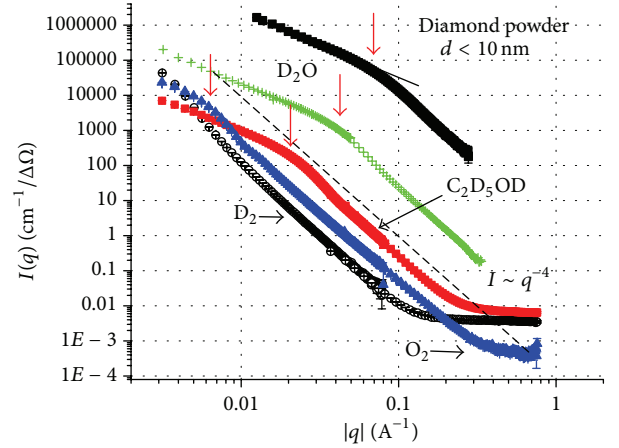


FIGURE 1: The intensity of small angle neutron scattering on impurities-helium gel samples and diamond nanopowder.

preparation of a sample was about 1 hour. The time of storage of superfluid He-II in the cryostat was longer than 10 hours.

The samples were prepared by means of condensation of a mixture of pure ^4He and the impurity vapors on the surface of He-II in the experimental quartz cell. For comparison, we have measured the scattering of neutrons on diamond nanopowder (by certificate, the size of diamond nanoparticles was $d \leq 10 \text{ nm}$). The results of SANS measurements are shown in Figure 1. All these measurements were carried out in He-II at a temperature of $T \sim 1.66 \text{ K}$ except diamond powder. A thin layer of the commercial powder of nanodiamond [21] in an Al envelope was studied at the room temperature.

The dashed line in Figure 1 corresponds to the Porod law: $I(q) \sim q^{-4}$ provided the condition $q * d \gg 1$ [22]. The arrows above the curves $I(q)$ indicate the points of cusps, which were defined by approximating the slope of the $I(q)$ curves at small and large q values.

Some results of numerical estimations of the intensity dependence $I(q)$ in the Born approximation [23] are shown in Figure 2. The dashed line corresponds to the Porod law $I \sim q^{-4}$; curve 1 shows scattering of neutrons on spherical nanoparticles with the radius of $R = 10 \text{ nm}$; curve 2 indicates results for the particle sizes distributed randomly from 1 nm to 19 nm (with the mean value 10 nm); and curve 3 is for the Gaussian distribution with the mean size of 10 nm. The change of the slope of the $I(q)$ curve at low q values is attributed to the transition to the Guinier region [24] in the range of $qR_g < 1$. Here, $R_g = (3/5)^{1/2} * R$ for spherical particles, and the particle diameter is $d < 2.6/q$. If the size of spherical particles $d > 2.6/q$, one could observe a number of interference minima in the $I(q)$ curve (1 curve in Figure 2). Whether the sizes of clusters are distributed randomly in the range from 1 nm to 19 nm (the mean value 10 nm, curve 2) or assuming the Gaussian distribution (with the mean size 10 nm and the width of the distribution curve equal to 4.5 nm) as shown in curve 3, the interference minima had disappeared and $I(q)$ became smooth enough. It is clear that with increasing the size of particles the kinks in the curves $I(q)$ are shifting to the lower q wave range (curves 1, 3, and 2).

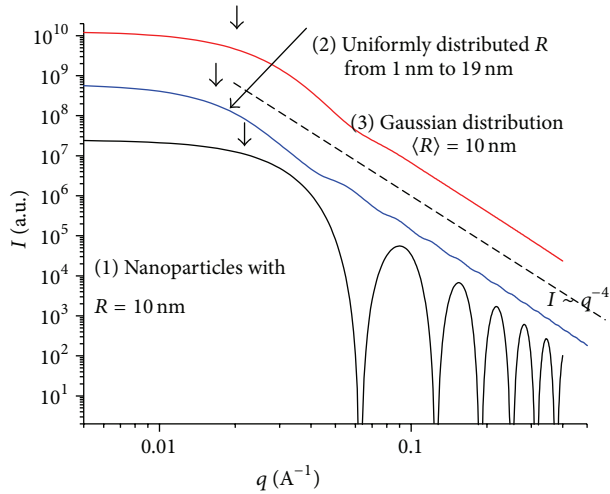


FIGURE 2: Results of calculation of neutron scattering in the Born approximation.

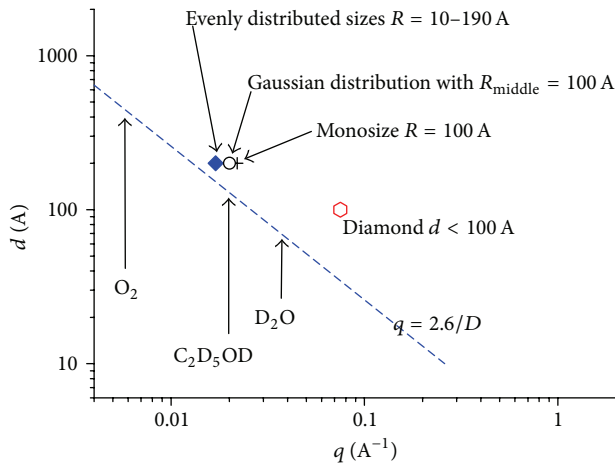


FIGURE 3: Estimation of sizes of nanoparticles in impurity-helium gels.

The results of our estimations of the size of nanoparticles in different IHG samples are plotted in Figure 3. The dotted line indicates the transition into the Guinier region. The points correspond to the positions of kinks in the calculation of the particle size distribution. The diamond point shows the position of the kink in the $I(q)$ curve for the diamond nanopowder (by the company certificate the size of particles was $d \leq 10$ nm).

As follows from Figure 3, the mean sizes of clusters in D_2O gel samples were equal to $d \sim 8$ nm and $d \sim 15$ nm for the deuterated ethanol sample. It is interesting to note that mean sizes of the bcc crystals in the icy powder, created following the decay of the IHG samples, were close to these sizes, as it was observed in our X-rays studies [25]. The icy powder was warming up first to the liquid nitrogen temperature and then we studied the transitions from amorphous to nanocrystalline structures with further increasing the temperature of the sample. In the beginning,

the total content of the amorphous phase in the water ice samples reached up to 40% in the normal water and up to 90% in the powder of heavy water. On heating the icy sample to the temperature of up to 110 K (for heavy water up to 130 K), the amorphous phase was transformed to crystalline cubic phase and then we observed the transformation into the convenient hexagonal phase. As mentioned above, the sizes of initial cubic ice crystals were 6–10 nm [19]. In the case of ethanol samples, the transition from amorphous to monoclinic phase occurred at a temperature of $T \sim 110$ K and the sizes of crystallites were close to 30–40 nm.

3. IHG Samples as Neutron Moderators

As pointed out in [7], small sizes of impurity clusters weakly interacting with each other in the frame of the gel sample and with superfluid He-II in nanopores might be useful for developing VCN moderators of a new type, in which the energy of VCNs is transferred into the helium bath cooled down to the temperature of a few mK via their inelastic interaction with the clusters.

According to [8], the most interesting for these moderators could be D_2O or the heavy alcohol C_2D_5OD gel samples. In principle, the total content of small (about 1 nm) particles in bulk of these samples can be increased significantly on heating the freshly prepared sample in liquid helium up to 4 K and subsequent cooling [25].

The time-of-flight measurements of inelastic neutron scattering on these samples could give any answer on efficiency of the inelastic scattering of CNs and VCNs on the gel samples as well as on the gel samples prepared from other materials.

Elastic Neutron Scattering. The first experiment on VCN scattering yielded very encouraging results. It was observed that the beam transmission through a heavy water-helium gel sample with the volume of ~ 3 cm³ in He-II at the temperature $T \sim 1.6$ K changed from $\sim 50\%$ to $\sim 0\%$ on decreasing the neutron velocity from 160 m/s to 30 m/s. The angular distribution of neutron scattering changes as well: at higher neutron energies, the scattering is directed into the front hemisphere mainly ($< 30^\circ$), and at low energies, the angular distribution of scattered neutrons is close to spherical [18]. The transition from straight to diffusion propagation of VCNs in the bulk of a massive gel sample with increasing the sample volume with diameter up to 25 cm might result in a significant increase in the time of propagation of neutrons between two consequent crossings of the vessel walls and thus in a corresponding increase of the probability of decreasing the energy of neutrons down to the temperature of the He-II bath cooled below 10 mK.

4. Conclusion

We have made neutron scattering measurements on impurity-helium gels—a new class of “soft-matter.” As an impurity, we used gases D_2 and O_2 and vapor of liquids D_2O and C_2D_5OD . The mean sizes of nanoparticles in the gels were 6–10 nm for heavy water gel and 15–30 nm for

deuterated ethanol samples. We propose that the massive IHG samples could be promising for the purposes of VCN cooling down to UCNs.

Conflict of Interests

The authors declare that there is no conflict of interests regarding the publication of this paper.

Acknowledgments

The authors are grateful to Dr. R. May and Dr. A. Wiedenmann for help in the experiments. The work was supported in part by Grant RFBR-13-02-00378.

References

- [1] J. Butterworth, P. Geltenbort, and E. Korobkina, "Proceedings of the International Workshop on Particle Physics with Slow Neutrons, Institut Laue-Langevin, Grenoble, France, October 22–24, 1998," *Nuclear Instruments and Methods in Physics Research A*, vol. 440, no. 3, p. 5, 2000.
- [2] V. V. Nesvizhevsky, C. Plonka-Spehr, and K. Protasov, "Particle physics with slow neutrons. Proceedings of the International Workshop on Particle Physics with Slow Neutrons, Institut Laue-Langevin, Grenoble, France, May 29–31, 2008," *Nuclear Instruments and Methods A*, vol. 611, no. 2-3, p. 7, 2009.
- [3] I. Antoniadis, S. Baessler, O. Bertolami et al., "Workshop GRANIT-2010, 14–19 February 2010, Les Houches, France," *Comptes Rendus Physique*, vol. 12, no. 8, pp. 703–706, 2011.
- [4] R. Golub and J. M. Pendlebury, "Super-thermal sources of ultracold neutrons," *Physics Letters A*, vol. 53, no. 2, pp. 133–135, 1975.
- [5] S. Baessler, M. Beau, M. Kreuz et al., "The GRANIT spectrometer," *Comptes Rendus Physique*, vol. 12, no. 8, pp. 707–728, 2011.
- [6] D. Roulier, F. Vezzu, S. Baessler et al., "Status of the GRANIT facility," <http://arxiv.org/abs/1410.1376>.
- [7] V. V. Nesvizhevsky, "Interaction of neutrons with nanoparticles," *Physics of Atomic Nuclei*, vol. 65, no. 3, pp. 400–408, 2002.
- [8] V. V. Nesvizhevsky, G. Pignol, and K. V. Protasov, "Nanoparticles as a possible moderator for an ultracold neutron source," *International Journal of Nanoscience*, vol. 6, no. 6, pp. 485–499, 2007.
- [9] V. Khmelenko, D. Lee, and S. Vasiliev, "Matrix isolation of H and D atoms: physics and chemistry from 1.5 to 0.1 K," in *Physics and Chemistry at Low Temperatures*, L. Khriachtchev, Ed., chapter 5, Pan Stanford Publishing, Singapore, 2011.
- [10] V. V. Khmelenko, E. P. Bernard, S. A. Vasiliev, and D. M. Lee, "Tunnelling chemical reactions of hydrogen isotopes in quantum solids," *Russian Chemical Reviews*, vol. 76, no. 12, pp. 1107–1121, 2007.
- [11] L. P. Mezhov-Deglin, "Impurity nanocluster structures in liquid helium," *Uspekhi Fizicheskikh Nauk*, vol. 48, no. 10, pp. 1061–1070, 2005.
- [12] V. Efimov and L. Mezhov-Deglin, "Method of preparation of nanoparticles from gases and vapor of fluids," Patent no. 2399581, 2010.
- [13] E. B. Gordon and A. F. Shestakov, "Helium localization around the microscopic impurities embedded into liquid helium," *Fizika Nizkikh Temperatur*, vol. 26, no. 1, pp. 5–33, 2000.
- [14] M. Barranco, R. Guardiola, S. Hernández, R. Mayol, J. Navarro, and M. Pi, "Helium nanodroplets: an overview," *Journal of Low Temperature Physics*, vol. 142, no. 1-2, pp. 1–81, 2006.
- [15] S. I. Kiselev, V. V. Khmelenko, and D. M. Lee, "Sound propagation in liquid He in impurity-helium solids," *Fizika Nizkikh Temperatur*, vol. 26, no. 9-10, pp. 874–883, 2000.
- [16] S. Kiselev, V. V. Khmelenko, D. M. Lee et al., "Structural studies of impurity-helium solids," *Physical Review B*, vol. 65, no. 2, Article ID 024517, 12 pages, 2001.
- [17] S. Kiselev, V. V. Khmelenko, D. M. Lee et al., "X-ray studies of structural changes of impurity-helium solids," *Journal of Low Temperature Physics*, vol. 126, no. 1-2, pp. 235–240, 2002.
- [18] L. P. Mezhov-Deglin, V. B. Efimov, A. V. Lokhov et al., "Scattering of cold neutrons on gel samples formed by impurity clusters in superfluid He-II," *Journal of Low Temperature Physics*, vol. 148, no. 5-6, pp. 833–837, 2007.
- [19] V. B. Efimov, A. N. Izotov, A. A. Levchenko, L. P. Mezhov-Deglin, and S. S. Khasanov, "Structural transitions in ice samples at low temperatures and pressures," *JETP Letters*, vol. 94, no. 8, pp. 621–625, 2011.
- [20] V. Efimov, L. Mezhov-Deglin, and A. Lokhov, "Combining cryostat for neutron investigation," *PTE*. In press.
- [21] Diamond nanopowder 95 +%, <http://www.sigmaaldrich.com/>.
- [22] G. Porod, "Die Röntgenkleinwinkelstreuung von dichtgepackten kolloiden Systemen—I. Teil," *Kolloid-Zeitschrift*, vol. 124, no. 2, pp. 83–114, 1951.
- [23] M. Born, "Zur Quantenmechanik der Stoßvorgänge," *Zeitschrift für Physik*, vol. 37, no. 12, pp. 863–867, 1926.
- [24] A. Gunier and G. Fournet, *Small Angle Scattering of X-Rays*, John Wiley & Sons, 1955.
- [25] L. P. Mezhov-Deglin, V. B. Efimov, A. V. Lokhov et al., "Neutron studies of impurity gels of heavy water and deuterium in superfluid He-II," *Journal of Low Temperature Physics*, vol. 150, no. 3-4, pp. 206–211, 2008.

Research Article

UCN Source at an External Beam of Thermal Neutrons

**E. V. Lychagin,¹ A. Yu. Muzychka,¹ G. V. Nekhaev,¹ V. V. Nesvizhevsky,²
E. I. Sharapov,¹ and A. V. Strelkov¹**

¹*Joint Institute for Nuclear Research, 6 Joliot-Curie, Ru-141980, Dubna, Russia*

²*Institute Max von Laue-Paul Langevin, 71 avenue des Martyrs, F-38000, Grenoble, France*

Correspondence should be addressed to A. Yu. Muzychka; muz@nf.jinr.ru

Received 19 June 2014; Accepted 18 August 2014

Academic Editor: Stefan Baessler

Copyright © 2015 E. V. Lychagin et al. This is an open access article distributed under the Creative Commons Attribution License, which permits unrestricted use, distribution, and reproduction in any medium, provided the original work is properly cited. The publication of this article was funded by SCOAP³.

We propose a new method for production of ultracold neutrons (UCNs) in superfluid helium. The principal idea consists in installing a helium UCN source into an external beam of thermal or cold neutrons and in surrounding this source with a solid methane moderator/reflector cooled down to ~ 4 K. The moderator plays the role of an external source of cold neutrons needed to produce UCNs. The flux of accumulated neutrons could exceed the flux of incident neutrons due to their numerous reflections from methane; also the source size could be significantly larger than the incident beam diameter. We provide preliminary calculations of cooling of neutrons. These calculations show that such a source being installed at an intense source of thermal or cold neutrons like the ILL or PIK reactor or the ESS spallation source could provide the UCN density 10^5 cm^{-3} , the production rate 10^7 UCN/s^{-1} . Main advantages of such an UCN source include its low radiative and thermal load, relatively low cost, and convenient accessibility for any maintenance. We have carried out an experiment on cooling of thermal neutrons in a methane cavity. The data confirm the results of our calculations of the spectrum and flux of neutrons in the methane cavity.

1. Introduction

Further progress in the field of studies with ultracold neutrons (UCNs) [1, 2], as a tool for nuclear and particle physics [3–5], is often limited by available UCN densities. Therefore many projects of new advanced UCN sources are pursued in various scientific centers in the world; they are aiming to increase the available UCN densities and fluxes by at least 1-2 orders of magnitude.

The principle of production of UCNs in superfluid helium was proposed already in 1975 in [6]. It is based on the fact that a neutron could excite a phonon with the energy of 1.02 meV in liquid ^4He . If the energy of incident neutron exceeds slightly this value (1.02 meV), the neutron will be scattered to the UCN energy. UCNs could be produced via this mechanism only from incident cold neutrons with energies from a very narrow range as the UCN energy is as small as <300 neV. A neutron could also excite two or more phonons in helium simultaneously. The cross section of such multiphonon scattering is lower by several orders of magnitude than the

cross section of one-phonon scattering. However the total energy of excited phonons could be found within a much broader energy range, and thus UCNs could be produced in a multiphonon process from a much broader energy range of incident neutrons. Therefore both processes would give comparable contributions to the UCN production provided that the initial cold neutron spectrum is broad.

It was also shown in the cited work that the produced UCNs could be stored in superfluid helium for a long time if the helium temperature is ~ 1 K or lower. This fact allows building up the UCN density in a source of this type up to very high values.

Helium UCN sources, as well as solid-deuterium UCN sources, seem to be most promising at present. There are several projects of helium UCN sources in the stage of their realization or design [7–11]. A drawback of helium sources as compared to solid-deuterium sources consists of very low temperatures needed in order to provide long UCN lifetimes in superfluid ^4He : thus the lifetime drops down from 10^4 s to 1 s if the temperature increases from 0.6 K to 2 K [12, 13].

Advantages of helium sources consist of the transparency of the physical processes involved, the relatively low cost, and the possibility to install them outside of a reactor/spallation source zone.

2. The Concept of UCN Sources at External Beams of Thermal Neutrons

It was noted in [14] in 1998 that if an UCN source filled in with liquid helium at the temperature of below 1 K is installed in a beam of cold neutrons surrounded with a cold neutron reflector (i.e., the reflector provides a trap for cold neutrons used to produce UCNs), then one could noticeably increase the flux of cold neutrons in the source and thus increase the UCN generation rate. Beryllium oxide and Plexiglas at a temperature of several degrees were considered as possible materials for the reflector. The mean path of cold neutrons in the source of a cylindrical or spherical shape could increase by the factors 2.2 and 2.5 accordingly. This idea has not been realized as such gains could be achieved only in relatively small volumes. The reason is in the fact that the angular distribution of reflected neutrons is isotropic in contrast to the initial narrow angular distribution. Thus one could not use a section of a neutron guide (with the length several times larger than the width) for such a source; the path of cold neutrons in a guide-shaped source (and thus the generation rate) would be higher anyway than in a spherical source of equal volume.

However if we replace the reflector material by another one providing simultaneously good moderation and reflection properties, then one could (1) considerably increase the flux of cold neutrons in the source and thus its production rate and also (2) use “cheap” and intense thermal neutrons instead of “expensive” and less intense cold neutrons for UCN production [15]. In fact such a moderator/reflector plays the role of a cold neutron source. Thus the maximum flux density in beams of cold neutrons at the ILL reactor reaches $\sim 10^{10} \text{ cm}^{-2} \text{ s}^{-1}$, while the maximum flux density in beams of thermal neutrons at the same reactor could reach $\sim 10^{11} \text{ cm}^{-2} \text{ s}^{-1}$ as it will be shown in the next section.

Such an UCN source is shown schematically in Figure 1; it is surrounded with a moderator/reflector, which plays the role of an external cold neutron source. The moderator/reflector in the figure surrounds also the input neutron guide in order to avoid leakages of neutrons (from the trap) with the angular divergence exceeding the narrow angular divergence in the initial neutron beam. The larger the albedo of the reflector is, the higher the saturated neutron flux density in the source is; in the limit of the reflector albedo equal unity, the neutron flux density accumulated in the cavity is strictly equal to the neutron flux density in the thermal neutron source. For the PIK and ILL reactors it would be equal to $\sim 10^{15} \text{ n}\cdot\text{cm}^{-2} \text{ s}^{-1}$.

A matter with maximum albedo for cold neutrons, which we have found, is solid methane in phase II at the temperature of $\sim 4 \text{ K}$ (we leave aside composite materials based on nanoparticle reflectors [16–18], which we are analyzing currently in view of even further increase in the attainable albedo). On the one hand, albedo of methane is slightly

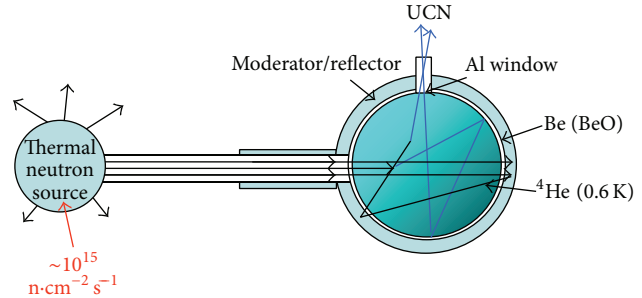


FIGURE 1: A scheme of an UCN source surrounded by a moderator/reflector.

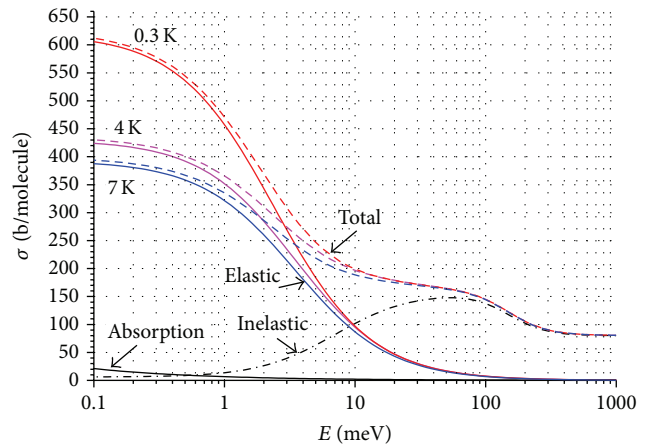


FIGURE 2: The cross section of neutron scattering normalized to one molecule of solid methane (CH_4) in the phase II at different temperatures is shown as a function of neutron energy.

higher than albedo of reflectors considered in [9]. On the other hand, solid methane is simultaneously one of the best cold moderators. This latter property of methane is due to the fact that it is a molecular crystal with a very round molecule; thus it provides rather flexible rotational degrees of freedom even at very low temperatures.

Another particularity of solid methane is parallel alignment of spins of hydrogen atoms in the methane molecule at low temperatures. The scattering of low energy neutrons becomes coherent for one molecule and stays incoherent for different molecules. Therefore there is no optical potential for neutrons of low energy as there is for materials with coherent scattering, and the cross section increases with decreasing the neutron energy. Cross sections of neutron scattering in solid methane at different temperatures are presented in Figure 2 as a function of neutron energy; the data are taken from [19, 20].

Solid color lines correspond to the cross sections of elastic scattering at respective temperatures. Black dashed-dotted line indicates the cross section of inelastic scattering. Color dashed lines show the total scattering cross section at a given temperature. Black solid line gives the absorption cross section.

3. Estimation of Thermal Neutron Flux Density in a Neutron Guide

Before calculating parameters of the proposed UCN source, we estimate the flux of thermal neutrons, which could be achieved in an external neutron guide of existing neutron sources.

The most intense worldwide steady neutron source is currently the ILL reactor; it provides the thermal neutron flux density of $J_0 = 1.2 \cdot 10^{15}$ n/(cm² s) in the vicinity of its active zone. The distance from its active zone to the outside surface of its biological shielding is about 4 m. There are holes with the maximum diameter of 20 cm in the biological shielding of the reactor for the installation of neutron guides. It is realistic to install an UCN source at the end of a neutron guide with the diameter of 20 cm at the distance of 5 m from the center of the reactor active zone.

So, let us assume that there is a cylindrical tube with the length of $L = 5$ m and the diameter of $D = 20$ cm (the square area cross section is thus $S = 314$ cm²). Let us assume also that one end of the tube is an isotropic source of thermal neutrons with the flux density equal to $J_0 = 1.2 \cdot 10^{15}$ n/(cm² s). Then the neutron flux density through the opposite end of the tube is

$$J = J_0 \frac{S}{4\pi L^2} = J_0 \cdot 10^{-4} = 1.2 \cdot 10^{11} \text{ n/(cm}^2 \text{ s)}. \quad (1)$$

The integral flux will be equal to

$$F = 3.8 \cdot 10^{13} \text{ n/s}. \quad (2)$$

Note that a real neutron flux could be about twice larger due to the radiation of neutrons through side walls of the tube and reflection of neutrons from the biological shielding.

Note also that the flux density is proportional to the square of the tube diameter, and the integral flux is proportional to the 4th power of the diameter.

4. Modeling of Neutron Spectrum in the Solid Methane Cavity

We have simulated the spectrum of neutrons accumulated in a solid methane cavity. The simulation was carried out using the program *MCNP 4c* with a special kern for solid methane; the kern was used in [20, 21] and was kindly provided to us by the authors.

As a result of this model calculation, we established the optimum parameters of moderator/reflector. We found that the optimum thickness of methane is ~ 3 cm; an increase in its thickness does not increase noticeably the number of neutrons in the cavity. The optimum temperature of methane is ~ 4 K; a decrease in the temperature also does not increase the number of neutrons in the cavity. The optimum diameter of the cavity is 40–50 cm if the input neutron guide diameter is 20 cm.

Figures 3 and 4 show spectra of neutrons accumulated in a spherical cavity with the internal diameter of 40 cm surrounded with solid methane. Here Φ is the neutron fluence averaged over the cavity volume per one incident neutron.

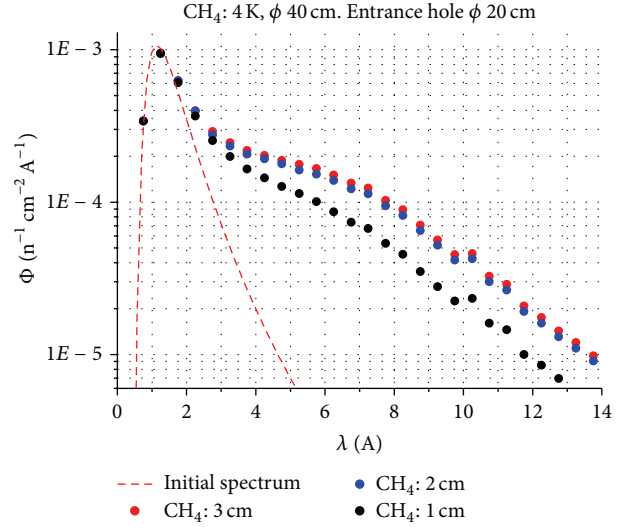


FIGURE 3: Mean neutron fluence in a spherical cavity with the diameter of 40 cm surrounded with solid methane at the temperature of 4 K is shown as a function of neutron wavelength.

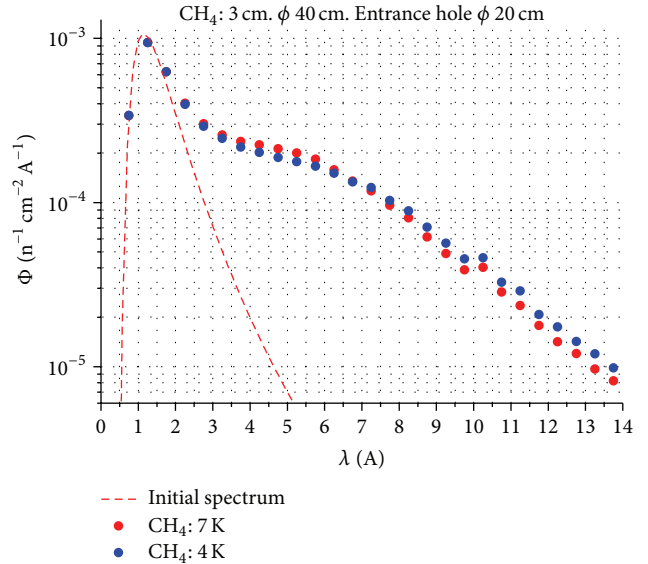


FIGURE 4: Mean fluence in a spherical cavity with the diameter of 40 cm surrounded with solid methane walls with the thickness of 3 cm.

The velocity distribution of incident neutrons is Maxwellian with the temperature of 300 K; they enter the cavity through the input guide with the diameter of ϕ 20 cm.

Line indicates the mean fluence of incident neutrons with the temperature of 300 K normalized per 1 neutron.

Points show the mean fluence of accumulated neutrons, normalized per 1 incident neutron, for different thicknesses of the cavity walls equal to 1, 2, and 3 cm.

Line indicates the mean fluence of incident neutrons with the temperature of 300 K normalized per 1 neutron.

Points show the mean fluence of accumulated neutrons, normalized per 1 incident neutron, for different temperatures of methane equal to 7 K and 4 K.

5. Estimation of the Generation Rate in the Source

For one-phonon processes only and for the UCN energy below the beryllium optical potential, the UCN generation rate in liquid helium [22] equals

$$R_1 = 4.55 \cdot 10^{-8} \frac{dJ}{d\lambda} (8.9 \text{ \AA}) \text{ cm}^{-3} \text{ s}^{-1}. \quad (3)$$

For the input flux (2), a spherical cavity with the diameter of 40 cm, and the mean fluence $d\Phi/d\lambda (8.9 \text{ \AA}) = 6.7 \cdot 10^{-5} \text{ n}/(\text{cm}^2 \text{ \AA})$, (see Figures 3 and 4) one could get

$$\begin{aligned} \frac{dJ}{d\lambda} (8.9 \text{ \AA}) &= 2.5 \cdot 10^9 \text{ n}/\text{cm}^2 \text{ s \AA}, \\ R_1 &= 116 \text{ n}/(\text{cm}^3 \text{ s}). \end{aligned} \quad (4)$$

Estimations of UCN production due to multiphonon processes differ in different works. Thus for the spectra of accumulated neutrons as shown in Figures 3 and 4, multiphonon processes could contribute with a factor of increase in the UCN production rate equal to a value ranging from 1.25 to 3.5 [22–24]. Thus the lower estimation of the UCN production rate is $R = 145 \text{ n}/(\text{cm}^3 \text{ s})$.

The total number of UCNs produced in the source per second is $5 \cdot 10^6 \text{ UCN/s}$.

One could propose the following characteristics of the source: the number of UCNs produced in the source per one incident thermal neutron is $1.3 \cdot 10^{-7} \text{ UCN/s/n}$.

For the coefficient of loss of UCNs in the walls of the UCN accumulation volume equal to $\eta = 10^{-4}$, the mean partial storage time of UCNs related to wall losses is $\tau_w \approx 450 \text{ s}$; with account for the neutron β -decay lifetime the storage time will be equal to $\tau \approx 300 \text{ s}$.

Preliminary estimations indicate that the thermal heat to the source with the diameter of 40 cm will raise to $\sim 0.2 \text{ W}$ for the input neutron flux (2); at such a heat load the source could be cooled down to the temperature of 0.6 K.

If the helium temperature is 0.8 K, the UCN storage time in helium is equal to the neutron β -decay lifetime. If the helium temperature is 0.6 K, it is a factor of 10 larger and thus such losses even could be neglected.

Thus, the maximum UCN density in the source is

$$n_{\text{UCN}} = R \cdot \tau = 4.4 \cdot 10^4 \text{ UCN}/\text{cm}^3. \quad (5)$$

We have given the lower estimate for the UCN production rate in the source. The upper estimation would be a factor of ~ 5 larger.

These estimations are valid for a source with the diameter of 40 cm and the neutron guide diameter of 20 cm. If the source diameter is 30 cm, the UCN density would practically stay the same because the leakage of 8.9 \AA “parent neutrons” through the input neutron guide will increase. On the other

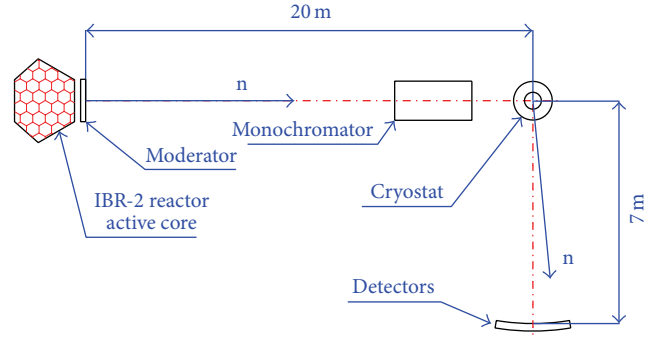


FIGURE 5: A scheme of measurement of the spectra and intensities of neutrons accumulated in a methane cavity performed with the instrument DIN-2Pi.

hand, the total number of produced UCNs (“children”) would decrease by a factor of ~ 2 . An increase of the source size will increase the production rate proportionally to the diameter value; however it will decrease the UCN density proportional to the reciprocal diameter square.

6. Measurements

In order to verify validity of the calculations presented in Figures 3 and 4, we have measured the spectra and intensities of neutrons accumulated in a solid methane cavity.

The measurements were performed using the instrument DIN-2Pi [25] at the reactor IBR-2 [26] (JINR, Dubna). The instrument was designed to measure inelastic scattering of neutrons using the time-of-flight method. The length of the input arm of DIN-2Pi is 20 m; it is measured between the reactor and a sample, which scatters neutrons (a cryostat with solid methane in our case). The output arm length is 7 m; it is measured between the sample and the detectors. Choppers are installed in the input arm of the spectrometer; they select a monoline with the wavelength (time-of-flight) resolution of $\sim 1\%$.

A scheme of measurement is shown in Figure 5.

A sample of solid methane with a cylindrical cavity measuring $12 \times 12 \text{ cm}$ with the wall thickness of 3 cm was grown in the cryostat. The temperature of methane was slightly different in different points of the sample within the range from 6 K to 7.2 K. The temperature was stable in time. Two holes were left in the walls of methane cavity, one for the neutron entrance and another one for their exit, at the angle of 90° relative to each other. The square area of every hole was equal to $\sim 7 \text{ cm}^2$. The cryostat was surrounded with Cd-shielding so that thermal neutrons could enter into the cryostat only through the entrance window, and they could escape from the cavity to the detectors only through the exit window. Before escaping into the detector, neutrons had to have two or more reflections from the cavity walls.

7. Results of the Measurements

We selected only one monoline of incident thermal neutrons with the energy of 25.0 meV (1.81 \AA). There were also many

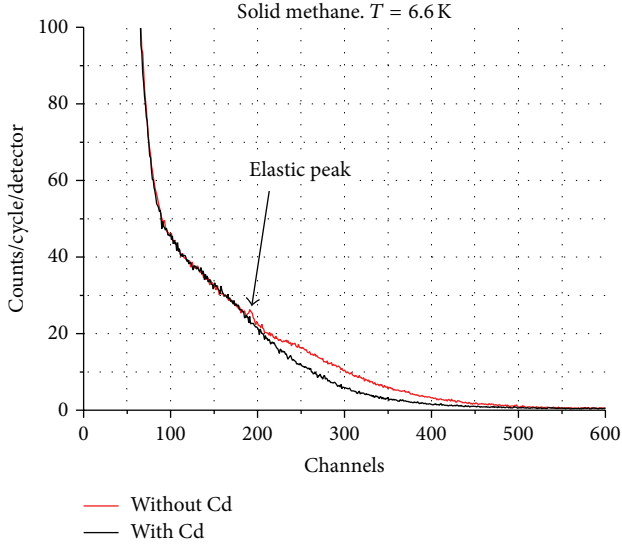


FIGURE 6: Count rate in the detector as a function of the time interval after a reactor pulse. Results of measurements with the initial beam open are shown with red line. Results of measurements with a sheet of cadmium in the incident neutron beam are indicated with black line. The width of one time channel is $64 \mu\text{s}$.

“background” fast and epithermal neutrons (that could pass through a cadmium sheet) in the initial beam. A major fraction of these neutrons could be separated using the time-of-flight technique. However some faster neutrons could penetrate into the cryostat, scatter in methane, and escape to the detector during the same time intervals as neutrons from the initial thermal monoline do. To exclude an influence of fast neutrons, we measured the so-called cadmium difference, that is, the difference of the count rate with the input beam open and the count rate with a sheet of cadmium in the input beam, which totally absorbed the initial thermal beam. Figure 6 shows the results of these measurements.

The difference of these measurements allows calculating the spectrum of neutrons thermalized in methane.

Figure 7 presents the results of measurements of the spectrum of neutrons escaping from the methane cavity through the exit window. We performed a numerical simulation of our experiment using the same computer MCNP 4c code as used for the source simulation. The numerical simulation almost ideally coincides with the measurements, except for one feature, which is not important in this case. Namely, one clearly observes measured extra neutrons, which did not change their energy during their storage in the cavity, the elastic peak. We do not reproduce this peak in simulations.

Also we show Maxwellian spectra in Figure 7 for comparing them with the measured results. One spectrum (dashed line) provides the maximum number of neutrons with the wavelength of 8.9 \AA (our “ideal” spectrum). Another one (solid blue line) provides a shape closest to the measured data. This latter spectrum is also very close to cold neutron spectra in beams at the ILL. The integrals under all spectra are equal to each other.

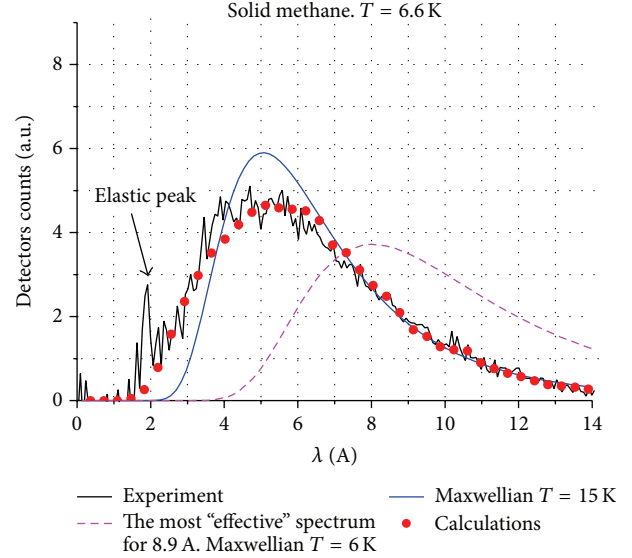


FIGURE 7: Spectrum of neutrons escaping from the methane cavity through the exit window. Thin line indicates the results of measurements. Points correspond to the numerical simulation of our experiment. Dashed line illustrates the Maxwellian distribution, which provides the largest count rate of neutrons with the wavelength of 8.9 \AA . Blue line shows a Maxwellian distribution fitting the data in the best way. The integrals under all curves are equal to each other.

As an additional verification of validity of simulations of neutron fluxes accumulated in the methane cavity, we performed an analogous measurement with methane replaced with distilled water at the temperature of 292 K . In this test, the number of initial neutrons entering the cryostat was the same, and the spectrum was the same, as in measurements with methane. Results of this measurement are shown in Figure 8.

The initial spectrum, as mentioned above, is a monoline with the wavelength width smaller than 1%. Such a width could not be shown graphically in the scale in Figure 8 (the “elastic peak” in Figures 6 and 7 has larger width as it is washed out due to time-of-flight spread caused by some delay of neutrons in the methane cavity).

As clear from this figure, the results of numerical simulations perfectly agree with the measured data. Also the ratios of integrals under the spectra for water and methane agree with results of simulations and measurements.

Experiment:

$$\frac{\int N_{\text{det}}^{\text{H}_2\text{O}}(\lambda) d\lambda}{\int N_{\text{det}}^{\text{CH}_4}(\lambda) d\lambda} = 2.01 \pm 0.02. \quad (6)$$

Simulation:

$$\frac{\int N_{\text{det}}^{\text{H}_2\text{O}}(\lambda) d\lambda}{\int N_{\text{det}}^{\text{CH}_4}(\lambda) d\lambda} = 1.94 \pm 0.04. \quad (7)$$

Here $N_{\text{det}}^{\text{H}_2\text{O}}$ is the count rate for water at the temperature of 292 K and $N_{\text{det}}^{\text{CH}_4}$ is the count rate for methane at the temperature of 6.6 K .

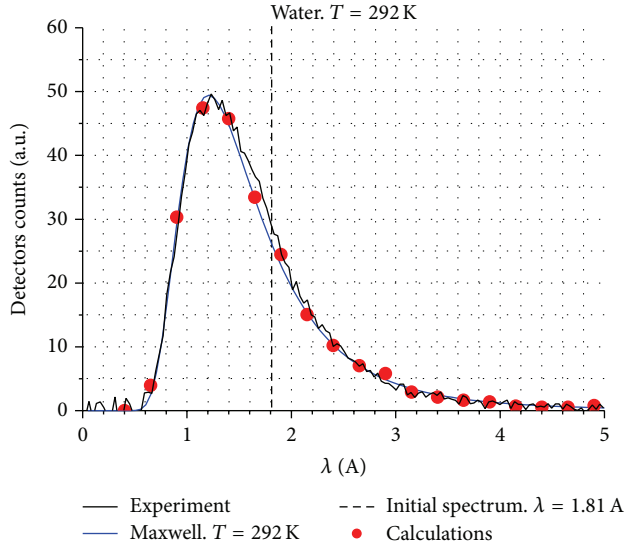


FIGURE 8: The spectrum of neutrons escaping from the water cavity through the exit window is shown as a function of neutron wavelength. Thin line indicates the measured results. Points correspond to the results of numerical simulations of this experiment. Blue line indicates the Maxwellian distribution for the temperature equal to 292 K.

All these performed measurements demonstrated high accuracy of simulations both in terms of absolute values of neutron fluxes accumulated in a methane cavity and also in terms of spectra of accumulated neutrons. Accordingly, we confirm all simulated characteristics of the UCN source. On the other hand, one should underline that now we could provide rather precise estimations of these characteristics basing these estimations solely on the measured data, even without simulations.

In fact, if we know the value of albedo of thermal neutrons from water, then relation (6) and a known geometry of the cavity (see above) allow calculating the albedo from solid methane.

MCNP simulations of neutron albedo from water at the temperature of 292 K, for normal incidence of neutrons with the energy of 25 meV, provide the value 0.787 ± 0.008 . Nearly the same value could be obtained for isotropic incidence of neutrons with the Maxwellian distribution with the temperature of 292 K: 0.806 ± 0.008 . Thus, in all cases typical for experiments, the albedo from water is about 0.8. Taking into account that we observe in experiments the neutrons after their second and further reflections from the cavity walls and also taking into account the sizes of entrance and exit holes and relation (6), we get albedo from methane equal to 0.65. Assuming the spectrum of neutrons in the methane cavity is the same as that shown in Figure 7, one could calculate the neutron flux in a methane cavity of any geometry and thus the UCN production rate in the source.

The characteristics of the UCN source estimated in this way are higher by $\sim 20\%$ than those given above that means a very good accuracy. The main reason for this deviation consists of the fact that the neutron energy after their first

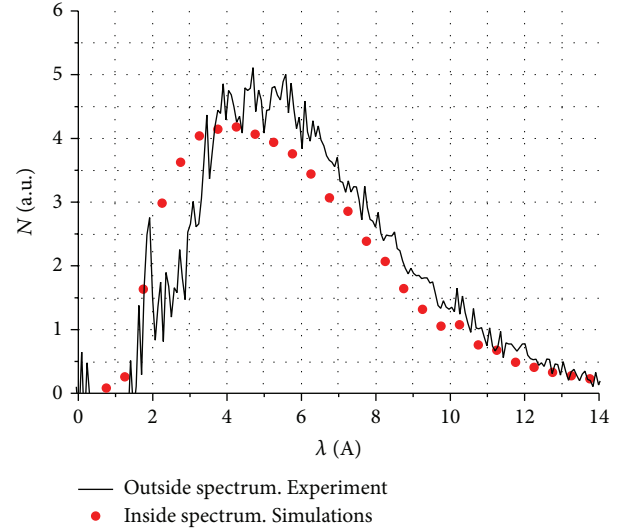


FIGURE 9: The neutron spectrum inside the methane cavity and the spectrum of neutrons escaping through the exit hole are compared. Thin line indicates results of measurements outside of the cavity. Points correspond to the numerical simulation of the spectrum inside the cavity.

reflection from a methane cavity wall is higher than their energy after subsequent reflections, and the contribution of such neutrons into the total neutron flux is more important (as the number of neutrons decreases after each reflection).

The measured spectrum (Figure 7) is compared with the simulated spectrum inside the cavity (Figures 3 and 4) in Figure 9. For convenience of normalization, we excluded from the simulated spectrum inside the cavity a contribution of neutrons from the initial beam; they marginally affect the UCN production.

8. Conclusion

Our calculations showed that the installation of a helium UCN source in an external beam of thermal neutrons at the ILL reactor in Grenoble, at the PIK reactor in Gatchina, or at the ESS spallation source in Lund would allow achieving the UCN density of $\sim 10^5$ UCN \cdot cm $^{-3}$. The production rate of such an UCN source is $\sim 10^7$ UCN \cdot s $^{-1}$. Our measurements confirmed validity of these calculations.

The main source of thermal load in such a source, if it is installed at a heavy-water reactor like that at the ILL, for instance, consists of gamma-quanta produced in the capture of neutrons in the moderator/reflector itself. The estimated value of the heat load caused by such gamma-quanta in helium of the UCN source is 0.2 W for the considered geometry and the neutron flux (2). This estimation of the heat load means that one could even considerably increase the flux of incoming neutrons, and thus one could increase the density and the flux of UCNs in the source. For instance, an increase of the diameter of the input neutron guide from 20 cm to 30 cm would increase the input neutron flux by a factor of ~ 5 . However, one should take into account that a

further increase of the heat load over 1-2 W would complicate cooling of liquid helium in the source below the required temperature of 0.8 K provided that the method of pumping of ^3He vapors or the method of dilution of ^3He in ^4He is used. Therefore the limit of production rate in such a source is probably close to $\sim 10^8 \text{ n}\cdot\text{s}^{-1}$.

On the one hand, the proposed UCN source provides parameters much better than those of existing UCN sources; in particular the UCN density would be a factor of 10^3 higher. On the other hand, its parameters are similar to those in most optimistic alternative projects while the price is much lower.

Conflict of Interests

The authors declare that there is no conflict of interests regarding the publication of this paper.

Acknowledgments

The authors are sincerely grateful to the staff of the DIN 2Pi instrument, in particular to V. I. Morozov, for their help during this experiment. Also they are sincerely grateful to Y. Shin, C. M. Lavelle, W. Mike Snow, David V. Baxter, Xin Tong, Haiyang Yan, and Mark Leuschner for providing them with the program for calculations of the interaction of neutrons with cold methane.

References

- [1] Y. B. Zel'dovich, "Storage of cold neutrons," *Soviet Physics JETP*, vol. 9, p. 1389, 1959.
- [2] V. I. Luschnikov, Pokotilovsky, N. Yu, A. V. Strelkov, and F. L. Shapiro, "Observation of ultracold neutrons," *JETP Letters*, vol. 9, pp. 23–26, 1969.
- [3] J. Butterworth, P. Geltenbort, E. Korobkina et al., "Proceedings of the international workshop on particle physics with slow neutrons, held at the Institut Laue-Langevin, Grenoble, France, October 22–24, 1998. Preface," *Nuclear Instruments and Methods in Physics Research A*, vol. 440, p. 5, 2000.
- [4] V. V. Nesvizhevsky, C. Plonka-Spehr, K. Protasov et al., "Particle physics with slow neutrons. Proceedings of the international workshop on particle physics with slow neutrons, Institut Laue-Langevin, Grenoble, France, May 29–31, 2008. Preface," *Nuclear Instruments and Methods in Physics Research A*, vol. 611, p. 7, 2009.
- [5] I. Antoniadis, S. Baessler, O. Bertolami et al., "Workshop GRANIT-2010, 14–19 February 2010, Les Houches, France," *Comptes Rendus Physique*, vol. 12, no. 8, pp. 703–706, 2011.
- [6] R. Golub and J. M. Pendlebury, "Super-thermal sources of ultracold neutrons," *Physics Letters A*, vol. 53, no. 2, pp. 133–135, 1975.
- [7] P. Schmidt-Wellenburg, K. H. Andersen, P. Courtois et al., "Ultracold-neutron infrastructure for the gravitational spectrometer GRANIT," *Nuclear Instruments and Methods in Physics Research Section A*, vol. 611, pp. 267–271, 2009.
- [8] Y. Masuda, T. Kitagaki, K. Hatanaka et al., "Spallation ultracold-neutron production in superfluid helium," *Physical Review Letters*, vol. 89, no. 28, part 1, Article ID 284801, 2002.
- [9] G. Greene, V. Cianciolo, P. Koehler et al., "The fundamental neutron physics beamline at the spallation neutron source," *Journal of Research of NIST*, vol. 110, pp. 149–152, 2005.
- [10] <http://nuclear.uwinnipeg.ca/ucn/triumf/post-acot-5-26-8/ucn-post-acot-may08.pdf>.
- [11] A. P. Serebrov, V. A. Mityukhlyayev, A. A. Zakharov et al., "Project of the ultracold and cold neutron source at the WWR-M reactor with superfluid helium as a moderator," *Physics of the Solid State*, vol. 52, p. 1034, 2010.
- [12] R. Golub, C. Jewell, P. Ageron et al., "Operation of a superthermal ultra-cold neutron source and the storage of ultra-cold neutrons in superfluid Helium," *Zeitschrift für Physik B Condensed Matter*, vol. 51, no. 3, pp. 187–193, 1983.
- [13] Y. Abe and N. Morishima, "Quantitative evaluation of ultracold neutron production and storage in superfluid helium," *Nuclear Instruments and Methods in Physics Research Section A*, vol. 463, no. 1-2, pp. 293–298, 2001.
- [14] P. D. Bangert, M. D. Cooper, and S. K. Lamoreaux, "Enhancement of superthermal ultracold neutron production by trapping cold neutrons," *Nuclear Instruments and Methods in Physics Research A*, vol. 410, pp. 264–272, 1998.
- [15] S. Baessler, A. M. Gagarski, E. V. Lychagin et al., "New methodical developments for GRANIT," *Comptes Rendus Physique*, vol. 12, no. 8, pp. 729–754, 2011.
- [16] V. V. Nesvizhevsky, E. V. Lychaginb, A. Y. Muzychka, A. V. Strelkovb, G. Pignolc, and K. V. Protasov, "The reflection of very cold neutrons from diamond powder nanoparticles," *Nuclear Instruments and Methods in Physics Research A*, vol. 595, pp. 631–636, 2008.
- [17] E. V. Lychagin, A. Y. Muzychka, V. V. Nesvizhevsky, G. Pignol, K. V. Protasov, and A. V. Strelkov, "Storage of very cold neutrons in a trap with nano-structured walls," *Physics Letters B*, vol. 679, pp. 186–190, 2009.
- [18] V. V. Nesvizhevsky, "Interaction of neutrons with nanoparticles," *Physics of Atomic Nuclei*, vol. 65, no. 3, pp. 400–408, 2002.
- [19] S. Grieger, H. Friedrich, K. Guckelsberger et al., "The total neutron scattering cross section of solid methane in phase II," *Journal of Chemical Physics*, vol. 109, p. 3161, 1998.
- [20] Y. Shin, W. Mike Snow, C. Y. Liu, C. M. Lavelle, and D. V. Baxter, "Microscopic model for the neutron dynamic structure factor of solid methane in phase II," *Nuclear Instruments and Methods in Physics Research A*, vol. 620, no. 2-3, pp. 382–390, 2010.
- [21] Y. Shin, C. M. Lavelle, W. M. Snow et al., "Measurements of the neutron brightness from a phase II solid methane moderator at the LENS neutron source," *Nuclear Instruments and Methods in Physics Research Section A*, vol. 620, no. 2-3, pp. 375–381, 2010.
- [22] C. A. Baker, S. N. Balashova, J. Butterworth et al., "Experimental measurement of ultracold neutron production in superfluid ^4He ," *Physics Letters A*, vol. 308, pp. 67–74, 2003.
- [23] E. Korobkina, R. Golub, B. W. Wehring, and A. R. Young, "Production of UCN by downscattering in superfluid He," *Physics Letters A*, vol. 301, pp. 462–469, 2002.
- [24] P. Schmidt-Wellenburg, K. H. Andersena, and O. Zimmera, "Ultra cold neutron production by multiphonon processes in superfluid helium under pressure," *Nuclear Instruments and Methods in Physics Research A*, vol. 611, pp. 259–262, 2009.
- [25] I. V. Kalinin, V. M. Morozov, A. G. Novikov et al., "Characteristics of the DIN-2PI spectrometer with a neutron concentrator," *Technical Physics*, vol. 59, pp. 307–310, 2014.
- [26] Y. G. Dragunov, Y. S. Cherepnin, and V. A. Lukichev, "Conversion of research reactors to low-enrichment fuel," *Atomic Energy*, vol. 113, no. 1, pp. 39–43, 2012.

Review Article

Prospects for Studies of the Free Fall and Gravitational Quantum States of Antimatter

**G. Dufour,¹ D. B. Cassidy,² P. Crivelli,³ P. Debu,⁴ A. Lambrecht,¹
V. V. Nesvizhevsky,⁵ S. Reynaud,¹ A. Yu. Voronin,⁶ and T. E. Wall²**

¹Laboratoire Kastler-Brossel, CNRS, ENS, Collège de France, UPMC, Campus Jussieu, 75252 Paris, France

²Department of Physics and Astronomy, University College London, Gower Street, London WC1E 6BT, UK

³ETH Zurich, 8093 Zurich, Switzerland

⁴Institut de Recherche sur les lois Fondamentales de l'Univers, CEA Saclay, 91191 Gif-sur-Yvette, France

⁵Institut Max von Laue-Paul Langevin, 6 rue Jules Horowitz, 38042 Grenoble, France

⁶P.N. Lebedev Physical Institute, 53 Leninsky Prospekt, 117924 Moscow, Russia

Correspondence should be addressed to G. Dufour; gabriel.dufour@upmc.fr

Received 29 July 2014; Accepted 1 October 2014

Academic Editor: Ignatios Antoniadis

Copyright © 2015 G. Dufour et al. This is an open access article distributed under the Creative Commons Attribution License, which permits unrestricted use, distribution, and reproduction in any medium, provided the original work is properly cited. The publication of this article was funded by SCOAP³.

Different experiments are ongoing to measure the effect of gravity on cold neutral antimatter atoms such as positronium, muonium, and antihydrogen. Among those, the project GBAR at CERN aims to measure precisely the gravitational fall of ultracold antihydrogen atoms. In the ultracold regime, the interaction of antihydrogen atoms with a surface is governed by the phenomenon of quantum reflection which results in bouncing of antihydrogen atoms on matter surfaces. This allows the application of a filtering scheme to increase the precision of the free fall measurement. In the ultimate limit of smallest vertical velocities, antihydrogen atoms are settled in gravitational quantum states in close analogy to ultracold neutrons (UCNs). Positronium is another neutral system involving antimatter for which free fall under gravity is currently being investigated at UCL. Building on the experimental techniques under development for the free fall measurement, gravitational quantum states could also be observed in positronium. In this contribution, we report on the status of the ongoing experiments and discuss the prospects of observing gravitational quantum states of antimatter and their implications.

1. Introduction

At present, together with the dark matter problem, one of the most tantalizing open questions in physics is the baryon-antibaryon asymmetry; that is, why are we living in a matter-dominated universe? Where did all the antimatter go? Different theoretical and experimental efforts trying to address this question are ongoing, including activities focusing on the gravitational behavior of antimatter [1–5]. No compelling theoretical argument seems to support that a difference between the gravitational behavior of matter and antimatter should be expected [6], although some attempts have been made to show the contrary [7–11]. Moreover observations and experiments have been interpreted as evidence against

the existence of “antigravity” type forces [12–15]. However, those could be argued to be model dependent and, therefore, a simple free fall measurement is preferable. This justifies ongoing experimental efforts in that direction. A first attempt in this direction was made recently by the ALPHA collaboration [1] that bounds the ratio of gravitational mass to inertial mass of antihydrogen between -65 and 110 .

The idea of directly measuring the gravitational force acting on antiparticles in the Earth's field goes back many decades, from the work of Witteborn and Fairbank, attempting to measure the acceleration of gravity for electrons and, eventually, positrons [16] to the PS200 experiment at CERN in the 1980s which included measurements on antiprotons [17]. Such measurements are extremely difficult because

measuring the force of gravity on a charged particle requires a physically unrealistic elimination of stray electromagnetic fields. The obvious solution to this problem is to use neutral antimatter particles. However, at the present time, it is not technically feasible to do so; antineutrons cannot be produced in a controllable manner and antineutrinos are similarly elusive to experimenters. One may instead consider using composite systems that are electrically neutral, in which case it is only necessary to contend with dipole moments. Only a few systems that are composed of or contain some fraction of antimatter are available for scientific study. These are antihydrogen, muonium, and positronium, which have all been suggested as possible candidates for gravity measurements [18].

Selecting between different experimental methods, one should aim at precision experiments as they are much more strongly motivated theoretically. Among these, the method of quantum gravitational spectroscopy stands out by its remarkable statistical sensitivity and its cleanness from a systematic point of view.

Gravitational quantum states are solutions of the Schrödinger equation in a gravity field above a surface. They are characterized by the following energy (E_n) and spatial scale (H_n):

$$E_n = \varepsilon_0 \lambda_n, \quad \varepsilon_0 = \sqrt[3]{\frac{\hbar^2 M^2 g^2}{2m}}, \quad (1)$$

$$H_n = \frac{E_n}{Mg}, \quad (2)$$

$$\text{Ai}(-\lambda_n) = 0, \quad (3)$$

$$\lambda_n \approx \{2.34, 4.09, 5.52, 6.79, 7.94, 9.02, 10.04, \dots\}.$$

Here, M is the gravitational mass of the particle, m is its inertial mass (we distinguish between M and m in view of discussing EP tests), g is the gravitational field intensity near the Earth's surface, $\bar{g} = Mg/m$ is the acceleration of the particle in that field, and $\text{Ai}(x)$ is the Airy function [19, 20]. For neutrons and antihydrogen atoms, the height of the lowest gravitational level is $13.7 \mu\text{m}$. For positronium, whose mass is approximately 1000 times smaller, it extends over 1.3 mm. The frequency of transitions between first and second quantum states equals 254 Hz for neutrons and antihydrogen and 26 Hz for positronium. The corresponding characteristic times needed to form quantum states are 0.5 ms and 5 ms, respectively.

Quantum gravitational states were observed for the first time with neutrons by measuring their transmission through a slit made of a mirror and an absorber in the GRANIT experiment [21]. If the distance between the mirror and the absorber (which is a rough surface used as a scatterer to mix the velocity components) is much higher than the turning point for the corresponding gravitational quantum state, the neutrons pass through the slit without significant losses. As the slit size decreases, the absorber starts approaching the size of the neutron wave function and the probability of neutron loss increases. If the slit size is smaller than the characteristic size of the neutron wave function in the lowest quantum state,

the slit is not transparent for neutrons as was demonstrated experimentally.

Here, we analyze, in detail, several experiments which will study the free fall of antiatoms and argue that the observation of gravitational quantum states of antimatter is feasible. In Section 2, we describe the forthcoming $\bar{\text{H}}$ experiment GBAR. We explain in Section 3 the quantum reflection mechanism which allows the formation of gravitational quantum states of $\bar{\text{H}}$ above material surfaces. In Section 4, we show how the filtering scheme of the GRANIT experiment could be implemented in GBAR and, in Section 5, we describe a possible spectroscopy of gravitational quantum states of $\bar{\text{H}}$. Section 6 reviews the status of positronium free fall experiment at UCL and Section 7 explores the possibility of observing gravitational quantum states of positronium.

2. The GBAR Experiment

GBAR is an experiment in preparation at CERN. Its goal is to measure the gravitational acceleration ($\bar{g} = Mg/m$) imparted to freely falling antihydrogen atoms, in order to perform a direct experimental test of the Weak Equivalence Principle with antimatter. The objective is to reach a relative precision on \bar{g} of 1% in a first stage, with the perspective to reach a much higher precision using quantum gravitational states in a second stage, as is described in Section 5.

The principle of the experiment is described in detail in [22] and is briefly recalled here. It is based on an idea proposed in [23]. Antihydrogen ions $\bar{\text{H}}^+$ are produced, trapped, and sympathetically cooled to around $10 \mu\text{K}$. The excess positron is detached by a laser pulse, which gives the start signal for the free fall of the ultracold antihydrogen atom $\bar{\text{H}}$. The $\bar{\text{H}}$ subsequent annihilation on a plate is detected and provides the information to measure \bar{g} . The choice of producing $\bar{\text{H}}^+$ ions to get ultracold antihydrogen atom is the specificity of the GBAR experiment. It is very costly in statistics but makes the cooling to μK temperatures a realistic aim.

We report, in this section, on three recent progresses in the preparation of the experiment: estimations of the $\bar{\text{H}}^+$ production cross-sections, accumulation of positrons, and cooling of the $\bar{\text{H}}^+$ ions.

2.1. Production Cross-Sections of $\bar{\text{H}}^+$ Ions. The $\bar{\text{H}}$ production proceeds in two steps: $\bar{p} + \text{Ps} \rightarrow \bar{\text{H}} + e^-$ (1) followed by $\bar{\text{H}} + \text{Ps} \rightarrow \bar{\text{H}}^+ + e^-$ (2). The Ps symbol stands for positronium. The cross-sections of these reactions are not well known and are very low. The matter counterpart of the first one has been measured. It is around 10^{-15} cm^2 (10^9 barn) for tens of keV protons [24]. The second one is estimated to be around 10^{-16} cm^2 (10^8 barn) [25].

New calculations of these reactions have been performed in which the first excitations levels for the Ps (up to $n = 3$) and the $\bar{\text{H}}$ (up to $n = 5$) have been considered. The results suggest that the production of $\bar{\text{H}}^+$ can be efficiently enhanced by using either a fraction of Ps(2p) and a 2 keV antiproton beam or a fraction Ps(3d) and antiprotons with kinetic energy below 1 keV [26]. The product of the cross-sections of reactions

(1) and (2) reaches values around 10^{-29} cm^4 (10^{19} barn^2) for an optimized fraction of excited Ps. Simulations are underway to estimate the effective gain with a realistic experimental setup.

This shows that very low energy antiprotons are needed. The extremely low energy antiproton (ELENA) ring which is in construction at CERN and which will complement the antiproton decelerator (AD) will provide 75 ns rms bunches of 5×10^6 100 keV antiprotons every 100 s. Those have to be further decelerated and cooled to match the GBAR requirements. The decelerator is under construction at CSNSM (Centre de Sciences Nucléaires et de Sciences de la Matière) in Orsay, France.

2.2. Positron Accumulation. In addition to a high flux of low energy antiprotons, the production of \bar{H}^+ via reactions (1) and (2) requires to form a dense cloud of positronium. It has been shown that Ps can be efficiently produced by dumping few keV positrons on mesoporous silica films. Yields of 30 to 40% depending on the incident positron energy (few keV) have been measured [27, 28]. The accumulation of a very large number of positrons, around 2×10^{10} , between two ejections of antiprotons from ELENA is thus necessary to produce a dense enough positronium cloud.

A demonstration facility for the production and accumulation of positrons is currently running at CEA/Saclay. It consists of a low energy electron linear accelerator (LINAC), a high field Penning-Malmberg trap from the Atomic Physics Laboratory in RIKEN, Japan, and a dedicated beam line for further studies of positron-positronium conversion and for applications in material science. In addition, a laser system is now being built at LKB (Laboratoire Kastler-Brossel) in Paris to test the excitation of the positronium which will be formed downstream of the trap.

The LINAC produces a 4.3 MeV electron bunched beam. The bunch length is 200 μs , and the LINAC runs at 200 Hz, producing a mean current of 120 μA . Electrons are sent onto a tungsten mesh moderator. A flux of typically 3×10^6 slow (few 100 eV) positrons per second is driven towards the Penning trap through a vacuum tube equipped with solenoid coils producing a 80 mT field. They are accelerated to around 1 keV to enter the high magnetic field (5 T) region. They reach the Penning trap which is made of 23 cylindrical electrodes, surrounded by 4 additional long electrodes to control the admission and the trapping of incident particles. Positrons make a round trip in less than 100 ns. In order to trap them, it is necessary to compress the 200 μs bunch. This is done by applying a varying voltage (20 to 150 V) when extracting the slow positron from the moderator. In this way, it is possible to close the entrance of the trap before the bunch escapes. With this method, one can trap one single bunch.

In order to accumulate a large number of bunches, positrons have to be slowed down and stored in a dedicated potential well formed by a subset of electrodes of the trap (see Figure 1) before the next bunch arrives. Positrons are cooled by passing through a preloaded electron plasma in another dedicated potential well. This method has been set up and demonstrated in [29] with a continuous positron beam issued

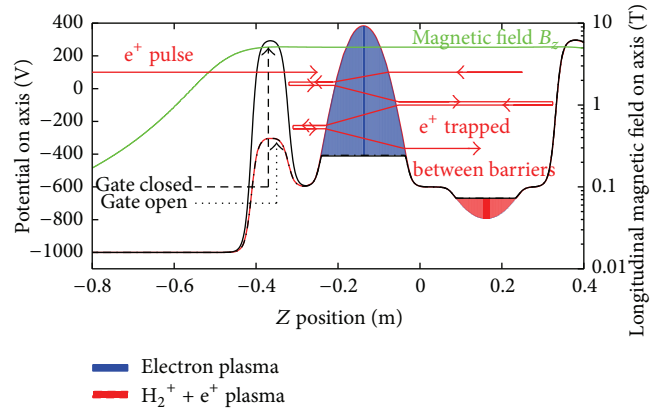


FIGURE 1: The positron trapping mechanism (from [30]). The horizontal axis is the position along the trap axis. The left vertical axis is the voltage seen by particles. The magnetic field strength is shown by the green curve, with the scale on the right vertical axis. In blue, the electron potential well filled with electrons is drawn, reducing the apparent voltage shown by black curve with the value on the left vertical axis. The positron potential is shown well in red. When a positron bunch arrives, the entrance electrode voltage is low (dashed dotted line). It is then increased and positrons go back and forth (it is depicted by red arrows) between this gate and the downstream part of the trap. They pass many times through the electron plasma and are eventually slowed down and fall into their well. The presence of residual H_2^+ helps the final catching of positrons. In order to reach the desired number of trapped positrons, the positron well has to be enlarged and deepened during the accumulation process from around 200 V to around 1 kV. Positrons may also be trapped in the potential well formed between the entrance electrode and the electron well, but its depth remains constant and the induced loss is small.

from a ^{22}Na source. With such a beam, it is not possible to close the entrance gate, and positrons must be slowed down in one step. This was done with a remoderator downstream of the trap. An efficiency of 1% was obtained. With a bunched positron beam, the remoderator is not necessary, and a much higher efficiency is expected.

The cooling time fixes the maximal LINAC frequency and depends on the density of the electron plasma. With $10^{17} \text{ e}^-/\text{m}^3$, simulations show that the cooling time is around 3 ms.

The principle of this accumulation scheme has now been successfully demonstrated at Saclay. The details of the experimental setup used during accumulation are given in [30]. The result of a successful set of accumulation trials is shown in Figure 2. Given the characteristics of the demonstrator facility at Saclay, a realistic objective is now to accumulate around 10^8 positrons in the trap within 2 minutes.

2.3. Cooling of the \bar{H}^+ Ions. Recent progresses have been made for the design of the cooling of \bar{H}^+ ions. The cooling proceeds in two steps: Doppler cooling at the mK level and Raman side band cooling to reach 10 μK .

In the first step, ions are captured in a linear Paul trap inside which Be^+ ions are preloaded and laser cooled. In the

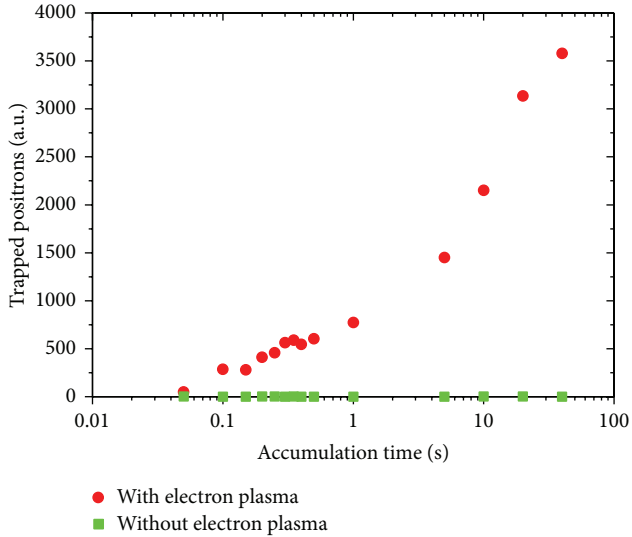


FIGURE 2: The accumulation of positrons (from [30]).

original scheme of GBAR, it was assumed that the \bar{H}^+ ions would be cooled by Coulomb interactions with the Be^+ ions (sympathetic cooling). Simulations show that this process is very slow. This is due to the large mass ratio between the ions. As a consequence, one cannot reach the mK level in a short enough time to avoid the destruction of the \bar{H}^+ : the laser cooling of Be^+ induces the photodetachment of the excess positron in a fraction of a second. However, the simulations show also that the addition of a third species of ions of intermediate mass, namely, HD^+ ions, makes the process efficient enough [31]. Starting with 1800 Be^+ and 200 HD^+ ions, cooling times of ms are achievable.

In the second step, to reach the $10 \mu K$ level necessary for the free fall experiment, a Be^+/\bar{H}^+ ion pair must be transferred to a precision trap to undergo a ground state Raman side band cooling. Calculations show that one may achieve the desired cooling in less than a second. This is shown in [31] and references therein. This method will be tested with matter ions (Ca^+/Be^+ , H_2^+/Be^+) before being implemented for the GBAR experiment. Traps are being mounted at LKB in Paris and at Mainz University.

Since the uncertainty on the measurement of \bar{g} is fully dominated by the initial velocity dispersion due to both the vertical velocity after cooling and the recoil due to the positron photodetachment, the implementation of a vertical velocity selector will allow a drastic gain in the statistics needed to reach the 1% precision on \bar{g} as is described in Section 4.

3. Quantum Reflection of Antihydrogen on Material Surfaces

In the ultracold regime, the interaction of antihydrogen (\bar{H}) atoms with a surface is governed by the phenomenon of quantum reflection. Although the atoms are strongly attracted to the surface, the atomic wave function can be partly

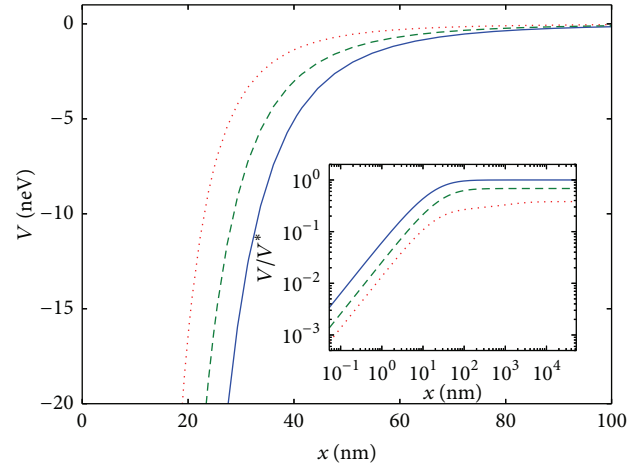


FIGURE 3: Casimir-Polder (CP) potential for antihydrogen in the vicinity of a material bulk; from top to bottom: perfect conductor (full line), silicon (dashed line), and silica (dotted line); inset: ratio V/V^* to the retarded potential V^* for a perfectly conducting mirror; see text.

reflected on the steep atom-surface potential, leading to a nonzero probability of classically forbidden reflection. This effect is relevant to experiments such as GBAR where ultracold \bar{H} atoms are detected by annihilation on a plate (see Section 2).

A single atom placed in vacuum near a material surface experiences an attractive Casimir-Polder (CP) force [32, 33]. This force is a manifestation of the electromagnetic quantum fluctuations which are coupled to the atomic dipole. Quantum reflection occurs if an atom impinges with low velocity on such a rapidly varying potential [34]. We will give a more explicit condition later on.

In this section, we first describe how the CP potential is calculated for realistic experimental conditions. We then go on to compute the scattering amplitudes of an atom on this potential. We show that quantum reflection can be understood as a deviation from the semiclassical approximation. Finally, we describe materials from which quantum reflection is enhanced and above which gravitationally bound states of \bar{H} could be observed.

3.1. Calculation of the Casimir-Polder Potential. We use the scattering approach to Casimir forces [35] to give a realistic estimation of the atom-surface interaction energy. In this approach, the interacting objects are described by reflection matrices for the electromagnetic field. Reflection on a plane is described by Fresnel coefficients, while reflection on the atom is treated in the dipolar approximation and depends on the dynamic polarizability [36]. This allows an evaluation of the CP potential for any material when its optical properties are known. Those used here are detailed in [37]. Note that since the typical length scale for quantum reflection (~ 100 nm) is below the thermal wavelength at 300 K ($\sim 1 \mu m$), we carried out all calculations at null temperature.

The CP potential for \bar{H} at a distance x of a perfectly conducting plane and thick silicon and silica slabs are presented in Figure 3. For a perfectly conducting mirror in

the long-distance regime, we recover the historic result of Casimir and Polder [32, 33]:

$$V(x) \underset{x \gg \lambda}{\approx} V^*(x) = -\frac{3\hbar c}{8\pi x^4} \frac{\alpha(0)}{4\pi\epsilon_0}, \quad (4)$$

where $\alpha(0)$ is the static polarizability of the atom.

For real mirrors, the potential is reduced but it shows the same power law dependence in the van der Waals (short distance) and retarded (long-distance) regimes:

$$V(x) \underset{x \ll \lambda}{\approx} -\frac{C_3}{x^3}, \quad V(x) \underset{x \gg \lambda}{\approx} -\frac{C_4}{x^4}, \quad (5)$$

where λ is a typical wavelength associated with the optical response of atom and plane.

3.2. Scattering on the Casimir-Polder Potential. We now solve the Schrödinger equation for an atom of energy $E > 0$ scattering on the CP potential $V(x)$:

$$\frac{d^2}{dx^2}\psi(x) + \frac{p(x)^2}{\hbar^2}\psi(x) = 0, \quad (6)$$

with $p(x) = \sqrt{2m(E - V(x))}$ being the classical momentum. We write the exact wave function as a sum of counter-propagating WKB waves whose coefficients are allowed to vary:

$$\begin{aligned} \psi(x) = & \frac{c_{\text{in}}(x)}{\sqrt{p(x)}} \exp\left(-\frac{i}{\hbar} \int^x p(x') dx'\right) \\ & + \frac{c_{\text{out}}(x)}{\sqrt{p(x)}} \exp\left(\frac{i}{\hbar} \int^x p(x') dx'\right). \end{aligned} \quad (7)$$

Upon insertion in the Schrödinger equation, we obtain coupled first-order equations for the coefficients $c_{\text{in}}(x)$, $c_{\text{out}}(x)$ [38]. The annihilation of \bar{H} on the material surface translates as a fully absorbing boundary condition on the surface: $c_{\text{out}}(x=0) = 0$. This is in contrast with matter atoms, for which more complicated surface physics is involved in the boundary condition. We emphasize that \bar{H} -surface interaction at distances below few atomic units differs significantly from H -surface interaction. It is remarkable that, due to complete annihilation of \bar{H} in the bulk of the surface, the details of such short-range physics are not important [39]. Indeed, any information about antiatom-wall interaction is encrypted in the reflected wave, which, as we will show in the following, is produced at asymptotically large distances.

Close to the surface, the energy becomes negligible compared with the potential, which takes the van der Waals form and $c_{\text{in}}(x)$, $c_{\text{out}}(x)$ can be solved analytically [37]. The equations are then integrated numerically until $c_{\text{in}}(x)$, $c_{\text{out}}(x)$ become constants.

The reflection probability $|r|^2 = \lim_{x \rightarrow \infty} |c_{\text{out}}(x)/c_{\text{in}}(x)|^2$ is plotted against the energy E in Figure 4 for various semi-infinite media. Note that the quantum reflection probability is larger for materials with a weaker CP interaction, such as silica.

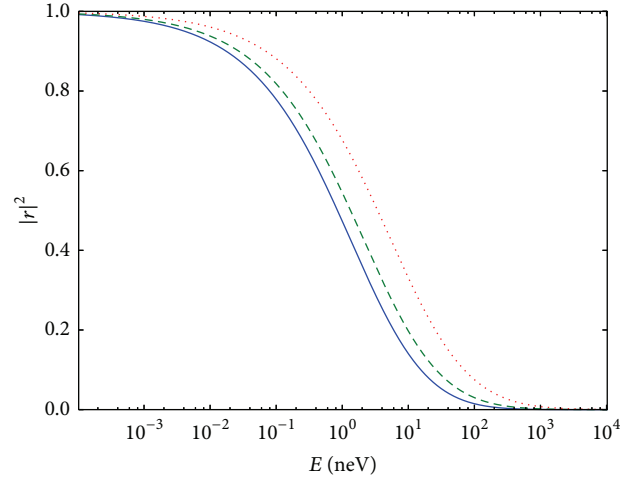


FIGURE 4: Quantum reflection probability $|r|^2$ as a function of the energy for antihydrogen atoms on bulk mirrors; from bottom to top: perfect conductor (full line), silicon (dashed line), and silica (dotted line).

3.3. The Badlands Function. To understand this surprising result, we look more closely at what distinguishes the exact solution of the Schrödinger equation from the reflectionless WKB approximation. If c_{in} , c_{out} are no longer allowed to vary, one can show that the wave function (7) obeys a modified Schrödinger equation where $p(x)^2$ is replaced by $\tilde{p}(x)^2 = p(x)^2(1 + Q(x))$ [38]. $Q(x)$ is known as the badlands function since the WKB approximation is not valid in regions where it is nonnegligible:

$$Q(x) = \frac{\hbar^2}{2p(x)^2} \left(\frac{p''(x)}{p(x)} - \frac{3}{2} \frac{p'(x)^2}{p(x)^2} \right). \quad (8)$$

For the CP potential, the badlands function exhibits a peak in the region where $|V(x)| = E$ but goes to zero both as $x \rightarrow \infty$ (where the potential cancels) and as $x \rightarrow 0$ (where the classical momentum diverges).

As the energy is decreased, the semiclassical approximation breaks down and the badlands function's peak becomes larger. But, for a given energy, the peak is larger and closer to the surface when the potential is weak, as shown in Figure 5. The difference between exact and WKB solutions is larger in weaker CP potentials, leading to enhanced quantum reflection.

3.4. Enhancing Quantum Reflection. Quantum reflection first appears as a bias in the context of the GBAR experiment, since it tends to exclude low energy atoms from the statistics. However, this phenomenon opens perspectives for the storage and guiding of antimatter with material walls. With this in mind, we consider materials which couple weakly to the electromagnetic field and are therefore good mirrors for atoms, as we have seen in the previous paragraph.

A simple strategy is to remove matter from the reflective medium, by using thin slabs or porous materials for example. Our versatile approach allowed us to compute the CP

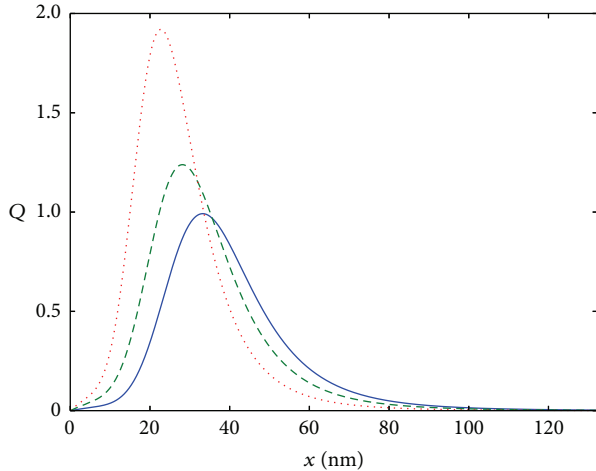


FIGURE 5: The badlands function $Q(x)$ for an antihydrogen atom with energy $E = 10$ neV; from bottom to top: perfect conductor (full line), silicon (dashed line), and silica (dotted line).

TABLE 1: The lifetime of the first gravitationally bound state of antihydrogen above various surfaces.

Surface (porosity)	Lifetime (s)
Perfect conductor	0.11
Bulk silicon	0.14
Bulk silica	0.22
Nanodiamond powder (95%)	0.89
Porous silicon (95%)	0.94
Silica aerogel (98%)	4.6

interaction near thin slabs, an undoped graphene sheet [37] and nanoporous materials [40]. The latter consist of a solid matrix which forms an array of nanometric pores. Aerogels, which are obtained by supercritically drying a silica gel, are a well-known example. We also consider porous silicon and powders of diamond nanoparticles formed by explosive shock.

From a distance larger than the typical pore size, such materials can be modeled as homogeneous effective media with properties averaged between that of vacuum and that of the solid matrix. In consequence, their effective dielectric constant is extremely low, as a result of which quantum reflection is exceptionally efficient. In Table 1, we show the lifetime of an antihydrogen atom in the first gravitationally bound state above a surface (see Section 5 for more details).

Note that this approach does not take into account the possible presence of stray charges on the surface, a question that would have to be addressed to observe the predicted reflection probabilities. Moreover, the effective medium approximation is applicable only for low atom velocities, such that the atom is reflected far enough from the surface. With these caveats, nanoporous materials are an outstanding candidate for the manipulation and study of antihydrogen and its gravitationally bound states over lifetimes of a few seconds.

4. Shaping of Vertical Velocity Components of Antihydrogen Atoms for GBAR

The main source of uncertainty on the determination of \bar{g} in the GBAR experiment is the width of the vertical velocity distribution of the atom at the beginning of the free fall. This spread in velocities is due to the quantum uncertainty on the momentum of \bar{H}^+ in the ground state of the harmonic Paul trap and to the additional recoil associated with the photodetachment of the extra positron (see Section 2).

In this section, we give an estimation of the uncertainty on the arrival time associated with the initial vertical velocity spread and show how it can be reduced by filtering out the fastest atoms. Since slow antihydrogen atoms bounce on material surfaces thanks to quantum reflection (see previous section), the filtering scheme used in GRANIT with ultracold neutrons [21] can also be applied in GBAR.

4.1. Width of the Arrival Time Distribution. We consider a wave packet falling in a linear gravitational potential and want to determine the arrival time distribution on a fixed horizontal plane, supposing there is no reflection from that (ideal) detector. In this case, classical and quantum calculations give identical results, as can be seen by noticing that the Wigner quasidistribution function obeys the classical equations of motion if the potential is at most quadratic. Therefore, in a linear potential, a given initial phase-space distribution simply propagates along the classical trajectories.

For a wave packet initially centered at a height H above the detector, with zero mean velocity and uncorrelated vertical position and velocity distributions of widths Δz and Δv , respectively, the spread of the arrival time distribution is

$$\frac{\Delta t}{t_H} = \sqrt{\left(\frac{\Delta z}{2H}\right)^2 + \left(\frac{\Delta v}{\sqrt{2gH}}\right)^2}, \quad (9)$$

with $t_H = \sqrt{2H/g}$ being the classical free fall time. This translates as a statistical uncertainty $\Delta\bar{g}/\bar{g} = 2\Delta t/\sqrt{N}t_H$ on the determination of \bar{g} after N independent measurements.

If the particle is initially in the ground state of a harmonic trap, the distribution is Gaussian and saturates the Heisenberg inequality: $\Delta z\Delta v = \hbar/2m$. Then, the time uncertainty is minimal for

$$\Delta v = \Delta v_{\text{opt}} = \sqrt{\frac{\hbar}{2m}} \sqrt{\frac{g}{2H}}. \quad (10)$$

For $H = 30$ cm and $\bar{g} = g$, this evaluates $\Delta v_{\text{opt}} \approx 3.6 \times 10^{-4}$ m/s, and the relative uncertainty on the arrival time is 2×10^{-4} . However, the current expected value for GBAR is three orders of magnitude larger $\Delta v_0 \approx 0.5$ m/s, which leads to a relative uncertainty of 0.2.

The uncertainty in GBAR is largely dominated by the vertical velocity dispersion. If the initial velocity dispersion can be reduced from Δv_0 to Δv by filtering out the hottest atoms, the single-shot precision and the number of atoms are both reduced by a factor $\Delta v/\Delta v_0$. Despite the loss in statistics,

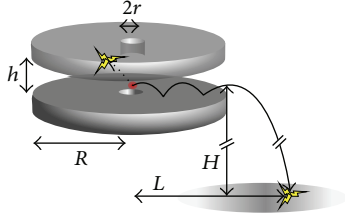


FIGURE 6: Scheme of the proposed device to reduce the vertical velocity spread of the falling wave packet (see text).

this results in a net reduction of the statistical uncertainty on \bar{g} .

4.2. Shaping of the Vertical Velocity Distribution. Our proposal [41] to realize this filtering is to let the atoms pass through a horizontal slit between two disks. The bottom disk has a smooth top surface on which atoms reflect with high probability whereas the top disk has a rough bottom surface which effectively acts as an absorber for the atoms (see Figure 6). Antihydrogen is initially trapped in the center of the two disks (openings are made in the center of the disks to allow operation of the trap). If its vertical velocity is high enough to reach the rough surface, it is reflected nonspecularly and remains inside the device until it annihilates with high probability. On the contrary, if it cannot reach the top disk, the atom will exit the device with high probability after bouncing on the bottom mirror a few times. It then falls freely to a detector located at a height H below. Since the horizontal velocity is conserved, the knowledge of the total time between photodetachment and annihilation and of the total horizontal L distance traveled allows one to correct for the time spent inside the device before the free fall.

If h is the height of the slit, the velocity spread at the output is $\Delta v \approx \sqrt{2\bar{g}h}$ and the proportion of atoms that exit the device is $N/N_0 \approx \Delta v/\sqrt{2\pi}\Delta v_0$. Using the shaping device therefore reduces the statistical uncertainty on \bar{g} by a factor which scales $h^{1/4}$.

Classically, going to ever smaller slit heights leads to arbitrarily good precision. For example, for $h = 1$ mm, $\Delta v \approx 0.14$ m/s, $N/N_0 \approx 5\%$, and the accuracy is improved by a factor 2, whereas, for $h = 50$ μm , $\Delta v \approx 0.03$ m/s, $N/N_0 \approx 1\%$, and the accuracy improved by a factor 4.

There are, however, two limits: the number of repetitions of the experiment must be large enough that at least some atoms make it through the filter, but, more fundamentally, the wave function of the atom must fit inside the slit. Indeed for slit sizes below 50 μm the discrete spectrum of states bound by gravity must be taken into account. For a slit size of 20 μm , only the ground state can travel through the guide; below that, the transmission drops to zero.

This fact has been used to demonstrate the existence of gravitationally bound states for neutrons [21]. The next section explores the possibilities of similar experiments with antihydrogen to further increase the precision of equivalence principle tests on antimatter.

5. Resonance Spectroscopy of Gravitational States of Antihydrogen Near Material Surface

In this section, we will study a motion of an $\bar{\text{H}}$ atom, localized in a gravitational state near a horizontal plane mirror. The existence of such states though counterintuitive is explained by the phenomenon of quantum reflection of ultracold (anti-)atoms from a steep attractive Casimir-Polder atom-surface potential. Such states have similar properties with those discovered for neutrons [21, 42–45].

To account for the interaction of $\bar{\text{H}}$ with a material wall, the gravitational quantum states (1) receive a complex energy shift $\varepsilon_0\Delta$, with $\Delta \approx -i0.005$ for a perfectly conducting wall [46]. All states, therefore, acquire equal shift and width, which is a function of a material surface substance $\Gamma = 2|\Delta|\varepsilon_0$. This width corresponds to the lifetime of 0.1 s in case of a perfectly conducting surface and is twice longer for silica [37, 39, 40], for instance. The equal shifts of all gravitational states energy levels mean that already small modification of gravitational states due to antiatom-surface interaction is canceled out in the transition frequencies. This makes resonance spectroscopy of gravitational states particularly interesting for measuring gravitational properties of $\bar{\text{H}}$.

The interest to study gravitational quasistationary states of $\bar{\text{H}}$ is due to their comparatively long life-time on one hand and easy identification of certain state because of it is mesoscopic spatial scale. This opens an interesting perspective to apply potentially very precise resonance spectroscopy method to establish the gravitational properties of antiatoms. These methods are based on inducing an observation of resonance transitions between gravitational states. One possible approach is to use an alternating inhomogeneous magnetic field for such a purpose.

The interaction of a magnetic field with a ground state H atom moving through the field [47–49] is dominated by the interaction of an average magnetic moment of the atom [20] in a given hyperfine state with the magnetic field. We are going to focus on an alternating magnetic field with a gradient in the vertical direction. This condition is needed for coupling the field and the center of mass (c.m.) $\bar{\text{H}}$ motion in the gravitational field of the Earth. It allows one to induce resonant transitions between quantum gravitational states of $\bar{\text{H}}$ [46].

We will consider the magnetic field in the following form:

$$\vec{B}(z, x, t) = B_0\vec{e}_z + \beta \cos(\omega t)(z\vec{e}_z - x\vec{e}_x). \quad (11)$$

Here, B_0 is the amplitude of a constant, vertically aligned, component of magnetic field, β is the value of magnetic field gradient, z is a distance measured in the vertical direction, and x is a distance measured in the horizontal direction, parallel to the surface of a mirror. A time-varying magnetic field (11) is accompanied with an electric field ($[\vec{\nabla}\vec{E}] = -(1/c)\partial\vec{B}/\partial t$). However, for the velocities of ultracold atoms, corresponding interaction terms are small and thus will be omitted.

An inhomogeneous magnetic field couples the spin and the spatial degrees of freedom. A $\bar{\text{H}}$ wave function is

described in this case using a four-component column (in a nonrelativistic treatise) in the spin space, each component being a function of the c.m. coordinate \vec{R} , relative $\vec{p} - \vec{e}$ coordinate $\vec{\rho}$, and time t . The corresponding Schrödinger equation is

$$\begin{aligned} i\hbar \frac{\partial \Phi_\alpha(\vec{R}, \vec{\rho}, t)}{\partial t} \\ = \sum_{\alpha'} \left[-\frac{\hbar^2}{2m} \Delta_R + Mgz \right. \\ \left. + V_{\text{CP}}(z) + \widehat{H}_{\text{in}} + \widehat{H}_m \right]_{\alpha, \alpha'} \Phi_{\alpha'}(\vec{R}, \vec{\rho}, t). \end{aligned} \quad (12)$$

A subscript α in this equation indicates one of four spin states of the $\vec{p} - \vec{e}$ system. The meaning of the interaction terms is the following. $V_{\text{CP}}(z)$ is an atom-mirror interaction potential, which turns into the Casimir-Polder potential at an asymptotic atom-mirror distance (see [39, 50] and references therein). \widehat{H}_{in} is the Hamiltonian of the internal motion, which includes the hyperfine interaction:

$$\widehat{H}_{\text{in}} = -\frac{\hbar^2}{2\mu} \Delta_\rho - \frac{e^2}{\rho} + \frac{\alpha_{\text{HF}}}{2} \left(\widehat{F}^2 - \frac{3}{2} \right). \quad (13)$$

Here, $\mu = m_1 m_2 / m$, m_1 is the antiproton mass, m_2 is the positron mass, $m = m_1 + m_2$, α_{HF} is the hyperfine constant, and \widehat{F} is the operator of the total spin of the antiproton and the positron. We will treat only $\bar{\text{H}}$ atoms in a 1S-state (below, we will show that the excitation of other states in the studied process is improbable). The term $(\alpha_{\text{HF}}/2)(\widehat{F}^2 - 3/2)$ is a model operator, which effectively accounts for the hyperfine interaction and reproduces the hyperfine energy splitting correctly. The term \widehat{H}_m describes the field-magnetic moment interaction:

$$\widehat{H}_m = -2\vec{B}(z, x, t) \left(\mu_{\bar{e}} \widehat{s}_{\bar{e}} \times \widehat{I}_{\bar{p}} + \mu_{\bar{p}} \widehat{s}_{\bar{p}} \times \widehat{I}_{\bar{e}} \right). \quad (14)$$

Here, $\mu_{\bar{e}}$ and $\mu_{\bar{p}}$ are magnetic moments of the positron and the antiproton, respectively, $\widehat{s}_{\bar{e}}$, $\widehat{s}_{\bar{p}}$ is a spin operator, acting on spin variables of positron (antiproton), and $\widehat{I}_{\bar{e}}$, $\widehat{I}_{\bar{p}}$ is a corresponding identity operator. As far as the field $\vec{B}(z, x, t)$ changes in space and in time, this term couples the spin and the c.m. motion.

We will assume that in typical conditions of a spectroscopy experiment the $\bar{\text{H}}$ velocity component v parallel to the mirror surface (directed along x -axis) is of the order of a few m/s and is much larger than a typical vertical velocity in lowest gravitational states (which is of the order of cm/s). We will treat the motion in a frame moving with the velocity v of the $\bar{\text{H}}$ atom along the mirror surface. Thus, we are going to consider the x -component motion as a classical motion with a given velocity v , and we will substitute a x -dependence by a t -dependence. We will also assume that $B_0 \gg \beta L$, where $L \sim 30$ cm is a typical size of an experimental installation of interest. This condition is needed for “freezing” the magnetic moment of an atom along the vertical direction; it provides the maximum transition probability.

We will be interested in the weak field case, such that the Zeeman splitting is much smaller than the hyperfine level spacing $\mu_B B_0 \ll \alpha_{\text{HF}}$. The hierarchy of all mentioned above interaction terms could be formulated as follows:

$$\frac{m_2 e^2}{\hbar^2} \gg \alpha_{\text{HF}} \gg \mu_{\bar{e}} |B_0| \gg E_n, \quad (15)$$

and, thus, it justifies the use of the adiabatic expansion for solving (12); it is based on the fact that an internal state of an $\bar{\text{H}}$ atom follows adiabatically the spatial and temporal variations of an external magnetic field. Neglecting nonadiabatic couplings, an equation system for the amplitude $C_n(t)$ of a gravitational state $\psi_n(z)$ has the following form:

$$i\hbar \frac{dC_n(t)}{dt} = \sum_k C_k(t) V_{n,k}(t) \exp(-i\omega_{nk}t). \quad (16)$$

The transition frequency $\omega_{nk} = (E_k - E_n)/\hbar$ is determined by the gravitational energy level spacing. This fact is used in the proposed approach to access the gravitational level spacing by means of scanning the applied field frequency, as will be explained in the following.

Within this formalism, the role of the coupling potential $V(z, t)$ is played by the energy of an atom in a fixed hyperfine state thought of as a function of (slowly varying) distance z and time t . Consider

$$V_{n,k}(t) = \int_0^\infty \psi_n(z) \psi_k(z) E(t, z) dz. \quad (17)$$

Here, $\psi_n(z)$ is the gravitational state wave function, which is known in terms of the Airy function [46].

The energy $E(z, t)$ is the eigenvalue of the internal and magnetic interactions $\widehat{H}_{\text{in}} + \widehat{H}_m$, where the c.m. coordinate \vec{R} and time t are treated as slow-changing parameters. Corresponding expressions for the eigenenergies of a 1S manifold are

$$\begin{aligned} E_{a,c} &= E_{1s} - \frac{\alpha_{\text{HF}}}{4} \mp \frac{1}{2} \sqrt{\alpha_{\text{HF}}^2 + |(\mu_B - \mu_{\bar{p}}) B(z, t)|^2}, \\ E_{b,d} &= E_{1s} + \frac{\alpha_{\text{HF}}}{4} \mp \frac{1}{2} |(\mu_B + \mu_{\bar{p}}) B(z, t)|. \end{aligned} \quad (18)$$

Subscripts a, b, c, d are standard notations for hyperfine states of a 1S manifold in a magnetic field. The presence of a constant field B_0 produces the Zeeman splitting between states b and d . As far as the energy of states b, d depends on magnetic field linearly, while, for states a, c , it depends on magnetic field quadratically, only transition between b, d states takes place in case of a weak field. In the following, we will consider only transitions between gravitational states in a 1S(b, d) manifold.

A qualitative behavior of the transition probability is given in the Rabi formula, which can be deduced by means of neglecting the high frequency terms compared to the resonance couplings of only two states, initial i and final f ,

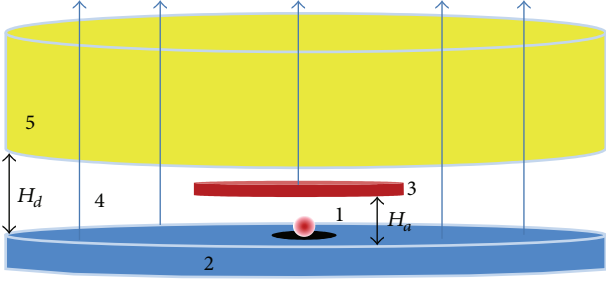


FIGURE 7: A sketch of the principle scheme of an experiment on magnetically induced resonant transitions between \bar{H} gravitational states. 1: a source of ultracold antihydrogen, 2: a mirror, 3: an absorber, 4: a magnetic field, and 5: a detector.

in case the field frequency ω is close to the transition frequency $\omega_{if} = (E_f - E_i)/\hbar$:

$$P = \frac{1}{2} \frac{(V_{if})^2}{(V_{if})^2 + \hbar^2 (\omega - \omega_{if})^2} \times \sin^2 \left(\frac{\sqrt{(V_{if})^2 + \hbar^2 (\omega - \omega_{if})^2}}{2\hbar} t \right) \exp(-\Gamma t). \quad (19)$$

The factor 1/2 appears in front of the right-hand side of the above expression due to the fact that only two (b, d) of four hyperfine states participate in the magnetically induced transitions.

It is important that the transition frequencies ω_{if} do not depend on the antiatom-surface interaction up to the second order in the splitting Δ . This is a consequence of the already mentioned fact that all energies of gravitational states acquire equal shift due to the interaction with a material surface.

A resonant spectroscopy of \bar{H} gravitational states could consist of observing \bar{H} atoms localized in the gravitational field above a material surface at a certain height as a function of the applied magnetic field frequency. A “flow-through type” experiment, analogous to the one discussed for the spectroscopy of neutron gravitational states [51], includes three main steps. A sketch of a principle scheme of an experiment proposed in [41] is shown in Figure 7 (see also Section 4).

First, an atom of \bar{H} is shaped in a ground gravitational state. This is achieved by means of passing \bar{H} through a slit, formed by a mirror and an absorber, which is placed above the mirror at a given height H_a . The mirror and the absorber form a waveguide with a state-dependent transmission [45]. The choice of $H_a = H_1 \approx 13.6 \mu\text{m}$ implies that only \bar{H} atoms in the ground gravitational state pass through the slit. Second, \bar{H} atoms are affected by an alternating magnetic field (11) while they are moving parallel to the mirror. An excited gravitational state is resonantly populated. Third, the number of \bar{H} atoms in an excited state is measured by means of counting the annihilation events in a detector, which is placed at a height H_d above the mirror. The value of H_d is chosen

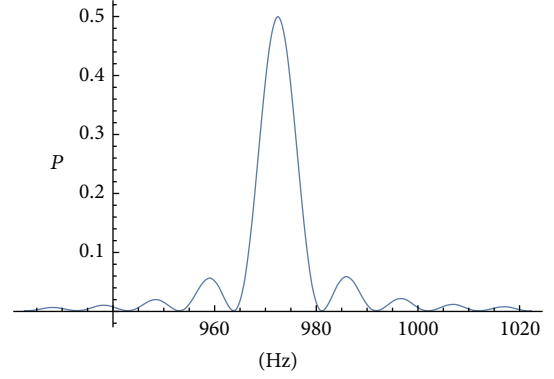


FIGURE 8: The transition probability as a function of the magnetic field frequency for the transition from the ground state to 6th gravitational state.

to be larger than the spatial size of the gravitational ground state and smaller than the spatial size of the final state (2), $H_1 \ll H_d < H_f$, so that the ground state atoms pass through, while atoms in the excited state are detected.

We present a simulation of the number of detected annihilation events as a function of the field frequency in Figure 8 for the transition from the ground to the 6th excited state, based on a numerical solution of the equation system (16). The corresponding resonance transition frequency is $\omega = 972.46 \text{ Hz}$. The value of the field gradient, optimized to obtain the maximum probability of $1 \rightarrow 6$ transition during the time of flight $t_{fl} = \tau = 0.1 \text{ s}$ turned to be equal to $\beta = 27.2 \text{ Gs/m}$; the corresponding guiding field value, which guarantees the adiabaticity of the magnetic moment motion, is $B_0 = 30 \text{ Gs}$.

It follows from (1) that the \bar{H} gravitational mass could be deduced from the measured transition frequency ω_{nk} as follows:

$$M = \sqrt{\frac{2m\hbar\omega_{nk}^3}{g^2(\lambda_k - \lambda_n)^3}}. \quad (20)$$

Let us mention that g in the above formula means the gravitational field intensity near the Earth’s surface, a value which characterizes properties of the field and is assumed to be known with a high precision. At the same time, all the information about gravitational properties of \bar{H} is included in the gravitational mass M . Equality of the gravitational mass M and the inertial mass m , imposed by the equivalence principle, results in the following expression:

$$M = \frac{2\hbar\omega_{nk}^3}{g^2(\lambda_k - \lambda_n)^3}. \quad (21)$$

Estimation of the accuracy of the above expression requires accounting for different effects, including dynamical Stark shift of the resonance line, nonadiabatic corrections to the transition probability, and interaction of alternating magnetic field with a mirror. The detailed study of different systematic effects is under way. Assuming that the spectral

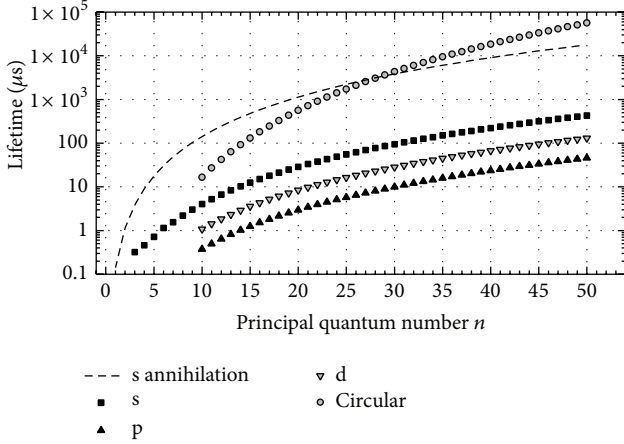


FIGURE 9: Radiative lifetimes of various Ps states as a function of the principal quantum number n . The lifetimes were calculated by summing the Einstein A coefficients of all electric-dipole-allowed decay channels from each Rydberg state. For each A coefficient the appropriate radial integrals were determined using analytic expressions for the radial wave functions in a pure Coulomb potential [53]. The dashed line is the annihilation lifetime of ns states. After [5].

line width is determined by the lifetime $\tau \approx 0.1$ s of gravitational states, we estimate that the gravitational mass M can be deduced with the relative accuracy $\epsilon_M \sim 10^{-3}$ for 100 annihilation events for the transition to the 6th state.

6. Gravitational Free Fall of Cold Positronium

Antihydrogen, muonium, and positronium are the possible candidates for gravity measurements on antimatter, with various pros and cons. Antihydrogen and muonium [4] are extremely difficult to produce, requiring large facilities (i.e., PSI, CERN), whereas positronium is relatively easy to produce in smaller university laboratories. However, Ps has an inconvenient propensity to self-annihilate; the triplet ground state vacuum lifetime of only 142 ns would seem to preclude using this system for a free fall measurement. As has been pointed out by various authors, in particular Mills, Jr., [52], this is not the case, since one need only excite Ps atoms into long-lived Rydberg states to prevent self-annihilation. Indeed, for any Ps state with $n > 1$ the radiative lifetime is always less than the annihilation lifetime. The only excited state for which this is not true is the metastable $2s$ state. That is to say, for excited states, the overlap of the positron and electron wave functions is sufficiently low that annihilation can be considered to be negligible (see Figure 9).

The radiative lifetimes of excited Ps states, shown in Figure 9, are almost twice those of the corresponding states in hydrogen. For practical reasons, the smallest Ps beam deflections one can expect to observe will be 10s of micrometers or more. Therefore, if Ps falls with the usual gravitational acceleration, it would be necessary to produce states with lifetimes of the order of a few ms to observe such deflections. As is evident from Figure 9, achieving such long radiative

TABLE 2: The n -dependence of several properties of Rydberg atoms, with examples shown for the 30 d state of Ps, H, and He. The state separation is calculated for 30 d \rightarrow 31 d. The orbital radius is defined here as the expectation value $\langle r \rangle = (1/2)(3n_{\text{eff}}^2 - l(l+1))$, where n_{eff} includes the relevant quantum defect. The electric dipole moment-to-mass ratios are calculated for the outermost state of the $n = 30$, $m = 2$ Stark manifold. The radiative lifetime n -dependence applies only to low l states: for circular states, the scaling is closer to n^5 (see Figure 9).

	n -Scaling	Ps	H	He
Binding energy (meV)	n^{-2}	-7.56	-15.11	-15.12
State separation (meV)	n^{-3}	0.48	0.96	0.96
Orbital radius (a_0)	n^2	2694	1347	1347
Radiative lifetime (μs)	n^3	28.4	14.2	12.2
Dipole moment/mass (ea_0/amu)	n^2	2.2×10^6	1206	304

lifetimes requires exciting either low l Rydberg levels (i.e., s or d) to extremely high principal quantum numbers, or going to lower n states (perhaps around $n = 30$ or so) and then transferring the atoms to circular states, or if not true circular states, at least states with higher angular momentum. For a discussion of the properties of circular states and methods for producing them, see [54].

Aside from the creation of sufficiently long-lived Rydberg levels, conducting a Ps free fall experiment will require solving many other problems. In order to accomplish an experiment of the type first outlined by Mills and Leventhal [55], it will be necessary to produce a small (10–50 micron) “point” source of slow positronium in a cryogenic environment. The resulting long-lived Rydberg atoms will then have to be formed into a beam, perhaps by electrostatic manipulation (focusing and deceleration) via their electric dipole moments [56], and finally detected with good spatial resolution (as a function of flight time) in order to observe a deflection due to gravity. A schematic view of such an experiment is presented in Figure 10. Possible methods to accomplish some of these tasks are considered elsewhere [5, 55].

The production of Ps Rydberg states with principal quantum numbers around 30 can be accomplished using a two-step process ($1s \rightarrow 2p \rightarrow nd$) and has already been experimentally demonstrated using broadband (~ 100 GHz) lasers to accommodate the large Doppler-broadened width of the transitions [57]. However, this methodology is not well suited to the requirement that these atoms are subsequently transferred to higher angular momentum states, and, in order to achieve the required state selectivity, it may be necessary to use a different excitation mechanism; that is, a Doppler-free two-photon transition from the ground state directly to a well-defined Rydberg Stark state [58].

As is well known, Rydberg atoms exhibit exaggerated properties [54] (see Table 2). In the present case, this is critical, since we seek to produce Ps atoms with very long lifetimes, and also take advantage of the large electric dipole moments of Rydberg atoms to create and control an atomic beam. However, insofar as we are compelled to make use of electrically neutral systems to measure the weak gravitational force acting on antimatter particles without extraneous

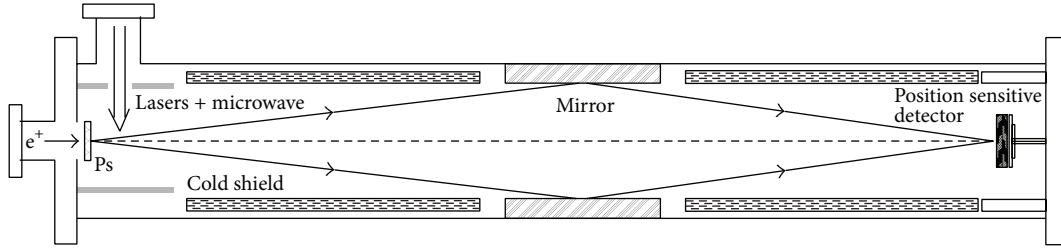


FIGURE 10: A schematic representation of a Mills-Leventhal type of Ps free fall experiment. A real experiment will undoubtedly be significantly different from this illustration, which is intended only to highlight some of the different steps involved. Of distinct practical concern will be the need to keep the apparatus at low temperatures to mitigate effects of black body radiation, as well as minimizing the Ps speed, which will determine the length of the flight path and hence the experiment.

electromagnetic fields dominating their motion, excitation to states with very large dipole moments brings us back to the original problem of extraneous field effects. The situation is considerably less dire when dealing with electric dipoles and, to a much lesser extent, magnetic dipoles, since, in this case, only field gradients give rise to forces; nevertheless, in an experiment designed to probe the weak force of gravity with Rydberg atoms, forces due to stray fields must be taken into account. Magnetic dipoles are less important in this regard. Ordinarily, atoms in weak magnetic fields will experience linear Zeeman shifts, but, in the case of ortho-Ps, there is no permanent magnetic dipole moment because the electron and positron contributions cancel exactly. Thus, only diamagnetic interactions or induced dipole moments have to be taken into account, which we expect to be negligible for realistic experimental conditions.

When an atom is placed in an external electric field of strength F and direction z , the field mixes the atom's angular momentum states. To first-order, the state $|n, l, m\rangle$ is mixed with states of adjacent l but the same n and m [59]. The resulting Stark states repel each other, causing them to spread out as the electric field strength is increased, as shown in Figure 11. Following the example of hydrogen, where the first-order Stark shift is analytically calculable, the Schrödinger equation for an atom in an electric field can be written in cylindrical coordinates, where the relevant quantum numbers are n , m and the parabolic quantum numbers are n_1 and n_2 , which together satisfy the condition $n = n_1 + n_2 + |m| + 1$.

The Stark states in a given $|n, m\rangle$ manifold are described by the index $k = n_1 - n_2$, where k has values in the range from $k_{\min} = -(n - |m| - 1)$ up to $k_{\max} = n - |m| - 1$ (with $\Delta k = 2$). The first-order Stark shift in Ps is given by $E_S = -\mu \times F$, where the electric dipole moment has magnitude $|\mu| = (3/2)n|k|a_{\text{Ps}}$ (where the Ps Bohr radius a_{Ps} is (almost) twice that of hydrogen, i.e., $2a_0$). For a high- n Rydberg state with low angular momentum, for example, the 30d state with $m = 2$, the value of the electric dipole moment can be very large. The Stark state with $k_{\max} = 27$ has an electric dipole moment of $2430ea_0$. This large electric dipole moment arises because within this n -state there are many degenerate angular momentum states with the same value of m that are coupled by the electric field. While this is extremely useful for atomic control [56, 60, 61], it presents a significant problem

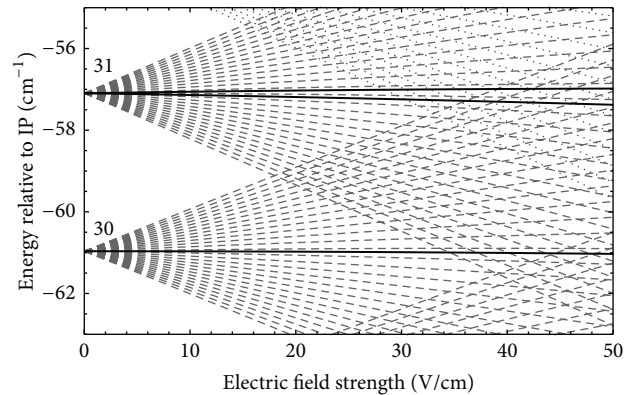


FIGURE 11: Stark states of $n = 30$ and 31 states of Ps, with $m = 2$ (grey dashed) and $m = 29$ (black). In the $n = 30$ level, the $m = 29$ state is a circular state and experiences no first-order Stark shift and only a very weak second-order shift, as explained in the text.

for gravity measurements, since the electric field gradient experienced by a Ps atom in this state which would result in a force equal to that of “normal” gravity ($\sim 2 \times 10^{-29}$ N) is only $\sim 10^{-3}$ V/m². Although this is by no means insignificant, it does compare favorably with the $\sim 5 \times 10^{-11}$ V/m electric field that would apply a g -like force to a bare positron (or electron).

States with the maximum absolute values for the orbital and magnetic quantum numbers for a given n , the so-called circular states, experience no first-order Stark shift. For these states, $m = |n| - 1$, meaning that there is only one Stark state associated with this value of m , which has $k = 0$, and, thus, to first-order, *no electric dipole moment* (see Figure 11). The explanation for this is that, within a given n -manifold, the circular states have unique values of m , and thus are not coupled to any other degenerate angular momentum states. In the classical limit, these states correspond to circular orbits, in which the average z -position of the electron is zero, resulting in no electric dipole moment, unlike the lower angular momentum Rydberg states where, in the classical limit, the electronic orbit is highly anisotropic, with the electron having a large average displacement from the atomic core. Although there is no atomic core or nucleus in the case of Ps, the wave function is nevertheless hydrogenic, and the same arguments apply. The circular states do experience a second-order Stark

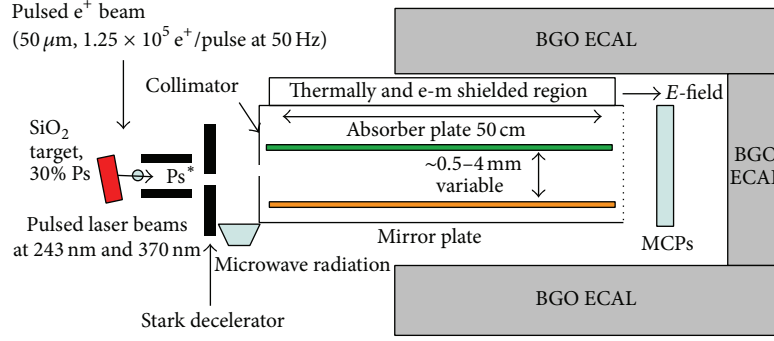


FIGURE 12: Possible scheme for the observation of the gravitational quantum states of positronium.

shift, from coupling of adjacent n -states; however, this shift is extremely weak. It should, therefore, be possible to produce Ps states with high angular momentum and minimize the effects of stray fields while simultaneously extending the lifetimes to useful levels. However, any manipulation techniques that rely on large dipole moments will obviously have to be performed after the optical excitation to the relevant n states, but before transferring the atoms to states with high angular momentum.

Performing a gravity measurement on any system containing antimatter is clearly very challenging, and many of the potential obstacles are currently being investigated. The ability to produce controllable beams of Ps atoms may also open the door to other types of experiments, such as interferometry [62, 63], which could provide an alternative route to an antimatter gravity measurement.

7. Can We Observe Gravitational Quantum States of Positronium?

Positronium is about 1000 times lighter than a neutron or antihydrogen. Therefore, the expected height of the gravitational quantum state is 100 larger corresponding to a macroscopic size of $H_1 = 1.3$ mm while the energy is 10 times smaller, $E_1 = 0.13$ peV (see (1)-(2)). The observation time to resolve a quantum gravitational state can be estimated using the Heisenberg uncertainty principle to be of the order of $\hbar/E_1 \approx 4.5$ ms. This value is much larger than the long-lived triplet positronium lifetime in the ground state which is 142 ns (the Ps singlet state only lives 125 ps and thus, in the following, we will only consider the triplet state and refer to it as Ps). Hence, as for the case of a measurement of the gravitational free fall of Ps described in the previous section, the Ps lifetime must be increased by excitation to a higher level. A possible scheme to observe the Ps gravitational quantum states could employ the flow-through technique used for the first observation of this effect with neutrons (see Figure 12). Greater details of the proposed experimental setup and technique are described in a dedicated contribution to this workshop [64]. Here, we describe the main idea.

Positronium is formed by implanting keV positrons from a remoderated pulsed slow positron beam in a positron-positronium converter. To observe the quantum mechanical

behavior of Ps in the gravitational field, its vertical velocity should be of the same order of the gravitational energy levels and thus $v_y < 0.15$ m/s. Furthermore, to resolve the quantum state, the Ps atom has to interact long enough with the slit and, therefore, it has to be laser excited to a Rydberg state with $n > 30$ and maximum l quantum number (see previous section). To keep a reasonable size of the experimental setup (i.e., a slit size of the order of 0.5 m) and minimize the number of detectors, the velocities in the horizontal plane should be smaller than $v_{x,z} < 100$ m/s. Similar to neutrons a collimator could be used to select the velocity components v_x, v_y of the positronium distribution. However, since no reliable thermal cold source of positronium exists, the velocity component perpendicular to the surface v_z has to be lowered by some other means. Relying on the fact that atoms in Rydberg states have a large dipole moment, Stark deceleration can be used for this purpose. This method has been demonstrated for different atomic species (including hydrogen) [61] and molecules [65]. Atoms in Rydberg states have large dipole moments; thus, electric field gradients can be used to manipulate them. The acceleration/deceleration a imparted to the Rydberg atoms is given by

$$a = 76 \nabla F \frac{1}{m} nk, \quad (22)$$

where ∇F is the gradient of the electric field in V cm^{-2} , m is the mass of the decelerated particles in atomic units, and n and k are the Stark state quantum numbers. H atoms in $n = 25$ and an initial velocity of 700 m/s can be brought at rest in 3 mm [61].

As Ps is 1000 times lighter, decelerations exceeding 10^9 m/s could be realized and therefore the vertical velocity of Ps emitted from thin silica films with initial velocities of the order of 10^5 m/s [66, 67] could be reduced to below 100 m/s. Since one is interested only in decelerating the distribution that is almost perpendicular to the surface of the Ps target, one can expect for those atoms an efficiency close to 100%. This is confirmed by preliminary simulations. The collimator will be placed after the deceleration stage and the microwave region where circularly polarized radiation will spin up the Ps to the maximum l so that kicks to the momentum imparted to the atoms in the vertical direction during these processes will be accounted for.

The fraction of atoms with $v_y < 0.15$, $v_x, v_z < 100$ m/s is estimated to be of the order of 2×10^{-9} . After the collimator, the Ps will fly through the slit made of a mirror and the absorber. If the distance between them is smaller than the first expected gravitational state (i.e. < 1 mm), this will not be transparent and, therefore, no signal will be detected above the expected background in the detectors. If the width of the slit is increased to a value lying between the first and the second gravitational state (i.e. < 2 mm), the Ps wave function can propagate and a signal is expected to be detected via field-ionization and subsequent detection with MCPs. This quantum jump would provide the unambiguous indication of the observation of a quantum gravitational state of positronium.

As a mirror for Ps, it was proposed to exploit a gradient of magnetic field created using wires arranged parallel to each other with a constant current to create a uniform gradient of the magnetic field. Only the Ps triplet atoms with $m = 0$ have a nonzero net magnetic moment. For the $m = \pm 1$, the electron and the positron magnetic moments cancel and therefore those are insensitive to the magnetic field. Therefore, only one third of the initial population will be reflected. To equate the $E_y = 0.1$ peV a field of few mG at the wire surface will be sufficient.

Because of the large spacial size of gravitational quantum states and the very large characteristic length of the mirror needed to form the gravitational states that is much larger than a characteristic interwire distance, we expect that the very weak magnetic gradient will not perturb the gravitational states. The strict theoretical analysis of this clearly mathematically defined problem is ongoing. A matter mirror could also be considered. Due to the large spacial size of the gravitational quantum state, the surface potential is expected to be very sharp and therefore results in efficient quantum reflection (see Section 3). In both cases (magnetic or material mirror), we expect to have effectively (quasiclassically) only a few collisions with the surface. Nevertheless, the transitions rates due to quenching and ionization caused by the electric or magnetic fields have to be calculated. The absorber as for the neutrons is a rough surface on which the impinging Ps will mix its velocity components and therefore be lost.

With such a scheme assuming a monoenergetic slow positron beam flux of 9×10^8 e⁺/s (this being the highest intensity reported so far reached at the FMR II NEMOPUC source in Munich [68]), an event rate of 0.8 events/day with a background 0.05 events/day might be achievable with a realistic extrapolation of current technologies. Possible losses due to spurious effects like stray electric or magnetic fields or black body radiation seem to be negligible but as for the case of a free gravity fall further calculations and preliminary experiments should be done to confirm this assumption and that all the required efficiencies (e.g., Ps excitation in the $n = 33, l = 32$ state) can be attained.

Note that the expected height of the gravitational state is related to the gravitational mass M by (2). This means that, for an uncertainty in the determination of H_1 of δH_1 , one can get an accuracy in the determination of M at the level of $\delta M/M = 3\delta H_1/H_1 \sqrt{N}$ where N is the number of detected signals. Assuming an uncertainty of $\delta H_1 = 0.1$ mm

which is mainly determined by the finite source size, the value of $\delta M/M$ can be determined to be at a level of 3% in three months. This precision is comparable to the one that is aimed for by the antihydrogen experiments at CERN [69–71]. Therefore, observation of Ps gravitational quantum states offers a complementary approach to test the effect of gravity on a pure leptonic system. Most of the techniques required for such an experiment are under development for the ongoing free gravity fall experiment of Ps (see Section 6) and Rydberg Ps deceleration experiments are being considered at ETH Zurich where Professor B. Brown's (Marquette University) buffer gas trap is being commissioned. The advantage of using gravitational quantum states is that unpredicted perturbations of the Ps atoms will not result in a systematic effect for the experiment but will only affect the signal rate. Therefore, as for the case of antihydrogen, this approach seems promising to provide a much higher accuracy than a free fall experiment.

8. Conclusion

In this contribution, we have reported the progress of ongoing experiments to measure gravitational free fall of antimatter. The GBAR experiment will produce antihydrogen atoms in the ultracold regime where quantum reflection from surfaces takes place. Quantum reflection will allow the observation of gravitational quantum states of antimatter which promise to lead to a very sensitive probe of the effect of gravity on antiatoms (2 orders of magnitude improvement compared to the free fall experiments).

The techniques developed in experiments designed to produce a cold beam of Ps for a free fall measurement will also eventually find application in creating ultracold Ps atoms, as required for observing gravitational quantum states. They will also enable a wide variety of other experimental areas, such as precision spectroscopy.

Antimatter atoms in gravitational quantum states also provide a unique opportunity to constrain experimentally extra short-range forces between the mirror and the antiatom with about the same sensitivity as we do for normal matter [72].

Conflict of Interests

The authors declare that there is no conflict of interests regarding the publication of this paper.

Acknowledgments

The authors wish to thank the GRANIT collaboration and the GBAR collaboration (<http://gbar.in2p3.fr/>) for providing excellent possibilities for discussions and exchange. In addition to the involved institutes and laboratories, preparatory work for GBAR has been funded by the “Conseil Général de l'Essonne,” by the “Agence Nationale de la Recherche” in France and by the LABEX P2IO. P. Crivelli acknowledges the support by the Swiss National Science Foundation (Grant PZ00P2.132059) and ETH Zurich (Grant ETH-47-12-1). D. B.

Cassidy and T. E. Wall gratefully acknowledge funding from the EPSRC (EP/K028774/1), the Leverhulme Trust (RPG-2013-055), and the ERC (CIG 630119). This work reviews contributions made at the GRANIT 2014 workshop on prospects for the observation of the free fall and gravitational quantum states of antimatter.

References

- [1] The ALPHA Collaboration and A. E. Charman, "Description and first application of a new technique to measure the gravitational mass of antihydrogen," *Nature Communications*, vol. 4, article 1785, 2013.
- [2] AEGIS Collaboration and M. G. Giammarchi, "AEGIS at CERN: measuring antihydrogen fall," *Few-Body Systems*, vol. 54, no. 5-6, pp. 779–782, 2013.
- [3] P. Pérez and Y. Sacquin, "The GBAR experiment: gravitational behaviour of antihydrogen at rest," *Classical and Quantum Gravity*, vol. 29, no. 18, Article ID 184008, 2012.
- [4] K. Kirch and K. S. Khaw, "Testing antimatter gravity with muonium," *International Journal of Modern Physics: Conference Series*, vol. 30, Article ID 1460258, 8 pages, 2014.
- [5] D. B. Cassidy and S. D. Hogan, "Atom control and gravity measurements using Rydberg positronium," *International Journal of Modern Physics: Conference Series*, vol. 30, Article ID 1460259, 9 pages, 2014.
- [6] M. M. Nieto and T. Goldman, "The arguments against "antigravity" and the gravitational acceleration of antimatter," *Physics Report*, vol. 205, no. 5, pp. 221–281, 1991.
- [7] J. Scherk, "Antigravity: a crazy idea?" *Physics Letters: B*, vol. 88, no. 3-4, pp. 265–267, 1979.
- [8] G. Chardin and J.-M. Rax, "CP violation. A matter of (anti) gravity?" *Physics Letters B*, vol. 282, no. 1-2, pp. 256–262, 1992.
- [9] G. Chardin, "CP violation and antigravity (revisited)," *Nuclear Physics, Section A*, vol. 558, pp. 477–495, 1993.
- [10] G. Chardin, "Motivations for antigravity in general relativity," *Hyperfine Interactions*, vol. 109, no. 1–4, pp. 83–94, 1997.
- [11] V. A. Kostelecky and J. D. Tasson, "Matter-gravity couplings and Lorentz violation," *Physical Review D*, vol. 83, no. 1, Article ID 016013, 2011.
- [12] M. L. Good, " K_2^0 and the equivalence principle," *Physical Review*, vol. 121, pp. 311–313, 1961.
- [13] S. Pakvasa, W. A. Simmons, and T. J. Weiler, "Test of equivalence principle for neutrinos and antineutrinos," *Physical Review D*, vol. 39, no. 6, pp. 1761–1763, 1989.
- [14] A. Apostolakis, E. Aslanides, G. Backenstoss et al., "Tests of the equivalence principle with neutral kaons," *Physics Letters B: Nuclear, Elementary Particle and High-Energy Physics*, vol. 452, no. 3-4, pp. 425–433, 1999.
- [15] G. Gabrielse, A. Khabbaz, D. S. Hall, C. Heimann, H. Kalinowsky, and W. Jhe, "Precision mass spectroscopy of the antiproton and proton using simultaneously trapped particles," *Physical Review Letters*, vol. 82, no. 16, pp. 3198–3201, 1999.
- [16] F. C. Witteborn and W. M. Fairbank, "Experimental comparison of the gravitational force on freely falling electrons and metallic electrons," *Physical Review Letters*, vol. 19, no. 18, pp. 1049–1052, 1967.
- [17] M. H. Holzscheiter, "Constraints on gravitational properties of antimatter from cyclotron-frequency measurements," *International Journal of Modern Physics: Conference Series*, vol. 30, Article ID 1460260, 9 pages, 2014.
- [18] Antimatter and Gravity, *International Journal of Modern Physics: Conference Series*, 2014.
- [19] M. Abramowitz and I. A. Stegun, *Handbook of Mathematical Functions with Formulas, Graphs, and Mathematical Tables*, Wiley, New York, ny, usa, 1972.
- [20] L. D. Landau, E. M. Lifshitz, J. B. Sykes, and J. S. Bell, *Quantum Mechanics: Non-Relativistic Theory*, Royaume-Uni, Oxford, UK, 1965.
- [21] V. V. Nesvizhevsky, H. G. Börner, A. K. Petukhov et al., "Quantum states of neutrons in the Earth's gravitational field," *Nature*, vol. 415, no. 6869, pp. 297–299, 2002.
- [22] G. Chardin, P. Grandemange, D. Lunney et al., "Proposal to measure the gravitational behaviour of antihydrogen at rest," Tech. Rep. CERN-SPSC-2011-029. SPSC-P-342, CERN, Geneva, Switzerland, 2011.
- [23] J. Walz and T. W. Hänsch, "A proposal to measure antimatter gravity using ultracold antihydrogen atoms," *General Relativity and Gravitation*, vol. 36, no. 3, pp. 561–570, 2004.
- [24] J. P. Merrison, H. Bluhme, J. Chevallier et al., "Hydrogen formation by proton impact on positronium," *Physical Review Letters*, vol. 78, no. 14, pp. 2728–2731, 1997.
- [25] H. R. J. Walters and C. Starrett, "Positron and positronium scattering," *Physica Status Solidi (C)*, vol. 4, no. 10, pp. 3429–3436, 2007.
- [26] P. Comini and P.-A. Hervieux, " \bar{H}^+ ion production from collisions between antiprotons and excited positronium: cross sections calculations in the framework of the GBAR experiment," *New Journal of Physics*, vol. 15, no. 9, Article ID 095022, 2013.
- [27] L. Liszskay, C. Corbel, P. Pérez et al., "Positronium reemission yield from mesostructured silica films," *Applied Physics Letters*, vol. 92, no. 6, Article ID 063114, 2008.
- [28] D. B. Cassidy, T. H. Hisakado, H. W. K. Tom, and A. P. Mills, "Photoemission of positronium from Si," *Physical Review Letters*, vol. 107, no. 3, Article ID 033401, 2011.
- [29] N. Oshima, T. M. Kojima, M. Niigaki, A. Mohri, K. Komaki, and Y. Yamazaki, "New scheme for positron accumulation in ultra-high vacuum," *Physical Review Letters*, vol. 93, no. 19, Article ID 195001, 2004.
- [30] P. Grandemange, *Piegeage et accumulation de positons issus d'un faisceau pulse produit par un accélérateur pour l'étude de l'interaction gravitationnelle de l'antimatière [Ph.D. thesis]*, Université Paris Sud, Paris, France, 2013.
- [31] L. Hilico, J.-P. Karr, A. Douillet, P. Indelicato, S. Wolf, and F. S. Kaler, "Preparing single ultra-cold antihydrogen atoms for free-fall in GBAR," *International Journal of Modern Physics: Conference Series*, vol. 30, Article ID 1460269, 11 pages, 2014.
- [32] H. B. G. Casimir and D. Polder, "Influence of retardation on the London-van der Waals forces," *Nature*, vol. 158, no. 4022, pp. 787–788, 1946.
- [33] H. B. G. Casimir, "On the attraction between two perfectly conducting plates," *Proceedings of the Koninklijke Nederlandse Akademie van Wetenschappen*, vol. 51, p. 793, 1948.
- [34] H. Friedrich, G. Jacoby, and C. G. Meister, "Quantum reflection by Casimir-van der Waals potentials tails," *Physical Review A*, vol. 65, no. 3 B, Article ID 032902, 2002.
- [35] A. Lambrecht, P. A. Maia Neto, and S. Reynaud, "The Casimir effect within scattering theory," *New Journal of Physics*, vol. 8, article no. 243, 2006.
- [36] R. Messina, D. A. R. Dalvit, P. A. M. Neto, A. Lambrecht, and S. Reynaud, "Dispersive interactions between atoms and

- nonplanar surfaces,” *Physical Review A*, vol. 80, no. 2, Article ID 022119, 2009.
- [37] G. Dufour, A. Gerardin, R. Guérout et al., “Quantum reflection of antihydrogen from the Casimir potential above matter slabs,” *Physical Review A*, vol. 87, no. 1, Article ID 012901, 2013.
- [38] M. V. Berry and K. E. Mount, “Semiclassical approximations in wave mechanics,” *Reports on Progress in Physics*, vol. 35, no. 1, article no. 306, pp. 315–397, 1972.
- [39] A. Y. Voronin, P. Froelich, and B. Zygelman, “Interaction of ultracold antihydrogen with a conducting wall,” *Physical Review A*, vol. 72, no. 6, Article ID 062903, 2005.
- [40] G. Dufour, R. Guerout, A. Lambrecht, V. V. Nesvizhevsky, S. Reynaud, and A. Y. Voronin, “Quantum reflection of antihydrogen from nanoporous media,” *Physical Review A*, vol. 87, no. 2, Article ID 022506, 2013.
- [41] G. Dufour, P. Debu, A. Lambrecht, V. V. Nesvizhevsky, S. Reynaud, and A. Y. Voronin, “Shaping the distribution of vertical velocities of antihydrogen in GBAR,” *European Physical Journal C*, vol. 74, no. 1, article 2731, 2014.
- [42] V. V. Nesvizhevsky, H. Börner, A. M. Gagarski et al., “Search for quantum states of the neutron in a gravitational field: gravitational levels,” *Nuclear Instruments and Methods in Physics Research, Section A: Accelerators, Spectrometers, Detectors and Associated Equipment*, vol. 440, no. 3, pp. 754–759, 2000.
- [43] V. V. Nesvizhevsky, H. G. Börner, A. M. Gagarski et al., “Measurement of quantum states of neutrons in the Earth’s gravitational field,” *Physical Review D*, vol. 68, no. 10, Article ID 102002, 2003.
- [44] V. V. Nesvizhevsky, A. K. Petukhov, H. G. Börner et al., “Study of the neutron quantum states in the gravity field,” *European Physical Journal C*, vol. 40, no. 4, pp. 479–491, 2005.
- [45] A. Y. Voronin, H. Abele, S. Baeßler et al., “Quantum motion of a neutron in a waveguide in the gravitational field,” *Physical Review D*, vol. 73, no. 4, Article ID 044029, 2006.
- [46] A. Y. Voronin, P. Froelich, and V. V. Nesvizhevsky, “Gravitational quantum states of Antihydrogen,” *Physical Review A: Atomic, Molecular, and Optical Physics*, vol. 83, no. 3, Article ID 032903, 2011.
- [47] W. E. Lamb, “Fine structure of the hydrogen atom. III,” *Physical Review*, vol. 85, no. 2, pp. 259–276, 1952.
- [48] L. P. Gor’kov and I. E. Dzyaloshinskii, “Contribution to the theory of the Mott exciton in a strong magnetic field,” *Soviet Physics—JETP*, vol. 26, pp. 449–453, 1968.
- [49] Y. E. Lozovik and S. Y. Volkov, “Hydrogen atom moving across a magnetic field,” *Physical Review A: Atomic, Molecular, and Optical Physics*, vol. 70, no. 2, Article ID 023410, 2004.
- [50] A. Y. Voronin and P. Froelich, “Quantum reflection of ultracold antihydrogen from a solid surface,” *Journal of Physics B: Atomic, Molecular and Optical Physics*, vol. 38, no. 18, pp. L301–L308, 2005.
- [51] M. Kreuz, V. V. Nesvizhevsky, P. Schmidt-Wellenburg et al., “A method to measure the resonance transitions between the gravitationally bound quantum states of neutrons in the GRANIT spectrometer,” *Nuclear Instruments and Methods in Physics Research A: Accelerators, Spectrometers, Detectors and Associated Equipment*, vol. 611, no. 2-3, pp. 326–330, 2009.
- [52] A. P. Mills Jr., “Positron moderation and remoderation techniques for producing cold positron and positronium sources,” *Hyperfine Interactions*, vol. 44, no. 1–4, pp. 105–123, 1989.
- [53] H. A. Bethe and E. E. Salpeter, *Quantum. Mechanics of One- And Two-Electron Atoms*, Dover, New York, NY, USA, 1957.
- [54] T. F. Gallagher, *Rydberg Atoms*, Cambridge University Press, Cambridge, UK, 1994.
- [55] A. P. Mills Jr. and M. Leventhal, “Can we measure the gravitational free fall of cold Rydberg state positronium?” *Nuclear Instruments and Methods in Physics Research, Section B: Beam Interactions with Materials and Atoms*, vol. 192, no. 1-2, pp. 102–106, 2002.
- [56] C. Seiler, S. D. Hogan, H. Schmutz, J. A. Agner, and F. Merkt, “Collisional and radiative processes in adiabatic deceleration, deflection, and off-axis trapping of a Rydberg atom beam,” *Physical Review Letters*, vol. 106, no. 7, Article ID 073003, 2011.
- [57] A. C. L. Jones, T. H. Hisakado, H. J. Goldman, H. W. K. Tom, A. P. Mills Jr., and D. B. Cassidy, “Doppler-corrected Balmer spectroscopy of Rydberg positronium,” *Physical Review A*, vol. 90, no. 1, Article ID 012503, 2014.
- [58] T. E. Wall, D. B. Cassidy, and S. D. Hogan, “This has not yet been demonstrated for positronium; the feasibility of doing so is considered, to be published.
- [59] T. F. Gallagher, “Rydberg atoms,” *Reports on Progress in Physics*, vol. 51, no. 2, pp. 143–188, 1988.
- [60] E. Vliegen and F. Merkt, “Normal-incidence electrostatic rydberg atom mirror,” *Physical Review Letters*, vol. 97, no. 3, Article ID 033002, 2006.
- [61] S. D. Hogan and F. Merkt, “Demonstration of three-dimensional electrostatic trapping of state-selected rydberg atoms,” *Physical Review Letters*, vol. 100, no. 4, Article ID 043001, 2008.
- [62] T. J. Phillips, “Antimatter gravity studies with interferometry,” *Hyperfine Interactions*, vol. 109, no. 1–4, pp. 357–365, 1997.
- [63] M. K. Oberthaler, “Anti-matter wave interferometry with positronium,” *Nuclear Instruments and Methods in Physics Research, Section B: Beam Interactions with Materials and Atoms*, vol. 192, no. 1-2, pp. 129–134, 2002.
- [64] P. Crivelli, V. V. Nesvizhevsky, and A. Y. Voronin, “Can we observe the gravitational quantum states of Positronium?,” *Advances in High Energy Physics*. In press.
- [65] S. D. Hogan, C. Seiler, and F. Merkt, “Rydberg-state-enabled deceleration and trapping of cold molecules,” *Physical Review Letters*, vol. 103, no. 12, Article ID 123001, 2009.
- [66] D. B. Cassidy, P. Crivelli, T. H. Hisakado et al., “Positronium cooling in porous silica measured via Doppler spectroscopy,” *Physical Review A: Atomic, Molecular, and Optical Physics*, vol. 81, no. 1, Article ID 012715, 2010.
- [67] P. Crivelli, U. Gendotti, A. Rubbia, L. Liskay, P. Pérez, and C. Corbel, “Measurement of the orthopositronium confinement energy in mesoporous thin films,” *Physical Review A—Atomic, Molecular, and Optical Physics*, vol. 81, no. 5, Article ID 052703, 2010.
- [68] C. Hugenschmidt, B. Löwe, J. Mayer et al., “Unprecedented intensity of a low-energy positron beam,” *Nuclear Instruments and Methods in Physics Research A: Accelerators, Spectrometers, Detectors and Associated Equipment*, vol. 593, no. 3, pp. 616–618, 2008.
- [69] A. Kellerbauer, M. Amoretti, A. S. Belov et al., “Proposed antimatter gravity measurement with an antihydrogen beam,” *Nuclear Instruments and Methods in Physics Research B: Beam Interactions with Materials and Atoms*, vol. 266, no. 3, pp. 351–356, 2008.
- [70] D. P. van der Werf, “The GBAR experiment,” *International Journal of Modern Physics: Conference Series*, vol. 30, Article ID 1460263, 2014.

- [71] A. I. Zhmoginov, A. E. Charman, R. Shaloo, J. Fajans, and J. S. Wurtele, "Nonlinear dynamics of anti-hydrogen in magnetostatic traps: implications for gravitational measurements," *Classical and Quantum Gravity*, vol. 30, no. 20, Article ID 205014, 2013.
- [72] I. Antoniadis, S. Baessler, M. Büchner et al., "Short-range fundamental forces," *Comptes Rendus Physique*, vol. 12, no. 8, pp. 755–778, 2011.

Research Article

Can We Observe the Gravitational Quantum States of Positronium?

P. Crivelli,¹ V. V. Nesvizhevsky,² and A. Yu. Voronin³

¹ETH Zurich, Institute for Particle Physics, Otto-Stern-Weg 5, 8093 Zurich, Switzerland

²Institut Laue-Langevin, 6 rue Jules Horowitz, 38046 Grenoble, France

³Lebedev Physical Institute, 53 Leninsky Prospect, Moscow 119991, Russia

Correspondence should be addressed to P. Crivelli; paolo.crivelli@cern.ch

Received 6 June 2014; Revised 17 August 2014; Accepted 29 August 2014

Academic Editor: Stefan Baessler

Copyright © 2015 P. Crivelli et al. This is an open access article distributed under the Creative Commons Attribution License, which permits unrestricted use, distribution, and reproduction in any medium, provided the original work is properly cited. The publication of this article was funded by SCOAP³.

We consider the feasibility of observing the gravitational quantum states of positronium. The proposed scheme employs the flow-throw technique used for the first observation of this effect with neutrons. Collimation and Stark deceleration of Rydberg positronium atoms allow selecting the required velocity class. If this experiment could be realized with positronium, it would lead to a determination of g for this matter-antimatter system at the few % level. As discussed in this contribution, most of the required techniques are currently available but important milestones have to be demonstrated experimentally before such an experiment could become reality. Those are the efficient focusing of a bunched positron beam, Stark deceleration of Rydberg positronium, and its subsequent excitation into states with large angular momentum. We provide an estimate of the efficiencies we expect for these steps and assuming those could be confirmed we calculate the signal rate.

1. Introduction

Quantum gravitational states were observed for the first time with neutrons by measuring their transmission through a slit made of a mirror and an absorber [1]. If the distance between the mirror and the absorber (which is a rough surface used as a scatterer to mix the velocity components) is much higher than the turning point for the corresponding gravitational quantum state, the neutrons pass through the slit without significant losses. As the slit size decreases the absorber starts approaching the size of the neutron wave function and the probability of neutron loss increases. If the slit size is smaller than the characteristic size of the neutron wave function in the lowest quantum state, the slit is not transparent for neutrons as this was demonstrated experimentally. The height and energies of the gravitational quantum states can be determined analytically and the solution of the Schrödinger equation contains airy functions. A more transparent and simple equation can be derived using a semiclassical approach [2]. This solution reproduces the energy of the gravitational states within 1% and is given by

$$E_n \simeq \sqrt[3]{\frac{9m}{8} \cdot \left(\pi\hbar g \left(n - \frac{1}{4}\right)\right)}, \quad (1)$$

where m is the particle mass, g the gravitational acceleration, n the principal quantum number, and \hbar the reduced Planck constant. The characteristic scale for the gravitational quantum states is equal to

$$z_0 = \sqrt[3]{\frac{\hbar^2}{2m^2g}}. \quad (2)$$

The corresponding classically allowed heights are given by

$$z_n = \frac{E_n}{mg} = \lambda_n z_0, \quad (3)$$

where $\lambda_n = \{2.34, 4.09, 5.52, 6.79, 7.94, 9.02, 10.04, \dots\}$ are the zeros of the airy function. For neutrons the height of the lowest gravitational level is 13.7 μm . For positronium, the electron-positron bound state, that is, 1000 times lighter than

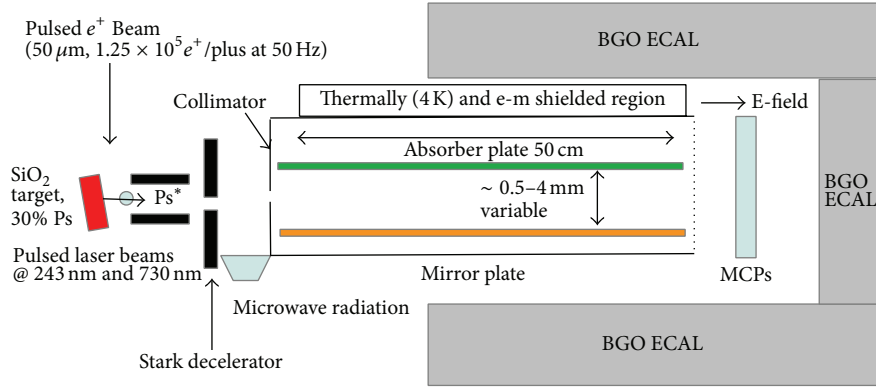


FIGURE 1: Scheme of the proposed experimental setup.

a neutron, one gets a 100 larger size corresponding to $z_1 = 1.3$ mm while the energy is 10 times smaller, $E_1 = 0.13$ peV. The observation time to resolve a quantum gravitational state can be estimated using the Heisenberg uncertainty principle to be of the order of $\hbar/E_1 \approx 4.5$ ms. This value is much larger than the long lived triplet positronium lifetime in the ground state which is 142 ns (the Ps singlet state lives only 125 ps and thus in the following we will only consider the triplet state and refer to it as Ps). Luckily, the Ps lifetime can be increased by exciting it to a higher level. In a Rydberg state the Ps lifetime against annihilation is increased by a factor of n^3 , where n is the principal quantum number, because of the decrease of the overlap of the positron and the electron wave functions. As for the case of a measurement of the gravitational free fall of Ps proposed by Mills and Leventhal [3], the usable lifetime to observe a quantum gravitation state of a Rydberg Ps atom (hereafter Ps*) is the one before it emits the first photon. In fact, after that the recoil will modify its trajectory and vertical energy; thus the Ps atom will be lost inside the slit. For this reason, the excited Ps has to be spun up to high l values with circularly polarized microwave radiation.

2. Experimental Technique

A scheme of the proposed experimental setup is shown in Figure 1. Positronium is formed by implanting keV positrons from a remoderated pulsed slow positron beam in a positron-positronium converter (see Section 3.3). To observe the quantum mechanical behavior of Ps in the gravitational field its vertical velocity should be of the same order as the gravitational energy levels and thus $v_y < 0.15$ m/s. Furthermore to resolve the quantum state the Ps atom has to interact long enough with the slit and therefore it has to be laser excited to a Rydberg state with $n > 30$ and maximum l quantum number. To keep a reasonable size of the experimental setup (i.e., a slit size of the order of 0.5 m) and minimize the number of detectors the velocities in the horizontal plane should be smaller than $v_{x,z} < 100$ m/s. Similar to neutrons a collimator will be used to select the velocity components v_x, v_y of the positronium distribution. However since no reliable thermal cold source of positronium exists, the velocity component perpendicular to the surface v_z has to be lowered by some other means. Relying to the fact that atoms in Rydberg states have a large dipole moment, Stark deceleration can be used

for this purpose. After deceleration the Ps* are driven by circularly polarized microwaves to a state with high l . If the slit width is smaller than the first expected gravitational state (i.e., < 1 mm), this will not be transparent and therefore no signal will be detected above the expected background in the detectors. If the width is increased to a value lying between the first and the second gravitational state (i.e., < 2 mm) the Ps wavefunction can propagate and a signal is expected to be detected. This quantum jump provides the unambiguous indication of the observation of a quantum gravitational state of positronium.

3. Experimental Setup

3.1. Positron Beam. Few facilities around the world are nowadays capable of producing fluxes of positrons exceeding 1×10^8 e⁺/s [4–11]. The highest intensity reported so far has been reached at the FMR II NEMOPUC source in Munich where a monoenergetic slow positron beam of 9×10^8 e⁺/s has been achieved [12]. We will base our estimation of the signal rate assuming that such a beam could be used. In principle, even higher fluxes are conceivable (see, e.g., [13, 14]) and hopefully those will be available in the near future.

The beam will be coupled to a buffer gas trap. This is necessary in order to produce positron pulses at a rate of tens of Hz to synchronize positronium formation with pulsed lasers in order to drive the transition of Ps in a Rydberg state. The typical trapping efficiency is 20% and the positron lifetime in the trap is 2 s. Therefore above a few Hz repetition rate, the losses are minimized. The positrons are dumped in bunches of 20 ns using the standard electrodes of the trap and by adding a buncher one can achieve < 1 ns pulses [15, 16]. The typical positron beam size of such a system is 1 mm (FWHM). This has to be reduced via positron remoderation in order to achieve a good geometrical overlap of the Ps source with the opening of the slit (mirror-absorber).

Note that a new concept for a positron buffer gas trap with the prospect of obtaining up to 92% trapping efficiencies has been recently proposed [17].

3.2. Remoderation. Remoderation of positron beam allows brightness enhancement. Microbeams of 1–2 μm were developed by the use of two successive stages of focusing, acceleration, and remoderation [18]. The loss of beam intensity is

about a factor 10 per stage in reflection geometry. To achieve a positron beam of $50 \mu\text{m}$, only one moderator stage will be required. One can use a Ni(100) foil in transmission geometry which even being a factor 2 less efficient allows the beam to be extracted from the magnetic field region with a transmission of 71% [19, 20]. Such a remoderator leads to about 5% of the incoming positrons in a beam of $50 \mu\text{m}$ [19, 20]. This was achieved using a continuous positron beam but it has not been yet demonstrated for a bunched beam. Such a scheme is currently under investigation at the University College of London (UCL) for their ongoing free fall measurement of Ps. Their preliminary simulations show that one should be able to obtain 1 ns positron bunches of about $25 \mu\text{m}$ spot size [21]. Assuming that a remoderation efficiency of 5% could be attained, the positron flux at the target will be of the order of $6.3 \times 10^6 e^+/\text{s}$ ($1.25 \times 10^5 e^+$ per bunch at a repetition rate of 50 Hz).

3.3. Positronium Source. Positrons implanted in silica thin films with 3 keV will form Ps emitted into vacuum with an efficiency of about 30% and an energy of 75 meV [22, 23]. The vacuum yield is basically constant in the temperature range from 50 K to 400 K [22]. The emission energy of Ps is determined by the diameter of the pores (3 nm). In fact for Ps energies of a few hundred meV, the Ps de Broglie wavelength is comparable with the energy levels of positronium confined inside a pore of this size and therefore it has to be treated quantum mechanically. A simple particle in a box model is a good approximation to describe Ps in such porous materials [22, 24, 25]. Ps formed inside the film with an initial energy of 1 eV (corresponding to the negative workfunction of Ps in silica) starts diffusing through the interconnected pore network tunneling from one pore to the other and loses energy via collision until the ground state energy is attained. A fraction of those atoms (30% of the incoming positrons) will make it to the surface before decaying and are emitted into vacuum. At temperatures below 100 K in films of 3–4 nm diameter only the ground state of Ps in the pore is populated. Therefore, Ps emitted into vacuum is basically monoenergetic. Since the pore orientation at the surface of these materials is random, the emission distribution follows a $\cos\theta$ distribution [22, 23].

At 3 keV, the positrons have a mean implantation depth of 150 nm. The time required for the Ps atoms to exit the film and be emitted into vacuum has been measured to be about 1 ns [26]. Since the areal density per pulse is of the order of $10^9 \text{Ps}/\text{cm}^2$, the spin exchange quenching and formation of molecular positronium inside the films should be considered. The total cross section in those targets for these processes has been determined to be $3.4 \times 10^{-14} \text{cm}^2$ [27]. In those measurements, a source based positron beam was used and at areal densities of $4 \times 10^{10} \text{Ps}/\text{cm}^2$ a saturation of the quenching process was observed. A fraction of 0.3 of the initial positronium population survives since the positrons from a radioactive source are spin polarized (due to parity violation). For positrons produced in a reactor, this is not the case and therefore the losses will be higher. However, using the measured cross sections and taking into account

that once emitted into vacuum after 1 ns the Ps cloud expands and therefore the density decreases rapidly, we estimated that this effect can be neglected.

To reduce the perpendicular velocity $v_z \approx 10^5 \text{m/s}$, we plan to use Stark deceleration. This method has been applied to different atomic species (including hydrogen) [28] and molecules [29]. Atoms in Rydberg states have large dipole moments; thus electric field gradients can be used to manipulate them. The acceleration/deceleration a imparted to the Rydberg atoms is given by

$$a = 76\nabla F \frac{1}{m}nk, \quad (4)$$

where ∇F is the gradient of the electric field in Vcm^{-2} , m the mass of the decelerated particles in atomic units, and n and k the Stark state quantum numbers. H atoms in $n = 25$ and an initial velocity of 700 m/s can be brought at rest in 3 mm [28]. For Ps being 1000 times lighter, decelerations exceeding 10^9m/s could be realized. Since one is interested only in decelerating the distribution that is almost perpendicular to the surface of the Ps target, one can expect an efficiency close to 100%. This is confirmed by preliminary simulations (private communication with Dr. C. Seiler). The collimator will be placed after the deceleration stage and the microwave region where circularly polarized radiation will spin up the Ps to the maximum l so that kicks to the momentum imparted to the atoms in the vertical direction during these processes will be accounted for.

The fraction of atoms with $v_y < 0.15$, $v_x, v_z < 100 \text{m/s}$ is estimated using a Monte Carlo simulation taking into account the angular of the Ps emitted into vacuum from porous silica to be of the order of 2×10^{-9} .

Other promising candidates for Ps formation that should be considered for this experiment are aluminum oxidized nanochannels of 5–8 nm [30], Si and Ge surfaces [31], and hydrophobic silica aerogels [32].

To produce a source of cold Ps, another option would be to use the tails of the distribution of Ps thermally desorbed and emitted into vacuum. For Al(111) kept at 600 K, the conversion efficiency e^+ -Ps was measured to be as high as 30% [33]. However, the surface quality is very important, and degradation is observed in a short time scale especially when a laser is positioned near the surface [31, 34]. Therefore, until stable desorption at room temperature (or lower) could be demonstrated, this does not seem to be an attractive path.

3.4. Laser for Rydberg Excitation. Positronium excitation in Rydberg states was first demonstrated by Ziocck et al. [35]. Recently, an excitation of Rydberg Ps with a two-step process $1S \rightarrow 2P$ and $2P \rightarrow 25$ with an efficiency of 25% was reported [36, 37]. Two broadband (150 GHz) dye lasers were used in order to maximize the overlap with the large Doppler profile of the Ps atoms. This led to an occupation of the Stark levels that could not be resolved. In the experiment proposed here, one is interested to excite only a small fraction of the atoms with the correct velocity characteristic. The lasers axis will be set parallel to the v_x component. For $v_x = 100 \text{m/s}$, the Doppler profile will be of the order of 1 GHz and thus

narrow dye lasers at 243 nm and 730 nm can be used. One has to consider that in both cases the photon absorbed by the atom will result in recoil and therefore the laser frequency has to be tuned in order to compensate for this effect. This can be optimized by detecting the Rydberg atoms via field ionization after the collimator slit maximizing their flux. In such a scheme, the excitation probability will be at least as large as 25% (as for the case of broadband excitation) with the advantage of populating only the desired Stark state ($n = 33$ and $k = 19$). As a base for our estimation of the signal rate, we take conservatively this value. An alternative might be to use Doppler free two-photon excitation from the ground state directly to $n = 33$. This could lead to higher efficiencies exceeding 50% [21, 38] but it has not been yet realized for Ps. After deceleration, the Ps^* will be driven to its highest circular state $l = 32$ using polarized microwave radiation.

3.5. Mirror and Absorber. As a mirror for Ps, we propose to exploit a gradient of magnetic field created using wires arranged parallel to each other with a constant current to create a uniform gradient of the magnetic field. Only the Ps triplet atoms with $m = 0$ have a nonzero net magnetic moment. For the $m = \pm 1$, the electron and the positron magnetic moments cancel and therefore those are insensitive to the magnetic field. Therefore, only one-third of the initial population will be reflected. To equate the $E_y = 0.1$ peV, a field of a few mG at the wire surface will be sufficient.

Because of the large spatial size of gravitational quantum states and the very large characteristic length of the mirror needed to form the gravitational states that is much larger than a characteristic interwire distance, we expect that the very weak magnetic gradient will not perturb the gravitational states. The strict theoretical analysis of this clearly mathematically defined problem is ongoing.

It is important to note that a well-defined (n, l) state should be used in order to avoid the fact that the spread in the magnetic moment would wash out the transmission versus the slit height dependence.

A matter mirror should also be considered. Due to the large spatial size of the gravitational quantum state, the surface potential is expected to be very sharp and therefore result in efficient quantum reflection [39]. In both cases (magnetic or material mirror), we expect to have effectively (quasi-classically) only a few collisions with surface. Nevertheless, the transitions rates due to quenching and ionization caused by the electric or magnetic fields have to be calculated.

The absorber as for the neutrons is a rough surface on which the impinging Ps will mix its velocity components and therefore be lost (i.e., it will not be reflected by the mirror).

3.6. Detectors. The detectors are made of an array of ten standard rectangular MCPs (e.g., Hamamatsu F4772-01, $55 \times 8 \text{ mm}^2$) placed 50 mm from the end of the mirror-absorber region. A uniform electric field will ionize the Ps^* and guide the positrons to the MCPs where they can be detected with high efficiency (80%). In order to reduce accidental background, the MCPs will be surrounded by an almost 4π calorimeter made of 100 BGOs (hexagonal shape of 55 mm

outer diameter and 200 mm length) placed outside of the vacuum chamber to detect the back to back 511 keV annihilation gamma rays from the e^+ annihilation. This detector was used in the search for $\text{Ps} \rightarrow$ invisible decays where the efficiency for detection of two 511 keV photons was larger than 99.99999% [40]. An energy cut of $400 \text{ keV} < E < 600 \text{ keV}$ will be applied and the coincidence between the two back to back crystals within 10 ns will be required. Based on simulation with Geant 4 (validated with measurements that used a BGO calorimeter), this will result in an efficiency for the detection of the photons from the positrons annihilation of more than 80% (arising from the geometrical limitations that do not allow for a full coverage). The measured background for such a signature for the BGO detectors is of the order of 0.25 events/s. By adding the requirement that a positron is detected in the MCP (dark count of 100 counts/s) within 10 ns will result in 0.04 background event/day accidental rate (this includes environmental, internal BGO radioactivity, and cosmic rays). The combination of the coincidence between the positron detection in the MCP and the detection of its annihilation photons will result in an efficiency of 64%. The positronium time-of-flight will be used to suppress accidentals from the prompt positron and positronium annihilation.

3.7. Experimental Environment Considerations. Due to their sensitivity to black body radiation, the absorber and the mirror have to be kept at 4 K. Furthermore, special care has to be taken in order to avoid stray electric and magnetic fields. A mumetal shielding should be foreseen. The target and the electrodes for the Rydberg deceleration can be kept at higher temperature of 150 K since the collimator will act as a thermal shielding and in addition it will prevent a leak of the electric fields from the deceleration stage. The MCPs are also kept at this higher temperature.

4. Expected Rate

The expected signal rate can be estimated using

$$\begin{aligned} R_{\text{signal}} &= R_{e^+} \cdot \epsilon_{\text{Ps}} \cdot \epsilon_{n33} \cdot \epsilon_{l32} \cdot \epsilon_{\text{collimator}} \cdot \epsilon_{\text{tau}} \cdot \epsilon_{\text{dec}} \cdot \epsilon_{\text{det}} \\ &= 8.7 \times 10^{-6} \text{ events/s,} \end{aligned} \quad (5)$$

where

- (i) $R_{e^+} = 6.25 \times 10^6 e^+/s$ is the positron flux on target. This was estimated assuming that one could use the full intensity of the currently strongest existing positron source, a buffer gas trap efficiency of 20%, extraction losses to a field free magnetic field region of 70%, and a remoderation efficiency of 5%. This last one was realized for a continuous positron beam but not yet for a bunched beam as required for this experiment (see Section 3.2);
- (ii) $\epsilon_{\text{Ps}} = 0.1$ is the fraction of Ps emitted into vacuum from the proposed porous silica film. This includes the losses due to spin quenching and Ps_2 molecule formation and the fact that only the $m = 0$ triplet state will be reflected from the proposed mirror;

- (iii) $\epsilon_{n33} = 0.25$ is the excitation probability in the $n = 33$, $k = 19$ state;
- (iv) $\epsilon_{l32} = 0.1$ is the efficiency to drive the Ps in the $n = 33$, $l = 32$ state. This has been realized for other atomic species (see, e.g., [41] and reference therein) but never for Ps;
- (v) $\epsilon_{\text{collimator}} = 2 \times 10^{-9}$ is the fraction of Ps atoms remaining after the collimator ($v_x < 100$ m/s and $v_y < 0.15$ m/s). This was estimated with a Monte Carlo simulation (see Section 3.3);
- (vi) $\epsilon_{\text{tau}} = 0.5$ is the fraction of atoms in the $n = 33$, $l = 32$ state, which has a lifetime of about 8 ms, surviving the 5 ms time-of-flight;
- (vii) $\epsilon_{\text{dec}} = 0.8$ is the deceleration efficiency for the $v_z < 100$ m/s estimated with preliminary simulations validated for different atomic species;
- (viii) $\epsilon_{\text{det}} = 0.64$ is the efficiency of signal detection.

Assuming that all the efficiencies quoted above could be confirmed experimentally, a rate of 0.7 events/day with a background 0.05 events/day is anticipated. Possible losses due to spurious effects like stray electric or magnetic fields or black body radiation seem to be negligible but further calculations and preliminary experiments should be done to confirm this assumption.

Note that the expected height of the gravitational state is related to g by (3). This means that for an uncertainty in the determination of z_1 of dz_1 one can get an accuracy in the determination of g at the level of $dg/g = 3dz_1/z_1\sqrt{N}$, where N is the number of detected signals. Assuming an uncertainty of $dz_1 = 0.1$ mm which is mainly determined by the finite source size, the value of dg/g can be determined to 3% in three months. This is comparable to the accuracy that is aimed for by the antihydrogen experiments at CERN [42–44]. Therefore, observation of Ps gravitational quantum states offers a complementary approach to test the effect of gravity on a pure leptonic system. In comparison to a free-fall experiment [21], perturbations of the Ps atoms arising from uncontrolled patch electric fields will not result in a systematic effect for the experiment but will only affect the signal rate.

5. Conclusions

The observation of the gravitational quantum states of positronium is very challenging and at this point we cannot conclude that it is feasible. In fact, even though most of the techniques are currently available, some essential milestones have to be demonstrated experimentally before such an experiment could be realized. Those are the efficient focusing of a bunched positron beam, the Stark deceleration of Rydberg positronium, and the subsequent excitation of Rydberg positronium into states with large angular momentum. In this contribution, we provide our expectations for the efficiencies of these various steps based on published work with Ps and other atomic species. Our estimation of the signal rate is encouraging thus justifying and stimulating preliminary

experiments, further calculations, and simulations. Furthermore, the developed techniques could also find an application in other fields. Rydberg deceleration of Ps atoms would be a major step to open a new era in Ps spectroscopy. If this would be realized, the main systematic effects (second order Doppler shift and time-of-flight broadening) would be reduced by two orders of magnitude (well below its natural linewidth of 1.2 MHz); thus an uncertainty in the measurement of the 1S-2S interval of positronium at the few kHz level might be possible. Assuming that the QED corrections could be calculated at the same level, this would lead to a new, independent (Ps, being purely leptonic, is free of nuclear size effects) determination of the Rydberg constant at the same level of precision as the current one [45]. This might help to shed some light on the proton size puzzle [46, 47] since this can be solved by shifting by 5 standard deviations the value of the Rydberg constant [48].

If an observation of the gravitational quantum states of positronium could be realized, this would result in a determination of dg/g for positronium at a level of 3% assuming 70 events could be detected. If successful, the ongoing efforts to increase the positron buffer gas trap efficiency [17], the available slow positron fluxes, seeking to produce a source of colder Ps [30–32], would certainly help to make the observation of the gravitational quantum states of positronium feasible.

Conflict of Interests

The authors declare that there is no conflict of interests regarding the publication of this paper.

Acknowledgments

The authors wish to thank the GRANIT collaboration for providing excellent possibilities for discussions and exchange. P. Crivelli acknowledges the support by the Swiss National Science Foundation (Grant PZ00P2 132059) and ETH Zurich (Grant ETH-47-12-1) and the very useful discussions with F. Merkt, C. Seiler, D. A. Cooke, and D. J. Murtagh.

References

- [1] V. V. Nesvizhevsky, H. G. Börner, A. K. Petukhov et al., “Quantum states of neutrons in the Earth’s gravitational field,” *Nature*, vol. 415, no. 6869, pp. 297–299, 2002.
- [2] L. D. Landau and E. M. Lifshitz, *Quantum Mechanics*, Pergamon Press, Oxford, UK, 1976.
- [3] A. Mills and M. Leventhal, “Can we measure the gravitational free fall of cold Rydberg state positronium?” *Nuclear Instruments and Methods B*, vol. 192, pp. 102–106, 2002.
- [4] A. van Veen, H. Schut, F. Labohm, and J. de Roode, “Positron extraction and transport in a nuclear-reactor-based positron beam,” *Nuclear Instruments and Methods in Physics Research A*, vol. 427, no. 1-2, pp. 266–270, 1999.
- [5] A. W. Hunt, L. Pilant, D. B. Cassidy et al., “The development of the intense positron beam at Washington State University,” *Applied Surface Science*, vol. 194, no. 1–4, pp. 296–300, 2002.

- [6] R. Krause-Rehberg, G. Brauer, M. Jungmann, A. Krille, A. Rogov, and K. Noack, "Progress of the intense positron beam project EPOS," *Applied Surface Science*, vol. 255, no. 1, pp. 22–24, 2008.
- [7] AIST, <http://unit.aist.go.jp/riif/adcg/english>.
- [8] N. Oshima, R. Suzuki, T. Ohdaira et al., "A positron annihilation lifetime measurement system with an intense positron microbeam," *Radiation Physics and Chemistry*, vol. 78, no. 12, pp. 1096–1098, 2009.
- [9] N. Oshima, R. Suzuki, T. Ohdaira et al., "Development of positron microbeam in AIST," *Materials Science Forum*, vol. 607, pp. 238–242, 2009.
- [10] A. I. Hawari, D. W. Gidley, J. Xu et al., "The intense slow positron beam facility at the NC State University PULSTAR reactor," *AIP Conference Proceedings*, vol. 1099, pp. 862–865, 2009.
- [11] A. I. Hawari, D. W. Gidley, J. Moxom, A. G. Hathaway, and S. Mukherjee, "Operation and testing of the PULSTAR reactor intense slow positron beam and PALS spectrometers," *Journal of Physics: Conference Series*, vol. 262, no. 1, Article ID 012024, 2011.
- [12] C. Hugenschmidt, B. Löwe, J. Mayer et al., "Unprecedented intensity of a low-energy positron beam," *Nuclear Instruments and Methods in Physics Research A*, vol. 593, no. 3, pp. 616–618, 2008.
- [13] S. Chemerisov and C. D. Jonah, "Development of high intensity source of thermal positrons APosS (Argonne Positron Source)," *Journal of Physics: Conference Series*, vol. 262, Article ID 012012, 2011.
- [14] S. Golge, B. Vlahovic, and B. Wojtsekhowski, "High intensity low-energy positron source at Jefferson," in *Proceedings of the International Particle Accelerator Conference (IPAC '12)*, 2012.
- [15] D. B. Cassidy, S. H. M. Deng, R. G. Greaves, and A. P. Mills Jr., "Accumulator for the production of intense positron pulses," *Review of Scientific Instruments*, vol. 77, no. 7, Article ID 073106, 2006.
- [16] N. Alberola, T. Anthonioz, A. Badertscher et al., "Development of a high-efficiency pulsed slow positron beam for measurements with orthopositronium in vacuum," *Nuclear Instruments and Methods A*, vol. 560, no. 2, pp. 224–232, 2006.
- [17] D. J. Murtagh, "A positron buncher-cooler," *The European Physical Journal D*, vol. 68, p. 213, 2014.
- [18] G. R. Brandes, K. F. Canter, T. N. Horsky, P. H. Lippel, and A. P. Mills Jr., "Scanning positron microbeam," *Review of Scientific Instruments*, vol. 59, no. 2, pp. 228–232, 1988.
- [19] N. Oshima, R. Suzuki, T. Ohdaira et al., "Brightness enhancement method for a high-intensity positron beam produced by an electron accelerator," *Journal of Applied Physics*, vol. 103, no. 9, Article ID 094916, 2008.
- [20] M. Fujinami, S. Jinno, M. Fukuzumi, T. Kawaguchi, K. Oguma, and T. Akahane, "Production of a positron microprobe using a transmission remoderator," *Analytical Sciences*, vol. 24, no. 1, pp. 73–79, 2008.
- [21] D. B. Cassidy and S. Hogan, "Atom control and gravity measurements using Rydberg positronium," *International Journal of Modern Physics: Conference Series*, vol. 30, Article ID 1460259, 9 pages, 2014.
- [22] P. Crivelli, U. Gendotti, A. Rubbia, L. Liszkay, P. Perez, and C. Corbel, "Measurement of the orthopositronium confinement energy in mesoporous thin films," *Physical Review A*, vol. 81, no. 5, Article ID 052703, 2010.
- [23] D. B. Cassidy, P. Crivelli, T. H. Hisakado et al., "Positronium cooling in porous silica measured via Doppler spectroscopy," *Physical Review A*, vol. 81, no. 1, Article ID 012715, 12 pages, 2010.
- [24] D. W. Gidley, H.-G. Peng, and R. S. Vallery, "Positron annihilation as a method to characterize porous materials," *Annual Review of Materials Research*, vol. 36, pp. 49–79, 2006.
- [25] P. Crivelli, D. Cooke, B. Barbiellini et al., "Positronium emission spectra from self-assembled metal-organic frameworks," *Physical Review B*, vol. 89, Article ID 241103(R), 2014.
- [26] D. B. Cassidy, T. H. Hisakado, V. E. Meline, H. W. K. Tom, and A. P. Mills Jr., "Delayed emission of cold positronium from mesoporous materials," *Physical Review A*, vol. 82, Article ID 052511, 2010.
- [27] D. B. Cassidy and A. P. Mills, "Enhanced Ps-Ps interactions due to quantum confinement," *Physical Review Letters*, vol. 107, Article ID 213401, 2011.
- [28] S. D. Hogan and F. Merkt, "Demonstration of three-dimensional electrostatic trapping of state-selected rydberg atoms," *Physical Review Letters*, vol. 100, Article ID 043001, 2008.
- [29] S. D. Hogan, C. Seiler, and F. Merkt, "Rydberg-state-enabled deceleration and trapping of cold molecules," *Physical Review Letters*, vol. 103, Article ID 123001, 2009.
- [30] S. Mariazzi, P. Bettotti, and R. S. Brusa, "Positronium cooling and emission in vacuum from nanochannels at cryogenic temperature," *Physical Review Letters*, vol. 104, Article ID 243401, 2010.
- [31] D. B. Cassidy, T. H. Hisakado, H. W. K. Tom, and A. P. Mills, "Optical spectroscopy of molecular positronium," *Physical Review Letters*, vol. 108, no. 13, Article ID 133402, 2012.
- [32] G. Consolati, R. Ferragut, A. Galarneau, F. di Renzo, and F. Quasso, "Mesoporous materials for antihydrogen production," *Chemical Society Reviews*, vol. 42, no. 9, pp. 3821–3832, 2013.
- [33] A. P. Mills, "Positronium formation at surfaces," *Physical Review Letters*, vol. 41, article 1828, 1978.
- [34] M. S. Fee, A. P. Mills Jr., S. Chu et al., "Measurement of the positronium 13S1-23 S1 interval by continuous-wave two-photon excitation," *Physical Review Letters*, vol. 70, no. 10, pp. 1397–1400, 1993.
- [35] K. P. Ziocck, R. H. Howell, F. Magnotta, R. A. Failor, and K. M. Jones, "First observation of resonant excitation of high-n states in positronium," *Physical Review Letters*, vol. 64, no. 20, pp. 2366–2369, 1990.
- [36] D. B. Cassidy, T. H. Hisakado, H. W. K. Tom, and A. P. Mills, "Optical spectroscopy of molecular positronium," *Physical Review Letters*, vol. 108, Article ID 133402, 2012.
- [37] A. C. L. Jones, T. H. Hisakado, H. J. Goldman, H. W. K. Tom, A. P. Mills Jr., and D. B. Cassidy, "Doppler-corrected Balmer spectroscopy of Rydberg positronium," *Physical Review A*, vol. 90, Article ID 012503, 2014.
- [38] P. Crivelli, D. A. Cooke, and S. Friedreich, "Experimental considerations for testing antimatter antigravity using positronium 1S-2S spectroscopy," *International Journal of Modern Physics: Conference Series*, vol. 30, Article ID 1460257, 10 pages, 2014.
- [39] G. Dufour, A. Gerardin, R. Guerout et al., "Quantum reflection of antihydrogen from the Casimir potential above matter slabs," *Physical Review A*, vol. 87, Article ID 012901, 2013.
- [40] A. Badertscher, P. Crivelli, W. Fetscher et al., "Improved limit on invisible decays of positronium," *Physical Review D*, vol. 75, no. 3, Article ID 032004, 2007.
- [41] T. F. Gallagher, *Rydberg Atoms*, Cambridge University Press, Cambridge, Mass, USA, 1994.

- [42] A. Kellerbauer, M. Amoretti, A. S. Belov et al., “Proposed antimatter gravity measurement with an antihydrogen beam,” *Nuclear Instruments and Methods in Physics Research B*, vol. 266, pp. 351–356, 2008.
- [43] D. P. van der Werf and GBAR collaboration, “The GBAR experiment,” *International Journal of Modern Physics: Conference Series*, vol. 30, Article ID 1460263, 2014.
- [44] A. I. Zhmoginov, A. E. Charman, R. Shaloo, J. Fajans, and J. S. Wurtele, “Nonlinear dynamics of anti-hydrogen in magnetostatic traps: implications for gravitational measurements,” *Classical and Quantum Gravity*, vol. 30, no. 20, Article ID 205014, 2013.
- [45] P. J. Mohr, B. N. Taylor, and D. B. Newell, “CODATA recommended values of the fundamental physical constants: 2010,” *Reviews of Modern Physics*, vol. 84, article 1527, 2012.
- [46] R. Pohl, A. Antognini, F. Nez et al., “The size of the proton,” *Nature*, vol. 466, pp. 213–216, 2010.
- [47] A. Antognini, F. Nez, K. Schuhmann et al., “Proton structure from the measurement of 2S-2P transition frequencies of muonic hydrogen,” *Science*, vol. 339, no. 6118, pp. 417–420, 2013.
- [48] F. Nez, A. Antognini, F. D. Amaro et al., “Is the proton radius a player in the redefinition of the international system of units?” *Philosophical Transactions of the Royal Society A*, vol. 369, no. 1953, pp. 4064–4077, 2011.

Research Article

Regge Poles in Neutron Scattering by a Cylinder

K. V. Protasov¹ and A. Y. Voronin²

¹ *Laboratoire de Physique Subatomique et de Cosmologie (LPSC), Université Grenoble Alpes, IN2P3-CNRS, 53 Avenue des Martyrs, 38026 Grenoble, France*

² *P.N. Lebedev Physical Institute, 53 Leninsky Prospekt, Moscow 119991, Russia*

Correspondence should be addressed to A. Yu. Voronin; dr.a.voronin@gmail.com

Received 20 July 2014; Accepted 24 August 2014; Published 16 September 2014

Academic Editor: Valery V. Nesvizhevsky

Copyright © 2014 K.V. Protasov and A. Yu. Voronin. This is an open access article distributed under the Creative Commons Attribution License, which permits unrestricted use, distribution, and reproduction in any medium, provided the original work is properly cited. The publication of this article was funded by SCOAP³.

We establish asymptotic expressions for the positions of Regge poles for cold neutron scattering on mesoscopic cylinder mirror as well as for the S -matrix residuals. We outline the correspondence between Regge poles and near-surface quasi-stationary neutron states. Such states are of practical importance for studying subtle effects of neutron-surface interaction.

1. Introduction

Neutron scattering on curved surface has all peculiar features characteristic for wave scattering known in acoustics, optics, and matter waves. The most intriguing phenomena are related to localization of neutrons in long-living states near a curved surface. Such localization is responsible for large angle scattering of cold neutrons on macroscopic radius cylinder mirror, discovered in [1–4]. It is a matter-wave analog of the so-called whispering gallery wave [5–10].

Neutron localization in a resonant state in effective potential, which originates from superposition of centrifugal potential and optical Fermi-potential of the cylinder, results in a large time spent by neutron near the material surface at distances from tens to hundreds nanometers. Thus neutron scattering on curved mirror is particularly sensitive to neutron-surface interaction at such distances. This opens interesting perspective of using interference pattern produced by neutrons scattered from curved surface as a sensitive tool for studying neutron-surface interactions. The detailed information about neutron-surface interaction could be of importance for multiple problems related to surface physics. Another important field is the study of extra forces with characteristic range $10 < \lambda < 1000$ nm. These forces are predicted in the extensions of the standard model as a result of exchange of hypothetical light bosons.

We have developed an approach based on a linear approximation of the potential in Schrödinger equation in [4]. Here we propose an alternative method based on exact solution with consequent approximations in the exact result. The approach obtained in present paper could be applied at least formally in wider parameter range than that obtained in [4] and, in particular, for neutrons of lower energies. This method allows us also to give another vision to the problem and to establish more clear analogies with another extensively studied case, that is, scattering of light by a sphere and, in particular, useful similarities with phenomena of rainbow, Gloria, surface waves, and so forth, treated in detail in a book by Nussenzweig [11]. The complex angular momentum (CAM) method plays an essential role in this study.

The concept of Regge poles, which are S -matrix singularities, thought of as a function of complex angular momentum is essential for establishing relation between scattering phenomena and the properties of long-living near-surface states of neutron.

In this paper we find asymptotic expressions for the positions of Regge poles in the limit of large angular momenta, which mainly contribute to large angle scattering of cold neutrons. We study a case of cold neutron scattering, as far as comparatively large amount of cold neutrons available makes possible high statistical accuracy in resolving interference pattern of scattered neutron wave.

2. Formal Solution and Regge Poles

In this section we develop the formalism describing the scattering of a plane neutron wave by a cylindrical mirror. We will study cases of both attractive and repulsive optical Fermi-potential of a cylinder material.

The scattering obeys the following Schrödinger equation in the cylindrical coordinates:

$$\left[-\frac{\hbar^2}{2M} \left(\frac{\partial^2}{\partial \rho^2} + \frac{1}{\rho} \frac{\partial}{\partial \rho} \right) - \frac{\hbar^2}{2M\rho^2} \frac{\partial^2}{\partial \varphi^2} + U(\rho) - \frac{\hbar^2 k^2}{2M} \right] \times \Psi(\rho, \varphi) = 0. \quad (1)$$

Here $\Psi(\rho, \varphi)$ is the neutron wave function, $\hbar k$ is the neutron momentum, ρ is the radial distance from the cylinder axis, φ is the angle, and $U(\rho)$ is the value of mirror optical potential:

$$U(\rho) = U_0 \Theta(R - \rho) = \begin{cases} U_0, & \rho \leq R, \\ 0, & \rho > R. \end{cases} \quad (2)$$

Here R is the cylinder radius and $\Theta(R - \rho)$ is the step function. U_0 is negative for attractive potential and positive for repulsion one. In (1), we omit the trivial dependence on z coordinate directed along the cylinder axis. By standard substitution of an analytical form of a wave function $\Psi(\rho, \varphi) = \Phi(\rho, \varphi)/\sqrt{\rho}$, (1) is transformed into the following form:

$$\left[-\frac{\hbar^2}{2M} \left(\frac{\partial^2}{\partial \rho^2} \right) - \frac{\hbar^2}{2M\rho^2} \left(\frac{\partial^2}{\partial \varphi^2} + \frac{1}{4} \right) + U_0 \Theta(R - \rho) - \frac{\hbar^2 k^2}{2M} \right] \times \Phi(\rho, \varphi) = 0. \quad (3)$$

The wave function $\Phi(\rho, \varphi)$ asymptotic behavior at large ρ values is

$$\Phi(\rho, \varphi) \longrightarrow \sqrt{\rho} \exp(ik\rho \cos(\varphi)) + f(\varphi) \exp\left(ik\rho + \frac{i\pi}{4}\right), \quad (4)$$

where $f(\varphi)$ is the scattering amplitude. The standard expansion of the two-dimensional wave function $\Phi(\rho, \varphi)$ in the complete basis of the angular momentum states $\exp(i\mu\varphi)$ is

$$\Phi(\rho, \varphi) = \sum_{\mu=-\infty}^{\infty} \chi_{|\mu|}(\rho) e^{i\mu\varphi}, \quad (5)$$

where $\chi_{|\mu|}(\rho)$ are the radial wave functions.

The scattering amplitude $f(\varphi)$ expansion in the complete basis of the angular momentum states $\exp(i\mu\varphi)$ follows from (5) and has the following form [12]:

$$f(\varphi) = \frac{-i}{\sqrt{2\pi k}} \sum_{\mu=-\infty}^{\infty} (S(\mu, k) - 1) e^{i\mu\varphi} \equiv \sum_{\mu=-\infty}^{\infty} f(\mu, k) e^{i\mu\varphi}. \quad (6)$$

Here $S(\mu, k) = \exp(2i\delta_{\mu}(k))$ is the scattering matrix in partial wave with angular momentum μ and $\delta_{\mu}(k)$ is the

scattering phase shift, which can be found by solving the corresponding radial equation:

$$\left[-\frac{\hbar^2}{2M} \left(\frac{\partial^2}{\partial \rho^2} \right) + \frac{\hbar^2}{2M\rho^2} \left(\mu^2 - \frac{1}{4} \right) + U_0 \Theta(R - \rho) - \frac{\hbar^2 k^2}{2M} \right] \times \chi_{\mu}(\rho) = 0, \quad (7)$$

$$\chi_{\mu}(\rho \rightarrow 0) = 0, \quad (8)$$

$$\chi_{\mu}(\rho \rightarrow \infty) = \sqrt{\frac{2}{\pi k}} \sin\left(k\rho + \delta_{\mu} - \frac{\pi}{2} \left(|\mu| - \frac{1}{2} \right)\right). \quad (9)$$

The typical values of angular momentum $\mu_0 \equiv kR \gg 1$. In particular, in case of cold neutron scattering on macroscopic cylinder with few centimeters radius the corresponding value $\mu_0 \sim 10^8$.

In order to perform a sum over a large number of partial waves we will use the method of complex angular momentum. We introduce, following the Regge approach, $f(\mu, k)$ as a function of complex momentum μ , which coincides with the scattering matrix for integer values of μ and has standard analytical properties in the complex plane of μ [13, 14]. The sum (6) over integer μ is then transformed to an integral in the complex μ plane, which is calculated by using the residue theorem and is replaced by a sum over poles contributions. In two-dimensional problems, an elegant way to perform such a transformation is to use Poisson sum formula [15]:

$$f(\varphi) = \sum_{n=-\infty}^{\infty} \int_{-\infty}^{\infty} f(\mu, k) e^{i\mu(\varphi+2\pi n)} d\mu. \quad (10)$$

Here $f(\mu, k)$ is the analytical function of μ as mentioned above. The integer number n has a sense of the number of neutron wave rotations around the cylinder surface. Using the analytical properties of the amplitude we transform the above integral to the sum of the amplitude poles contribution:

$$f(\varphi) = 2\pi i \sum_{n=-\infty}^{\infty} \sum_j \text{Res} f(\mu_j, k) e^{i\mu_j(\varphi+2\pi n)}. \quad (11)$$

Here μ_j is the j th pole of the amplitude f and $\text{Res} f(\mu_j, k)$ is a residue of the amplitude in this pole. In the above expression the integration contour is chosen such that $\text{Im}\mu_j\varphi > 0$ and $\text{Im}\mu_j(\pi - \varphi) > 0$. The summation over n can be performed after taking into account that the amplitude in our case is symmetric under substitution $\mu \rightarrow -\mu$. Such an expression takes the form

$$f(\varphi) = 2\pi i \sum_j \text{Res} f(\mu_j, k) \frac{\sin(\mu_j(\pi - \varphi))}{\sin(\mu_j\pi)}. \quad (12)$$

The above expression clearly demonstrates the role of Regge poles; namely, the scattering amplitude can be expressed as a converging sum of Regge poles contributions. Each contribution can be associated with decaying quasi-stationary states. The states with the longest lifetime contribute to scattering on largest deflection angles. In the following section we will get formal mathematical expressions for the Regge poles and discuss their physical meaning.

2.1. *Equation for Regge Poles.* The formal solution of (3) can be easily expressed in terms of Bessel functions.

Inside the cylinder $\rho < R$, the regular solution (8) of (7) is proportional to the Bessel function

$$\chi_\mu(\rho) \sim J_\mu(\kappa\rho) \quad (13)$$

with $\kappa = \sqrt{k^2 - 2MU_0/\hbar^2} \approx k - MU_0/k\hbar^2$. Let us remind the reader that U_0 is negative for attractive potential and positive for repulsion one. Outside the cylinder one has a sum of two independent solutions of Bessel equation:

$$\chi_\mu(\rho) \sim \cos\delta_\mu J_\mu(k\rho) + \sin\delta_\mu N_\mu(k\rho). \quad (14)$$

The condition of continuity of the logarithmic derivative of the wave function on the boundary of the cylinder $\rho = R$ gives the equation

$$\kappa \frac{J'_\mu(\kappa R)}{J_\mu(\kappa R)} = k \frac{\cos\delta_\mu J'_\mu(kR) + \sin\delta_\mu N'_\mu(kR)}{\cos\delta_\mu J_\mu(kR) + \sin\delta_\mu N_\mu(kR)} \quad (15)$$

which allows us to determine the value of the phase-shift δ_μ . Finally, one obtains

$$\tan\delta_\mu = \frac{(\kappa/k) \left(J'_\mu(\kappa R) / J_\mu(\kappa R) \right) J_\mu(kR) - J'_\mu(kR)}{(\kappa/k) \left(J'_\mu(\kappa R) / N_\mu(\kappa R) \right) J_\mu(kR) - N'_\mu(kR)}. \quad (16)$$

For the S-matrix, one obtains

$$S(\mu, p) = \exp(2i\delta_\mu), \quad (17)$$

$$S(\mu, p) = \left(N'_\mu(kR) + iJ'_\mu(kR) - \frac{\kappa J'_\mu(\kappa R)}{k J_\mu(\kappa R)} (N_\mu(kR) + iJ_\mu(kR)) \right) \times \left(N'_\mu(kR) - iJ'_\mu(kR) - \frac{\kappa J'_\mu(\kappa R)}{k J_\mu(\kappa R)} (N_\mu(kR) - iJ_\mu(kR)) \right)^{-1} \quad (18)$$

which coincides with the solution for 3-dimensional problem (scattering by a spherical potential well) if one replaces $\mu \rightarrow l + 1/2$.

These general expressions for Bessel $J_\mu(z)$ and Neumann $N_\mu(z)$ functions can be simplified in the limit of very big index μ which is close to the value of the argument of the Bessel function:

$$\mu \sim \mu_0 \equiv kR \sim \kappa R \gg 1. \quad (19)$$

Let us use the asymptotic for the Bessel function [16] in the form $J_\mu(\mu z)$ with two complex variables μ and z .

In the limit of large index one can use the following asymptotic behaviour for Bessel functions (only a leading in μ term is written here):

$$J_\mu(\mu z) \approx \left(\frac{4\zeta}{1-z^2} \right)^{1/4} \frac{\text{Ai}(\mu^{2/3}\zeta)}{\mu^{1/3}}, \quad (20)$$

where

$$\frac{2}{3}\zeta^{3/2} = \int_z^1 \frac{\sqrt{1-t^2}}{t} dt = \ln \frac{1 + \sqrt{1-z^2}}{z} - \sqrt{1-z^2} \quad (21)$$

or equivalently

$$\frac{2}{3}(-\zeta)^{3/2} = \int_1^z \frac{\sqrt{t^2-1}}{t} dt = \sqrt{z^2-1} - \frac{1}{i} \ln \frac{1 + i\sqrt{z^2-1}}{z}. \quad (22)$$

$\text{Ai}(z)$ is the Airy function.

For z close to 1,

$$\zeta \approx 2^{1/3}(z-1). \quad (23)$$

Analogous expression can be obtained for Neumann function as well as for the derivatives of Bessel and Neumann functions

$$N_\mu(\mu z) \approx - \left(\frac{4\zeta}{1-z^2} \right)^{1/4} \frac{\text{Bi}(\mu^{2/3}\zeta)}{\mu^{1/3}}, \quad (24)$$

$$J'_\mu(\mu z) \approx - \frac{2}{z} \left(\frac{1-z^2}{4\zeta} \right)^{1/4} \frac{\text{Ai}'(\mu^{2/3}\zeta)}{\mu^{2/3}}, \quad (25)$$

$$N'_\mu(\mu z) \approx \frac{2}{z} \left(\frac{1-z^2}{4\zeta} \right)^{1/4} \frac{\text{Bi}'(\mu^{2/3}\zeta)}{\mu^{2/3}}. \quad (26)$$

$\text{Bi}(z)$ is an Airy function of the second kind.

If one introduces the notations

$$\zeta_{\text{in}} = 2^{1/3} \left(\frac{\kappa R}{\mu} - 1 \right), \quad \zeta_{\text{out}} = 2^{1/3} \left(\frac{kR}{\mu} - 1 \right), \quad (27)$$

one finds the expression for the S-matrix

$$S(\mu, k) = \frac{T^-(\mu, k)}{T^+(\mu, k)} \quad (28)$$

with

$$T^\pm(\mu, k) = \text{Bi}'(\mu^{2/3}\zeta_{\text{out}}) \pm i\text{Ai}'(\mu^{2/3}\zeta_{\text{out}}) - \frac{\text{Ai}'(\mu^{2/3}\zeta_{\text{in}})}{\text{Ai}(\mu^{2/3}\zeta_{\text{in}})} \left[\text{Bi}(\mu^{2/3}\zeta_{\text{out}}) \pm i\text{Ai}(\mu^{2/3}\zeta_{\text{out}}) \right]. \quad (29)$$

The poles of the S-matrix can be found from the equation

$$T^+(\mu, k) = 0, \quad (30)$$

or in explicit form:

$$\frac{\text{Ai}'(\mu^{2/3}\zeta_{\text{in}})}{\text{Ai}(\mu^{2/3}\zeta_{\text{in}})} = \frac{\text{Bi}'(\mu^{2/3}\zeta_{\text{out}}) + i\text{Ai}'(\mu^{2/3}\zeta_{\text{out}})}{\text{Bi}(\mu^{2/3}\zeta_{\text{out}}) + i\text{Ai}(\mu^{2/3}\zeta_{\text{out}})}. \quad (31)$$

2.2. Asymptotic Expressions for Regge Poles. In the following we will be interested in the extremely large values of angular momentum. These are angular momenta which contribute to large angle neutron scattering. Indeed, the energy of cold neutrons is much larger than optical Fermi-potential of a cylinder; thus, most neutrons would pass without significant deflection. Only a small fraction of neutrons which moves parallel to the cylinder surface is captured into comparatively long-living near-surface states, which explains large angle scattering.

An argument of Airy function equation (31) can be further expanded, taking into account large values of $\mu \sim \mu_0 \gg 1$:

$$\mu^{2/3} \zeta_{\text{in}} = \left(\frac{2}{\mu}\right)^{1/3} (\kappa R - \mu) \approx -u_0 - xm, \quad (32)$$

$$\mu^{2/3} \zeta_{\text{out}} = \left(\frac{2}{\mu}\right)^{1/3} (kR - \mu) = -x.$$

Here,

$$u_0 = \frac{MU_0 R}{\hbar^2 k} \left(\frac{2}{\mu_0}\right)^{1/3} = \frac{2MU_0}{\hbar^2 k^2} \left(\frac{\mu_0}{2}\right)^{2/3}, \quad (33)$$

$$x = (\mu - \mu_0) \left(\frac{2}{\mu_0}\right)^{1/3}.$$

The complex variable x is proportional to the difference between actual angular momentum μ and ‘‘edge scattering’’ angular momentum μ_0 .

Equation (31) for the Regge poles in new variable x_n takes the form

$$\frac{\text{Ai}'(-u_0 - x_n)}{\text{Ai}(-u_0 - x_n)} = \frac{\text{Bi}'(-x_n) + i\text{Ai}'(-x_n)}{\text{Bi}(-x_n) + i\text{Ai}(-x_n)}. \quad (34)$$

This form of equation is convenient for further asymptotic expansions for large values of x_n . The particular form of asymptotic expansion of Airy function in complex plane of x depends on the argument of x . This is known as Stock’s phenomenon. Thus we will study different domains of complex momentum plane.

First we study a case of narrow resonances which are situated close to real axis of complex momentum plane. In this case the following asymptotic form of Airy functions can be used:

$$\text{Ai}(-z) \sim \frac{1}{\sqrt{\pi z^{1/4}}} \cos\left(\frac{2}{3}z^{3/2} - \frac{\pi}{4}\right), \quad (35)$$

$$\text{Bi}(-z) \sim -\frac{1}{\sqrt{\pi z^{1/4}}} \sin\left(\frac{2}{3}z^{3/2} - \frac{\pi}{4}\right)$$

with $|\arg(z)| < 2\pi/3$ and

$$\text{Ai}(z) \sim \frac{1}{2\sqrt{\pi z^{1/4}}} \exp\left(-\frac{2}{3}z^{3/2}\right) \quad \text{with } |\arg(z)| < \pi, \quad (36)$$

$$\text{Bi}(z) \sim \frac{1}{\sqrt{\pi z^{1/4}}} \exp\left(\frac{2}{3}z^{3/2}\right) \quad \text{with } |\arg(z)| < \frac{\pi}{3}.$$

In case of attractive potential ($u_0 < 0$) there could be poles with $u_0 < \text{Re}x_n < 0$, $|\text{Im}x_n| \ll |\text{Re}x_n|$. For $|u_0| \gg 1$ (34) takes the form

$$\sqrt{\frac{|u_0| + x_n}{-x_n}} \tan\left[\frac{2}{3}(|u_0| + x_n)^{3/2} - \frac{\pi}{4}\right] = 1 - i \exp\left[-\frac{4}{3}(-x_n)^{3/2}\right]. \quad (37)$$

The approximate solution of the above equation gives exponentially small values for the imaginary part:

$$\text{Im}x_n \sim \exp\left[-\frac{4}{3}\text{Re}(-x_n)^{3/2}\right], \quad (38)$$

with real part $\text{Re}x_n$ being a solution of equation:

$$\sqrt{\frac{|u_0| + x_n}{-x_n}} \tan\left[\frac{2}{3}(|u_0| + x_n)^{3/2} - \frac{\pi}{4}\right] = 1. \quad (39)$$

In the limiting case of deeply bound states $|u_0| + x_n \ll |x_n|$ one gets, for real part $\text{Re}x_n$,

$$\text{Re}x_n \approx -\left[\frac{3}{2}\pi\left(n - \frac{1}{4}\right)\right]^{2/3}. \quad (40)$$

In case of weakly bound states $|u_0| + x_n \gg |x_n|$,

$$\text{Re}x_n \approx -\left[\frac{3}{2}\pi\left(n - \frac{3}{4}\right)\right]^{2/3}. \quad (41)$$

Here and further on $n = 1, 2, \dots$

There are a limited number of such resonances determined by the value of dimensionless depth of optical potential u_0 .

Narrow resonances $|\text{Im}x_n| \ll |\text{Re}x_n|$ with positive real part $\text{Re}x_n > 0$ in case of attractive potential and $\text{Re}x_n > u_0$ in case of repulsive potential are given by the following asymptotic form of (34):

$$\tan\left[\frac{2}{3}(x_n - u_0)^{3/2} - \frac{\pi}{4}\right] = i\sqrt{\frac{x_n}{x_n - u_0}}. \quad (42)$$

Its approximative solutions are given by the following expressions:

$$\text{Re}x_n = \left[\frac{3}{2}\pi\left(n - \frac{3}{4}\right)\right]^{2/3} + |u_0| \Theta(U_0), \quad (43)$$

$$\text{Im}x_n = -\frac{1}{\sqrt{\text{Re}x_n}} \left(\frac{1}{2} \ln \frac{4\text{Re}x_n}{|u_0|} - \frac{|u_0|}{4\text{Re}x_n}\right).$$

Here $\Theta(U_0)$ is equal to unity for repulsive potential and is equal to zero for attractive potential.

Formally, there are an infinite number of mentioned above-barrier resonances. However, for too large n the approximation based on asymptotic expansion of Bessel functions (20) and (24) is no longer valid, as far as their validity is limited with cases when $|\mu - \mu_0| \ll \mu_0$. In opposite

case one has to take into account exact form of the S-matrix, given by (18).

These are the Regge poles of so-called class I [14] corresponding to the narrow resonances. The corresponding values of complex angular momentum μ_n are

$$\mu_n = \pm \left[\mu_0 - x_n \left(\frac{\mu_0}{2} \right)^{1/3} \right]. \quad (44)$$

They are situated in the complex μ -plane symmetrically related to the origin $\mu = 0$.

Long-living quasi-bound states and narrow over-barrier resonances play important role in the phenomena of whispering gallery scattering of neutrons at large angles, studied in [4].

Another type of asymptotic expansion is obtained when the argument of the Airy functions $|\arg(z)| \geq 2\pi/3$. To study this case we make the following substitution:

$$x_n = -z_n \exp\left(\frac{i\pi}{3}\right). \quad (45)$$

With the use of the following relations between Airy functions

$$\text{Ai}(-z) = e^{i\pi/3} \text{Ai}(ze^{i\pi/3}) + e^{-i\pi/3} \text{Ai}(ze^{-i\pi/3}), \quad (46)$$

$$\text{Bi}(-z) = e^{-i\pi/6} \text{Ai}(ze^{i\pi/3}) + e^{i\pi/6} \text{Ai}(ze^{-i\pi/3}),$$

(34) turns into

$$\frac{\text{Ai}'(u_0 + z_n e^{i\pi/3})}{\text{Ai}(u_0 + z_n e^{i\pi/3})} = \frac{\text{Ai}'(-z_n)}{\text{Ai}(-z_n)}. \quad (47)$$

For $|z_n| \gg 1$ we get the following asymptotic form equation:

$$\tan\left(\frac{2}{3}z_n^{3/2} - \frac{\pi}{4}\right) = \sqrt{\frac{z_n e^{i\pi/3} + u_0}{z_n}}. \quad (48)$$

Its solution for large n is

$$z_n = \left\{ \frac{3\pi}{2} \left[n - \frac{3}{4} + \arctan(e^{i\pi/6}) \right] \right\}^{2/3}. \quad (49)$$

The corresponding Regge poles are

$$\mu_n = \pm \left(\mu_0 + z_n e^{i\pi/3} \left(\frac{\mu_0}{2} \right)^{1/3} \right). \quad (50)$$

There are an infinite number of Regge poles of this type; their imaginary part increases rapidly with n and they correspond to the so-called surface wave states. Such states have much shorter lifetimes than narrow resonances, described above.

The positions of these poles in the upper half plane of complex variable μ are presented in Figures 1 and 2 for attractive and repulsive potential, respectively.

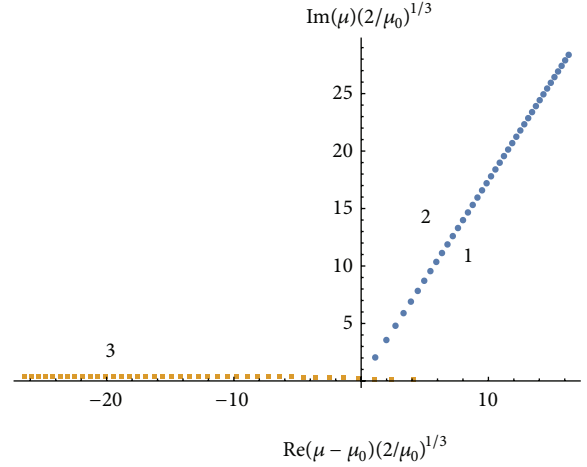


FIGURE 1: Position of Regge poles for attractive Fermi-potential. Shown are the poles, corresponding to near-surface states. 1: narrow quasi-bound states (whispering gallery states), 2: surface waves, and 3: narrow over-barrier resonances.

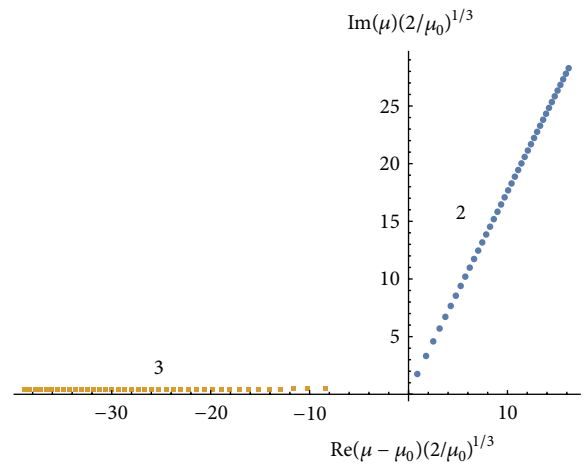


FIGURE 2: Position of Regge poles for repulsive Fermi-potential. Shown are the poles, corresponding to near-surface states. 2: surface waves and 3: narrow over-barrier resonances.

3. Residuals

Complex angular momentum methods require knowledge of the residuals of S-matrix in the Regge poles. Here we obtain corresponding expressions for residuals, which follow from expression (28). In the vicinity of the pole x_n the corresponding S-matrix written in variable x is

$$S(x) \approx \frac{T^-(x_n)}{T^{+'}(x_n)(x - x_n)}. \quad (51)$$

Function T in the above expression has the form

$$T^\pm(x) = \text{Ai}(-u_0 - x) \left(\text{Bi}'(-x) \pm i \text{Ai}' \right) - \text{Ai}'(-u_0 - x) \left(\text{Bi}(-x) \pm i \text{Ai}(-x) \right). \quad (52)$$

Thus residual is

$$\text{ResS}(x_n) = \frac{T^-(x_n)}{T^{+'}(x_n)}. \quad (53)$$

The above expression can be further simplified if one takes into account that x_n is a root of equation $T^+(x_n) = 0$. One can get for the nominator of fraction (53) the following expression:

$$T^-(x_n) = -\frac{2i}{\pi} \frac{\text{Ai}(-u_0 - x_n)}{\text{Bi}(-x_n) + i\text{Ai}(-x_n)}. \quad (54)$$

In derivation of the above equation we took into account that the Wronskian $\text{Ai}'(-x)\text{Bi}(-x) - \text{Bi}'(-x)\text{Ai}(-x) = 1/\pi$.

The corresponding expression for the denominator of fraction (53) reads

$$T^{+'}(x_n) = -u_0 \text{Ai}(-u_0 - x_n) (\text{Bi}(-x_n) + i\text{Ai}(-x_n)). \quad (55)$$

One should use the equation for Airy functions $\text{Ai}''(-x) = x\text{Ai}(-x)$ to establish the above expression.

Combining these results we finally get the following expression for the residual:

$$\text{ResS}(x_n) = \frac{2i}{\pi u_0 (\text{Bi}(-x_n) + i\text{Ai}(-x_n))^2}. \quad (56)$$

4. Physical Meaning of Regge Poles

In order to establish physical meaning of the Regge poles found in the previous section we will establish a relation between Regge poles and quasi-stationary states of neutrons near a curved surface of macroscopic mirror. For such a purpose we will study an effective potential produced by superposition of optical Fermi-potential of the mirror and the centrifugal potential near the mirror surface.

We expand the expression for the centrifugal energy in (7) in the vicinity of $\rho = R$ introducing the deviation from the cylinder surface $\xi = \rho - R$. In the first order of small ratio ξ/R , we get the following equation:

$$\left[-\frac{\hbar^2}{2M} \frac{\partial^2}{\partial \xi^2} + U_0 \Theta(-\xi) + \hbar^2 \frac{\mu^2 - 1/4}{2MR^2} \left(1 - \frac{2\xi}{R} \right) - E \right] \times \chi_\mu(\xi) = 0. \quad (57)$$

Introducing a new variable

$$\varepsilon_\mu = E - \hbar^2 \frac{\mu^2 - 1/4}{2MR^2} \approx \frac{(MvR)^2 - \hbar^2 \mu^2}{2MR^2} \quad (58)$$

we get the following equation for the neutron *radial* motion near the surface of the cylinder:

$$\left[-\frac{\hbar^2}{2M} \frac{\partial^2}{\partial \xi^2} + U_0 \Theta(-\xi) - \frac{Mv^2}{R} \xi - \varepsilon_\mu \right] \chi_\mu(\xi) = 0. \quad (59)$$

Equation (59) describes the neutron motion in a constant effective field $a = -v^2/R$ superposed with the mirror optical

potential $U_0 \Theta(-\xi)$. A sketch of the corresponding potential for attractive and repulsive optical potential is shown in Figure 3. The value ε_μ can be understood as the radial motion energy within the linear expansion used above for the angular momentum $|\mu - \mu_0| \ll \mu_0$.

Characteristic spatial and energy scales of the above equation are

$$l_0 = \sqrt[3]{\frac{\hbar^2 R}{2M^2 v^2}} = \frac{R}{2} \left(\frac{2}{\mu_0} \right)^{2/3}, \quad (60)$$

$$\varepsilon_0 = \sqrt[3]{\frac{\hbar^2 M v^4}{2R^2}} = \frac{Mv^2}{2} \left(\frac{2}{\mu_0} \right)^{2/3}.$$

Equation (59) in units of l_0 and ε_0 is

$$\left[-\frac{\partial^2}{\partial x^2} + u_0 \Theta(-x) - x - \lambda_\mu \right] \chi_\mu(x) = 0. \quad (61)$$

Here $x = \xi/l_0$, $\lambda_\mu = \varepsilon_\mu/\varepsilon_0$, and $u_0 = U_0/\varepsilon_0$.

The regular solution of (61) is given by the Airy function $\text{Ai}(\xi)$:

$$\chi_\mu(x) \sim \begin{cases} \text{Ai}(-x - \lambda_\mu) & \text{if } x > 0 \\ \text{Ai}(u_0 - x - \lambda_\mu) & \text{if } x \leq 0. \end{cases} \quad (62)$$

Let us mention that the case of attractive cylinder potential U_0 could be practically realised if cold neutrons are scattered in the bulk of the media with positive optical potential $+U_0$ on a cylinder hole [4].

By matching the logarithmic derivatives of the ‘‘out’’ (incoming plus reflected wave, $\xi > 0$) and ‘‘in’’ (wave function inside cylinder, $\xi < 0$) solutions at $\xi = 0$ one can get exactly the same equation for the S-matrix as (28) and, correspondingly, the same equation for the S-matrix poles as (34).

Thus the complex values of x_n in (34) could be interpreted as the complex values of the radial energy λ_n (in units ε_0) of the quasi-stationary centrifugal states of neutrons near the cylinder surface [17].

Let us mention that for extremely large angular momenta of interest neutron motion along angular variable φ is classical; thus we can establish direct relation between angle and time: $\varphi \approx \hbar\mu_0/(MR^2)t$. This turns the problem of neutron scattering on a cylinder into a problem of temporal evolution of resonant states in effective potential of the neutron radial motion.

For attractive potential there are states bound inside an effective potential well. These are quasi-stationary states given by (37). The quasi-stationary nature of such states is explained by the nonvanishing probability of the neutron penetration through the triangular barrier (Figure 3) into the mirror bulk. This probability strongly depends on the effective triangular barrier height u_0 , which is a function of neutron velocity,

$$u_0 = \frac{U_0}{\varepsilon_0} = \frac{2MU_0}{\hbar^2 k^2} \left(\frac{\mu_0}{2} \right)^{2/3} \quad (63)$$

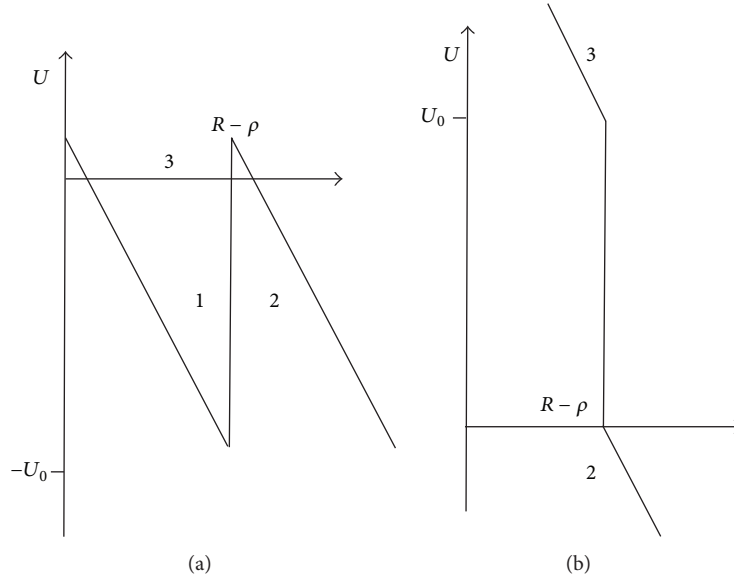


FIGURE 3: A sketch of the potential in the mirror surface vicinity is shown for the case of attractive (a) and repulsive (b) optical Fermi-potentials. The potential step at $\xi = 0$ is equal to the mirror optical potential U_0 . The potential slope at $\xi \neq 0$ is governed by the centrifugal effective acceleration $a = v^2/R$. The regions, responsible for different type of resonances, are indicated with numbers: 1: long-living quasi-bound states, 2: surface waves, and 3: narrow over-barrier resonances.

and determines the width Γ_n of the centrifugal state. These states are particularly important for a whispering gallery neutron scattering [4].

Another type of states, given by (42), is narrow over-barrier resonances. They are explained by phenomenon of so-called quantum reflection from the sharp edge of the effective potential. The condition of efficient quantum reflection consists in smallness of the characteristic scale of potential change compared to the wave-length of the neutron *radial motion*. It was shown in [4] that the widths of such resonances are particularly sensitive to the shape of the edge of effective potential, and its smoothing results in fast increase of the width of such states.

Let us mention that these narrow over-barrier resonances exist in case of both attractive and repulsive optical Fermi-potential. In case of cold neutrons scattering on a cylinder of few centimeters radius they contribute to scattering to few degrees angles. Such states are analogous to the gravitational quasi-stationary states of antiatoms above material surface, predicted in [18, 19].

Finally, resonances given by (48) are responsible for phenomenon of so-called surface waves. They can be interpreted as a result of neutron evanescent wave reflection from the sharp edge of the optical Fermi-potential when neutron tunnels through the centrifugal barrier and penetrate to the cylinder surface. Due to rapidly increasing width as a function of n and correspondingly short lifetimes only few lowest states contribute to the neutron scattering at large angles.

Figure 3 illustrates the regions of effective potential, responsible for “production” of resonances of certain type.

5. Conclusion

We studied the position of Regge poles in complex momentum plane for the case of cold neutron scattering on a macroscopical curved mirror. Typical angular momenta which contribute to large angle scattering are of order of 10^8 , so asymptotic methods are required. We establish the corresponding equations for the Regge poles and find two types of such poles: narrow resonances and wide surface waves resonances. We establish the direct relation between the values of complex angular momenta, corresponding to Regge poles and complex radial energies of quasi-stationary states of neutron, bound near the curved surface by effective potential. The Regge poles imaginary part gives the width of such states. These states are particularly important for large angle scattering. Such scattering, determined by near-surface neutron states, is particularly sensitive to the details of neutron-surface interaction. It could be a promising tool for studying such kind of interactions.

Conflict of Interests

The authors declare that there is no conflict of interests regarding the publication of this paper.

References

- [1] V. V. Nesvizhevsky, A. Y. Voronin, R. Cubitt, and K. V. Protasov, “Neutron whispering gallery,” *Nature Physics*, vol. 6, no. 2, pp. 114–117, 2010.
- [2] V. V. Nesvizhevsky, A. K. Petukhov, K. V. Protasov, and A. Y. Voronin, “Centrifugal quantum states of neutrons,” *Physical*

- Review A—Atomic, Molecular, and Optical Physics*, vol. 78, no. 3, Article ID 033616, 2008.
- [3] R. Cubitt, V. V. Nesvizhevsky, A. K. Petukhov et al., “Methods of observation of the centrifugal quantum states of neutrons,” *Nuclear Instruments and Methods in Physics Research A*, vol. 611, no. 2-3, pp. 322–325, 2009.
- [4] V. V. Nesvizhevsky, R. Cubitt, K. V. Protasov, and A. Y. Voronin, “The whispering gallery effect in neutron scattering,” *New Journal of Physics*, vol. 12, Article ID 113050, 2010.
- [5] J. W. S. Rayleigh, *The Theory of Sound*, vol. 2, Macmillan, London, UK, 1878.
- [6] L. Rayleigh, “IX. Further applications of Bessel’s functions of high order to the Whispering Gallery and allied problems,” *Philosophical Magazine*, vol. 27, no. 157, p. 100, 1914.
- [7] G. Mic, *Annalen der Physik*, vol. 25, p. 371, 1908.
- [8] P. Debye, *Annalen der Physik*, vol. 30, p. 57, 1909.
- [9] A. N. Oraevsky, “Whispering-gallery waves,” *Quantum Electronics*, vol. 32, no. 5, pp. 377–400, 2002.
- [10] K. J. Vahala, “Optical microcavities,” *Nature*, vol. 424, no. 6950, pp. 839–846, 2003.
- [11] H. M. Nussenzweig, *Diffraction Effects in Semiclassical Scattering*, Cambridge University Press, 1992.
- [12] L. D. Landau and E. M. Lifshitz, *Quantum Mechanics. Nonrelativistic Theory*, Pergamon Press, London, UK, 1965.
- [13] V. de Alfaro and T. Regge, *Potential Scattering*, North-Holland, Amsterdam, The Netherlands, 1965.
- [14] H. M. Nussenzweig, *Causality and Dispersion Relations*, Academic Press, 1972.
- [15] Y. Décanini and A. Folacci, “Resonant magnetic vortices,” *Physical Review A*, vol. 67, Article ID 042704, 2003.
- [16] M. Abramowitz and I. E. Stegun, *Handbook of Mathematical Functions*, Dover Publications, New York, NY, USA, 1965.
- [17] A. I. Baz, Y. B. Zeldovich, and A. M. Perelomov, *Scattering, Reactions and Decays in the Nonrelativistic Quantum Mechanics*, Israel Program for Scientific Translations, Jerusalem, Israel, 1969.
- [18] A. Y. Voronin, P. Froelich, and B. Zygelman, “Interaction of ultracold antihydrogen with a conducting wall,” *Physical Review A*, vol. 72, no. 6, Article ID 062903, 2005.
- [19] A. Y. Voronin, P. Froelich, and V. V. Nesvizhevsky, “Gravitational quantum states of Antihydrogen,” *Physical Review A—Atomic, Molecular, and Optical Physics*, vol. 83, no. 3, Article ID 032903, 2011.

Review Article

Precision Measurement of the Position-Space Wave Functions of Gravitationally Bound Ultracold Neutrons

Y. Kamiya,¹ G. Ichikawa,² and S. Komamiya¹

¹ Department of Physics, Graduate School of Science, and International Center for Elementary Particle Physics, The University of Tokyo, Tokyo 113-0033, Japan

² Department of Physics, Nagoya University, Nagoya 464-8601, Japan

Correspondence should be addressed to Y. Kamiya; kamiya@icepp.s.u-tokyo.ac.jp

Received 12 June 2014; Accepted 26 August 2014; Published 10 September 2014

Academic Editor: Valery V. Nesvizhevsky

Copyright © 2014 Y. Kamiya et al. This is an open access article distributed under the Creative Commons Attribution License, which permits unrestricted use, distribution, and reproduction in any medium, provided the original work is properly cited. The publication of this article was funded by SCOAP³.

Gravity is the most familiar force at our natural length scale. However, it is still exotic from the view point of particle physics. The first experimental study of quantum effects under gravity was performed using a cold neutron beam in 1975. Following this, an investigation of gravitationally bound quantum states using ultracold neutrons was started in 2002. This quantum bound system is now well understood, and one can use it as a tunable tool to probe gravity. In this paper, we review a recent measurement of position-space wave functions of such gravitationally bound states and discuss issues related to this analysis, such as neutron loss models in a thin neutron guide, the formulation of phase space quantum mechanics, and UCN position sensitive detectors. The quantum modulation of neutron bound states measured in this experiment shows good agreement with the prediction from quantum mechanics.

1. Introduction

Phenomena due to the gravitational field have been well understood at the macroscopic scales. However, there are only a few cases of experiments at microscopic scales, due to gravity's extreme weakness when compared to the other forces, such as electromagnetic and nuclear forces.

Even though quantum mechanics was established in the early 1900s, the first experiment to investigate a quantum effect under gravity was reported in 1975 by the group of Colella [1], where a neutron interference pattern induced by a gravitational potential was observed. The major systematic uncertainty was attributed to a bending effect of an interferometer when one rotates the system to manipulate a relative quantum phase difference between two neutron paths. A subsequent series of experiments were carried out with careful studies of systematic effects by measuring the bending effect using X-rays and considering the Sagnac effect [2] due to the rotation of the Earth [3, 4]. The latest attempt was performed using normal-symmetric and skew-symmetric interferometers and a two-wavelength difference

measurement method. The agreement with theoretical calculation is at the 1% level [5].

Another approach to observe quantum effects under gravity was carried out by the group of Nesvizhevsky [6, 7]. In this experiment, one measured a transmission of ultracold neutrons (UCNs) through a vertically thin neutron guide in the terrestrial gravitational field as a function of the slit thickness and showed the evidence of quantum bound states in the gravitational potential by analyzing the minimum height of a guide through which UCN can be transmitted. In a later detailed analysis, the characteristic sizes of position-space wave functions for the first and second quantum states were evaluated with an uncertainty of around 10% [8]. The major systematic uncertainty in this evaluation came from the difficulty in modeling the rough surface of a scatterer used on the ceiling of the guide, which causes some deformation of the wave functions. To minimize the effects of the deformation, a "differential method" was designed, in which one directly measures the wave functions using a position sensitive detector. In this method, a neutron guide of moderate height can be used and the deforming effect

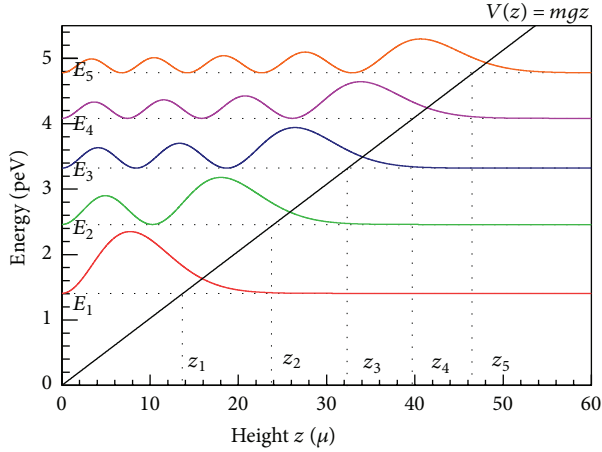


FIGURE 1: Probability distributions of gravitationally bound states of neutrons for the first five states [35]. Horizontal lines indicate eigenenergies E_n and vertical lines show the classical turning points z_n for each state.

was kept rather small compared to the previous “integrated method.” The first attempt of the differential method was reported in [8], where a plastic nuclear track detector (CR39) with a uranium coating [9] was used as the detector.

These quantum systems, in which the UCN bounces on a smooth floor, are expressed by the time-independent Schrödinger equation

$$\left\{ -\frac{\hbar^2}{2m} \frac{d^2}{dz^2} + V(z) \right\} \psi_n(z) = E_n \psi_n(z) \quad (1)$$

with the linear potential

$$V(z) = \begin{cases} mgz, & z \geq 0, \\ \infty, & z \leq 0, \end{cases} \quad (2)$$

where ψ_n and E_n are the eigenfunctions and eigenenergies, \hbar is the reduced Planck constant, m is the neutron mass, and g is the standard gravitational acceleration. Equation (1) can be rewritten in dimensionless form as

$$\left(\frac{d^2}{d\xi_n^2} - \xi_n \right) \psi_n(\xi_n) = 0, \quad (3)$$

where $\xi_n \equiv z/z_0 - E_n/E_0$ and the characteristic length and energy are given by

$$\begin{aligned} z_0 &= \left(\frac{\hbar^2}{2m^2 g} \right)^{1/3} \sim 6 \mu\text{m}, \\ E_0 &= \left(\frac{mg^2 \hbar^2}{2} \right)^{1/3} \sim 0.6 \text{ peV}. \end{aligned} \quad (4)$$

This is the Airy equation and solutions are described by Airy special functions, $\text{Ai}(\xi_n)$ and $\text{Bi}(\xi_n)$. Calculated probability distributions for the first five states are illustrated in Figure 1. Note that $\xi_n = 0$, where $z_n \equiv z_0 E_n/E_0$, are the classical

turning points of a classical bouncing ball, which are denoted in the cross points of each eigenenergy and the potential line of mgz in Figure 1.

This system is a suitable device with which to test the inverse square law of standard Newtonian gravity and to search for new gravity-like short-range interactions around these scales. The first limit to a non-Newtonian force with a Yukawa-type interaction potential using this microscopic system was reported in [10]. The limits for a CP-violating Yukawa-type potential were shown in [11, 12]. Several experimental schemes have been proposed to improve the sensitivity to such hypothetical new physics. One idea to achieve a better resolution on the measurement of the characteristic length is to utilize a convex reflection mirror to magnify the neutron distributions [13, 14]. In this review, we discuss an experiment using this scheme to precisely measure the UCN position-space wave functions, performed by the group of Komamiya of the University of Tokyo [15]. Experiments exploiting other ideas for measuring the energy scale, that is, the energy differences between quantum states, are proposed by observing resonance transitions induced by a magnetic field [16–19] and mechanical vibrations [20]. These projects are called GRANIT [21] and qBounce, respectively. The first measurement of the resonance transition from the ground to the third state was reported by the group of Abele in [22]. Recently, a new limit for the CP-violating Yukawa-type potential using the resonance method was reported in [23]. It also shows a limit for the chameleon field [24–26], a dark energy candidate.

2. Precision Measurement and Issues Related to This Analysis

The precision measurement with a convex magnification mirror [15] was performed using a UCN source provided at ILL (Institut Laue-Langevin) [27]. The velocity distribution was measured by a TOF method and is well characterized by a Gaussian distribution with mean of 9.4 m/s and standard deviation of 2.8 m/s. Figure 2(a) shows a schematic drawing of the experiment. The entire system was mounted on an antivibration table and magnetically shielded by a Permalloy sheet. The main components can be separated into three parts: a vertically thin collimating guide, a magnification mirror (rod), and a pixelated position sensitive detector. The layout of these components is shown in Figure 2(b).

2.1. Collimating Guide. The guide settles gravitationally bound quantum states. To clearly distinguish each quantum state, which has energy differences of order of $\Delta E \sim 1$ peV, a resolving time of $\Delta t \sim \hbar/\Delta E \sim 1$ msec is required. Considering that the horizontal velocities of UCNs which we use are less than 15 m/s, the collimating guide was designed to have a sufficient length (192 mm in our setup) to form each quantum state. The bottom mirror is made of polished glass with roughness of R_a (arithmetic average) = $0.03 \mu\text{m}$. The ceiling scatterer is a Gd-Ti-Zr alloy (54/35/11) deposited on glass, with a Fermi potential tuned to be nearly zero and roughness of $R_a = 0.4 \mu\text{m}$ [28], which scatters out neutrons

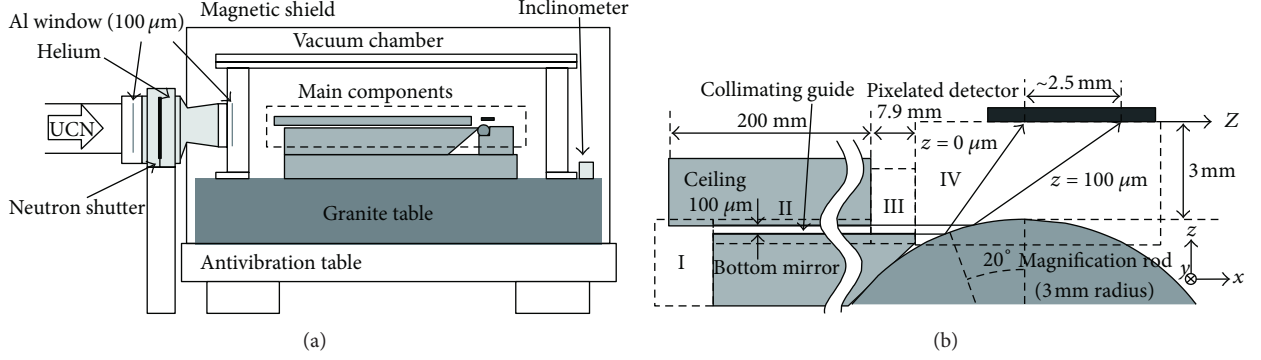


FIGURE 2: Schematic drawing of the precision measurement experiment using a convex magnification mirror [15]. (a) is an overview of the system and (b) shows the geometry of the main components.

in the higher states. The guide selects lower states with appropriate populations to improve the contrast of the quantum spatial modulation. (The eigenfunctions modulate somewhat coherently, especially around the lower region, except for the ground state, as seen in Figure 1. To improve the contrast of the quantum modulation, a method using a negative step of several tens of μm , which transfers neutrons from the ground state to higher states, was considered in [9]. Results were reported in [29–31].) The neutron loss models for the scatterer or rough surface have been discussed in detail in [32–34], and they are still interesting issues not only for UCN guiding applications but also for storage experiments such as neutron EDM measurements. In the experiment reviewed in this paper, empirical models of the loss rates are adopted [15]. The loss rate by the scatterer, Γ_n , is assumed to be proportional to the probability of finding neutron in the roughness region and is given by

$$\Gamma_n = \gamma \int_{h-2\delta}^h |\tilde{\psi}_n|^2 dz, \quad (5)$$

where γ is a scaling constant, estimated from data to be $9.5_{-0.9}^{+0.7} \times 10^4 \text{ s}^{-1}$, h is the height of the guide ($100 \mu\text{m}$), δ is the roughness of the scatterer ($0.4 \mu\text{m}$), and $\tilde{\psi}_n$ are deformed wave functions in the guide. Neutron losses at the bottom mirror due to absorption, nonspecular reflection, upscattering, and other processes are modeled empirically as

$$B_n = \beta \frac{g}{2\sqrt{2}} \sqrt{\frac{m}{\tilde{E}_n}}, \quad (6)$$

in which the loss rate is assumed to be proportional to the classical bouncing number per unit time, $g/2\tilde{v}_{z,n,\text{max}}$, where β is a scaling constant (estimated to be $0.38_{-0.03}^{+0.04}$), $\tilde{v}_{z,n,\text{max}} \equiv \sqrt{2\tilde{E}_n}/m$ is the maximum vertical velocity of a neutron in the n th state, and \tilde{E}_n is the eigenenergy of the deformed wave functions. The transmissivity of the guide for each state can be written as

$$\tilde{p}_n \propto \left\langle \exp \left[-\frac{l}{v_x} (\Gamma_n + B_n) \right] \right\rangle_{v_x}, \quad (7)$$

where $\langle \dots \rangle_{v_x}$ indicate the average over the neutron horizontal velocities. By applying a diabatic transition from region II to III, the population distribution (a probability in [15]) of neutrons for each state at the end of region III is estimated as in Figure 3(a).

2.2. Magnification Mirror. A Ni coated cylindrical rod is used as a magnifying convex mirror. Its radius is 3 mm and it is placed to have a grazing angle of 20 deg. for horizontally moving neutrons at the bottom floor level ($z = 0$). Figure 4 shows the magnification power as a function of the height [35]. It gives about 20 times magnification around the lower region of $z \sim 20 \mu\text{m}$. Before depositing the Ni coating, the cylinder was polished at the Research Center for Ultra-Precision Science and Technology, Osaka University. The roughness of the rod after the depositing was measured to be $R_a = 1.9 \text{ nm}$, two orders of magnitude smaller than the neutron wavelength.

To calculate the detected position distribution on the detector surface, the wave function at the end of the bottom floor is reexpressed by the Wigner phase space distribution [36, 37]:

$$W(z, p_z) \equiv \frac{1}{2\pi\hbar} \int_{-\infty}^{\infty} \delta\eta e^{-i(\hbar)p_z\eta} \left\langle z + \frac{1}{2}\eta | \hat{\rho} | z - \frac{1}{2}\eta \right\rangle, \quad (8)$$

where p_z is the momentum and $\hat{\rho}$ is a density operator. The Wigner distribution is known as a phase space formulation of quantum mechanics and is widely used for quantum optics, for example, in the study of decoherence [38]. As an application to massive particles, one can find a paper which shows a phase space tomography of the Wigner distribution for a coherent atomic beam in a double-slit experiment [39]. Figure 3(b) shows the Wigner distribution constructed from the estimated populations in our experiment [15]. The time evolution of the Wigner distribution is calculated by the evolution of the density operator described by the Liouville-von Neumann equation

$$\frac{\partial \hat{\rho}}{\partial t} = -\frac{i}{\hbar} [\hat{H}, \hat{\rho}], \quad (9)$$

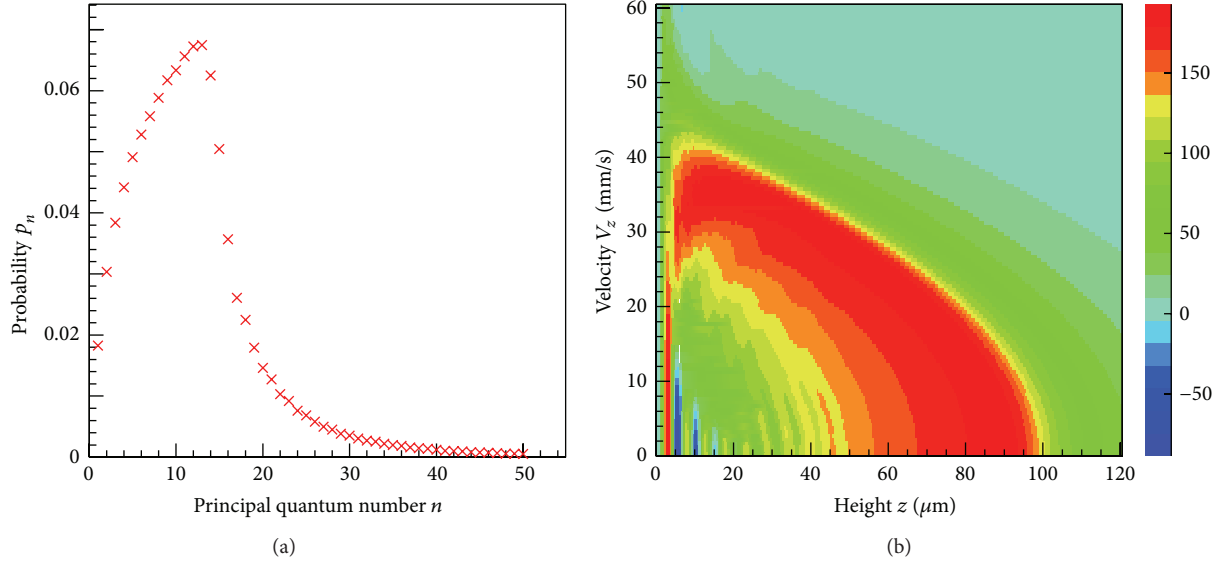


FIGURE 3: (a) is an estimated population distribution (probability distribution of the guide transmission) at the end of region III and (b) shows the corresponding Wigner phase space distribution [15].

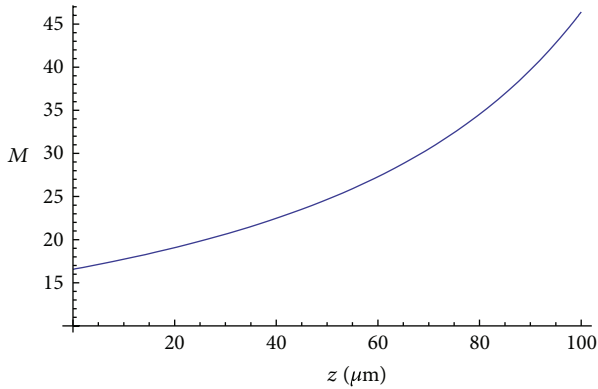


FIGURE 4: Magnification power M of the cylindrical rod as a function of the height z [35]. It is about 20 times magnification around the lower region.

where

$$\widehat{H} = \frac{\widehat{p}_z^2}{2m} + V(\bar{z}). \quad (10)$$

By evaluating the kinetic part as

$$T = -\frac{p_z}{m} \frac{\partial}{\partial z} W(z, p_z) \quad (11)$$

and the potential part as

$$\sum_{l=0}^{\infty} U_l = \sum_{l=0}^{\infty} \frac{(-1)^l (\hbar/2)^{2l}}{(2l+1)!} \frac{d^{2l+1} V(z)}{dz^{2l+1}} \frac{\partial^{2l+1}}{\partial p_z^{2l+1}} W(z, p_z), \quad (12)$$

one can obtain the quantum Liouville equation for the Wigner distribution [40]

$$\left(\frac{\partial}{\partial t} + \frac{p_z}{m} \frac{\partial}{\partial z} - \frac{dV(z)}{dz} \frac{\partial}{\partial p_z} \right) W(z, p_z) = \sum_{l=1}^{\infty} U_l. \quad (13)$$

In the case of $V(z) = mgz$, the right-hand side of the equation vanishes and it becomes the classical Liouville equation. Therefore, in region IV, one can treat the evolution of each phase point of the Wigner distribution as a classical path under gravity. Figure 5 shows the measured data and the best theoretical estimation using this model. The corresponding P value is 0.715, and the experimental data support the quantum features described by the phase space formulation using the Wigner distribution [15].

2.3. Position Sensitive Detector for UCNs. A back-thinned CCD (HAMAMATSU S7030-1008) with thin Ti- ^{10}B -Ti layers is used for the position sensitive detector in the experiment [15]. Its pixel size is $24 \mu\text{m} \times 24 \mu\text{m}$ and the thickness of the active volume is about $20 \mu\text{m}$. The ^{10}B layer converts neutrons into charged particles by the nuclear reaction $^{10}\text{B}(n, \alpha)^7\text{Li}$. The secondary particles are emitted in a nearly back-to-back configuration. One of them deposits its kinetic energy in the active area and creates a charge cluster, which typically spreads into nine pixels. The weighted center of the charge cluster is a good estimation of the incident neutron position. The thicknesses of the layers are 20 nm and 200 nm for Ti and ^{10}B , respectively, and they are formed by evaporating directly on the CCD surface. The spatial resolution is measured to be $3.35 \pm 0.09 \mu\text{m}$ by evaluating the line spread function (LSF) (see Figure 6) using very cold neutron beams at ILL [35]. For the details of the evaluation scheme, see [14, 41]. A neutron converter of ^6Li using $^6\text{Li}(n, \alpha)^3\text{H}$ reaction was also investigated. It is concluded that the use of ^{10}B gives better spatial resolution [41].

Other detectors using a silicon pixel device, Timepix [42], with ^6LiF and ^{10}B converter were studied in [43]. Its pixel pitch is $55 \mu\text{m} \times 55 \mu\text{m}$ and the thickness of its silicon layer is about $300 \mu\text{m}$. The spatial resolution for the ^6LiF converter was evaluated by LSF to be $2.3 \mu\text{m}$, corresponding to about

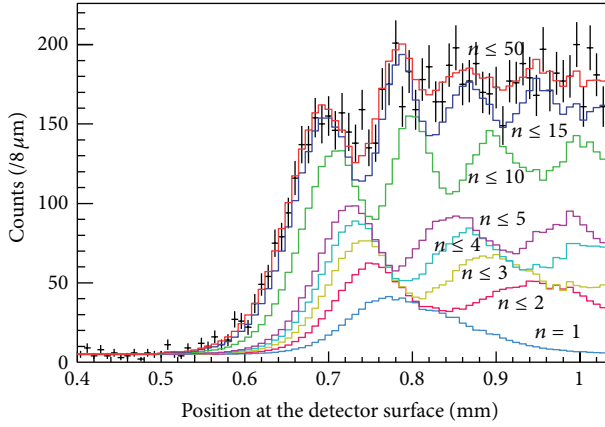


FIGURE 5: Black crosses show measured neutron position distribution [15]. Modulated distribution was clearly measured. The result shows good agreement with the quantum expectation calculated using phase space formalization by Wigner distribution (P value is 0.715). The best estimated line is shown by a red solid curve and the other lines indicate contributions of each state to the distribution. For definitions of fitting parameters, best fit values, systematic uncertainties, and the other details, see [15].

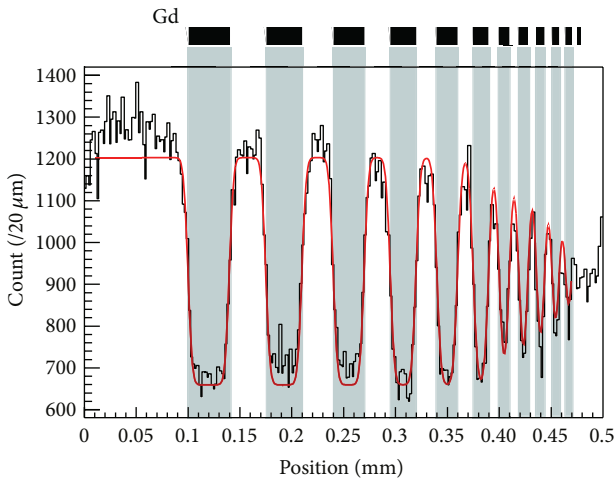


FIGURE 6: Fitting results of a Gd shadow pattern [35]. Spatial resolution is measured to be $3.35 \pm 0.09 \mu\text{m}$ by evaluating these line spread functions. For details of evaluation method, see [14, 41].

$5.3 \mu\text{m}$ in FWHM of the point spread function (PSF). The performance of the ^{10}B converter is estimated by Monte-Carlo simulations to be better than $3 \mu\text{m}$ in FWHM of the PSF.

Another detector concept of uranium coated plastic nuclear tracker (CR39) [9] was used in several experiments [8, 29–31, 44]. Usually two fission fragments are emitted from a thin ^{235}U coating, and one of the daughter nuclei makes a track of defects in the CR39. By chemical etching, the diameter of track points is increased up to $1 \mu\text{m}$, allowing us to scan these vertexes using an optical microscope. Position resolution is around $1 \mu\text{m}$ [9]. By carefully analyzing the

vertex shape, the spatial resolution can be improved to $0.7 \mu\text{m}$ [44].

3. Summary

The quantum system of a gravitationally bound neutron is one of the most suitable tools to investigate gravity or gravity-like hypothetical interactions around the scale of $10 \mu\text{m}$ in length or 1peV in energy. After establishing this research field by the pioneering work in observation of the quantum state [6], experimental schemes for precision measurements of these characteristic scales have developed rapidly, and nowadays one can establish limits for parameter spaces of new physics experimentally [10–12, 23]. Furthermore one can start discussing a phase space formulation of quantum physics for the gravitationally bound quantum state [15]. An experiment for a possible test of phase space formalization using spatial interference is under preparation.

Conflict of Interests

The authors declare that there is no conflict of interests regarding the publication of this paper.

Acknowledgments

The authors would like to thank Valery V. Nesvizhevsky (Institut Laue-Langevin), Hartmut Abele (Vienna University of Technology), William Snow (Indiana University), Peter Geltenbolt (Institut Laue-Langevin), and all participants in the GRANIT-2014 Workshop for interesting discussions and helpful suggestions. This material is based upon work supported by JSPS KAKENHI Grants no. 20340050 and no. 24340045 and Grant-in-Aid for JSPS Fellows no. 22.1661.

References

- [1] R. Colella, A. W. Overhauser, and S. A. Werner, “Observation of gravitationally induced quantum interference,” *Physical Review Letters*, vol. 34, no. 23, pp. 1472–1474, 1975.
- [2] J. J. Sakurai, “Comments on quantum-mechanical interference due to the Earth’s rotation,” *Physical Review D*, vol. 21, Article ID 2993, 1980.
- [3] J.-L. Staudenmann, S. A. Werner, R. Colella, and A. W. Overhauser, “Gravity and inertia in quantum mechanics,” *Physical Review A*, vol. 21, no. 5, pp. 1419–1438, 1980.
- [4] S. A. Werner, H. Kaiser, M. Arif, and R. Clothier, “Neutron interference induced by gravity: New results and interpretations,” *Physica B*, vol. 151, no. 1–2, pp. 22–35, 1988.
- [5] K. C. Littrell, B. E. Allman, and S. A. Werner, “Two-wavelength-difference measurement of gravitationally induced quantum interference phases,” *Physical Review A*, vol. 56, article 1767, 1997.
- [6] V. V. Nesvizhevsky, H. G. Börner, A. K. Petukhov et al., “Quantum states of neutrons in the Earth’s gravitational field,” *Nature*, vol. 415, no. 6869, pp. 297–299, 2002.
- [7] V. V. Nesvizhevsky, H. G. Börner, A. M. Gagarski et al., “Measurement of quantum states of neutrons in the Earth’s gravitational field,” *Physical Review D*, vol. 67, Article ID 102002, 2003.

- [8] V. V. Nesvizhevsky, A. K. Petukhov, H. G. Börner et al., “Study of the neutron quantum states in the gravity field,” *The European Physical Journal C*, vol. 40, no. 4, pp. 479–491, 2005.
- [9] V. V. Nesvizhevsky, H. Börner, A. M. Gagarski et al., “Search for quantum states of the neutron in a gravitational field: gravitational levels,” *Nuclear Instruments and Methods in Physics Research A*, vol. 440, no. 3, pp. 754–759, 2000.
- [10] V. V. Nesvizhevsky and K. V. Protasov, “Constraints on non-Newtonian gravity from the experiment on neutron quantum states in the earth’s gravitational field,” *Classical and Quantum Gravity*, vol. 21, no. 19, pp. 4557–4566, 2004.
- [11] S. Baeßler, V. V. Nesvizhevsky, K. V. Protasov, and A. Y. Voronin, “A new constraint for the coupling of axion-like particles to matter via ultra-cold neutron gravitational experiments,” *Physical Review D*, vol. 75, Article ID 075006, 2007.
- [12] S. Baeßler, V. V. Nesvizhevsky, G. Pignol et al., “Constraints on spin-dependent short-range interactions using gravitational quantum levels of ultracold neutrons,” *Nuclear Instruments and Methods in Physics Research Section A: Accelerators, Spectrometers, Detectors and Associated Equipment*, vol. 611, pp. 149–152, 2009.
- [13] V. V. Nesvizhevsky, Preprint ILL 96NE14T, 1994.
- [14] T. Sanuki, S. Komamiya, S. Kawasaki, and S. Sonoda, “Proposal for measuring the quantum states of neutrons in the gravitational field with a CCD-based pixel sensor,” *Nuclear Instruments and Methods in Physics Research A*, vol. 600, pp. 657–660, 2009.
- [15] G. Ichikawa, S. Komamiya, Y. Kamiya et al., “Observation of the spatial distribution of gravitationally bound quantum states of ultracold neutrons and its derivation using the wigner function,” *Physical Review Letters*, vol. 112, Article ID 071101, 2014.
- [16] P. Schmidt-Wellenburg, K. H. Andersena, P. Courtois et al., “Ultracold-neutron infrastructure for the gravitational spectrometer GRANIT,” *Nuclear Instruments and Methods in Physics Research Section A*, vol. 611, no. 2-3, pp. 267–271, 2009.
- [17] M. Kreuz, V. V. Nesvizhevsky, P. Schmidt-Wellenburg et al., “A method to measure the resonance transitions between the gravitationally bound quantum states of neutrons in the GRANIT spectrometer,” *Nuclear Instruments and Methods in Physics Research Section A: Accelerators, Spectrometers, Detectors and Associated Equipment*, vol. 611, no. 2-3, pp. 326–330, 2009.
- [18] S. Baeßler, M. Beau, GRANIT Collaboration et al., “The GRANIT spectrometer,” *Comptes Rendus Physique*, vol. 12, pp. 707–728, 2011.
- [19] V. V. Nesvizhevsky, “Gravitational quantum states of neutrons and the new granit spectrometer,” *Modern Physics Letters A*, vol. 27, Article ID 1230006, 2012.
- [20] H. Abele, T. Jenke, H. Leeb, and J. Schmiedmayer, “Ramsey’s method of separated oscillating fields and its application to gravitationally induced quantum phaseshifts,” *Physical Review D*, vol. 81, Article ID 065019, 2010.
- [21] D. Roulier, F. Vezzu, S. Baessler et al., “Status of the GRANIT facility,” *Advances in High Energy Physics*, vol. 2014, Article ID 730437, 2014.
- [22] T. Jenke, P. Geltenbort, H. Lemmel, and H. Abele, “Realization of a gravity-resonance-spectroscopy technique,” *Nature Physics*, vol. 7, no. 6, pp. 468–472, 2011.
- [23] T. Jenke, G. Cronenberg, J. Burgdorfer et al., “Gravity resonance spectroscopy constrains dark energy and dark matter scenarios,” *Physical Review Letters*, vol. 112, Article ID 151105, 2014.
- [24] J. Khoury and A. Weltman, “Chameleon fields: awaiting surprises for tests of gravity in space,” *Physical Review Letters*, vol. 93, no. 17, Article ID 171104, 2004.
- [25] D. F. Mota and D. J. A. Shaw, “Strongly coupled chameleon fields: new horizons in scalar field theory,” *Physical Review Letters*, vol. 97, Article ID 151102, 2006.
- [26] J. Khoury, “Chameleon field theories,” *Classical and Quantum Gravity*, vol. 30, Article ID 214004, 2013.
- [27] A. Steyeri, H. Nagel, F. X. Schreiber et al., “A new source of cold and ultracold neutrons,” *Physics Letters A*, vol. 116, pp. 347–352, 1986.
- [28] Y. Kamiya, S. Kawasaki, G. Ichikawa et al., “Development of the CCD-based Detector with Fine Spatial Resolution,” KURRI Progress Report COI-1, 2008, <http://www.rri.kyoto-u.ac.jp/PUB/report/PR/ProgRep2008/COI.pdf>.
- [29] V. V. Nesvizhevsky, H. G. Borner, A. K. Retoukhov et al., “Quantum falling in the gravitational field,” ILL Annual Report, Institut Laue-Langevin, 2004, <http://www.ill.eu/quick-links/publications/annual-report/>.
- [30] H. Abele, T. Jenke, D. Stadler, and P. Geltenbort, “QuBounce: the dynamics of ultra-cold neutrons falling in the gravity potential of the Earth,” *Nuclear Physics A*, vol. 827, pp. 593c–595c, 2009.
- [31] T. Jenke, D. Stadler, H. Abele, and P. Geltenbort, “Q-BOUNCE—experiments with quantum bouncing ultracold neutrons,” *Nuclear Instruments and Methods in Physics Research A*, vol. 611, no. 2-3, pp. 318–321, 2009.
- [32] A. E. Meyerovich and V. V. Nesvizhevsky, “Gravitational quantum states of neutrons in a rough waveguide,” *Physical Review A*, vol. 73, Article ID 063616, 2006.
- [33] A. Y. Voronin, H. Abele, S. Baeßler et al., “Quantum motion of a neutron in a waveguide in the gravitational field,” *Physical Review D*, vol. 73, Article ID 044029, 2006.
- [34] A. Westphal, H. Abele, S. Baeßler, V. V. Nesvizhevsky, K. V. Protasov, and A. Y. Voronin, “A quantum mechanical description of the experiment on the observation of gravitationally bound states,” *The European Physical Journal C*, vol. 51, pp. 367–375, 2007.
- [35] G. Ichikawa, *Observation of gravitationally bound quantum states of Ul-tracold neutrons using a pixelated detector [PhD. dissertation]*, The University of Tokyo, 2013.
- [36] E. Wigner, “On the quantum correction for thermodynamic equilibrium,” *Physical Review*, vol. 40, no. 5, pp. 749–759, 1932.
- [37] M. Hillery, R. F. O’Connell, M. O. Scully, and E. P. Wigner, “Distribution functions in physics: fundamentals,” *Physics Reports*, vol. 106, no. 3, pp. 121–167, 1984.
- [38] L. Mandel and E. Wolf, *Optical Coherence and Quantum Optics*, Cambridge University Press, 1995.
- [39] C. Kurtsiefer, T. Pfau, and J. Mlynek, “Measurement of the wigner function of an ensemble of helium atoms,” *Nature*, vol. 386, no. 6621, pp. 150–153, 1997.
- [40] W. P. Schleich, *Quantum Optics in Phase Space*, Wiley-VCH, 2001.
- [41] S. Kawasaki, G. Ichikawa, M. Hino et al., “Development of a pixel detector for ultra-cold neutrons,” *Nuclear Instruments and Methods in Physics Research A*, vol. 615, no. 1, pp. 42–47, 2010.
- [42] X. Llopart, R. Ballabriga, M. Campbell, L. Tlustos, and W. Wong, “Timepix, a 65 k programmable pixel readout chip for arrival time, energy and/or photon counting measurements,” *Nuclear Instruments and Methods in Physics Research A: Accelerators, Spectrometers, Detectors and Associated Equipment*, vol. 581, pp. 485–494, 2007.

- [43] J. Jakubek, P. Schmidt-Wellenburg, P. Geltenbort et al., "A coated pixel device TimePix with micron spatial resolution for UCN detection," *Nuclear Instruments and Methods in Physics Research A*, vol. 600, no. 3, pp. 651–656, 2009.
- [44] T. Jenke, G. Cronenberg, H. Filter et al., "Ultracold neutron detectors based on ^{10}B converters used in the qBounce experiments," *Nuclear Instruments and Methods in Physics Research Section A*, vol. 732, pp. 1–8, 2013.

Research Article

Error-Disturbance Uncertainty Relations in Neutron-Spin Measurements

Stephan Sponar, Georg Sulyok, Jaqueline Erhart, and Yuji Hasegawa

Atominstytut, Vienna University of Technology, Stadionallee 2, 1020 Vienna, Austria

Correspondence should be addressed to Stephan Sponar; sponar@ati.ac.at

Received 2 June 2014; Accepted 28 July 2014; Published 8 September 2014

Academic Editor: Guillaume Pignol

Copyright © 2014 Stephan Sponar et al. This is an open access article distributed under the Creative Commons Attribution License, which permits unrestricted use, distribution, and reproduction in any medium, provided the original work is properly cited. The publication of this article was funded by SCOAP³.

In his seminal paper, which was published in 1927, Heisenberg originally introduced a relation between the precision of a measurement and the disturbance it induces onto another measurement. Here, we report a neutron-optical experiment that records the error of a spin-component measurement as well as the disturbance caused on a measurement of another spin-component to test error-disturbance uncertainty relations (EDRs). We demonstrate that Heisenberg's original EDR is violated and the Ozawa and Branciard EDRs are valid in a wide range of experimental parameters.

1. Introduction

The uncertainty principle represents, without any doubt, one of the most important cornerstones of the Copenhagen interpretation of quantum theory. In his celebrated paper from 1927 [1], Heisenberg gives at least two distinct statements about the limitations on preparation and measurement of physical systems: (i) incompatible observables cannot be measured with arbitrary accuracy: a measurement of one of these observables disturbs the other one accordingly, and vice versa; (ii) it is impossible to prepare a system such that a pair of noncommuting (incompatible) observables are arbitrarily well defined. In [1], the observables are represented by position and momentum.

In his original paper [1], Heisenberg proposed a reciprocal relation for measurement *error* and *disturbance* by the famous γ -ray microscope thought experiment: “At the instant when the position is determined—therefore, at the moment when the photon is scattered by the electron—the electron undergoes a discontinuous change in momentum. This change is the greater the smaller the wavelength of the light employed—that is, the more exact the determination of the position. . .” [1]. Heisenberg follows Einstein's realistic view, that is, to base a new physical theory only on observable quantities (*elements of reality*), arguing that terms like velocity or position make

no sense without defining an appropriate apparatus for a measurement. By solely considering the Compton effect, Heisenberg gives a rather heuristic estimate for the product of the inaccuracy (error) of a position measurement p_1 and the disturbance q_1 induced on the particles momentum, denoted by

$$p_1 q_1 \sim h. \quad (1)$$

According to (1), it can be referred to as a *measurement uncertainty* (i) or as an error-disturbance uncertainty relation (EDR).

Heisenberg's original formulation [1, 2] can be read in modern treatment as $\epsilon(Q)\eta(P) \geq \hbar/2$, for error $\epsilon(Q)$ of a measurement of the position observable Q and disturbance $\eta(P)$ of the momentum observable P induced by the position measurement. However, most modern textbooks introduce the uncertainty relation in terms of a *preparation uncertainty* (ii) relation denoted by

$$\Delta(Q)\Delta(P) \geq \hbar/2. \quad (2)$$

Equation (2) was proved by Kennard in 1927 [3] for the standard deviations $\Delta(Q)$ and $\Delta(P)$ of the position observable Q and the momentum observable P , given by $\Delta(X) = \sqrt{\langle X^2 \rangle - \langle X \rangle^2}$. But this is a different physical situation: here

statistical distributions of not a joint but a single measurement of either Q or P are considered. Kennard's relation addresses an intrinsic uncertainty which every quantum system must possess, independent of whether it is measured or not. The unavoidable recoil caused by the measuring device is ignored here. Later Robertson generalized Kennard's relation between standard deviations to arbitrary pairs of observables A and B :

$$\Delta(A) \Delta(B) \geq \frac{1}{2} |\langle \psi | [A, B] | \psi \rangle|. \quad (3)$$

Robertson's relation (3) has been confirmed by many different experiments [4–6] and is uncontroversial.

A corresponding generalized form of Heisenberg's original error-disturbance uncertainty relation would read

$$\epsilon(A) \eta(B) \geq \frac{1}{2} |\langle \psi | [A, B] | \psi \rangle|. \quad (4)$$

However, certain measurements do not obey (4) [7–9], proving (4) to be formally incorrect.

In 2003, Ozawa introduced the correct form of a generalized error-disturbance uncertainty relation based on rigorous theoretical treatments of quantum measurements:

$$\epsilon(A) \eta(B) + \epsilon(A) \Delta(B) + \Delta(A) \eta(B) \geq \frac{1}{2} |\langle \psi | [A, B] | \psi \rangle|, \quad (5)$$

where $\epsilon(A)$ denotes the root-mean-square (r.m.s.) error of an arbitrary measurement for an observable A , $\eta(B)$ is the r.m.s. disturbance on another observable B induced by the measurement, and $\Delta(A)$ and $\Delta(B)$ are the standard deviations of A and B in the state $|\psi\rangle$ before the measurement. Ozawa's inequality (5) was tested experimentally with neutronic [10, 11] and photonic [12–14] systems.

Though universally valid, Ozawa's relations (5) are not optimal. Recently, Branciard [15] has revised Ozawa's EDR, resulting in a tight EDR, describing the now optimal trade-off relation between error $\epsilon(A)$ and disturbance $\eta(B)$:

$$\begin{aligned} \epsilon(A)^2 \Delta(B)^2 + \Delta(A)^2 \eta(B)^2 \\ + 2 \sqrt{\Delta(A)^2 \Delta(B)^2 - C_{AB}^2} \epsilon(A) \eta(B) \geq C_{AB}^2, \end{aligned} \quad (6)$$

with $C_{AB} = 1/2 |\langle \psi | [A, B] | \psi \rangle|$. Experimental demonstrations of (6) using photons are reported in [16, 17].

2. Materials and Methods

In our experiment the error-disturbance uncertainty relations, as defined in (5) and (6), are tested via a successive measurement for spin observables A and B . The experimental scheme is depicted in Figure 1. The observables A and B are set as the x and y components of the neutron 1/2 spin. (For simplicity, $\hbar/2$ is omitted for each spin component.) The error $\epsilon(A)$ and the disturbance $\eta(B)$ are defined for a joint measurement apparatus, so that apparatus **A1** measures the observable $A = \sigma_x$ with error $\epsilon(A)$ and disturbs the

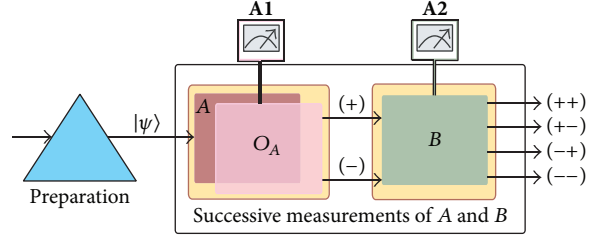


FIGURE 1: A successive measurement scheme of observables A and B exploited for the demonstration of the error-disturbance uncertainty relation. After state preparation (blue) apparatus **A1** carries out a projective measurement of O_A instead of A (light red), thereby disturbing observable B which is detected by apparatus **A2** (green), error $\epsilon(A)$ and disturbance $\eta(B)$ are quantitatively determined by the four possible outcomes denoted by $(++)$, $(+-)$, $(-+)$, and $(--)$.

observable $B = \sigma_y$, thereby with disturbance $\eta(B)$ during the measurement (here σ_x and σ_y denote the Pauli matrices). Finally apparatus **A2** measures $B = \sigma_y$. To control the error $\epsilon(A)$ and the disturbance $\eta(B)$, apparatus **A1** is designed to actually carry out not the maximally disturbing projective measurement $A = \sigma_x$, but the projective measurement along a distinct axis $\vec{o}_a(\theta, \phi)$ denoted by $O_A = \vec{o}_a(\theta, \phi) \cdot \vec{\sigma}$, where $\vec{\sigma} = (\sigma_x, \sigma_y, \sigma_z)^T$. Here θ, ϕ denote polar and azimuthal angle of the measurement direction \vec{o}_a and are experimentally controlled detuning parameters, so that $\epsilon(A)$ and $\eta(B)$ are determined as a function of ϕ and θ . A schematic illustration of the experimental apparatus for successive neutron-spin measurements is given in Figure 2.

For (5) and (6), error $\epsilon(A)$ and disturbance $\eta(B)$ are defined via an indirect measurement model for an apparatus **A** measuring an observable A of an object system **S** as

$$\epsilon(A) = \left\| \left(U^\dagger (1 \otimes M) U - A \otimes 1 \right) |\psi\rangle |\xi\rangle \right\|, \quad (7a)$$

$$\eta(B) = \left\| \left(U^\dagger (B \otimes 1) U - B \otimes 1 \right) |\psi\rangle |\xi\rangle \right\|, \quad (7b)$$

where $|\psi\rangle$ is the state before the measurement of system **S**, which is described by a Hilbert space \mathcal{H}^{obj} , and $|\xi\rangle$ and M are the initial state of the probe system **P** (in Hilbert space \mathcal{H}^{pro}) and an observable M , referred to as *meter observable*, of **P** which accounts for the meter of the apparatus. A unitary operator U on $\mathcal{H}^{\text{obj}} \otimes \mathcal{H}^{\text{pro}}$ describes the time evolution of the composite system **S** + **P** during the measurement interaction. Here the Euclidean norm is used where the norm of a state vector in Hilbert space $X|\psi\rangle$ is given by the square root of its inner product: $\|X|\psi\rangle\| = \langle \psi | X^\dagger X | \psi \rangle^{1/2}$. A schematic illustration of a measurement apparatus **A** is given in Figure 3.

A nondegenerate meter observable M has a spectral decomposition $M = \sum_m m |m\rangle \langle m|$, where m varies over eigenvalues of M , and then the apparatus **A** has a family $\{M_m\}$ of operators, called the *measurement operators*, acting on \mathcal{H}^{obj} and defined as $M_m = \langle m | U | \xi \rangle$. Hence, the error is given by $\epsilon(A)^2 = \sum_m \|M_m(m - A)|\psi\rangle\|^2$. If M_m are mutually orthogonal, projection operators sum and norm can be exchanged and the error can be written in compact form as

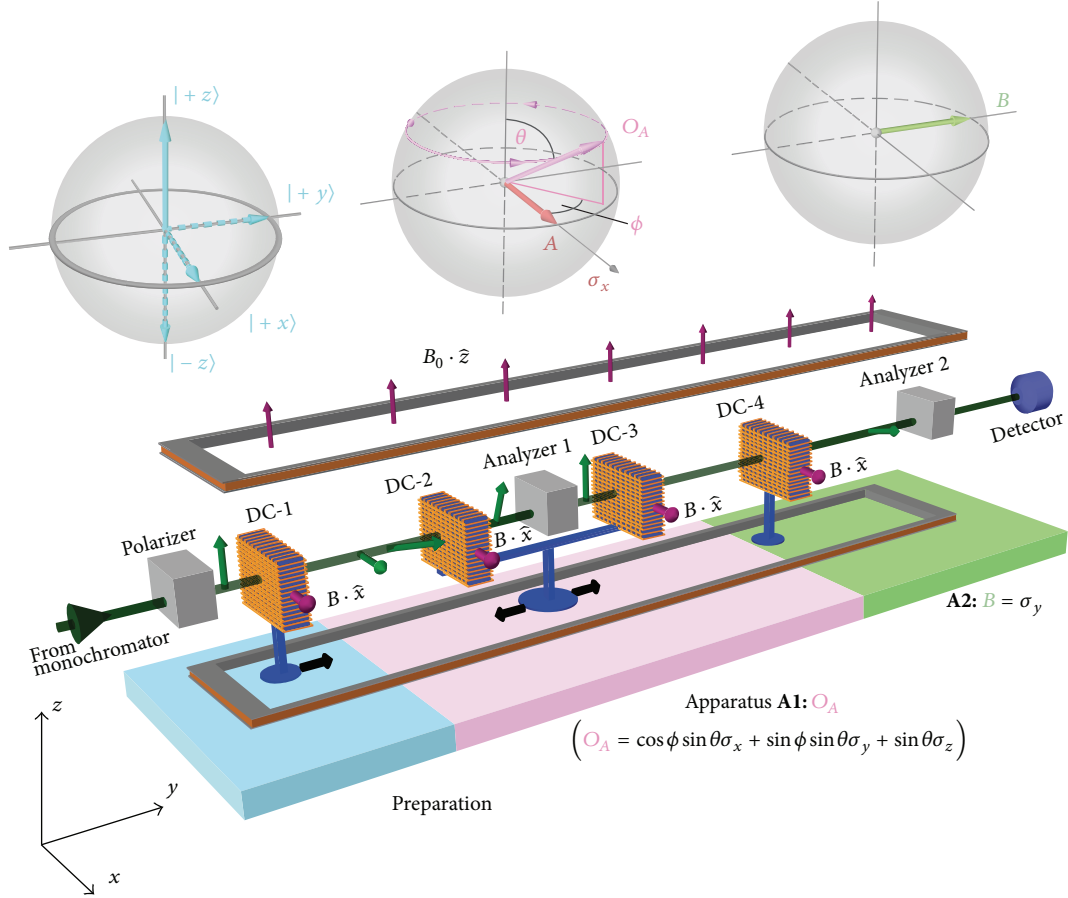


FIGURE 2: Neutron polarimetric setup for demonstration of the universally valid uncertainty relation for error and disturbance in neutron spin measurements. The setup is divided into three stages: state preparation (blue region), apparatus A1 carrying out the measurement of observable $O_A = \vec{o}_a(\theta, \phi) \cdot \vec{\sigma}$ (red region), and apparatus A2 performing the measurement of observable $B = \sigma_y$ (green region). All required terms of (5), that is, error $\epsilon(A)$ and disturbance $\eta(B)$ as well as the standard deviations $\Delta(A)$ and $\Delta(B)$, are determined from the expectation values of the successive measurement.

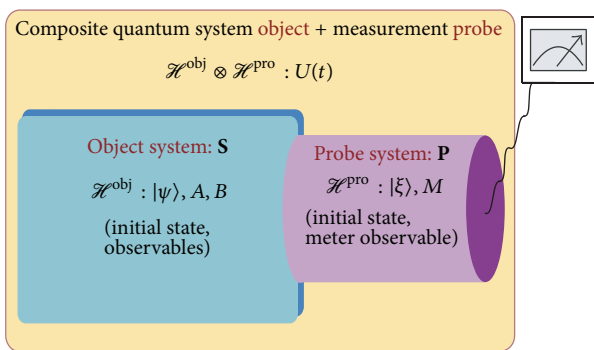


FIGURE 3: An indirect measurement model for apparatus A measuring an object system S, defined on Hilbert space \mathcal{H}^{obj} , is specified by a quadruple $(\mathcal{H}^{\text{pro}}, |\xi\rangle, U(t), M)$.

$\epsilon(A)^2 = \sum_m \|(O_A - A)|\psi\rangle\|^2$, where O_A is the *output operator* given as $O_A = \sum_m m M_m$. The disturbance can be written as $\eta(B)^2 = \sum_m \|[M_m, B]|\psi\rangle\|^2$. All these calculations are elaborated in detail in [18].

In our experiment, the measuring apparatus A1 is considered to carry out a projective spin measurement along a distinct axis $\vec{o}_a(\theta, \phi)$ denoted by $O_A = \vec{o}_a(\theta, \phi) \cdot \vec{\sigma} = M_{+1} - M_{-1}$ (where $M_{\pm 1} = 1/2(1 \pm \vec{o}_a(\theta, \phi) \cdot \vec{\sigma})$) instead of precisely $A = \sigma_x$. In order to detect the disturbance $\eta(B)$ on the observable B , induced by measuring O_A , apparatus A2 carries out the projective measurement of $B = \sigma_y$ in the state just after the first measurement. Though claimed to be experimentally inaccessible [19, 20], in the case of projection operators error $\epsilon(A)$ and disturbance $\eta(B)$ can be expressed as a sum of expectation values in three different states, applying the method proposed in [21]. Using the *modified output operators* of the apparatus A2 defined as $X_B = M_{+1} B M_{+1} + M_{-1} B M_{-1}$ and $X_B^{(2)} = M_{+1} B^2 M_{+1} + M_{-1} B^2 M_{-1}$, measurement error and disturbance are given by

$$\epsilon(A)^2 = 2 + \langle \psi | O_A | \psi \rangle + \langle \psi | A O_A A | \psi \rangle - \langle \psi | (A + 1) O_A (A + 1) | \psi \rangle, \quad (8a)$$

$$\eta(B)^2 = 2 + \langle \psi | X_B | \psi \rangle + \langle \psi | B X_B B | \psi \rangle - \langle \psi | (B + 1) X_B (B + 1) | \psi \rangle. \quad (8b)$$

The expectation values of O_A in a state $|\psi\rangle$ (see (8a) and (8b)), necessary for the determination of error $\epsilon(A)$, are derived from the intensities at the four possible output ports, depicted in Figure 4, denoted by I_{++} , I_{+-} , I_{-+} , and I_{--} . The expectation value is obtained from the following combination of count rates: $\langle\psi|O_A|\psi\rangle = (I_{++} + I_{+-} - I_{-+} - I_{--})/(I_{++} + I_{+-} + I_{-+} + I_{--})$, using intensities at the four possible output ports, indicating which projections have been carried out. As already discussed due to the prior measurement of O_A , the operator of apparatus **A2** is modified from B to X_B , with the corresponding expectation value expressed as $\langle\psi|X_B|\psi\rangle = (I_{++} + I_{-+} - I_{+-} - I_{--})/(I_{++} + I_{+-} + I_{-+} + I_{--})$, required to determine the disturbance $\eta(B)$. Consequently all expectation values necessary to determine error $\epsilon(A)$ and disturbance $\eta(B)$ can be derived from the intensities in the three input states $|\psi\rangle$, $A|\psi\rangle$, $(A + 1)|\psi\rangle$ and $|\psi\rangle$, $B|\psi\rangle$, $(B + 1)|\psi\rangle$, respectively.

These states are generated by spinor rotations within DC-1 and induced by the guide field, due to an appropriate coil position within the preparation section (blue) of the neutron-optical setup depicted in Figure 2. The projective measurement of O_A (apparatus **A1**, light red in Figure 2) consists of two sequential steps: first the initially prepared state is projected onto the eigenstates of O_A by DC-2, which rotates the respective spin component of $\vec{\sigma}_a$ belonging to O_A in $+z$ direction. Then, in order to complete the projective measurement the spin, which is pointing in $+z$ after the analyzer, has to be prepared in an eigenstate of O_A . This is achieved by proper positioning and magnetic field of DC-3 (thereby applying the same procedure as that for DC-1 in the initial state preparation). Finally the B measurement is performed (apparatus **A2**, green in Figure 2) utilizing DC-4 and the second analyzer. Unlike the O_A -measurement, subsequent preparation of the eigenstates of B is not necessary since the detector is insensitive to the spin state. For the measurement of the standard deviations of the observables A and B , which are also required to test Ozawa's relation (see (5)), the two measurement apparatuses are used individually.

3. Results and Discussion

The experiment was carried out at the polarimeter beam line of the tangential beam port of the research reactor facility TRIGA Mark II at the Atominstitut, Vienna University of Technology, where mainly fundamental aspects of quantum mechanics are investigated [22–25]. The experimental settings for initial state $|\psi\rangle = |\uparrow\rangle_z \equiv | + z \rangle$ and observables $A = \sigma_x$ and $B = \sigma_y$, require the auxiliary input states $|A\psi\rangle = |B\psi\rangle = |\downarrow\rangle_z \equiv | - z \rangle$, $|(A + 1)\psi\rangle = |\uparrow\rangle_z + |\downarrow\rangle_z \equiv | + x \rangle$, and finally $|(B + 1)\psi\rangle = |\uparrow\rangle_z + i|\downarrow\rangle_z \equiv | + y \rangle$ to be prepared. In Figure 4, explicit examples of related intensity sets for different values of ϕ are depicted. Standard deviations yield $\Delta(A) = \Delta(B) = 1$ and the right-hand side of the uncertainty relations gives a lower bound of $(1/2)\langle\psi|[A, B]|\psi\rangle = 1$.

In a first experimental run, O_A is varied along the equator ($\theta = \pi/2$) parameterized by its azimuthal angle ϕ . The theory curves for $\epsilon(A)$ and $\eta(B)$ are then given by

$$\epsilon(A) = 2 \sin \frac{\phi}{2}, \quad \eta(B) = \sqrt{2} |\cos \phi|. \quad (9)$$

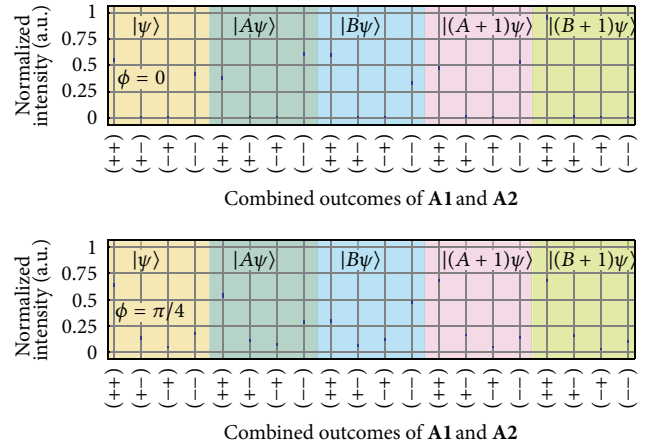


FIGURE 4: Normalized intensity of the successive measurements carried out by apparatuses **A1** and **A2**. The combined projective measurements of O_A and B have four outcomes, denoted by $(++)$, $(+-)$, $(-+)$, and $(--)$, and have to be recorded for each initial state, that is, $|\psi\rangle$, $|A\psi\rangle$, $|B\psi\rangle$, $|(A + 1)\psi\rangle$, and $|(B + 1)\psi\rangle$. Here O_A is varied within the xy -plane with azimuthal angle given by $\phi = 0, \pi/4$. Error bars represent \pm one standard deviation of the normalized intensities. Some error bars are at the size of the markers.

For $\phi = 0$, the error $\epsilon(A)$ vanishes and the disturbance $\eta(B)$ is maximal. The disturbance $\eta(B)$ vanishes for $O_A = B$ ($\phi = \pi/2$) and reaches a second maximum for $O_A = -A$. Note that at this point also the error $\epsilon(A)$ has its (only) maximum. The famous *trade-off relation*, that is, the reciprocal relation for error and disturbance, only holds for $-\pi/2 \leq \phi \leq \pi/2$, which can be seen in Figure 5(a). The product of error and disturbance $\epsilon(A)\eta(B)$ —left-hand side of (4) or *Heisenberg term*—is below the limit given by $(1/2)\langle\psi|[A, B]|\psi\rangle$ in a wide range of ϕ -values, thereby revealing a violation of the generalized Heisenberg relation (see (4)). On the contrary, the left-hand side of Ozawa's relation $\epsilon(A)\eta(B) + \epsilon(A)\Delta(B) + \Delta(A)\eta(B)$ (see (5)) is always above the lower bound defined by the expectation value of the commutator demonstrating the validity of Ozawa's new relation.

In the following experimental setting, O_A is rotated out of the equatorial plane, when the evolution is on circles of latitude on the Bloch sphere (fixed polar angle θ), which yields $\epsilon(A) = \sqrt{2 - 2 \cos \phi \sin^2 \theta}$ and $\eta(B) = \sqrt{2 - 2 \sin^2 \phi \sin^2 \theta}$.

The observed values are depicted in Figure 5(b). Now neither the error $\epsilon(A)$ nor the disturbance $\eta(B)$ vanishes, since they never coincide with A , B , or $-B$. This behaviour affects the curves in such a way that they are now shrunken from below. The smaller θ is, the less regions the polar angle of O_A gets where the Heisenberg term $\epsilon(A)\eta(B)$ remains below the limit. Ozawa's inequality is again fulfilled over the entire range of ϕ . The relations shown in Figure 5 are verified for all directions of O_A .

A modification of the measurement apparatus allows for reducing the disturbance and saturating Branciard's EDR given in (6). If we apply an arbitrary unitary rotation after the first measurement, the error remains unchained but the disturbance is altered. By investigating all possible rotation

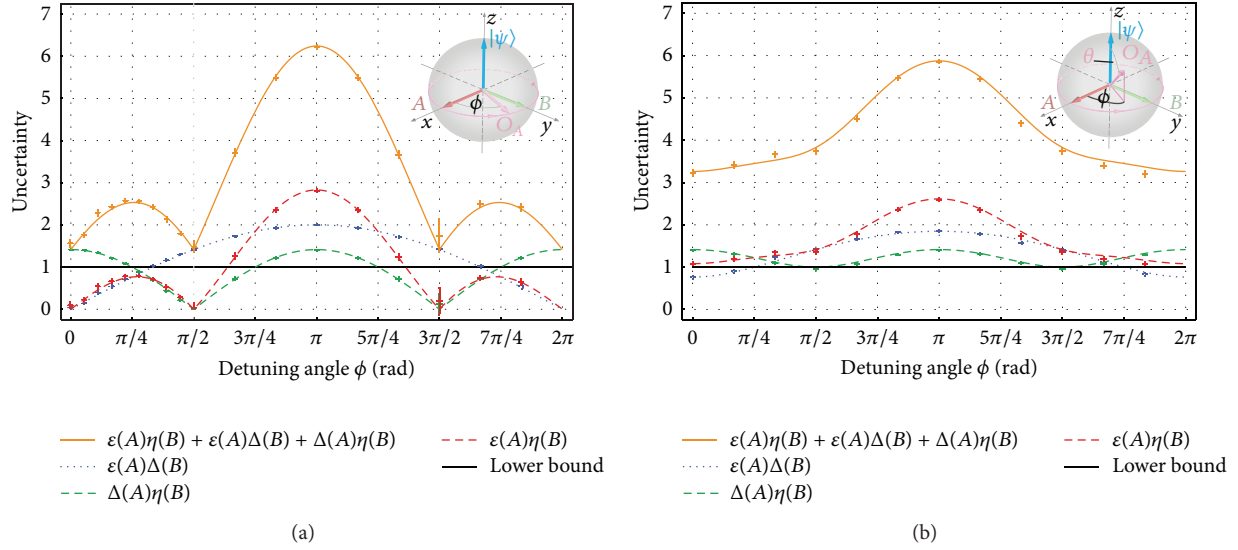


FIGURE 5: Experimentally determined values of $\epsilon(A)\Delta(B)$, $\Delta(A)\eta(B)$, and $\epsilon(A)\eta(B)$. This last term corresponds to the left-hand side of the Heisenberg relation (4), and the sum of the three terms corresponds to the left-hand side of Ozawa's relation (5), including Bloch sphere representation of observables and initial state.

axes and angles, one finds out that $U_R = e^{-i((\phi_{AB}-\phi)/2)\sigma_z}$ minimises the disturbance yielding

$$\epsilon(A) = 2 \sin \frac{\phi}{2}, \quad \eta(B) = 2 \sin \frac{\phi_{AB} - \phi}{2}, \quad (10)$$

where ϕ_{AB} is the relative angle between the A and B measurement direction in the equatorial plane. Note that this particular rotation just generates the eigenstates of observable B , that is, $|\pm y\rangle$, making the result of the optimisation procedure more intuitive. For a detailed calculation see [15].

This is experimentally achieved by an appropriate displacement of DC-3, such that the required rotation is induced, and by additional Larmor precision in the guide field. The results, both for modified and for original apparatuses, are plotted in Figure 6, demonstrating the tightness of Branciard's inequality, defined in (6).

4. Conclusions

To summarize, we have experimentally tested the Ozawa and Branciard error-disturbance uncertainty relations in successive neutron-spin measurements. Our experimental results clearly demonstrated the validity of Ozawa and Branciard EDRs and that the original Heisenberg EDR is violated throughout a wide range of experimental parameters.

Conflict of Interests

The authors declare that there is no conflict of interests regarding the publication of this paper.

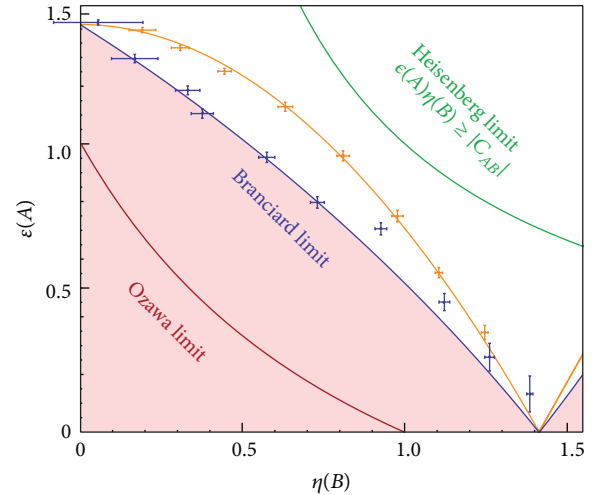


FIGURE 6: Results of error and disturbance plotted as ϵ_A versus $\eta(B)$. Blue curve: the Branciard bound as defined in (6). Blue marker: experimental results using the modified apparatus for $\epsilon(A)$ and $\eta(B)$, as defined in (10). Orange curve error and disturbance as in (9). Green curve: bound imposed by Heisenberg's original error-disturbance relation $\epsilon(A)\eta(B) \geq |C_{AB}|$, which is violated by our experimental results. Red curve: Ozawa's relation (5), which is indeed satisfied but is not saturated.

Acknowledgments

The authors thank M. Ozawa for valuable discussion. This work has been supported by the Austrian Science Fund (FWF), Projects nos. P25795-N02 and P24973-N20.

References

- [1] W. Heisenberg, "Über den anschaulichen inhalt der quantentheoretischen kinematik und mechanik," *Zeitschrift für Physik*, vol. 43, pp. 172–198, 1927.
- [2] W. Heisenberg, *The Physical Principles of Quantum Mechanics*, University of Chicago Press, Chicago, Ill, USA, 1930.
- [3] E. H. Kennard, "Zur Quantenmechanik einfacher Bewegungstypen," *Zeitschrift für Physik*, vol. 44, no. 4-5, pp. 326–352, 1927.
- [4] C. G. Shull, "Single-slit diffraction of neutrons," *Physical Review*, vol. 179, no. 3, pp. 752–754, 1969.
- [5] H. P. Yuen, "Two-photon coherent states of the radiation field," *Physical Review A*, vol. 13, p. 2226, 1976.
- [6] G. Breitenbach, S. Schiller, and J. Mlynek, "Measurement of the quantum states of squeezed light," *Nature*, vol. 387, no. 6632, pp. 471–475, 1997.
- [7] E. Arthurs and M. S. Goodman, "Quantum correlations: a generalized Heisenberg uncertainty relation," *Physical Review Letters*, vol. 60, no. 24, pp. 2447–2449, 1988.
- [8] S. Ishikawa, "Uncertainty relations in simultaneous measurements for arbitrary observables," *Reports on Mathematical Physics*, vol. 29, no. 3, pp. 257–273, 1991.
- [9] M. Ozawa, *Quantum Aspects of Optical Communications*, vol. 378 of *Lecture Notes in Physics*, Springer, 1991.
- [10] J. Erhart, S. Sponar, G. Sulyok, G. Badurek, M. Ozawa, and Y. Hasegawa, "Experimental demonstration of a universally valid error–disturbance uncertainty relation in spin measurements," *Nature Physics*, vol. 8, pp. 185–189, 2012.
- [11] G. Sulyok, S. Sponar, J. Erhart, G. Badurek, M. Ozawa, and Y. Hasegawa, "Violation of Heisenberg's error-disturbance uncertainty relation in neutron-spin measurements," *Physical Review A*, vol. 88, Article ID 022110, 2013.
- [12] L. A. Rozema, A. Darabi, D. H. Mahler, A. Hayat, Y. Soudagar, and A. M. Steinberg, "Violation of Heisenberg's measurement-disturbance relationship by weak measurements," *Physical Review Letters*, vol. 109, Article ID 100404, 2012.
- [13] M. M. Weston, M. J. W. Hall, M. S. Palsson, H. M. Wiseman, and G. J. Pryde, "Experimental test of universal complementarity relations," *Physical Review Letters*, vol. 110, no. 22, Article ID 220402, 2013.
- [14] S.-Y. Baek, F. Kaneda, M. Ozawa, and K. Edamatsu, "Experimental violation and reformulation of the Heisenberg's error-disturbance uncertainty relation," *Scientific Reports*, vol. 3, article 2221, 2013.
- [15] C. Branciard, "Error-tradeoff and error-disturbance relations for incompatible quantum measurements," *Proceedings of the National Academy of Sciences of the United States of America*, vol. 110, no. 17, pp. 6742–6747, 2013.
- [16] M. Ringbauer, D. N. Biggerstaff, M. A. Broome, A. Fedrizzi, C. Branciard, and A. G. White, "Experimental joint quantum measurements with minimum uncertainty," *Physical Review Letters*, vol. 112, Article ID 020401, 2014.
- [17] F. Kaneda, S. Y. Baek, M. Ozawa, and K. Edamatsu, "Experimental test of error-disturbance uncertainty relations by weak measurement," *Physical Review Letters*, vol. 112, Article ID 020402, 2014.
- [18] M. Ozawa, "Universal uncertainty principle in the measurement operator formalism," *Journal of Optics B: Quantum and Semiclassical Optics*, vol. 7, article S672, 2005.
- [19] R. F. Werner, "The uncertainty relation for joint measurement of position and momentum," *Quantum Information and Computation*, vol. 4, no. 6, pp. 546–562, 2004.
- [20] K. Koshino and A. Shimizu, "Quantum Zeno effect by general measurements," *Physics Reports A: Review Section of Physics Letters*, vol. 412, no. 4, pp. 191–275, 2005.
- [21] M. Ozawa, "Uncertainty relations for noise and disturbance in generalized quantum measurements," *Annals of Physics*, vol. 311, no. 2, pp. 350–416, 2004.
- [22] Y. Hasegawa and G. Badurek, "Noncommuting spinor rotation due to balanced geometrical and dynamical phases," *Physical Review A*, vol. 59, article 4614, 1999.
- [23] J. Klepp, S. Sponar, S. Filipp, M. Lettner, G. Badurek, and Y. Hasegawa, "Observation of nonadditive mixed-state phases with polarized neutrons," *Physical Review Letters*, vol. 101, no. 15, Article ID 150404, 2008.
- [24] S. Sponar, J. Klepp, C. Zeiner, G. Badurek, and Y. Hasegawa, "Violation of a Bell-like inequality for spin-energy entanglement in neutron polarimetry," *Physics Letters A: General, Atomic and Solid State Physics*, vol. 374, no. 3, pp. 431–434, 2010.
- [25] S. Sponar, J. Klepp, K. Durstberger-Rennhofer et al., "High-efficiency manipulations of triply entangled states in neutron polarimetry," *The New Journal of Physics*, vol. 14, Article ID 053032, 2012.

Research Article

Gravitational Resonance Spectroscopy with an Oscillating Magnetic Field Gradient in the GRANIT Flow through Arrangement

G. Pignol,¹ S. Baeßler,² V. V. Nesvizhevsky,³ K. Protasov,¹
D. Rebreyend,¹ and A. Voronin⁴

¹ LPSC, Université Grenoble-Alpes, CNRS/IN2P3, 53 rue des Martyrs, 38026 Grenoble, France

² Physics Department, University of Virginia, 382 McCormick Road, Charlottesville, VA 22904, USA

³ Institut Laue-Langevin, 71 avenue des Martyrs, 38000 Grenoble, France

⁴ Lebedev Institute, 53 Leninskii Prospekt, Moscow 119991, Russia

Correspondence should be addressed to G. Pignol; guillaume.pignol@lpsc.in2p3.fr

Received 6 June 2014; Accepted 4 August 2014; Published 24 August 2014

Academic Editor: Ignatios Antoniadis

Copyright © 2014 G. Pignol et al. This is an open access article distributed under the Creative Commons Attribution License, which permits unrestricted use, distribution, and reproduction in any medium, provided the original work is properly cited. The publication of this article was funded by SCOAP³.

Gravitational resonance spectroscopy consists in measuring the energy spectrum of bouncing ultracold neutrons above a mirror by inducing resonant transitions between different discrete quantum levels. We discuss how to induce the resonances with a flow through arrangement in the GRANIT spectrometer, excited by an oscillating magnetic field gradient. The spectroscopy could be realized in two distinct modes (so called DC and AC) using the same device to produce the magnetic excitation. We present calculations demonstrating the feasibility of the newly proposed AC mode.

1. Introduction

Ultracold neutrons bouncing over a horizontal mirror are used to probe quantum effects of a particle in the gravitational field [1]. The vertical motion of such neutrons bouncing at submillimeter distance from the mirror has discrete energy spectrum that can be calculated from the stationary Schrödinger equation:

$$\frac{\hbar^2}{2m} \frac{d^2}{dz^2} \psi_n + mgz\psi_n = E_n \psi_n, \quad (1)$$

where m is the neutron mass, $g = 9.81 \text{ m/s}^2$ is the local gravitational acceleration, and $\psi_n(z)_{n=1,2,\dots}$ are the stationary wavefunctions with associated energy E_n . The existence of the quantization of the vertical motion was demonstrated a decade ago [2], profiting from the relatively large spatial extension of the ground state wavefunction characterized by $z_0 = (\hbar^2/2m^2g)^{1/3} \approx 5.87 \text{ } \mu\text{m}$.

Precision study of the quantum states is motivated by their sensitivity to extra short range interactions (see [3] and references therein), in particular, those induced by Chameleon Dark Energy [4–6]. In addition, the neutron quantum states provide a unique test of the weak equivalence principle in a quantum regime, since the inertial and gravitational masses in (1) do not cancel.

High precision measurements can be achieved with the gravitational resonance spectroscopy technique, where transitions between quantum states are induced by a periodic excitation [7]. The characteristic frequencies of the transitions, as low as $f_0 = mgz_0/2\pi\hbar \approx 145 \text{ Hz}$, are accessible by electrical as well as mechanical oscillators. More precisely, the quantum frequencies for a transition $n \rightarrow m$ from the state of energy E_n to the state of energy E_m is given by $f_{nm} = (E_n - E_m)/2\pi\hbar$. Solving the problem (1), one can show that

$$f_{nm} = f_0 (\epsilon_n - \epsilon_m), \quad (2)$$

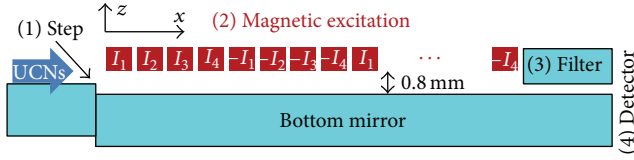


FIGURE 1: Sketch of the flow through setup. Ultracold neutrons enter from the left; they go through the step to depopulate the ground quantum state (1), 16 cm long transition region (2), 9 cm long analyzer (3), and detector (4).

where $\epsilon_n = [2.338, 4.088, 5.521, 6.787, \dots]$ is the series of the negative zeros of the Airy function. To perform the spectroscopy of the bouncing neutron, the interaction that couples different quantum states can be a vibration of the bottom mirror or an oscillating magnetic field gradient [8]. The former has been used by the QBounce collaboration [7]; the latter will be used in the GRANIT spectrometer [9].

As a first step of GRANIT, a flow through measurement of the resonant transitions magnetically excited between the first three quantum states will be realized as first proposed in [10]. According to this proposal, a space periodic (but static) magnetic field gradient will be generated at the surface of the bottom mirror. The frequency of the excitation seen by a neutron will thus vary according to its horizontal velocity. A detailed analysis of this scheme is provided in [9]. Another mode of operation (the AC mode) can be implemented with the same setup, consisting in generating a homogeneous gradient but oscillating in time, which should allow a more direct probe of the resonances.

The paper is organized as follows: in Section 2, we present the flow through setup, in Section 3, we describe in some details the magnetic excitation, in Section 4, we calculate the conditions for the adiabaticity of spin transport, and, in Section 5, we present a theoretical description of the magnetically induced transitions in the AC mode.

2. The GRANIT Flow through Setup

The sketch of the flow through setup is shown in Figure 1. Ultracold neutrons are produced from a dedicated superthermal source installed at a cold beamline of the high flux reactor of the Institut Laue-Langevin. The source relies on downscattering of neutrons with a wavelength of 0.89 nm in a superfluid helium bath cooled down to 0.8 K [11, 12]. According to a preliminary measurement of the UCN velocity spectrum [13], we expect the v_x velocity along the beam to be distributed with a mean value of $v_0 = 4$ m/s and a standard deviation of 1.5 m/s. In the rest of this paper, we will assume a Gaussian profile for the v_x distribution with those parameters. UCNs are extracted using a narrow slit to accept only those with practically no vertical velocity. The spectroscopy is performed with four steps: (1) state preparation, (2) resonant transition, (3) state analysis, and (4) detection of transmitted flux.

- (i) UCNs are first prepared in an excited state by going down step (1) of height $15 \mu\text{m}$. The populations p_n of

the quantum states after the step are expected to be about $p_1 = 0.02, p_2 = p_3 = p_4 = 0.3$. Thus, the population of the ground quantum state is suppressed as compared to the populations of excited states.

- (ii) Next, transitions between quantum states are induced with a periodic magnetic field gradient. The length of the transition region is $L = 16$ cm, corresponding to an average passage time $t_0 = 40$ ms. Two different schemes could be implemented in principle: the AC excitation and the DC excitation. In the DC mode, the field gradient is static and spatially oscillating in the x direction with a period of $d = 1$ cm. In this case, only neutrons with specific horizontal velocities meet the resonance condition. The deexcitation $2 \rightarrow 1$ is expected to be induced by an excitation frequency $f_{21} = 254$ Hz, corresponding to the resonant horizontal velocity of $v_{21} = df_{21} = 2.54$ m/s; for the $3 \rightarrow 1$ case, we expect $f_{31} = 462$ Hz and $v_{31} = 4.62$ m/s. In the AC mode, the field gradient is spatially uniform, oscillating in time. One would then find the resonances by directly scanning the excitation frequency.
- (iii) A second horizontal mirror above the main mirror serves as a state analyzer. For a slit opening of about $25 \mu\text{m}$, only ground state neutrons are accepted; higher quantum states are rejected. The length of the analyzer in the x direction is 9 cm.
- (iv) Finally, neutrons are detected at the exit of the analyzer. In AC mode, the flux of transmitted neutrons should display a resonance pattern as a function of the excitation frequency. In DC mode, one has to measure the horizontal velocity of the transmitted neutrons to deduce the resonant frequency. This is achieved by measuring the height of the neutrons with a position sensitive detector after a free fall distance of 30 cm.

Before developing the details, let us estimate the strength of the needed oscillating magnetic field gradient. The interaction of a neutron with a magnetic field \vec{B} is described by the operator $-\hat{\mu} \cdot \vec{B}$, where $\hat{\mu}$ is the neutron magnetic moment observable acting on the internal spin degree of freedom. When the variation of the magnetic field is slow compared to the Larmor frequency, the spin will follow the direction of the magnetic field. This adiabaticity condition will be addressed in Section 4. In this case, the neutron trajectory and the spin dynamics are effectively decoupled. Then, the motion of the neutron is determined by the potential $s\mu|\vec{B}|$ where $\mu = 60.3$ neV/T is the magnetic moment of the neutron and $s = 1$ for “spin up” neutrons and $s = -1$ for “spin down” neutrons. Classically, a vertical force is applied on the neutron by the field gradient $\partial_z|\vec{B}|$. Let us now assume a magnetic excitation of the form $|\vec{B}| = \beta z \cos(\omega t)$. The quantum mechanical excitation potential reads

$$\hat{V} = s\mu\beta z \cos(\omega t). \quad (3)$$

When the excitation frequency is close to a resonance, $\omega \approx 2\pi f_{nm}$, a Rabi oscillation between states $|n\rangle$ and $|m\rangle$ will take place at the angular frequency

$$\Omega_{nm} = \frac{\mu}{\hbar} \langle n | \hat{z} | m \rangle \beta, \quad (4)$$

where the matrix elements of \hat{z} can be expressed as (see, e.g., [14])

$$\begin{aligned} \langle n | \hat{z} | m \rangle &= \frac{2z_0}{(\epsilon_n - \epsilon_m)^2} \quad (n \neq m), \\ \langle n | \hat{z} | n \rangle &= \frac{2}{3} z_0 \epsilon_n. \end{aligned} \quad (5)$$

To maximize the transition probability at resonance, the excitation strength β should verify $\Omega t_0 = \pi$, where t_0 is the excitation time. This condition can be expressed using (4) and (5) as

$$\beta_{\text{needed}} = \frac{\pi}{2} \frac{\hbar}{\mu z_0} \left(\frac{f_{nm}}{f_0} \right)^2 \frac{1}{t_0}. \quad (6)$$

One finds a needed field gradient of $\beta = 0.22$ T/m to induce the $2 \rightarrow 1$ transition and $\beta = 0.74$ T/m to induce the $3 \rightarrow 1$ transition.

3. The Magnetic Excitation

The magnetic field excitation will be generated by an array of 128 copper wires with square section arranged as shown in Figure 1. In practice, the system is constituted of four modules, each one holding 32 adjacent wires. A wire has a section of 1 mm^2 and a length of 30 cm in the y direction. Adjacent wires are separated by a gap of 0.25 mm. Electrical connectors are arranged so that the following 8-periodic pattern current could be applied $I_1, I_2, I_3, I_4, -I_1, -I_2, -I_3, -I_4, I_1, \dots$. Thus, the magnetic field will be 1 cm periodic. The system will be placed above the horizontal mirror in the transition region as shown in Figure 1 at a distance of 0.8 mm from the mirror.

The magnetic field generated by a single infinitely long square wire can be calculated analytically; the corresponding formulas are reported in the appendix. The magnetic field components $B_x(x)$, $B_z(x)$ and gradients $\partial_z B_x(x)$, $\partial_z B_z(x)$ at the surface of the mirror are obtained by summing the corresponding quantities for each of the 128 wires weighted by the individual currents. Then, the field gradient is calculated according to

$$\partial_z |B| = \frac{B_x \partial_z B_x + B_z \partial_z B_z}{|B|}. \quad (7)$$

It is possible to tune the currents to obtain a homogeneous gradient at the surface of the mirror. We show, in Figure 2, the result for $I_1 = I_4 = 1.4$ A and $I_2 = I_3 = 3.5$ A where a field gradient of 0.52 T/m is obtained, as needed to induce resonant transitions between quantum states. This will be the benchmark configuration for the rest of the paper. The residual ‘‘noise’’ seen in Figure 2 has an amplitude of

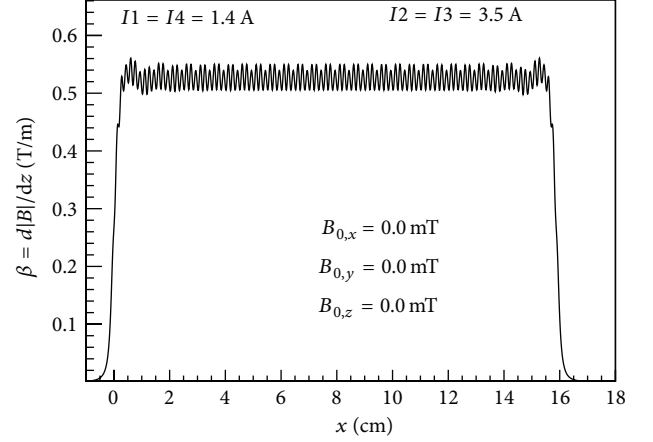


FIGURE 2: Magnetic field gradient $\partial_z |B|$ produced at the surface of the main mirror, without any external magnetic field.

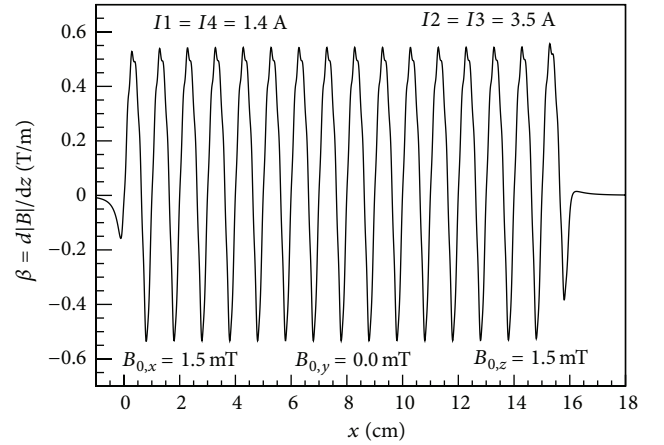


FIGURE 3: Magnetic field gradient $\partial_z |B|$ produced at the surface of the main mirror with external magnetic field applied in the x, z plane.

0.02 T/m; this noise would increase for a wire array closer to the mirror. The frequency of this noise seen by a neutron passing at 4 m/s is about 2 kHz, much higher than the frequencies of interest for resonant transitions between low lying quantum states.

Note that the result shown in Figure 2 assumes that no external field is applied. By applying an external field \vec{B}_0 , with, for example, $B_{0,x} = B_{0,z} = 1.5$ mT and $B_{0,y} = 0$, the situation changes dramatically as shown in Figure 3. With a strong external field applied, a gradient oscillating in the x direction with a period of 1 cm is generated.

As a result, the wire array is a versatile device to generate the field gradient that can be used for the AC excitation mode as well as for the DC excitation mode. In the DC mode, we apply DC current in the wire array and apply a strong external field in the x, z direction. The vertical force exerted by the

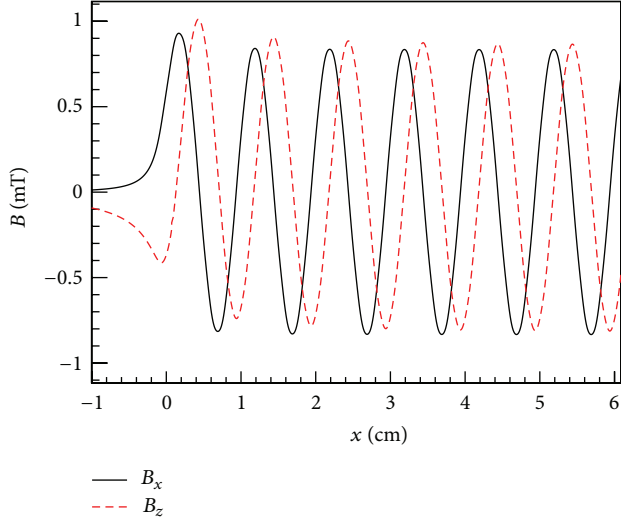


FIGURE 4: Magnetic field generated at the surface of the main mirror assuming the benchmark configuration $I_1 = I_4 = 1.4$ A and $I_2 = I_3 = 3.5$ A.

field gradient on the neutron will oscillate in space. In the AC mode, we apply AC current in the wire array and a small external field $B_{0,y}$ to satisfy the adiabaticity of spin transport, as detailed in the next section.

4. The Adiabaticity of Spin Transport

The magnetic field gradient produced by the array of wires described in the previous section will exert a force on the passing neutrons. The sign of the force depends on the relative orientation between the neutron spin and the magnetic field. To induce resonant transitions between quantum states, a neutron should feel a well-defined oscillating vertical force. Thus, one must make sure that the magnetic field is strong enough to hold the neutron spins parallel or antiparallel to the magnetic field at any time. If the adiabaticity condition for spin transport along the wire array is fulfilled, then the spin dynamics and the neutron trajectory are decoupled.

In the AC mode of excitation, the input current in the wire array is oscillating with driving frequency f . The magnetic field amplitude created by the wire array at the surface of the mirror is given by the pattern shown in Figure 4, with the whole pattern oscillating in time at the driving frequency f . Thus, the magnetic field generated by the wire array will not be sufficient to hold the neutron spin, since the magnitude of the field crosses zero at a frequency f . To maintain a nonzero value of the field magnitude at any time, a static, homogeneous external field $B_{0,y}$ is applied in the transverse y direction. The purpose of this section is to calculate the minimum $B_{0,y}$ field to apply in order to guarantee the adiabaticity of neutron spin transport when passing by the magnetic excitation.

Here, we calculate the spin dynamics only, assuming that a neutron pass below the wire array in a straight horizontal line trajectory, at the surface of the bottom mirror. A neutron

with velocity v along the x direction sees a time dependent magnetic field in its rest frame given by

$$\begin{aligned} B_x(t) &= B_1 \cos(2\pi ft + \phi) \sin\left(\frac{2\pi vt}{d}\right), \\ B_y(t) &= B_{0,y}, \\ B_z(t) &= -B_1 \cos(2\pi ft + \phi) \cos\left(\frac{2\pi vt}{d}\right). \end{aligned} \quad (8)$$

It results from the combination of the oscillation of the field in space with period d and the oscillation in time with frequency f . We will set $B_1 = 0.8$ mT for the benchmark wire currents described in the previous section.

The spin dynamics is given by the Bloch equation for the polarization vector $\vec{\Pi}$:

$$\frac{d\vec{\Pi}}{dt} = \gamma \vec{\Pi} \times \vec{B}(t), \quad (9)$$

where $\gamma = 2\mu/\hbar = 183$ kHz/mT is the neutron gyromagnetic ratio.

We have solved numerically the Bloch equation using a Runge Kutta solver. The initial condition for the polarization vector $\vec{\Pi}(0)$ was set to the unit vector aligned with $\vec{B}(0)$, describing a “spin up” neutron. We define the spin-flip probability at time t as $p(t) = (1 - \vec{\Pi} \cdot \vec{B}/|\vec{B}|)/2$. With this definition, $p(t) = 0$ if the spin is aligned with the magnetic field at time t and $p(t) = 1$ if the spin has reversed its direction relative to the magnetic field at time t . As an adiabaticity criterion, we take p_{\max} , the maximum spin-flip probability during the passage of a neutron below the wire array of duration L/v . For a given set of parameters $B_{0,y}$, f , v , and ϕ , the criterion p_{\max} was numerically calculated. The result was then averaged over the phase ϕ and the velocity spectrum v . The final result is presented in Figure 5 as a function of the driving frequency f , for different values of the external field $B_{0,y}$.

As a conclusion of the numerical study, the value of the external field $B_{0,y} = 0.3$ mT is sufficient to hold the neutron spin with an accuracy better than one percent, in the frequency range of interest between 0 and 300 Hz. In the following calculations, the external holding transverse field will thus be set to $B_{0,y} = 0.3$ mT.

5. The Resonant Transitions in the AC Mode

We have now defined a magnetic configuration for the AC mode with the wire array (oscillating currents at variable frequency f and fixed amplitudes $I_1 = I_4 = 1.4$ A and $I_2 = I_3 = 3.5$ A) and the external field ($B_{0,y} = 0.3$ mT) that (i) holds the neutron spin and (ii) generates an oscillating gradient with the required amplitude to induce resonant transitions between quantum states. Note that the time dependent gradient $\beta(t)$ seen by the neutrons is not

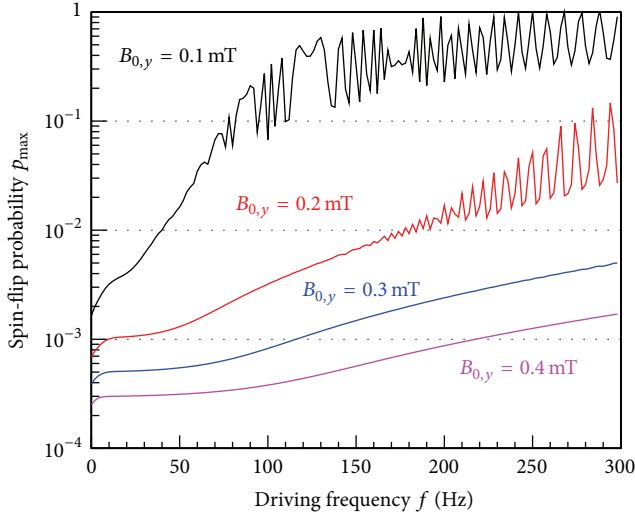


FIGURE 5: Numerically calculated neutron spin-flip probability during the passage below the wire array in the benchmark configuration $I_1 = I_4 = 1.4$ A and $I_2 = I_3 = 3.5$ A, as a function of the driving frequency, for different values of the external $B_{0,y}$ field.

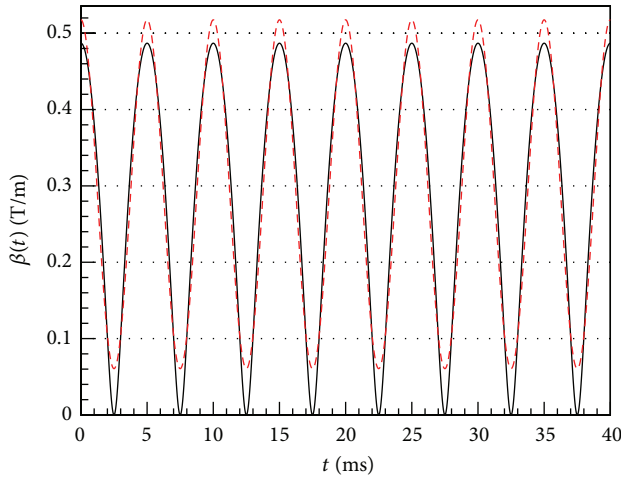


FIGURE 6: Time dependent gradient $\beta(t)$ for a driving frequency of $f = 100$ Hz, corresponding to an excitation frequency of 200 Hz. Solid black line: (10), dashed red line: first order Fourier expansion equation (14).

perfectly harmonic. Following (7), the expression of the time dependent gradient is

$$\beta(t) = \partial_z |\vec{B}| = \hat{\beta} \frac{B_1 \cos^2(2\pi ft + \phi)}{\sqrt{B_1^2 \cos^2(2\pi ft + \phi) + B_{0,y}^2}}, \quad (10)$$

where f is the driving frequency of the current in the wire array, $B_1 = 0.8$ mT, and $\hat{\beta} = 0.52$ T/m. We plot $\beta(t)$ in Figure 6, where it is apparent that the excitation frequency (the frequency of the $\beta(t)$ excitation) is twice the driving frequency f (the frequency of the oscillating currents in the wire array).

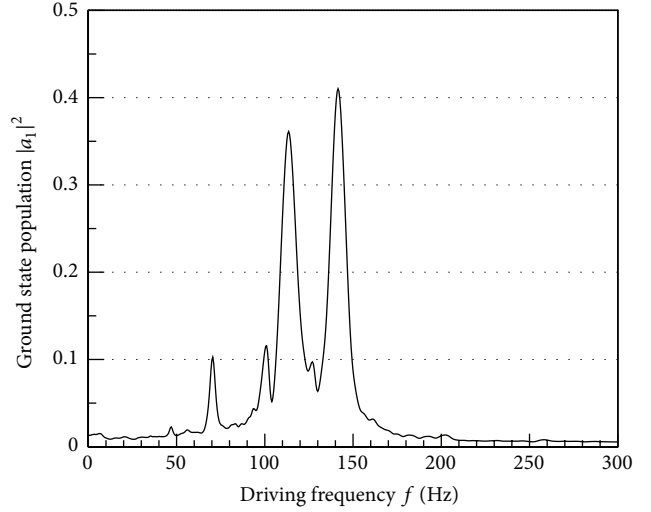


FIGURE 7: Numerical solution of the Schrödinger equation (12). The probability of the $2 \rightarrow 1$ transition is plotted as a function of the driving frequency.

We will now simulate the transition probabilities that could be observed in the GRANIT flow through setup as described in Section 2, assuming the benchmark magnetic configuration resulting in the excitation (10). The problem consists in calculating the time evolution of a neutron quantum state

$$|\psi(t)\rangle = \sum_n a_n(t) |n\rangle, \quad (11)$$

which is the solution of the time dependent Schrödinger equation

$$i \frac{da_n}{dt} = \frac{E_n}{\hbar a_n} + \sum_m^s \frac{s}{2} \gamma \beta(t) \langle n | \hat{z} | m \rangle a_m. \quad (12)$$

Here, we assume that the adiabaticity condition is fulfilled. The initial condition of the state is chosen to be $|\psi(0)\rangle = |2\rangle$ immediately after the preparation step. Then, we solved (12) with a Runge-Kutta algorithm for a given set of parameters f , v , s , and ϕ , where the sum is restricted to the first four quantum states. For a given horizontal velocity v , the probability $|a_1(L/v)|^2$ for the neutron to be detected in the ground state at the exit of the magnetic excitation is calculated. The result is then averaged over the excitation phase ϕ , the spin state $s = \pm 1$, and the velocity spectrum. We plot in Figure 7 the transition probability as a function of the driving frequency f .

According to this numerical calculation, we expect to see two resonances in the transmitted UCN flux associated with the $2 \rightarrow 1$ transition, with frequencies

$$f^+ = 141.5 \text{ Hz}, \quad f^- = 113.5 \text{ Hz}, \quad (13)$$

where f^+ and f^- are the maxima of the resonance curve corresponding to spin “up” neutrons ($s = 1$) and spin “down” neutrons ($s = -1$), respectively.

The splitting of the resonances depending on the spin state could be interpreted as a ‘‘Stern-Gerlach’’ split due to a constant magnetic field gradient. To see this, it is useful to perform the Fourier expansion of the gradient excitation $\beta(t)$ given by (10)

$$\beta(t) = \beta_0 + \beta_1 \cos(4\pi ft + 2\phi) + \dots, \quad (14)$$

where $\beta_0 = 0.289$ T/m and $\beta_1 = 0.228$ T/m. The constant term β_0 of the excitation should be thought of as a spin-dependent effective modification of g . This is done by identification of the total constant vertical force (gravity plus constant gradient) to an effective gravitational force:

$$mg^\pm = mg \pm \mu\beta_0. \quad (15)$$

Thus, we expect a spin-dependent resonance frequency of the $n \rightarrow m$ transition given by

$$f_{nm}^\pm = \frac{(mg^\pm)^{2/3}}{2\pi(2m\hbar)^{1/3}} (\epsilon_n - \epsilon_m) = f_{nm} \left(1 \pm \frac{\mu\beta_0}{mg}\right)^{2/3}, \quad (16)$$

where f_{nm} is the unperturbed transition frequency. The splitting of the resonances obtained by the numerical resolution of the full Schrödinger equation (12) is in quantitative agreement with (16).

In addition, (16) motivates a combination of the two resonant frequencies f^+ and f^- to extract the unperturbed transition frequency f_{21} , namely,

$$f_{21} = \left(\frac{(2f^+)^{3/2} + (2f^-)^{3/2}}{2} \right)^{2/3}. \quad (17)$$

Remember that f^+ and f^- refer to driving frequencies, that correspond to excitation frequencies of $2f^+$ and $2f^-$. When applied to the maxima of the curve shown in Figure 7, one extracts $f_{21} = 255.8$ Hz which differs from the true resonance frequency $f_{21,\text{true}} = 253.8$ Hz given by (2) by 2 Hz. In fact, there are several features of the full problem (given by (12)) that the simple estimate (16) does not catch. The simplified formula (16) can be obtained by assuming a two-level system (states $|1\rangle$ and $|2\rangle$) excited by a harmonic force given by (14) that couple states $|1\rangle$ and $|2\rangle$, neglecting the self-couplings of the types $\langle 1|\hat{z}|1\rangle$ and $\langle 2|\hat{z}|2\rangle$. The full calculation (12) takes into account the nonharmonic excitation given by (10) that couples all states $|1\rangle$, $|2\rangle$, $|3\rangle$, and $|4\rangle$ including self-couplings. All these complications are potential sources of frequency shifts of the resonance line. We then conclude that these shifts are below the percent level.

6. Conclusion

In the GRANIT flow through arrangement, two possible modes to induce resonant transitions between the quantum states could be used. In the DC mode, where the magnetic field gradient oscillates spatially along the x direction, the excitation frequency is controlled by the horizontal neutron velocity. In the AC mode, where the gradient is homogeneous in space and oscillates in time, the excitation frequency is

selected directly by the frequency of the current driving the magnetic excitation. We have shown that the condition of adiabaticity of spin transport can also be fulfilled in the AC mode using a moderate horizontal magnetic field normal to the neutron propagation axis. Finally, a calculation of the expected resonance line for the $2 \rightarrow 1$ transition indicates that a measurement of the transition frequency at a precision better than a percent is possible. A detailed comparison describing the relative merits of the two methods with the associated systematic effects is left for a future work.

Appendix

Magnetic Field of a Square Wire

Here, we provide formulas for the magnetic field generated by an infinitely long square wire with current I flowing uniformly in the wire in the y direction. The magnetic field lies in the (x, z) plane. We assume that $(x = 0, y = 0)$ corresponds to the center of the wire. The length of the square is denoted by c ($c = 1$ mm for the purpose of this paper). Formulas are valid outside the wire. We define the following quantities:

$$\begin{aligned} x_m &= x - \frac{c}{2}, & z_m &= z - \frac{c}{2}, \\ x_p &= x + \frac{c}{2}, & z_p &= z + \frac{c}{2}, \\ L_1 &= \ln \left(\frac{(x_m^2 + z_m^2)(x_p^2 + z_p^2)}{(x_p^2 + z_m^2)(x_m^2 + z_p^2)} \right), \\ L_2 &= \ln \left(\frac{(x_m^2 + z_m^2)(x_p^2 + z_m^2)}{(x_m^2 + z_p^2)(x_p^2 + z_p^2)} \right), \\ L_3 &= \ln \left(\frac{(x_m^2 + z_m^2)(x_m^2 + z_p^2)}{(x_p^2 + z_m^2)(x_p^2 + z_p^2)} \right), \\ A_{mm} &= \arctan \left(\frac{x_m}{z_m} \right), & A_{pm} &= \arctan \left(\frac{x_p}{z_m} \right), \\ A_{mp} &= \arctan \left(\frac{x_m}{z_p} \right), & A_{pp} &= \arctan \left(\frac{x_p}{z_p} \right). \end{aligned} \quad (A.1)$$

By integrating the Biot-Savart law over the volume of the wire, we find the following expressions for the field components:

$$\begin{aligned} B_x(x, z) &= -\frac{\mu_0 I}{4\pi c^2} \left[xL_1 - \frac{c}{2}L_2 + 2z_m(A_{mm} - A_{pm}) \right. \\ &\quad \left. + 2z_p(A_{pp} - A_{mp}) \right], \\ B_z(x, z) &= \frac{\mu_0 I}{4\pi c^2} \left[zL_1 - \frac{c}{2}L_3 + 2x_m(A_{mp} - A_{mm}) \right. \\ &\quad \left. + 2x_p(A_{pm} - A_{pp}) \right]. \end{aligned} \quad (A.2)$$

By taking the derivative, we find the following expressions for the gradients:

$$\begin{aligned}\partial_z B_x &= \frac{\mu_0 I}{2\pi c^2} [A_{mp} - A_{mm} + A_{pm} - A_{pp}], \\ \partial_z B_z &= \frac{\mu_0 I}{4\pi c^2} L_1.\end{aligned}\tag{A.3}$$

Conflict of Interests

The authors declare that there is no conflict of interests regarding the publication of this paper.

References

- [1] V. V. Nesvizhevsky, “Near-surface quantum states of neutrons in the gravitational and centrifugal potentials,” *Physics-Uspekhi*, vol. 53, no. 7, pp. 645–675, 2010.
- [2] V. V. Nesvizhevsky, H. G. Börner, A. K. Petukhov et al., “Quantum states of neutrons in the Earth’s gravitational field,” *Nature*, vol. 415, no. 6869, pp. 297–299, 2002.
- [3] I. Antoniadis, S. Baessler, M. Buchner et al., “Short-range fundamental forces,” *Comptes Rendus Physique*, vol. 12, pp. 755–778, 2011.
- [4] P. Brax and G. Pignol, “Strongly coupled chameleons and the neutronic quantum bouncer,” *Physical Review Letters*, vol. 107, Article ID 111301, 2011.
- [5] P. Brax, G. Pignol, and D. Roulier, “Probing strongly coupled chameleons with slow neutrons,” *Physical Review D*, vol. 88, Article ID 083004, 2013.
- [6] T. Jenke, G. Cronenberg, J. Burgdörfer et al., “Gravity resonance spectroscopy constrains dark energy and dark matter scenarios,” *Physical Review Letters*, vol. 112, no. 15, Article ID 151105, 2014.
- [7] T. Jenke, P. Geltenbort, H. Lemmel, and H. Abele, “Realization of a gravity-resonance-spectroscopy technique,” *Nature Physics*, vol. 7, no. 6, pp. 468–472, 2011.
- [8] V. V. Nesvizhevsky and K. V. Protasov, “Quantum states of neutrons in the Earth’s gravitational field: state of the art, applications, perspectives,” in *Trends in Quantum Gravity Research*, D. C. Moore, Ed., pp. 65–107, Nova Science, New York, NY, USA, 2006.
- [9] S. Baessler, M. Beau, M. Kreuz et al., “The GRANIT spectrometer,” *Comptes Rendus Physique*, vol. 12, pp. 707–728, 2011.
- [10] M. Kreuz, V. V. Nesvizhevsky, P. Schmidt-Wellenburg et al., “A method to measure the resonance transitions between the gravitationally bound quantum states of neutrons in the GRANIT spectrometer,” *Nuclear Instruments and Methods in Physics Research A*, vol. 611, no. 2-3, pp. 326–330, 2009.
- [11] P. Schmidt-Wellenburg, “Ultracold-neutron infrastructure for the gravitational spectrometer GRANIT,” *Nuclear Instruments and Methods in Physics Research A: Accelerators, Spectrometers, Detectors and Associated Equipment*, vol. 611, pp. 267–271, 2009.
- [12] O. Zimmer, F. M. Piegsa, and S. N. Ivanov, “Superthermal source of ultracold neutrons for fundamental physics experiments,” *Physical Review Letters*, vol. 107, Article ID 134801, 2011.
- [13] D. Roulier, F. Vezzu, S. Baessler et al., “Status of the GRANIT facility,” *Advances in High Energy Physics*, vol. 2014, Article ID 730437, 2014.
- [14] C. Caudau, V. V. Nesvizhevsky, M. Fertl, G. Pignol, and K. V. Protasov, “Transitions between levels of a quantum bouncer induced by a noise-like perturbation,” *Nuclear Instruments and Methods in Physics Research A*, vol. 677, pp. 10–13, 2012.

Research Article

Rough Mirror as a Quantum State Selector: Analysis and Design

M. Escobar,¹ F. Lamy,^{2,3} A. E. Meyerovich,¹ and V. V. Nesvizhevsky³

¹ Department of Physics, University of Rhode Island, Kingston, RI 02881-0817, USA

² ICFP, Physics Department, École Normale Supérieure, 24 rue Lhomond, 75005 Paris, France

³ Institut Max von Laue—Paul Langevin, 38042 Grenoble, France

Correspondence should be addressed to A. E. Meyerovich; alexander_meyerovich@uri.edu

Received 14 May 2014; Accepted 23 June 2014; Published 4 August 2014

Academic Editor: Stefan Baessler

Copyright © 2014 M. Escobar et al. This is an open access article distributed under the Creative Commons Attribution License, which permits unrestricted use, distribution, and reproduction in any medium, provided the original work is properly cited. The publication of this article was funded by SCOAP³.

We report analysis of rough mirrors used as the gravitational state selectors in neutron beam and similar experiments. The key to mirror properties is its roughness correlation function (CF) which is extracted from the precision optical scanning measurements of the surface profile. To identify CF in the presence of fluctuation-driven fat tails, we perform numerical experiments with computer-generated random surfaces with the known CF. These numerical experiments provide a reliable identification procedure which we apply to the actual rough mirror. The extracted CF allows us to make predictions for ongoing GRANIT experiments. We also propose a radically new design for rough mirrors based on Monte Carlo simulations for the 1D Ising model. The implementation of this design provides a controlled environment with predictable scattering properties.

1. Introduction

One of the intriguing options for designing quantum state selectors which separate particles in desirable quantum states from all other particles is to use rough mirrors [1]. The idea is quite simple: the particles that reach the rough mirror are scattered away, while the particles locked in quantum states without an access to the rough mirror remain in the system.

Recent first experimental observation of gravitationally quantized ultracold neutrons (UCNs) [2–6] stimulated use of mirrors with random rough surfaces as state selectors instead of simple absorbers in beam and similar experiments with UCNs [7–9], as well as for shaping UCN spectra [10–12] or exploring the whispering gallery quantum states of cold neutrons [13]. In these experiments a beam of UCNs with large horizontal and small vertical velocities propagates between two horizontal mirrors. The upper mirror is rough and serves as a state selector by scattering away the neutrons in the highest gravitational states which can reach it. The lower mirror is an ideal specular reflector for the neutrons. In the end, only the neutrons in the lowest gravitational states (neutrons with the lowest vertical velocities) remain in the system and continue bouncing along the lower mirror

without scattering. Thus the absence of roughness is crucial for flat bottom mirrors [14, 15].

These types of selectors may have a wide range of applications and can be built not only for neutron beams, but also for other experiments with UCNs, ultracold atoms, and antiatoms [16–19], in particular within the GBAR project with ultracold antihydrogen at CERN [20], as well as, probably, with positronium [21] and so forth.

The ultimate resolution and precision for experiments of this kind with gravitational and whispering gallery quantum states of UCNs in the framework of GRANIT project [22–24] benefits from the method of long storage of UCNs in closed quantum traps as well as from high UCN space-phase density in a dedicated UCN source [25]. More examples and details could be found in proceedings of dedicated GRANIT workshops [26, 27].

The ability of rough mirrors to serve as state selectors hinges on producing a desired pattern in scattering of particles by surface inhomogeneities. This scattering is determined by the correlation function of surface roughness (see, e.g., [28] and references therein). In beam experiments, scattering by the rough upper mirror turns the velocity vector thus increasing its vertical component. When the component of

velocity normal to the mirrors exceeds a certain threshold velocity v_c , the neutrons can penetrate the mirror material and get absorbed; this threshold velocity can be translated into the absorption potential $U_c = mv_c^2/2 \sim 10^{-26}$ J. The roughness-driven transition probabilities between the quantum states (j, \mathbf{q}) and (j', \mathbf{q}') for a mirror with slight roughness and the absorption threshold U_c are [28]

$$W_{jj'}(\mathbf{q}, \mathbf{q}') = \zeta(\mathbf{q} - \mathbf{q}') U_c^2 |\Psi_j(H)|^2 |\Psi_{j'}(H)|^2, \quad (1)$$

where \mathbf{q} is the particle momentum along the wall, $\Psi_j(H)$ is the value of the wave function in quantum state j on the mirror in the absence of roughness, and $\zeta(\mathbf{q})$ is the Fourier image of the correlation function of surface roughness (the so-called power spectrum). If the threshold is very high or the particle cannot penetrate the mirror material at all, $U_c \rightarrow \infty$, (1) becomes [28]

$$W_{jj'} = \frac{1}{4m^2} \zeta(\mathbf{q} - \mathbf{q}') |\Psi_j'(H)|^2 |\Psi_{j'}'(H)|^2. \quad (2)$$

In essence, the roughness correlation function $\zeta(\mathbf{q})$ plays the same role for scattering by surface roughness as the impurity cross-section for scattering by static bulk impurities. It is known that surface scattering depends not only on the main parameters of roughness, such as its average amplitude or correlation radius, but also on the functional form of the correlation function (see, e.g., [29, 30] and references therein). Therefore, the proper identification of the surface correlator is paramount for the use of rough mirrors in precision measurements. It turns out that such *accurate* identification of the correlation function, which is necessary for precision experiments, is not trivial. The difficulties in identifying the correlation parameters go well beyond the recognized ones [31, 32] such as a tip profile [33] or the step size [34].

The purpose of this paper is to analyze and compare the properties of real and computationally generated rough mirrors and find out the limits on their use as state selectors by evaluating the accuracy of predictions for the observables. We also propose a radically new design for rough mirrors, what we call an Ising mirror, which might provide a much more controllable environment for experiment.

2. Experiment

2.1. Mirror Design and Roughness Measurements. The experimental part of the paper deals with a new large rough glass mirror produced for ongoing GRANIT experiments at ILL (Figure 1) [22–24].

The design and construction of the mirror are determined by the following considerations. This mirror should serve for shaping of the initial UCN spectrum and will be installed at the most upstream part of the transport mirror. In first test experiments, it will be used also for measurements of parameters of gravitational quantum states of UCNs. Since the principle application of the mirror is to serve as a gravitational state selector, our choice is to have large roughness amplitudes thus maximizing its efficiency at the

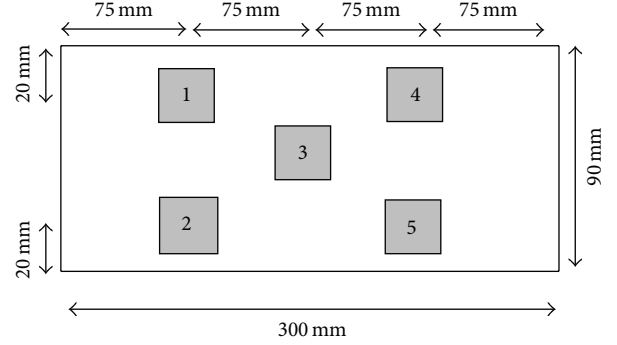


FIGURE 1: The rough mirror with five control patches. The surface roughness is assumed to be uniform across the mirror.

expense of precision of absolute measurements with this rough scatterer/absorber. The total length along the beam of UCNs is restricted by a length of the flat bottom mirror; therefore, we limited the length of the rough mirror by some reasonable small value (9 cm). The width of the rough mirror is similar to the width of the bottom mirror (30 cm).

The surface profile for this new mirror has been measured at ESRF using the vertical scanning interferometry (VSI) technique (see, e.g., [35]). Light is split into two coherent light beams. One beam is sent onto the measured mirror and is coupled after reflection with another light beam reflected from a perfectly flat sample (with the roughness of 0.5 \AA). The resulting beam is analyzed in a CCD camera and the interference patterns give the profile of the rough mirror. Scanning over a certain surface area of the rough mirror allows one to measure the distribution of roughness. If the roughness is too sharp in a particular point, the beam deviates from its vertical trajectory and does not get back into the detector resulting in a “bad” point in the data set. The fabrication of the rough mirror favors producing moderate roughness without large angles between the local surface and the global reference plane (too large amplitudes have been eliminated by the surface production technique). There are about 1.5–2% of “bad” points among the whole data. Most of the “bad” points are isolated, but some form small clusters (the largest cluster contains 8 “bad” points).

An alternative method to the VSI technique would have been the atomic force spectroscopy (AFM). However, using the VSI technique in this particular case had several advantages. First, the characteristic size of the surface to be scanned has to be much larger than the correlation length of the roughness, that is, at least a few hundreds of micrometers. Such areas are too large for a standard AFM. Second, the amplitude of the roughness should be comparable to the characteristic quantum gravitational length scale [2–6] equal to

$$l_0 = \hbar^{2/3} (2m^2 g)^{-1/3} \sim 5.871 \text{ \mu m} \quad (3)$$

in order to provide high efficiency of neutron absorption in this rough mirror. Such amplitudes are too large for an AFM which measures irregularities in the angstrom range.

The raw data set contains surface profiles $y_i(s, t)$ measured in five patches ($i = 1; 2; 3; 4; 5$), Figure 1. The mirror is 90 mm long in the direction of the beam and 300 mm wide. The size of each patch is $0.504 \times 0.504 \text{ mm}^2$. The data set for each patch contains $2,557 \times 2,557 \approx 6.5 \times 10^6$ points. The distance between individual data points is $0.19 \mu\text{m}$ which is much smaller than l_0 and the characteristic amplitude and correlation length of the roughness.

2.2. Extraction of the Roughness Correlation Function. The data analysis consists of several steps. First, the ‘‘bad’’ points have been replaced by the averages of surrounding points. Second, the proper reference planes for individual patches are restored by fitting each of the five data sets $y_i(s, t)$ to the planes $a_i + b_i s + c_i t$ to eliminate the tilting and ensure the zero average for the roughness profile $\langle y_i(s, t) \rangle = 0$. The set of coefficients a_i, b_i, c_i provides the best fit to the profile data for the patch i and the values of $a_i + b_i s + c_i t$ are subtracted from $y_i(s, t)$. By itself, eliminating the tilting in this way is not controversial. The only potential problem here could arise if the mirror as a whole is slightly curved and the reference planes for the individual patches are different from each other.

Since the primary designation of this mirror is to serve as a state selector in new GRANIT experiments aimed at selecting and identifying neutron states in quantizing gravitational field, it is convenient to measure all length parameters, including the roughness correlation function, in units of l_0 , (3), which is the size of the lowest quantum state for a neutron in the Earth gravity field in open geometry. Below all lengths in the figures and tables are given in the corresponding dimensionless units.

The analysis of the data sets and the results are similar to [36] in which we analyze computationally generated rough surfaces. The two-dimensional (2D) correlation function is defined as

$$\begin{aligned} \zeta(s, t) &= \langle y(s', t') y(s' + s, t' + t) \rangle_{x, y} \\ &\equiv \frac{1}{A} \int y(s', t') y(s' + s, t' + t) ds' dt', \end{aligned} \quad (4)$$

where A is the averaging area. The discrete analog of this equation is

$$\zeta(s > 0, t > 0) = \frac{1}{(N-s)(N-t)} \sum_{t'=1+t}^N \sum_{s'=1}^{N-s} y_{t', s'} y_{t'+t, s'+s}. \quad (5)$$

We try to improve the accuracy by maximizing utilization of the data points though the finite size of the patches degrades the accuracy of the computations in (5) for large s, t . This degradation (the so-called wagging tails) becomes very rapid at $s, t > N/2$.

The extraction of the correlation information from the profile data sets is routine with the only limitation being the large volume of profile data. A typical 2D correlation function for one of the patches is given in Figure 2 (light blue surface). For comparison, the dark blue surface presents the best fit of this correlation surface $\zeta(s, t)$ by an isotropic exponential

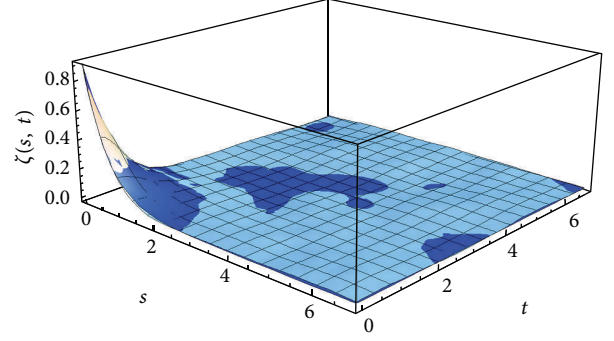


FIGURE 2: 2D correlation function $\zeta(s, t)$ for the Patch 5 (light blue surface). All axes are in units of l_0 , (3). The darker surface is given by the best fit for $\zeta(s, t)$ by an isotropic exponential fitting function $\zeta(r) = \zeta(0, 0) \exp(-r/r_E)$ with $r = \sqrt{s^2 + t^2}$. The best fitting values of the correlation radius r^E are summarized in Tables 1 and 2 for all five patches.

TABLE 1: The parameterization of the extracted correlation functions $\zeta(s, t)$ by anisotropic exponential and power law fitting functions, (6). Rows 1–5 give the data for the individual patches and the last row for the correlation function averaged over all patches.

#	η	$r_s^E, r_t^E, \sigma_E \times 10^2$	$r_s^{\text{PL}}, r_t^{\text{PL}}, u, \sigma_{\text{PL}} \times 10^2$
1	1.03	0.62, 0.63, 1.42	0.45, 0.45, 0.9997, 1.56
2	1.14	0.70, 0.73, 2.69	0.44, 0.46, 0.864, 2.04
3	0.97	0.64, 0.74, 2.71	0.28, 0.31, 0.658, 1.37
4	0.99	0.64, 0.66, 2.35	0.32, 0.34, 0.73, 1.26
5	0.96	0.57, 0.60, 0.83	0.46, 0.48, 1.10, 1.20
Av.	1.02	0.64, 0.67, 1.84	0.38, 0.40, 0.842, 1.33

surface. The figure demonstrates that the anisotropy of the roughness correlation function is noticeable but not very large.

We checked the isotropy of five extracted correlation functions by fitting them to anisotropic exponential and power law fitting functions:

$$\zeta_E = \eta_E^2 \exp \left(-\sqrt{\left(\frac{s}{r_s^E}\right)^2 + \left(\frac{t}{r_t^E}\right)^2} \right), \quad (6)$$

$$\zeta_{\text{PL}} = \frac{\eta_{\text{PL}}^2}{\left(1 + (s/r_s^{\text{PL}})^2 + (t/r_t^{\text{PL}})^2\right)^u}.$$

The best fit parameters are summarized in Table 1.

The first five rows in the table provide the data for the individual patches, while the last row describes the correlation function averaged over all patches. One can make two conclusions. First, the statistical quality of the fit by each fitting function ζ_{fit} , which is measured by σ_{fit} ,

$$\sigma_{\text{fit}}^2 = \frac{\langle (\zeta - \zeta_{\text{fit}})^2 \rangle}{\zeta^2(0, 0)}, \quad (7)$$

for each patch is roughly the same for both fitting functions ζ_E and ζ_{PL} . Second, the anisotropy of the correlation function

TABLE 2: Results of the fit of the extracted correlation functions for five patches and for the averaged correlation function (last row) by the exponential (E), Gaussian (G), and power law (PL) fitting functions, (8)–(10). For each fitting function the table shows the correlation radii $r_{E,G,PL}$ and the quality of the fits σ , (7). The last column shows the calculated parameter $\Phi_{E,G,PL}$ [37] responsible for the exit neutron count.

#	η	$r_E, \sigma_E \times 10^2$	$r_G, \sigma_G \times 10^2$	$r_{PL}, \sigma_{PL} \times 10^2$	$(\Phi_E, \Phi_G, \Phi_{PL}) \times 10^{-3}$
1	1.03	0.62, 1.42	0.49, 3.93	0.66, 2.04	5.44, 3.94, 4.18
2	1.14	0.72, 2.44	0.56, 5.75	0.76, 3.15	6.23, 4.52, 4.78
3	0.97	0.68, 2.61	0.50, 4.94	0.70, 3.23	4.63, 3.46, 3.6
4	0.99	0.65, 2.25	0.49, 4.56	0.68, 2.80	4.92, 3.64, 3.81
5	0.96	0.58, 0.68	0.47, 3.0	0.62, 1.48	4.87, 3.50, 3.75
Av.	1.02	0.65, 1.75	0.50, 4.39	0.69, 2.44	5.22, 3.83, 4.01

as measured by difference in the correlation radii $r_{s,t}$ in s and t directions is of the order of several percent and is small, smaller than the difference between the patches which is rather pronounced. For this reason we neglect the anisotropy and concentrate on analyzing the extracted correlation functions averaged over the angles, $\zeta(x)$, $x = \sqrt{s^2 + t^2}$.

2.3. *Identification of the Correlation Function.* We fitted the correlation functions averaged over the angles with the isotropic exponential, Gaussian, and power law fitting functions:

$$\zeta_E = \eta^2 \exp\left(\frac{-x}{r_E}\right), \quad (8)$$

$$\zeta_G = \eta^2 \exp\left(\frac{-x^2}{2r_G^2}\right), \quad (9)$$

$$\zeta_{PL} = \frac{\eta^2}{(1 + x^2/r_{PL}^2)^{3/2}}. \quad (10)$$

The results of best fits are summarized in Table 2.

Table 2 is structured similarly to Table 1 but has an extra column with $\Phi_{E,G,PL}$ calculated using the fitting functions with parameters from the table. Without going into details, we just mention that Φ is a normalized linewidth for neutrons in the lowest gravitational state and is a complicated integral of the power spectrum $\zeta(\mathbf{q})$. Its value strongly depends not only on the time of flight through the waveguide, dimensionality of roughness, correlation radius, and amplitude of inhomogeneities, but also on the functional form of $\zeta(\mathbf{q})$ [37]. The value of Φ serves here as a descriptor for observables: it determines the exit neutron count for GRANIT-type experiments (see Section 4). In essence, the appropriateness of the choice of the fitting functions should be judged not by the standard deviation σ but by the value of Φ . But which value of Φ from the table is the closest to the “true” value of Φ in experiments with this mirror?

The statistical quality of the fits σ for all three fitting functions are close to each other, while the values of the observables, in this case Φ , are noticeably different. An explanation is simple. A typical correlation function consists of a peak area and long tail. For finite size samples the fluctuation-driven tail is rather fat and does not go to zero at large distances. As a result, the standard deviation σ

between the extracted correlator and *any* reasonable fitting function, which goes to zero relatively fast at large distances, is determined not by the peak area where the fitting functions differ from each other, but by the contributions from the tails, where all the fitting functions are zero. As a result, the values of σ for all three fitting functions are similar, while the values of the observable, Φ , are noticeably different. The main conclusion is that selection of the fitting function could not and should not be judged just by the value of σ , (7). An increase in sample size does not help much: though the size-driven fluctuations and, therefore, σ decrease with increasing sample as $\sqrt{2/N}$ (N is the sample size), the tails get longer with increasing N , and the values of σ go down for all fitting functions in the same way. We will explore this point in more detail in the next section.

There are several ways how to suppress fluctuations and make identification of the correlation function easier. One can average the correlation function over several samples and use the averaged values for identification as in, for example, [38, 39]. This is done in the last row in Tables 1 and 2. This assumes that the correlations are the same in all samples and that any long-range oscillations are non-physical and are purely fluctuation-driven. One can also disregard the tails and use for identification purposes only the peak and its immediate vicinity thus ignoring the long-range tails as spurious. We need to develop a reliable identification procedure. Our recommendation, based on the results of the next section, is given in the beginning of Section 4.

3. Numerical Experiments

The difficulties that we face when trying to identify the roughness correlation function for the rough mirror are typical. The best way to overcome these difficulties would be extracting the correlation functions from profile measurements for surfaces with *known* roughness correlation functions and comparing the results with these known correlators. Unfortunately, it is virtually impossible to prepare the surfaces with the predetermined roughness correlation functions.

The best available alternative is to numerically generate surfaces with the predetermined roughness correlators and extract the correlation function from a numerical experiment which emulates precise scanning measurements of the surface profile. Below we report numerical experiments of this

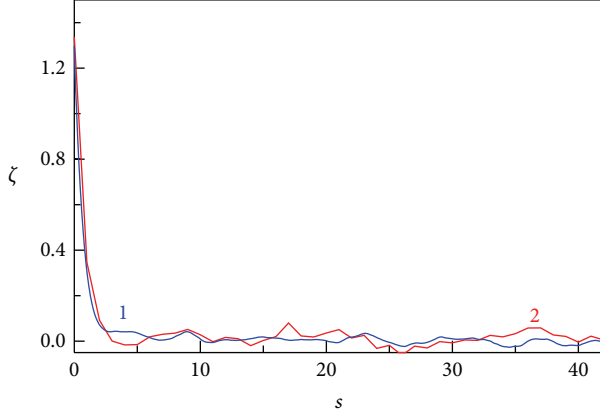


FIGURE 3: The illustration of the fluctuation-driven tails of the correlation function $\zeta(s, 0)$ for the Patch 2 of the actual mirror (curve 1, blue) and for the numerically generated surface with roughness emulating the exponential correlation function with the same amplitude and the correlation radius as in Table 2 (curve 2, red).

type and compare the extracted information with the physical experiments on the rough mirror in Section 2. The results allowed us to better understand the accuracy and pitfalls of the identification procedures.

3.1. Surfaces with any Predetermined Roughness Correlators. We can generate surfaces with any predetermined discrete correlation function $\zeta_{ik} = \zeta(i - k)$. The technique starts from using the Gaussian distribution, which is embedded in most random number generators, for generating uncorrelated random numbers g_i with the δ -type correlation function (white noise), $\langle g_i g_k \rangle = \delta_{ik}$. We then rotate this vector \vec{g} using the rotation matrix $\hat{A} = \hat{\zeta}^{1/2}$. The resulting set of numbers y_i , $\vec{y} = \hat{A}\vec{g}$, exhibits desired correlations, $\langle y_i y_k \rangle = \zeta_{ik}$ (for more details see [36, 37]). Next we “measure” the generated profile $y_i = y(x_i)$ by emulating the scanning technique and extract the “experimental” correlation function. We then try to identify this extracted correlator by fitting it to various fitting functions (in practice, Gaussian, exponential, and power law functions), calculate the observables (for the purpose of this paper, Φ), and compare the results with those obtained using the “true” correlation function ζ_{ik} . Below we report such experiments for both 1D and 2D roughness. For computational reasons the linear sizes of our 2D samples are smaller than in 1D cases, though the overall number of profile points is larger.

The difficulties that we encounter in our numerical experiments are exactly the same as in our analysis of the real mirror in Section 2. The main source of uncertainty is the fluctuations related to the final size of the samples. For illustration, in Figure 3 we plot the fluctuation-driven tails for the extracted roughness correlation function $\zeta(s, 0)$ for Patch 2 of the actual mirror (curve 1, blue) and for the correlation function $\zeta(x)$ for a generated 1D rough surface of the same size (2,500 points; curve 2, red) which emulates roughness with the exponential correlation function $\zeta = \eta^2 \exp(-x/r)$

with $\eta = 1.14$ and $r = 0.72$ as for this patch in Table 2. The similarity between these two fluctuation-driven tails is striking.

Our ability to generate surfaces with roughness emulating any predetermined correlation function allows us to analyze the use of fitting functions for our extracted correlators and to determine whether it is possible to avoid using the fitting functions by inputting the raw correlation data directly into equations for observables (Φ). Some of our findings are summarized in the following two tables.

The quality of the fits σ_G , σ_E , σ_{PL} for all three types of the fitting functions is more or less the same, about 5×10^{-4} , but the results for the physically important parameter $\Phi_{1G,E,PL}$, which predicts the exit neutron count in GRANIT experiments, differ considerably from each other by about 25%. In our numerical experiment, the “true” shape of the correlation function is known to be Gaussian and, not surprisingly, the fitting by the Gaussian function yields the values of Φ_1 very close to the “true” value 23.48. This brings us to an inevitable conclusion that the statistical quality of the fit σ by any reasonable ad hoc fitting function ζ_{fit} , (7), does not predict the quality of physical conclusions obtained using this fitting function. Note that the results for fitting by the power law and exponential correlation functions are relatively close to each other and very different from those for the Gaussian fit. The explanation is simple: the Gaussian function has a much shorter tail.

The last column in Table 3 shows the values of Φ_{1n} which are calculated by inputting the discrete raw correlation data directly into the equations for Φ_1 . In 1D this procedure works better than using the fitting function of the “wrong” shapes $\zeta_{E,PL}$, but still noticeably worse than for the “right” fitting function ζ_G though the statistical quality σ_n of the used spectral decomposition of the raw data σ_n is perfect.

The 2D results (Table 4) are different because of different dimensionality and smaller linear sizes of our samples. Here as an observable, which is used to compare the results, we use Φ_2 which describes the neutron count in experiments with 2D roughness [38, 41]. The generated rough surfaces are emulating the Gaussian roughness with the correlation function $\zeta(|\mathbf{x}|) = \exp(-|\mathbf{x}|^2/8)$ (i.e., $\eta = 1$, $r = 2$) for which $\Phi_2 = 2.58 \times 10^3$. The sample size is 61×61 points. The table contains the results extracted from the best fit of the extracted correlator to the Gaussian, exponential, and power law functions. The Gaussian fit is done independently for the correlation function $\zeta(|\mathbf{x}|)$ averaged over the angles and the 2D correlation function $\zeta(\mathbf{x})$; the results are close to each other. The statistical quality of the fits σ is worse than in the 1D case though the overall number of the data points in our 2D computations is larger (3,600 versus 2,000 points): the linear size of the sample is noticeably smaller while the correlation radius is slightly bigger. Table 4 provides the values of the extracted fitting parameters η and r , values of σ , and, most importantly, the corresponding values of the physical observable Φ_2 . The results for direct use of numerical data without fitting are too unstable to be included in the table; we are not sure whether this is a result of higher dimensionality or smaller linear sizes of the samples. The

TABLE 3: Three numerical runs for 1D surfaces emulate the Gaussian correlation of inhomogeneities $\eta^2 \exp(-x^2/2r^2)$ with $r = 1.19$ and $\eta = 0.119$ (the assumed [37] roughness of the mirror in earlier GRANIT experiments [2–4, 6]). The true value of the observable Φ_1 for such a surface is $\Phi_1 = 23.48$. The extracted correlators are fitted with Gaussian, $\eta_G \exp(-x^2/2r_G)$, exponential, $\eta_E \exp(-x/r_E)$, and power law, $\eta_{PL}/[1 + (x/r_{PL})^2]^{3/2}$ fitting functions. The table contains the best fitting values of $r_{G,E,PL}$, statistical quality of the fits $\sigma_{G,E,PL}$, and the recalculated values of $\Phi_{1G,E,PL}$. The best fitting values of $\eta_{G,E,PL}$ are close to each other and are not listed. The columns with Φ_n and σ_n give the values of Φ_1 and the standard deviation when the spectral decomposition of the raw correlation data is put directly into equations for Φ_1 [37] without using the fitting functions.

#	$r_G, \sigma_G \times 10^4$	$r_E, \sigma_E \times 10^4$	$r_{PL}, \sigma_{PL} \times 10^4$	$\sigma_n \times 10^{17}$	$\Phi_{1G}, \Phi_{1E}, \Phi_{1PL}, \Phi_{1n}$
1	1.19, 5.24	1.59, 5.81	1.44, 5.81	1.92	23.86, 18.19, 18.81, 21.96
2	1.15, 4.49	1.53, 4.56	1.36, 4.64	1.83	23.33, 17.84, 18.65, 21.14
3	1.25, 4.37	1.69, 4.40	1.54, 4.47	1.69	23.56, 17.26, 17.85, 20.96

TABLE 4: The same as in Table 3 for generated 2D rough Gaussian surfaces with $r = 2$ and $\eta = 1$. The expected value of $\Phi_2 \approx 2.58 \times 10^3$. The table contains the extracted fitting parameters $\eta_{G,E,PL}^{\text{fit}}$ and $r_{G,E,PL}^{\text{fit}}$, together with $\sigma_{G,E,PL}$, and the recalculated values of Φ_2 . The fourth row gives the results for the correlation function averaged over 10 independent runs.

#	$\eta_G, r_G, \sigma \times 10^2$	$\eta_E, r_E, \sigma \times 10^2$	$\eta_{PL}, r_{PL}, r_0^{\text{PL}}, \sigma \times 10^2$	$(\Phi_2^G, \Phi_2^E, \Phi_2^{\text{PL}}) \times 10^{-3}$
1	1.04, 1.97, 5.7	1.14, 2.04, 6.2	1.08, 2.45, 5.9	2.81, 5.51, 1.68
2	1.10, 1.80, 6.5	1.20, 1.76, 7.4	1.14, 2.15, 7.2	3.23, 6.56, 1.99
3	0.90, 1.84, 4.1	0.98, 2.05, 4.3	0.94, 2.40, 4.1	2.18, 4.06, 1.28
Av.	1.00, 1.98, 1.9	1.10, 2.11, 2.9	1.05, 2.49, 2.4	2.60, 5.05, 1.57

table contains results of three numerical runs and (the fourth row) the average for ten numerical runs.

3.2. Surfaces with Quantized Amplitudes of Inhomogeneities: Ising Roughness. The above approach allow us to create and analyze random rough surfaces with arbitrary correlation functions. The drawback of our procedure is that while it is appropriate for macroscopic roughness, it cannot produce roughness with quantized amplitudes which is desirable for the study of atomic-scale roughness.

It might be impossible to computationally emulate a random rough surface with an integer profile $y(x_i)$ with an *arbitrary* predetermined correlation function $\tilde{\zeta}(i-k) = \langle y_i y_k \rangle$ except, of course, for “classical” surfaces with very large amplitude of roughness. However, several specific “quantized” correlators can still be generated using Monte Carlo simulations for spin lattice models with various Hamiltonians. This might help in extracting the proper correlation functions from experimental data on the surface profile based on realistic assumptions on the interaction of the surface defects. This can also help to guess which correlation functions to use in theoretical calculations. Needless to say, many of the lattice models produce the correlation functions which are exponential at large distances and have complicated, often analytically unresolved structure in the peak area.

Unfortunately, the universe of the correlation functions which are accessible in this way is limited by the number of known exactly solvable lattice models, mostly in 1D, some of which may have little resemblance to real surfaces. It is even unclear whether there are any restrictions on allowed forms of the correlation functions. In 2D even the simplest models, such as the Ising model, lead to the correlation functions for which we do not have explicit analytical expressions making them virtually useless for our purposes.

The simplest example [36] is, of course, the ferromagnetic Ising lattice $y_i = \pm 1$ for which the correlation function is determined by the attractive coupling constant J in the Hamiltonian (or, what is the same, by the Boltzmann factors $\exp(\pm 2J/kT)$). In the 1D case the correlation function is exponential:

$$\zeta_E(x) = \eta^2 \exp\left(-\frac{x}{r}\right), \quad r = \frac{1}{2} \exp\left(\frac{2J}{kT}\right). \quad (11)$$

The correlation function for the 2D Ising model, though known in principle, [40, 42], is described by a set of complicated equations involving elliptical integrals.

In 1D computations we used 1000 positions x_i and performed 10^6 Monte Carlo cycles. The correlation function $\zeta(s)$ should emulate function (11) with $r = R/l_0 = 1.19$ and $\eta = \ell/l_0 = 0.119$ as in the earlier GRANIT experiments. The results for five runs are summarized in Table 5. The true value of Φ_1 for the exponential correlation function with $r = 1.19$ and $\eta = 0.119$ is $\Phi_E^{\text{th}} = 19.5$ (with the same values of r and η , $\Phi_G^{\text{th}} = 23.7$ and $\Phi_{PL}^{\text{th}} = 20.4$). Since the simulation is based on the Ising model with spins ± 1 , the extracted average amplitudes of roughness differ from $\eta = 0.119$ by less than 1% for all fitting functions and there is no need to present the values of $\eta_{E,G,PL}$. Of course, the fit using the exponential correlator provides the best values for Φ_1 though here again the values of σ for all fitting functions are practically indistinguishable. Of the other two fits, it is not clear why the power law fit provides much better values of Φ_1 than the Gaussian one. The last column in the table also shows the values of Φ_n which are obtained by direct spectral analysis with $N/2$ harmonics of the raw correlation data without any fitting. These data display the worst agreement with $\Phi_E^{\text{th}} = 19.5$, while the value of σ_n is by 13 orders of magnitude better than σ for any of our fitting functions. The explanation is the

TABLE 5: Five Monte Carlo runs for the 1D Ising model. The “true” correlation function is exponential with $r = 1.19$ and $\eta = 0.119$ and yields $\Phi_E^{\text{th}} = 19.5$. The correlation functions extracted from the generated rough surfaces were fitted with the exponential, Gaussian, and power law functions. The Table contains the best fitting values of $r_{E,G,PL}$ and the corresponding values of $\sigma_{E,G,PL}$ and $\Phi_{E,G,PL}$. Since the simulation is based on the Ising model with spins ± 1 , the best fitting values of η differed from 0.119 by less than 1% for all fitting functions. The values of Φ_n were obtained by direct spectral decomposition of the raw correlation data. The size of the sample was $N = 1000$ and we performed 10^6 Metropolis cycles.

#	$r_E, \sigma_E \times 10^4$	$r_G, \sigma_G \times 10^4$	$r_{PL}, \sigma_{PL} \times 10^4$	$\sigma_n \times 10^{17}$	$\Phi_1^E, \Phi_1^G, \Phi_1^{PL}, \Phi_n$
1	1.27, 6.69	0.85, 6.93	1.26, 6.72	3.79	18.6, 27.4, 19.6, 25.8
2	1.23, 6.83	0.88, 6.94	1.25, 6.84	1.49	19.1, 26.8, 19.7, 26.2
3	1.04, 6.51	0.73, 6.74	1.07, 6.54	2.82	20.7, 30.2, 21.4, 27.3
4	1.18, 6.65	0.87, 6.71	1.23, 6.62	3.01	19.7, 27.1, 20.0, 26.1
5	0.94, 6.44	0.74, 6.42	1.03, 6.38	1.91	22.2, 29.8, 21.9, 27.7

TABLE 6: Results for three rough surfaces generated using the 2D Ising model (the first three rows) and for the correlation function averaged over ten runs (the last row). The Monte Carlo simulations have been done at $T = 1.2T_c$ with 10^6 Metropolis cycles. The surface size is 101×101 . The Table is arranged similarly to Table 2. The table contains the best fitting values of $r_{E,G,PL}$ and the corresponding values of $\sigma_{E,G,PL}$ and $\Phi_2^{E,G,PL}$. The results for the exponential fits $\Phi_2^{E1,2}$ for $\zeta(|\mathbf{x}|)$ and $\zeta(\mathbf{x})$ should be the closest to the true physical parameters.

#	$r_{E1}, \sigma_{E1} \times 10^2$	$r_{E2}, \sigma_{E2} \times 10^2$	$r_G, \sigma_G \times 10^2$	$r_{PL}, \sigma_{PL} \times 10^2$	$(\Phi_2^{E1}, \Phi_2^{E2}, \Phi_2^G, \Phi_2^{PL}) \times 10^3$
1	1.56, 2.03	1.60, 2.75	1.06, 2.41	1.55, 2.12	3.37, 3.32, 2.53, 2.58
2	1.43, 1.56	1.43, 2.27	1.06, 1.89	1.48, 1.63	2.53, 2.53, 2.53, 2.64
3	1.53, 1.66	1.53, 2.49	1.11, 2.04	1.57, 1.75	3.40, 3.40, 2.48, 2.57
Av.	1.54, 0.69	1.57, 0.89	1.10, 1.42	1.57, 0.91	3.39, 3.36, 2.49, 2.57

same as before: the full set of raw data is dominated by the long correlation tails which come from the fluctuations.

The last table, Table 6, presents results for three rough surfaces generated using the 2D Ising model plus a row for the correlation function averaged over ten runs. The observable here is again Φ_2 .

The computations are done above the phase transition, $T = 1.2T_c$. At this temperature the correlation function is, probably, still close to the exponential, but it is not clear how close. Here we do not know exactly what should be the “true” value of Φ_2 but expect that the exponential correlator provides the best estimate. At this temperature the domains are relatively small and the relaxation times are manageable. The size of the surface is relatively large, 101×101 , and each computation runs 10^6 Metropolis cycles. The table is arranged similarly to Table 5. The values of σ for all fitting functions are again close to each other, while the values of Φ_2 and r are noticeably different. The results for the exponential fit should be the closest to the true physical parameters. The first column for the exponential fitting gives results obtained from the flat file $\zeta(|\mathbf{s}|)$. The second column gives the results of fitting $\zeta(\mathbf{s})$ by the 2D exponential function. For the Gaussian and power law correlators, columns 3 and 4, we used only the flat files $\zeta(|\mathbf{s}|)$. What is somewhat surprising is that the results for our choice of the power law correlator, which is the Fourier image of the exponential one, are again close to those using the exponential fit. What is even more surprising, the values of Φ_2 for the power law fit using $\zeta(|\mathbf{s}|)$ are systematically closer to the exponential fit using 2D $\zeta(\mathbf{s})$ than to the exponential fit using $\zeta(|\mathbf{s}|)$. The Gaussian fit yields very different Φ_2 , while the value of σ is comparable with the others. The direct spectral analysis of the raw correlator data again yields the worst physical results and changes from

run to run; these results are not even worth listing. The spectral analysis of the correlation function averaged over ten runs worked slightly better than the Gaussian fit. The difference between results obtained using different fitting functions once again illustrates the uncertainty in comparing computational and experimental data to theoretical results. One should have at least some information about the shape of the “true” correlation function.

4. Experimental Consequences

The main conclusion from the previous sections is that the difficulties that we experience trying to identify the correlation function for the actual mirror are exactly the same as in our numerical experiments. Our extensive numerical data show that the best way of identification seems to be the averaging over several samples in combination with the graphical and numerical analysis of the peak area without much reliance on the overall standard deviation σ . We do not recommend putting the discrete raw correlation data directly into equations for the observables.

Our reluctant conclusion from the analysis of experimental data on the roughness of the actual mirror in Section 2 is that its roughness correlation function is close to the isotropic exponential function (8) with the amplitude $\eta = 1.02$ and the correlation radius $r = 0.65$. This yields the value of $\Phi_2 \approx 5.22 \times 10^3$. The uncertainty in parameters is about 10% because of the presence of bad points in the data sets, residual anisotropy, and, most of all, difference in values between the patches.

Knowing the value of Φ_2 we can predict the exit neutron count in experiment with this mirror. Luckily, the uncertainty in Φ_2 in this range of values, in contrast to smaller Φ in

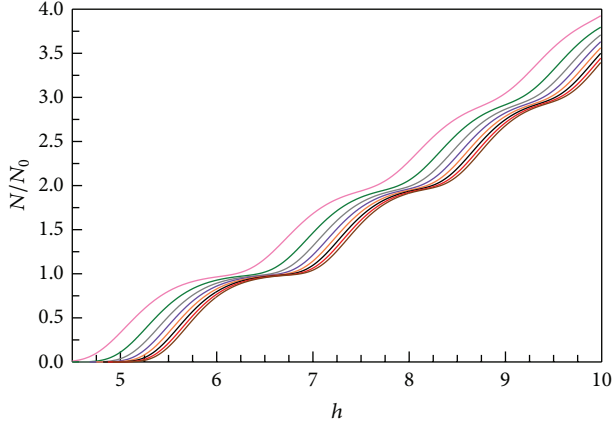


FIGURE 4: The exit neutron count N_e/N_0 as a function of the slit width h for several values of Φ_2 close to 5×10^3 (N_0 is the number of neutrons entering the slit in each quantum state). Eight curves from left to right correspond to $\Phi_2 \times 10^{-3} = 1; 2; 3; 4; 5; 6; 7; 8$; neutron count decreases with increasing Φ_2 .

[37, 43, 44], does not affect the dependence of the exit neutron count on the slit width much (see Figure 4). Eight curves in the figure correspond to the dependence of the exit neutron count N/N_0 on the slit width h for $\Phi_2 \times 10^{-3} = 1; 2; 3; 4; 5; 6; 7; 8$ (N_0 is the number of neutrons in each state entering the slit). All curves in Figure 4 demonstrate the well pronounced predicted quantum steps which is a very good news for the ongoing experiment.

There are factors that might limit the accuracy of this prediction. On the theoretical side, the value of the average amplitude of roughness η is too large considering the main theoretical assumption $\eta \ll r, h$. Also, there is still some uncertainty in the correlation parameters.

From the point of view of experiment, a large value of η is also not very good. It results in a noticeable broadening of the levels and in inability to measure precisely the height of the reference plane and, therefore, the width of the slit. The latter factor leads to uncertainty in the values of quantized energy levels thus limiting the use of the setup for precision measurements of fundamental forces.

In addition, both theory and experiment require better information on the distribution of neutrons entering the slit over the quantum states.

5. An Alternative Design: Ising Mirror

Many of the sources of errors mentioned above disappear if one uses an alternative mirror design based on the 1D Ising model described in Section 3. In essence, we are proposing to make the rough mirror like an interferometric grating with trenches of constant depth but with randomly varying widths and separations [36]. Such an Ising grating can be easily generated computationally as it is done in Section 3. Since the characteristic length is macroscopic, $l_0 = \hbar^{2/3}(2m^2g)^{-1/3} \sim 5.871 \mu\text{m}$, the generated pattern can then be transferred to the mirror surface.

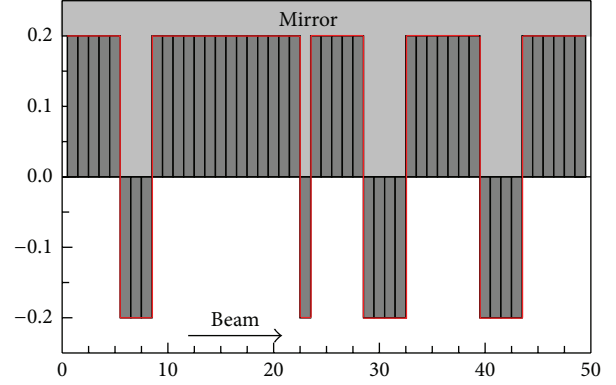


FIGURE 5: A fragment of the proposed rough upper mirror based on Monte Carlo simulations (10^6 cycles) for the 1D Ising model with $J/kT \approx 0.7$. Thick red line is the surface profile and dark bars are the ‘‘Ising spins.’’ Mirror material is above the red line (the filled area). The amplitude of roughness $\eta = 0.2$, the correlation radius $r = 2$, and the value of $\Phi_1 \approx 43.5$. Both axes are in units of $l_0 = \hbar^{2/3}(2m^2g)^{-1/3} \sim 5.871 \mu\text{m}$. The vertical scale is about 100 times smaller than the horizontal one. The value of η can be changed simply by rescaling the vertical axis.

An element of such a mirror is plotted in Figure 5. The thick (red) line shows the surface of the mirror (since this is an upper mirror for a GRANIT-like experiment, the mirror material is above the red line and the neutron beam is propagating below it). The dark rectangles of the width l_0 are the ‘‘Ising spins.’’ Both axes are measured in units of l_0 , but the vertical scale is about 100 times larger than the horizontal one and the roughness is actually very mild.

Since the real mirror is continuous in contrast to the discrete Ising model, the roughness correlation function coincides with the Ising exponent (11) only in the integer points and is slightly different elsewhere:

$$\zeta(x) = \eta^2 \left[\exp\left(-\frac{\lfloor x \rfloor}{r}\right) + (x - \lfloor x \rfloor) \times \left(\exp\left(-\frac{\lfloor x \rfloor}{r}\right) - \exp\left(-\frac{\lfloor x \rfloor}{r}\right) \right) \right]. \quad (12)$$

The neutron count predictor Φ_1 for the correlation function (12) can be calculated only numerically. It differs from the one for a purely exponential function by not more than 5%. The values of Φ_1 with $r = 2$ and $\eta = 0.2 \div 0.4$ are in the $42.5 \div 170$ range with the original waveguide parameters and in the $30.3 \div 121.5$ range with the new ones. Because the amplitude of roughness is quite small, these values are much smaller than the ones in Figure 4 and the quantum steps are less pronounced (Figure 6).

Most of the factors, which are listed in the previous section as affecting the accuracy, disappear for this design. The width of the slit can be easily measured and the energy levels are much better defined. The design is easily scalable in both vertical and horizontal directions and creates a well-controlled environment.

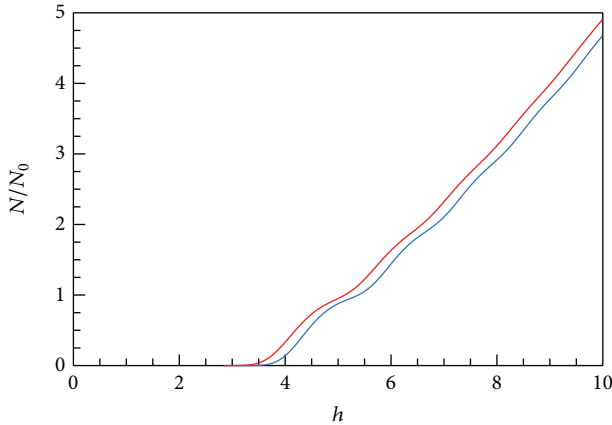


FIGURE 6: Predicted exit neutron count $N(h)/N_0$ for the mirror similar to the one in Figure 5 with roughness generated using Monte Carlo simulations for the 1D Ising model. The roughness amplitudes are $\eta = 0.3$ (red) and $\eta = 0.4$ (blue) and the correlation radius $r = 2$. One can make steps more pronounced by further increasing η .

6. Summary and Conclusions

In summary, we analyzed roughness of the rough mirror built as a gravitational quantum state selector for a new cycle of GRANIT experiments. We extracted the correlation parameters of this mirror which are important for determining its scattering properties. The straightforward identification of the correlation function $\zeta(\mathbf{q})$ was impossible because of the unavoidable fluctuations associated with the finite sizes of the samples. All reasonable fitting functions ζ_{fit} exhibited more or less the same statistical quality of the fit σ , (7) but led to considerably different predictions for the observables.

Independently, we performed a series of numerical experiments aimed at identification of the correlation function extracted by the same techniques as used for the actual mirror from computationally generated rough surfaces with predetermined $\zeta(\mathbf{q})$. Remarkably, the difficulties in the identification of the correlation functions in our numerical experiments were the same as we experienced with the real rough mirror and were associated with similar fluctuation-driven fat tails. However, since in numerical experiments we knew the true correlation functions, we were able to hone our identification techniques.

In our numerical experiments we also tried avoiding the use of fitting functions by inputting the spectral decomposition of extracted raw correlation data directly into the equations for the observables. This option turned out to be marginally acceptable for 1D rough surfaces and did not work at all for 2D surfaces. Our main conclusion here is that the direct use of the raw correlation data is worse than the careful analysis of the fitting functions.

The results of our numerical experiments led us to believe that the proper identification of $\zeta(\mathbf{q})$ required, in addition to measuring the statistical quality of the fittings σ , averaging of the correlation functions extracted from several independent samples plus graphical and numerical analysis of the averaged correlator in the peak area. Based on this experience, we

identified the correlation function for the actual mirror as an exponential one and obtained its parameters. This information allowed us to predict the exit neutron count for new GRANIT experiments utilizing this rough mirror as a function of the distance between the flat and rough mirrors. The predicted neutron count exhibited well-formed quantum steps which would allow us to use the setup for planned measurements of fundamental forces.

We also propose a radically new design for rough mirrors—what we called the Ising mirrors—for use as state selectors. The design is based on the Monte Carlo simulation of a 1D random pattern based on the 1D Ising model which is then transferred as a grating onto the actual mirror. Such transfer is feasible when the characteristic length is macroscopic as it is for the gravitational quantum state of neutrons in GRANIT experiments (about $6 \mu\text{m}$). Such Ising mirror should look like an interference grating of straight 1D trenches of the same depths but with randomly varying widths and separations. Since the correlation function for such a random surface is known, one can easily get the reliable predictors for the observables which depend on scattering parameters. In addition, the environment is much better controllable than for usual rough mirrors for which the random variations in profile heights from point to point makes it extremely difficult, if not impossible, to determine the reference plane and accurately measure the height of the mirror.

Conflict of Interests

The authors declare that they have no conflict of interests regarding the publication of this paper.

Acknowledgments

The results of this paper were reported at GRANIT-2014 Workshop (Les Houches, France, March 2–7, 2014). One of the authors (A. E. Meyerovich) is grateful to the organizers and other members of GRANIT collaboration for the hospitality and support during the Workshop.

References

- [1] V. V. Nesvizhevsky, H. Börner, A. M. Gagarski et al., “Search for quantum states of the neutron in a gravitational field: gravitational levels,” *Nuclear Instruments and Methods in Physics Research A: Accelerators, Spectrometers, Detectors and Associated Equipment*, vol. 440, no. 3, pp. 754–759, 2000.
- [2] V. V. Nesvizhevsky, H. G. Börner, A. K. Petukhov et al., “Quantum states of neutrons in the Earth’s gravitational field,” *Nature*, vol. 415, no. 6869, pp. 297–299, 2002.
- [3] V. V. Nesvizhevsky, H. G. Börner, A. M. Gagarski et al., “Measurement of quantum states of neutrons in the Earth’s gravitational field,” *Physical Review D*, vol. 67, Article ID 102002, 2003.
- [4] V. V. Nesvizhevsky, A. K. Petukhov, H. G. Börner et al., “Study of the neutron quantum states in the gravity field,” *The European Physical Journal C—Particles and Fields*, vol. 40, no. 4, pp. 479–491, 2005.

- [5] S. Baessler, “Gravitationally bound quantum states of ultracold neutrons and their applications,” *Journal of Physics G*, vol. 36, Article ID 104005, 2009.
- [6] V. V. Nesvizhevsky, “Near-surface quantum states of neutrons in the gravitational and centrifugal potentials,” *Physics-Usp ekhi*, vol. 53, no. 7, pp. 645–675, 2010.
- [7] M. Kreuz, V. V. Nesvizhevsky, P. Schmidt-Wellenburg et al., “A method to measure the resonance transitions between the gravitationally bound quantum states of neutrons in the GRANIT spectrometer,” *Nuclear Instruments and Methods in Physics Research A*, vol. 611, no. 2-3, pp. 326–330, 2009.
- [8] T. Jenke, P. Geltenbort, H. Lemmel, and H. Abele, “Realization of a gravity-resonance-spectroscopy technique,” *Nature Physics*, vol. 7, pp. 468–472, 2011.
- [9] G. Ichikawa, S. Komamiya, Y. Kamiya et al., “Observation of the spatial distribution of gravitationally bound quantum states of ultracold neutrons and its derivation using the Wigner function,” *Physical Review Letters*, vol. 112, Article ID 071101, 2014.
- [10] P. Schmidt-Wellenburg, J. Barnard, P. Geltenbort et al., “Efficient extraction of a collimated ultra-cold neutron beam using diffusive channels,” *Nuclear Instruments and Methods in Physics Research A: Accelerators, Spectrometers, Detectors and Associated Equipment*, vol. 577, no. 3, pp. 623–625, 2007.
- [11] J. Barnard and V. Nesvizhevsky, “Analysis of a method for extracting angularly collimated UCNs from a volume without losing the density inside,” *Nuclear Instruments and Methods in Physics Research A*, vol. 591, no. 2, pp. 431–435, 2008.
- [12] L. A. Chizhova, S. Rotter, T. Jenke et al., “Vectorial velocity filter for ultracold neutrons based on a surface-disordered mirror system,” *Physical Review E*, vol. 89, Article ID 032907, 2014.
- [13] V. V. Nesvizhevsky, A. Y. Voronin, R. Cubitt, and K. V. Protasov, “Neutron whispering gallery,” *Nature Physics*, vol. 6, no. 2, pp. 114–117, 2010.
- [14] V. V. Nesvizhevsky, “Polished sapphire for ultracold-neutron guides,” *Nuclear Instruments and Methods in Physics Research A*, vol. 557, no. 2, pp. 576–579, 2006.
- [15] V. V. Nesvizhevsky, G. Pignol, K. V. Protasov et al., “Comparison of specularly reflecting mirrors for GRANIT,” *Nuclear Instruments and Methods in Physics Research A*, vol. 578, no. 2, pp. 435–438, 2007.
- [16] A. Y. Voronin, P. Froelich, and V. V. Nesvizhevsky, “Gravitational quantum states of Antihydrogen,” *Physical Review A*, vol. 83, Article ID 032903, 2011.
- [17] A. Y. Voronin, V. V. Nesvizhevsky, and S. Reynaud, “Whispering-gallery states of antihydrogen near a curved surface,” *Physical Review A*, vol. 85, Article ID 014902, 2012.
- [18] G. Dufour, P. Debu, A. Lambrecht, V. V. Nesvizhevsky, S. Reynaud, and A. Yu. Voronin, “Shaping the distribution of vertical velocities of antihydrogen in GBAR,” *The European Physical Journal C*, vol. 74, p. 2731, 2014.
- [19] A. Y. Voronin et al., *Advances in High Energy Physics*, 2014.
- [20] G. Chardin, P. Grandemange, D. Lunney et al., “CERN-SPSC-2011-029. SPSC-P-342,” Tech. Rep., CERN, Geneva, Switzerland, 2011.
- [21] P. Crivelli, “Can we observe the gravitational quantum states of positronium?” *Advances in High Energy Physics*, 2014.
- [22] S. Baessler, M. Beau, M. Kreuz et al., “The GRANIT spectrometer,” *Comptes Rendus Physique*, vol. 12, no. 8, pp. 707–728, 2011.
- [23] V. V. Nesvizhevsky, “Gravitational quantum states of neutrons and the new granit spectrometer,” *Modern Physics Letters A*, vol. 27, no. 5, Article ID 1230006, 2012.
- [24] S. Baessler et al., *Advances in High Energy Physics*, 2014.
- [25] P. Schmidt-Wellenburg, K. H. Andersen, P. Courtoisa et al., “Ultracold-neutron infrastructure for the gravitational spectrometer GRANIT,” *Nuclear Instruments and Methods in Physics Research A*, vol. 611, no. 2-3, pp. 267–271, 2011.
- [26] I. Antoniadis, S. Baessler, O. Bertolami et al., “Workshop GRANIT-2010, 14–19 February 2010, Les Houches, France,” *Comptes Rendus Physique*, vol. 12, no. 8, pp. 703–706, 2011.
- [27] I. Antoniadis, S. Baessler, V. V. Nesvizhevsky et al., “Quantum gravitational spectroscopy with ultracold systems,” *Advances in High Energy Physics*. In press.
- [28] A. E. Meyerovich and A. Stepaniants, “Quantized systems with randomly corrugated walls and interfaces,” *Physical Review B*, vol. 60, no. 12, pp. 9129–9144, 1999.
- [29] A. E. Meyerovich and I. V. Ponomarev, “Surface roughness and size effects in quantized films,” *Physical Review B*, vol. 65, Article ID 155413, 2002.
- [30] Y. Y. Cheng and A. E. Meyerovich, “Mode coupling in quantized high-quality films,” *Physical Review B*, vol. 73, Article ID 85404, 2006.
- [31] J. A. Ogilvy and J. R. Foster, “Rough surfaces: gaussian or exponential statistics?” *Journal of Physics D: Applied Physics*, vol. 22, no. 9, article 1243, 1989.
- [32] A. Fubel, M. Zech, P. Leiderer, J. Klier, and V. Shikin, “Analysis of roughness of Cs surfaces via evaluation of the autocorrelation function,” *Surface Science*, vol. 601, no. 7, pp. 1684–1692, 2007.
- [33] J. A. Stroschio and W. J. Kaiser, Eds., *Scanning Tunneling Microscopy*, vol. 27 of *Methods of Experimental Physics*, Academic Press, New York, NY, USA, 1993.
- [34] R. C. Munoz, G. Vidal, M. Mulsow et al., “Surface roughness and surface-induced resistivity of gold films on mica: application of quantitative scanning tunneling microscopy,” *Physical Review B*, vol. 62, no. 4686, 2000.
- [35] I. Kurganskaya, A. Luttge, and A. R. Barron, *The Application of VSI (Vertical Scanning Interferometry) to the Study of Crystal Surface Processes*, Connexions, July 2009, <http://cnx.org/contents/2515fd85-46bf-42d5-8713-018032a6eb77@4>.
- [36] M. Escobar and A. E. Meyerovich, “Applications and identification of surface correlations,” <http://arxiv.org/abs/1404.1291>.
- [37] M. Escobar and A. E. Meyerovich, “Beams of gravitationally bound ultracold neutrons in rough waveguides,” *Physical Review A*, vol. 83, Article ID 033618, 2011.
- [38] M. Escobar and A. E. Meyerovich, “Quantum transport equation for systems with rough surfaces and its application to ultracold neutrons in quantizing gravity field,” *Journal of Experimental and Theoretical Physics*, to be published.
- [39] M. E. Robles, C. A. Gonzalez-Fuentes, R. Henriquez et al., “Resistivity of thin gold films on mica induced by electron-surface scattering: application of quantitative scanning tunneling microscopy,” *Applied Surface Science*, vol. 258, no. 8, pp. 3393–3404, 2012.
- [40] J. D. Johnson, S. Krinsky, and B. M. McCoy, “Vertical-arrow correlation length in the eight-vertex model and the low-lying excitations of the X-Y-Z Hamiltonian,” *Physical Review A*, vol. 8, no. 5, pp. 2526–2547, 1973.
- [41] M. Escobar and A. Meyerovich, “Quantized ultracold neutrons in rough waveguides: GRANIT experiments and beyond,” *Advances in High Energy Physics*. In press.
- [42] H. Cheng and T. T. Wu, “Theory of toeplitz determinants and the spin correlations of the two-dimensional ising model. III,” *Physical Review*, vol. 164, no. 2, pp. 719–735, 1967.

- [43] A. E. Meyerovich and V. V. Nesvizhevsky, "Gravitational quantum states of neutrons in a rough waveguide," *Physical Review A*, vol. 73, Article ID 063616, 2006.
- [44] R. Adhikari, Y. Cheng, A. E. Meyerovich, and V. V. Nesvizhevsky, "Quantum size effect and biased diffusion of gravitationally bound neutrons in a rough waveguide," *Physical Review A*, vol. 75, Article ID 063613, 2007.

Research Article

Quantized Ultracold Neutrons in Rough Waveguides: GRANIT Experiments and Beyond

M. Escobar and A. E. Meyerovich

Department of Physics, University of Rhode Island, Kingston, RI 02881-0817, USA

Correspondence should be addressed to A. E. Meyerovich; alexander_meyerovich@uri.edu

Received 12 May 2014; Accepted 9 July 2014; Published 23 July 2014

Academic Editor: Stefan Baessler

Copyright © 2014 M. Escobar and A. E. Meyerovich. This is an open access article distributed under the Creative Commons Attribution License, which permits unrestricted use, distribution, and reproduction in any medium, provided the original work is properly cited. The publication of this article was funded by SCOAP³.

We apply our general theory of transport in systems with random rough boundaries to gravitationally quantized ultracold neutrons in rough waveguides as in GRANIT experiments (ILL, Grenoble). We consider waveguides with roughness in both two and one dimensions (2D and 1D). In the biased diffusion approximation the depletion times for the gravitational quantum states can be easily expressed via each other irrespective of the system parameters. The calculation of the exit neutron count reduces to evaluation of a single constant which contains a complicated integral of the correlation function of surface roughness. In the case of 1D roughness (random grating) this constant is calculated analytically for common types of the correlation functions. The results obey simple scaling relations which are slightly different in 1D and 2D. We predict the exit neutron count for the new GRANIT cell.

1. Introduction

One of the most interesting recent achievements in neutron physics is a series of GRANIT [1–4] and GRANIT-inspired [5–7] experiments aimed at detection of quantization of neutron motion by the Earth gravitational field. The experiment hinges on sending a beam of ultracold neutrons between rough and flat mirrors. The rough mirror scatters away and, eventually, absorbs the neutrons in higher gravitational quantum states leaving only the particles in the lowest states which reach the neutron counter. The observation of these quantized ultralow energy levels in the peV range opens a door to using neutrons for probing weak fundamental forces. Success of these experiments stimulates similar proposals for studying atomic and antimatter beams [8–13].

Another potential application area is the use of such experiment as a test for a quantum transport theory in systems with random rough boundaries (see, for example, [14–23]; a brief review of relevant theoretical methods can be found in the beginning of [24]). The neutrons are sensitive only to geometrical and statistical properties of random surface inhomogeneities and their behavior in the rough

waveguide can serve as a perfect application of our transport theory including a model-free description of the GRANIT experiments which is the main goal of this paper. Some of our earlier results for a neutron waveguide with 1D roughness (a mirror with random grating) can be found in [25, 26].

2. General Equations

Recently we developed a consistent perturbative approach to quantum transport along rough surfaces [24]. Within our approach, the roughness-driven transition probabilities $W_{j,j'}(\mathbf{q} - \mathbf{q}')$ between the states $(j, \mathbf{q}) \rightarrow (j', \mathbf{q}')$ decouple into a product of the Fourier image of the correlation function of surface roughness $\zeta(\mathbf{q} - \mathbf{q}')$ and the boundary values of the wave functions in the absence of roughness (\mathbf{q} is the particle momentum along the surface; j, j' are the quantum numbers describing the spatial quantization for confined motion perpendicular to the walls). In essence, the correlation function of surface roughness plays the role similar to the impurity cross-section for transport in systems with bulk impurities.

In the case of neutron beams propagating between one rough mirror and one flat mirror, the transition probabilities have the form

$$W_{jj'}(\mathbf{q}, \mathbf{q}') = \zeta(\mathbf{q} - \mathbf{q}') U_c^2 |\Psi_j(H)|^2 |\Psi_{j'}(H)|^2, \quad (1)$$

where $\Psi_j(H)$ is the value of the wave function in quantum state j on the mirror in the absence of roughness and U_c is the neutron absorption barrier for the mirror material. If the absorption barrier is very high, $U_c \rightarrow \infty$ (1) becomes

$$W_{jj'} = \frac{1}{4m^2} \zeta(\mathbf{q} - \mathbf{q}') |\Psi_j(H)|^2 |\Psi_{j'}(H)|^2. \quad (2)$$

The wave functions Ψ_j and the gravitational quantum states ϵ_{jq} of neutrons between two horizontal mirrors are described in detail in [25, 27]. The transition probabilities $W_{jj'}(\mathbf{q}, \mathbf{q}')$ determine the collision operator in the transport equation which in this case is a set of coupled Boltzmann-like equations for the distribution functions n_{jq} :

$$\begin{aligned} \partial_t n_{jq} = 2\pi \sum_{j'} \int W_{jj'}(\mathbf{q}, \mathbf{q}') \\ \times [n_{j'q'} - n_{jq}] \delta(\epsilon_{jq} - \epsilon_{j'q'}) \frac{d^2 q'}{(2\pi\hbar)^2}. \end{aligned} \quad (3)$$

The contribution from transitions to the states within continuous spectrum above the absorption threshold U_c , for which there are no reverse processes, is negligible [25]. Integration with the energy δ -function in (3) reduces these equations in the relaxation time approximation $n_{jq}(\mathbf{q}) = \delta(q - q_j) N_j$ to

$$\begin{aligned} \partial_t N_j = \frac{m}{2\pi} \sum_{j'} \int d\theta [W_{jj'}(|\mathbf{q}_j - \mathbf{q}_{j'}|) N_{j'} \\ - W_{j'j}(|\mathbf{q}_j - \mathbf{q}_{j'}|) N_j], \end{aligned} \quad (4)$$

where $q_j^2/2m = E - \epsilon_j$ and θ is the angle between \mathbf{q}_j and $\mathbf{q}_{j'}$.

We use the dimensionless variables, which are common to the field (for details see [25]). All distances are measured in units of l_0 , where $l_0 = \hbar^{2/3} (2m^2 g)^{-1/3} \sim 5.871 \mu\text{m}$ is the size of the lowest quantum state for neutrons in the *infinite* gravitational trap (open geometry without an upper mirror). The dimensionless distance between the mirrors $h = H/l_0$ in experiment typically does not go down below 2. The average amplitude and the correlation radius of surface roughness $\eta = \ell/l_0$ and $r = R/l_0$ are usually within the 0.1 ÷ 1 range. The energies are scaled by $e_0 = mgl_0 \sim 0.602 \text{ peV} \sim 9.6366 \times 10^{-32} \text{ J}$ which is the energy of a neutron in the lowest gravitational quantum state. The quantized levels in the gravity field $\lambda_j(h) = \epsilon_j(H)/e_0$ start from about 2. In these units, the typical kinetic energy of particles in the beam $\epsilon = E/e_0$ and the absorption threshold $u_c = U_c/e_0$ are very large, $\epsilon, u_c \sim 10^5$, and low gravitational states $\lambda_j \ll \epsilon$ are not sensitive to the behavior of the potential near the absorption threshold u_c . Velocities (momenta) along the wall v_j in the

beam direction x are measured in units of $v_0 = \sqrt{2gl_0} = \hbar/ml_0 \sim 1.073 \times 10^{-2} \text{ m/s}$, $\beta_j = v_j/v_0 = \sqrt{\epsilon - \lambda_j} \equiv q_j l_0$. The characteristic times can be measured in units of τ_0 ,

$$\frac{1}{\tau_0} = \frac{\sqrt{2\pi} \hbar}{4m l_0^2} \approx 1148.7 \text{ s}^{-1}, \quad (5)$$

which provides the scale for the oscillation frequency of neutrons in the gravitational well. In the original GRANIT cell [1–3] $u_c/\epsilon \sim 0.16$ and the time of flight of neutrons through the cell t_L is $t_L/\tau_0 \approx 23$. In the new cell [28] $u_c \sim \epsilon$ and $t_L/\tau_0 \approx 26$.

Diffusion of neutrons between discrete states j has a strong directional bias upward, towards higher states [25]. The bias is explained by the rapid growth of the boundary values of the product of wave functions in (1) and (2) with increasing j and j' (roughly, as $j^2 j'^2$). This increase in the rate of jumps $j \rightarrow j'$ is checked by the decay of the correlation function $\zeta(|\mathbf{q}_j - \mathbf{q}_{j'}|)$ at large $|\mathbf{q}_j - \mathbf{q}_{j'}|$ which is determined by the value of the correlation radius R , $|\mathbf{q}_j - \mathbf{q}_{j'}| \leq 1/R$. In the end, the transition rates $j \rightarrow j'$ represent, as a function of j' , a relatively narrow peak around some $j_1 \gg j$.

This strong upward bias has two consequences. First, almost all the time τ_j necessary for a neutron, which is initially in a low gravitational state j , to go up in states and disappear over the absorption barrier u_c , is spent on the first transition upwards. Further transitions to higher and higher states are going faster and faster. And second, this bias allows one to neglect the return of particles back to the lowest states. This results in decoupling of (4):

$$\partial_t N_j = -\frac{N_j}{\tau_j}, \quad \frac{1}{\tau_j} = m \sum_{j'} \int \frac{d\theta}{2\pi} W_{jj'}(|\mathbf{q}_j - \mathbf{q}_{j'}|). \quad (6)$$

Since the high narrow peak for transitions rates $j \rightarrow j'$ is centered around some $j_1 \gg j$, the absorption times τ_j for neutrons that initially occupy low gravitational states j differ from each other, according to (1), only by the values of the wave functions on the rough mirror $\Psi_j^2(H)$,

$$\frac{1}{\tau_j} = \frac{b_j}{b_1} \frac{1}{\tau_1}, \quad b_j = \frac{10^5 l_0 \Psi_j^2(H)}{2}, \quad (7)$$

where τ_1 is the depletion time for the first—the lowest—gravitational state, and the coefficient 10^5 is inserted purely for the computational convenience. The ratios $\tau_j(h)/\tau_1(h)$ (7) are plotted in Figure 1 for $j = 2, 3, 4, 5$ as a function of the distance between the mirrors h . Note that these ratios τ_j/τ_1 in the biased diffusion approximation are the same for 1D and 2D roughness and do not depend on the roughness parameters at all. Though all the depletion times τ_j rapidly decrease with decreasing h (see below), the ratios $\tau_j(h)/\tau_1(h)$ are increasing.

In [29, 30] the linewidths $1/\tau_j$ were considered as independent fitting parameters. Equation (7) shows that these τ_j are not independent and are trivially related to each other. In the next two sections we calculate these τ_j and express

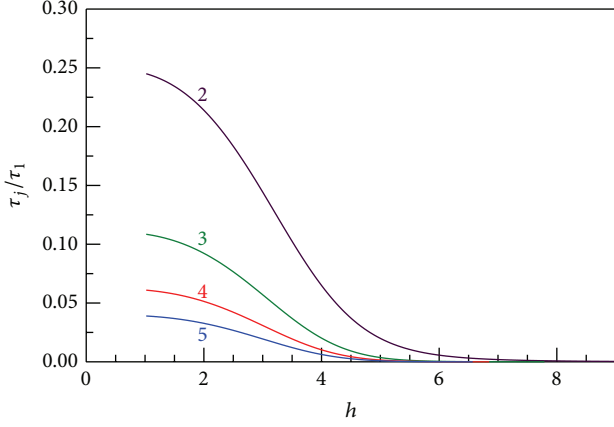


FIGURE 1: The ratios $\tau_j(h)/\tau_1(h)$ (7) for the lowest quantum levels $j = 2; 3; 4; 5$ as a function of the slit width h . The curves are marked by the values of j . These functions are the same for 1D and 2D roughness and in the biased diffusion approximation do not depend on the roughness parameters.

them via the parameters of the correlation function of surface roughness.

The fact that the depletion times τ_j can be relatively close to each other illustrates the difficulty in observing the stepwise dependence of the exit neutron count N_e on h ,

$$N_e = \sum N_j = \sum N_j(0) \exp\left(\frac{-L}{v_j \tau_j}\right), \quad (8)$$

where $N_j(0)$ is the number of neutrons in state j entering the waveguide of length L . For the lowest gravitational states the velocities v_j are more or less the same, $v_j \approx v_0 \sqrt{\epsilon}$, and the exit neutron count is

$$N_e = \sum N_j(0) \exp\left(\frac{-t_L}{\tau_j}\right) \equiv \sum N_j(0) \exp(-\Phi b_j), \quad (9)$$

$$\Phi = \frac{t_L}{b_1(h) \tau_1(h)}. \quad (10)$$

If all the states in front of the waveguide are equally populated, $N_j(0) = N_0$ (9) becomes

$$\frac{N_e(h)}{N_0} = \sum \exp(-\Phi b_j(h)) \quad (11)$$

and all parameters of the experimental setup collapse into the single constant Φ (or τ_1). What makes Φ the most important parameter in the problem, technically more important than even τ_1 , is that it does not depend on the waveguide width h while the relaxation time τ_1 is inversely proportional to $b_1(h)$. Constant Φ is obviously different for waveguides with 1D and 2D roughness, Φ_1 and Φ_2 , and these two situations should be considered separately.

The value of the dimensionless constant Φ depends on the properties of the waveguide, but the moment we calculate Φ we know the dependence of the exit neutron count on the waveguide width h , Figure 2, irrespective of the origin of these particular values of Φ .

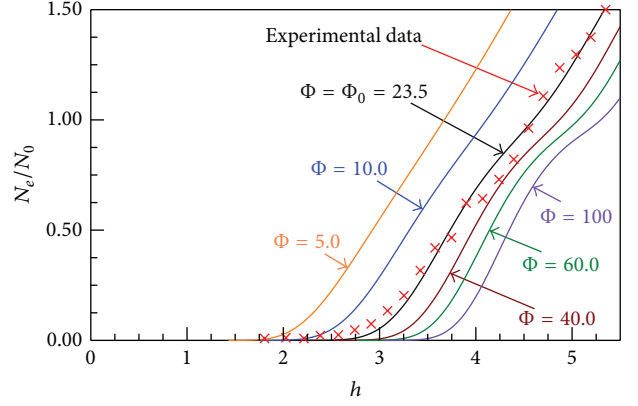


FIGURE 2: The dependence of the exit neutron count N_e/N_0 (11) on the waveguide width h for different values of Φ . The curves are marked by the values of Φ . The experimental data are fitted to the curve with $\Phi = 23.5$ which corresponds to 1D Gaussian roughness with $\eta = 0.19$ and $r = 1.19$.

In Figure 2 taken from [26] we plot the exit neutron count $N_e(h)/N_0$ (11) for several values of Φ . The noticeable quantum steps on the curves start appearing for $\Phi > 40$. These steps correspond to distinct consecutive depletions of the gravitational quantum states; at lower Φ the depletion processes overlap. The experimental data from [1–4] are fitted to the curve with $\Phi = 23.5$ which assumes 1D Gaussian roughness with $\eta = 0.19$ and $r = 1.19$ (see below). The fitting parameters are the number of neutrons entering the waveguide N_0 and, to a lesser degree, the width of the waveguide which cannot be measured precisely. This is much smaller than the set of fitting parameters used in [29, 30]. The quality of the fit is reasonably good taking into account that in earlier experiments [1–4] the absolute value of the width of the rough waveguide h could not be measured with an accuracy better than 10% and that the correlation function of surface roughness and the distribution of neutrons entering the waveguide $N_j(0)$ have not been measured at all.

The only remaining task is to calculate τ_1 ,

$$\frac{1}{\tau_1} = m \sum_{j' > 1} \int \frac{d\theta}{2\pi} W_{1j'}(|\mathbf{q}_1 - \mathbf{q}_{j'}|), \quad (12)$$

and, by extension, the dimensionless parameter Φ (10).

3. Waveguides with 1D Roughness

We start from waveguides with 1D roughness for which most of the calculations can be carried out analytically. Towards the end of the paper we will mention why 1D roughness is important though the existing rough mirrors exhibit 2D roughness [31].

It is more convenient to start not from (12) but from (6). 1D roughness is a random grating perpendicular to the direction of the beam and the 2D momentum both before and after scattering has only one component p along

the beam, $\mathbf{q} = (p, 0)$. The transition probabilities $W_{jj'}$ and the distribution function have the form

$$W_{jj'}(\mathbf{q}, \mathbf{q}') = \delta(q - q') W_{jj'}(p, p'), \quad (13)$$

$$n_j(\mathbf{q}) = \frac{(2\pi)^2}{L_p L_q} \delta(q) \delta(p - p_j) N_j, \quad (14)$$

where N_j is the number of particles in state j per unit length of the beam and $p_j = \sqrt{E - \epsilon_j}$, and E is the overall energy of the neutrons. Then (6) reduce to

$$\partial_t N_j = -\frac{N_j}{\tau_j}, \quad \frac{1}{\tau_j} = \sum_{j' > j} \frac{W_{jj'}(p_j - p_{j'})}{v_{j'}}. \quad (15)$$

In our dimensionless variables the scattering probabilities (1) and (13) in (15) obtain the form

$$\frac{1}{\tau_j} = \frac{1}{\tau_0} \sum_{j' > j} \frac{w_{jj'}(p_j - p_{j'})}{v_{j'}}, \quad (16)$$

$$w_{jj'} = \frac{4 \times 10^{-10} u_c^2 \eta^2 r \psi_1(y_{jj'}) b_j b_{j'}}{\beta_j}, \quad (17)$$

$$y_{jj'} = r(\beta_j - \beta_{j'}), \quad (18)$$

where ψ_1 stands for the dimensionless part of the Fourier image of 1D correlation function of surface roughness:

$$\zeta_1(p_j - p_{j'}) = \sqrt{2\pi} l_0^3 \eta^2 r \psi_1(y_{jj'}) \quad (19)$$

the lower index 1 indicates that this equation describes the case of 1D roughness.

Since the transition rate $j \rightarrow j'$ rapidly increases with increasing j' , only the terms with large j' make a noticeable contribution to the sum (16) which can be replaced by the integration:

$$\frac{\tau_0}{\tau_1} = 2 \times 10^{-5} u_c^2 \left(\frac{\eta^2}{r^2} \right) b_1(h) F_1(r, h), \quad (20)$$

$$F_1(r, h) = 2 \times 10^{-5} r^3 \epsilon^{-1/2} \sum b_j \psi_1(y_{1j}) \quad (21)$$

$$= \frac{2r^3 \epsilon}{\pi u_c} \int_0^1 dz \cdot z^2 \psi_1(y),$$

$$y = r \epsilon^{1/2} (1 - \sqrt{1 - z^2}). \quad (22)$$

In these notations our main parameter Φ_1 obtains a very simple form:

$$\Phi_1 = A_1 \eta^2 r \int_0^1 dz \cdot z^2 \psi_1(y), \quad (23)$$

$$A_1 = \frac{4 \times 10^{-5} t_L \epsilon}{\pi \tau_0 u_c}, \quad (24)$$

and the problem reduces to the integrations (21) and (23) of the correlation functions of various functional forms.

If, as it is often assumed, the correlation function is Gaussian, $\zeta_1(x/r) = l_0^2 \eta^2 \exp(-x^2/2r^2)$, its Fourier image is also Gaussian, $\psi_1(y) = \exp(-y^2/2)$ and

$$\frac{\Phi_1}{A_1 \eta^2} = \frac{1}{3\sqrt{r}} \left(\frac{8}{\epsilon} \right)^{3/4} \Gamma\left(\frac{7}{4}\right). \quad (25)$$

This equation has been used in [26] when fitting the experimental data from [1-4] (see Figure 2). The only information we have about the mirror roughness in those earlier experiments is that the average lateral size of inhomogeneities is of the order 1.19 and the average amplitude is approximately 0.119. Assuming that these numbers give the values of r and η and that we are dealing with the 1D Gaussian roughness, (25) yields $\Phi_1 \sim 23.5$. This value is used in the fit in Figure 1. Since these assumptions are somewhat arbitrary, the quality of the fit is actually much better than one might expect with all the uncertainties.

The Fourier image of a power law correlation function,

$$\zeta_1\left(\frac{x}{r}\right) = l_0^2 \eta^2 \frac{2\mu}{(1 + x^2/r^2)^{1+\mu}}, \quad (26)$$

behaves like an exponential function:

$$\psi_1(y) = \frac{y^\mu K_\mu(y)}{2^{\mu-1} \Gamma(\mu)}, \quad (27)$$

$$\frac{\Phi_1}{A_1 \eta^2} = \sqrt{\frac{\pi}{r}} \epsilon^{-3/4} 2^{1-\mu} \mu. \quad (28)$$

In the opposite case, when the power spectrum of roughness $\psi_1(y)$ is given by a power law function,

$$\psi_1(y) = \frac{1}{(1 + y^2)^{1+\lambda}}, \quad (29)$$

the correlation function itself behaves exponentially:

$$\zeta_1\left(\frac{x}{r}\right) = \frac{l_0^2 \eta^2 (x/r)^\lambda K_\lambda(x/r)}{2^\lambda \Gamma(1 + \lambda)} \quad (30)$$

and the constant Φ_1 has the form

$$\frac{\Phi_1}{A_1 \eta^2} = \frac{1}{3\sqrt{r}} \left(\frac{4}{\epsilon} \right)^{3/4} \frac{\Gamma(\lambda + 1/4)}{\Gamma(\lambda + 1)}. \quad (31)$$

The purely exponential correlation functions in configuration or momentum spaces emerge from (30) or (27) when $\lambda = 1/2$ or $\mu = 1/2$:

$$\exp(-s) = \sqrt{\frac{2s}{\pi}} K_{1/2}(s). \quad (32)$$

The parameter Φ_1 and the relaxation times τ_j exhibit a universal dependence on the amplitude η and the correlation

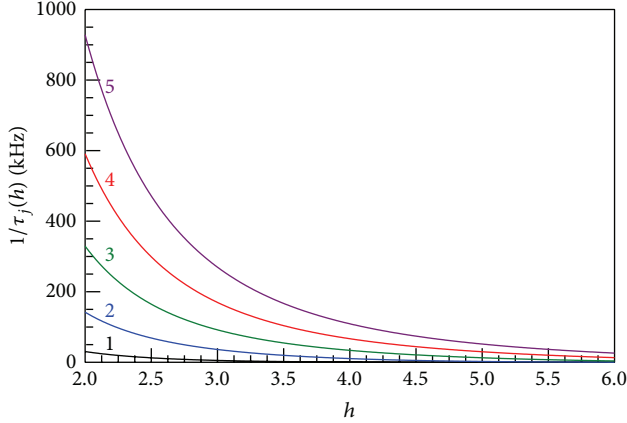


FIGURE 3: The inverse depletion times $1/\tau_j$ for the lowest gravitational states $j = 1; 2; 3; 4; 5$ for a waveguide with 1D exponential roughness with $\eta = r = 1$. The curves are marked by the values of j . The vertical scale is in kHz. Equation (33) extends the results to other values of η and r .

radius r of the surface roughness and on the overall kinetic energy of particles in the beam ε :

$$\Phi_1, \frac{1}{\tau_j} \propto \frac{\eta^2}{r^{1/2} \varepsilon^{3/4}}. \quad (33)$$

This scaling is precise only at $u_c \rightarrow \infty$. For finite u_c the powers of r and ε are slightly different (e.g., at $u_c \approx 10^5$ the scaling for the exponential correlator is $r^{-0.493}$).

These equations allow one to find the depletion times τ_j for each gravitational state, (7) and (10). Figure 3 presents inverse depletion times $1/\tau_j(h)$ in kHz for $j = 1; 2; 3; 4; 5$ in a waveguide with exponential roughness $\eta = r = 1$, (31) and (32). The values of the neutron velocity and time of flight entering A_1 (24) correspond to the original GRANIT cell [1–4]: $t_L/\tau_0 \approx 23$, $u_c/\varepsilon \approx 0.16$. The scaling (33) allows one to get $1/\tau_j$ for other values of η , r . The depletion becomes faster or slower depending on the value of $\eta^{-2} r^{1/2}$.

The depletion times τ_j determine both the disappearance of neutrons and broadening of the gravitational energy states $\varepsilon_j + i\hbar/\tau_j(h)$ with decreasing width of the waveguide h . The broadening of the state j increases dramatically and rapidly reaches the separation between the states after the width h becomes smaller than some critical value h_j . Below h_j the gravitational state ε_j loses its discrete quantum nature; this happens simultaneously with depletion of the neutron population of this state.

4. Waveguides with 2D Roughness

In contrast to systems with 1D roughness, most of the calculations in 2D cases can be done only numerically. We start from (12) which in our notations acquires the form similar to (20):

$$\frac{\tau_0}{\tau_1} = 2 \times 10^{-5} u_c^2 \left(\frac{\eta^2}{r^2} \right) b_1 F_2(r, h), \quad (34)$$

where

$$F_2(r, h) = 10^{-5} \sqrt{\frac{2}{\pi}} r^4 \sum b_j \psi_2^{(0)}(Q_1, Q_j), \quad (35)$$

$$Q_j = q_j r, \quad q_j = \sqrt{\varepsilon - \lambda_j}.$$

After replacing the summation by the integration, we get equations similar to (23) and (24):

$$\Phi_2 = A_2 \eta^2 r^2 \int_0^1 dz \cdot z^2 \psi_2^{(0)}(y_1, \tilde{y}), \quad (36)$$

$$y_1 = r \varepsilon^{1/2}, \quad \tilde{y} = r \varepsilon^{1/2} \sqrt{1 - z^2} \quad (37)$$

$$A_2 = 10^{-5} \left(\frac{2}{\pi} \right)^{3/2} \frac{t_L}{\tau_0} u_c \varepsilon^{3/2}. \quad (38)$$

The calculation of the zeroth angular harmonic of the 2D correlation function in momentum space $\psi_2^{(0)}$ can be done analytically [32] for the Gaussian

$$\psi_2^{(0)}(Q, Q') = 4\pi e^{-QQ'} I_0(QQ') e^{-(Q-Q')^2/2} \quad (39)$$

and exponential

$$\psi_2^{(0)}(Q, Q') = \frac{8E(\Omega)}{[1 + (Q - Q')^2] \sqrt{1 + (Q + Q')^2}}, \quad (40)$$

$$\Omega = 2 \sqrt{\frac{QQ'}{[1 + (Q + Q')^2]}}$$

correlation functions. Even in these cases all further calculations should be done numerically.

In contrast to the earlier experiments, the roughness correlation function for the ongoing GRANIT experiments in a new cell has been measured [31]. This correlation function is very close to the isotropic 2D exponential function with the correlation radius $r = 0.65$ and amplitude $\eta = 1.02$ while the time of flight $t_L/\tau_0 \approx 26$. This roughness yields $\Phi_2 = 5.22 \times 10^3$. The numerical examples below assume this setup. Our results for other correlation functions can be found in [31] in which we discuss the identification of the correlation function for the new rough mirror.

As in the case of 1D roughness, both Φ and $1/\tau_j$ remain proportional to η^2 . This scaling is obvious. The dependence on the correlation radius is more elusive and we cannot get an analytical expression similar to (33). The reason is the presence of $r \varepsilon^{1/2}$ in the argument of $\psi_2^{(0)}$ (40) in the integrand in (36). Our numerical data show that the scaling for $r > 0.3$ remains similar to (33):

$$\Phi, \frac{1}{\tau_j} \propto \eta^2 r^\gamma \varepsilon^\delta. \quad (41)$$

At $u_c \rightarrow \infty$ the index, $\gamma = -1/2$, the same as in the case of 1D roughness. The deviation from $\gamma = -1/2$ at finite u_c is more pronounced than in 1D case: at $u_c = 10^5$, as in experiment,

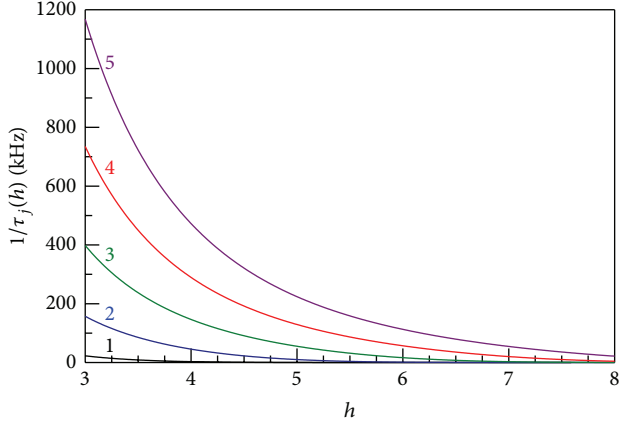


FIGURE 4: The same as Figure 3 for 2D exponential roughness in the new cell.

the index γ becomes -0.465 instead of -0.493 as in 1D. The scaling index for energy in the 2D case is obviously different from (33) because of different dependencies on velocities in the integrand. Instead of $\delta = -3/4$ as in (33), we find $\delta \approx -1.165$ though, in contrast to γ , the quality of the fit is not very good.

Figure 4 presents inverse depletion times $1/\tau_j(h)$ in kHz for $j = 1; 2; 3; 4; 5$ in a waveguide with 2D exponential roughness $\eta = r = 1$, (34), (36), and (40). The values of the neutron velocity and time of flight entering A_2 (38) correspond to the new GRANIT cell [1–4]: $t_L/\tau_0 \approx 26$, $u_c/\varepsilon \sim 1$. The scaling $\eta^2 r^\mu$ (41) allows one to get $1/\tau_j$ for other values of η, r .

The critical values of h_j , below which the depletion and the broadening of the gravitational state $\epsilon_j(h)$ explode, are slightly larger than those for the 1D roughness. This is explained by the role of the sideways scattering which is absent in the 1D case. Otherwise, Figures 3 and 4 are similar.

Our prediction for the neutron count $N_e(h)/N_0$ for the new GRANIT cell with the 2D exponential roughness with $\eta = 1.03$ and $r = 0.65$ ($\Phi_2 = 5.22 \times 10^3$) is given in Figure 5. The curve exhibits much more pronounced quantum steps than those in Figure 1. It is worth mentioning that the neutron count N_e is much less sensitive to the value of Φ when Φ is in $(2 \div 8) \times 10^3$ range than when it is in the range $5 \div 40$ as in Figure 1.

The presence of well-developed steps on the curve, which correspond to consecutive depletion of the gravitational quantum states, is explained mostly by a relatively large amplitude of roughness η , several times bigger than for the older cell. This large value of the amplitude of roughness η presents challenges for both theory and experiment and can potentially degrade the accuracy of information extracted from the experimental data. On a theoretical side, the main assumption of the theory, $\eta \ll r, h$, is violated. For experiment, the large amplitude of roughness means that it becomes virtually impossible to accurately measure the distance between the mirrors h . It also means that the energy levels become broad and not very well defined even if one disregards the interlevel transitions. The most likely

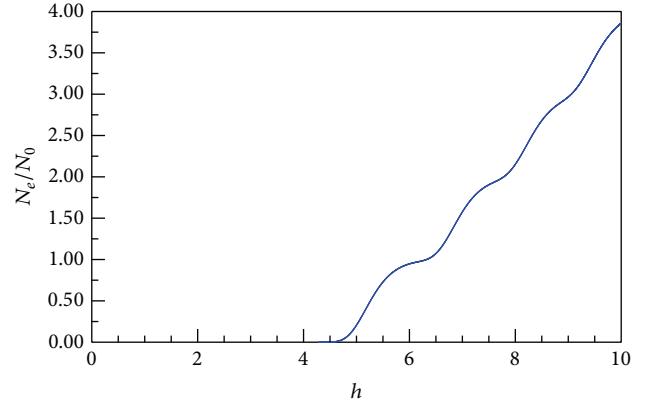


FIGURE 5: The prediction for the neutron count for the new waveguide with 2D exponential roughness with parameters $r = 0.65$, $\eta = 1.02$.

consequence of all these factors would be some smearing of the steps in comparison to those in Figure 5.

5. Conclusions

In summary, we developed a quantitative theory of propagation of ultracold neutrons through a rough waveguide. The immediate applications are the ongoing GRANIT experiments at ILL (Grenoble) aimed at analysis of quantization of neutrons by the gravity field. There are also other experimental groups exploring similar setups. If successful, these experiments will produce neutrons in well defined ultralow energy states in the peV range which can be used for precise measurements of fundamental forces.

We analyzed waveguides with 1D and 2D roughness. The ratios of the depletion times (line broadenings) in the biased diffusion approximation were the universal functions of the waveguide width and did not depend on the waveguide parameters. All relevant waveguide and roughness parameters collapsed into a single constant (essentially, a linewidth of the lowest quantum state), which was responsible for the exit neutron count. This constant strongly depended on the functional form of the roughness correlation function. We calculated this constant for various waveguides. In waveguides with 1D roughness the calculations could be carried out analytically for the most common types of the correlation functions; the 2D calculations were mostly numerical.

Our results were in good agreement with earlier experimental data despite the lack of experimental information about many important parameters. The predicted neutron count for the new experimental setup, for which the roughness profile was accurately measured, exhibited well-developed quantum step corresponding to consecutive depletion of the lower and lower gravitational states. Large amplitude of roughness in this setup could degrade the usability of the results. One of the possible ways to circumvent these difficulties and produce a much more controllable environment would be the use of a radically new design for a rough mirror which we called an Ising mirror [31, 33].

Conflict of Interests

The authors declare that there is no conflict of interests regarding the publication of this paper.

Acknowledgment

The results of this paper were reported at GRANIT-2014 Workshop (Les Houches, France, March 2–7, 2014). One of the authors (A. E. Meyerovich) is grateful to the organizers and other members of GRANIT collaboration for support and hospitality during the workshop.

References

- [1] V. V. Nesvizhevsky, H. G. Börner, A. K. Petukhov et al., “Quantum states of neutrons in the Earth’s gravitational field,” *Nature*, vol. 415, no. 6869, pp. 297–299, 2002.
- [2] V. V. Nesvizhevsky, A. K. Petukhov, H. G. Börner et al., “Measurement of quantum states of neutrons in the Earth’s gravitational field,” *Physical Review D*, vol. 67, Article ID 102002, 2003.
- [3] V. V. Nesvizhevsky, A. K. Petukhov, H. G. Börner et al., “Study of the neutron quantum states in the gravity field,” *European Physical Journal C*, vol. 40, no. 4, pp. 479–491, 2005.
- [4] V. V. Nesvizhevsky, “Near-surface quantum states of neutrons in the gravitational and centrifugal potentials,” *Physica-Uspeski*, vol. 53, no. 7, pp. 645–675, 2010.
- [5] T. Jenke, P. Geltenbort, H. Lemmel, and H. Abele, “Realization of a gravity-resonance-spectroscopy technique,” *Nature Physics*, vol. 7, no. 6, pp. 468–472, 2011.
- [6] L. A. Chizhova, S. Rotter, T. Jenke et al., “Vectorial velocity filter for ultracold neutrons based on a surface-disordered mirror system,” *Physical Review E*, vol. 89, Article ID 032907, 2014.
- [7] G. Ichikawa, S. Komamiya, Y. Kamiya et al., “Observation of the spatial distribution of gravitationally bound quantum states of ultracold neutrons and its derivation using the Wigner function,” *Physical Review Letters*, vol. 112, Article ID 071101, 2014.
- [8] A. Y. Voronin, P. Froelich, and V. V. Nesvizhevsky, “Gravitational quantum states of antihydrogen,” *Physical Review A*, vol. 83, Article ID 032903, 2011.
- [9] A. Y. Voronin, V. V. Nesvizhevsky, and S. Reynaud, “Whispering-gallery states of antihydrogen near a curved surface,” *Physical Review A*, vol. 85, Article ID 014902, 2012.
- [10] G. Dufour, P. Debu, A. Lambrecht, V. V. Nesvizhevsky, S. Reynaud, and A. Y. Voronin, “Shaping the distribution of vertical velocities of antihydrogen in GBAR,” *The European Physical Journal C*, vol. 74, Article ID 2731, 2014.
- [11] A. Y. Voronin et al., *Advances in High Energy Physics*, 2014, In press.
- [12] G. Chardin, P. Grandemange, D. Lunney et al., “Proposal to measure the gravitational behaviour of antihydrogen at rest,” Tech. Rep. CERN-SPSC-2011-029. SPSC-P-342, CERN, Geneva, Switzerland, 2011.
- [13] P. Crivelli et al., “Can we observe the gravitational quantum states of positronium?,” *Advances in High Energy Physics*. In press.
- [14] F. G. Bass and I. M. Fuks, *Wave Scattering from Statistically Rough Surfaces*, Pergamon Press, 1979.
- [15] J. A. DeSanto and D. S. Brown, *Analytical Techniques for Multiple Scattering from Rough Surfaces (Progress in Optics, v. 23)*, E. Wolf, Amsterdam, The Netherlands, 1986.
- [16] J. A. Ogilvy, *Theory of Wave Scattering from Random Surfaces*, Adam Hilger, Bristol, UK, 1991.
- [17] A. G. Voronovich, *Wave Scattering at Rough Surfaces*, Springer, Berlin, Germany, 1994.
- [18] G. Fishman and D. Calecki, “Surface-induced resistivity of ultrathin metallic films: a limit law,” *Physical Review Letters*, vol. 62, no. 11, pp. 1302–1305, 1989.
- [19] G. Fishman and D. Calecki, “Influence of surface roughness on the conductivity of metallic and semiconducting quasi-two-dimensional structures,” *Physical Review B*, vol. 43, no. 11, p. 11581, 1991.
- [20] Z. Tesanovic, M. V. Jaric, and S. Maekawa, “Quantum transport and surface scattering,” *Physical Review Letters*, vol. 57, p. 2760, 1986.
- [21] N. Trivedi and N. W. Ashcroft, “Quantum size effects in transport properties of metallic films,” *Physical Review B*, vol. 38, no. 17, pp. 12298–12309, 1988.
- [22] A. E. Meyerovich and S. Stepaniants, “Transport phenomena at rough boundaries,” *Physical Review Letters*, vol. 73, no. 2, pp. 316–319, 1994.
- [23] A. E. Meyerovich and S. Stepaniants, “Transport in channels and films with rough surfaces,” *Physical Review B*, vol. 51, no. 23, pp. 17116–17130, 1995.
- [24] A. E. Meyerovich and A. Stepaniants, “Quantized systems with randomly corrugated walls and interfaces,” *Physical Review B*, vol. 60, no. 12, pp. 9129–9144, 1999.
- [25] R. Adhikari, Y. Cheng, A. E. Meyerovich, and V. V. Nesvizhevsky, “Quantum size effect and biased diffusion of gravitationally bound neutrons in a rough waveguide,” *Physical Review A*, vol. 75, no. 6, Article ID 063613, 2007.
- [26] M. Escobar and A. E. Meyerovich, “Beams of gravitationally bound ultracold neutrons in rough waveguides,” *Physical Review A*, vol. 83, Article ID 033618, p. 033618, 2011.
- [27] A. E. Meyerovich and V. V. Nesvizhevsky, “Gravitational quantum states of neutrons in a rough waveguide,” *Physical Review A*, vol. 73, Article ID 063616, 2006.
- [28] V. V. Nesvizhevsky, “privatecommunication”.
- [29] A. Y. Voronin, H. Abele, S. Baessler et al., “Quantum motion of a neutron in a waveguide in the gravitational field,” *Physical Review D*, vol. 73, no. 4, Article ID 044029, 2006.
- [30] S. Baessler, M. Beau, M. Kreuz et al., “The GRANIT spectrometer,” *Comptes Rendus Physique*, vol. 12, pp. 707–728, 2011.
- [31] M. Escobar, F. Lamy, A. E. Meyerovich, and V. V. Nesvizhevsky, *Advances in High Energy Physics*, 2014, In press.
- [32] A. E. Meyerovich and I. V. Ponomarev, “Surface roughness and size effects in quantized films,” *Physical Review B*, vol. 65, Article ID 155413, 2002.
- [33] M. Escobar and A. E. Meyerovich, *Journal of Experimental and Theoretical Physics*. In press.

Research Article

In-Pile ^4He Source for UCN Production at the ESS

Esben Klinkby,^{1,2} Konstantin Batkov,¹ Ferenc Mezei,¹ Eric Pitcher,¹
Troels Schönfeldt,^{1,2} Alan Takibayev,¹ and Luca Zanini¹

¹ European Spallation Source ESS AB, P.O. Box 176, 221 00 Lund, Sweden

² DTU Nutech, Technical University of Denmark, DTU Risø Campus, Frederiksborgvej 399,
4000 Roskilde, Denmark

Correspondence should be addressed to Esben Klinkby; esbe@dtu.dk

Received 6 June 2014; Accepted 26 June 2014; Published 23 July 2014

Academic Editor: Valery V. Nesvizhevsky

Copyright © 2014 Esben Klinkby et al. This is an open access article distributed under the Creative Commons Attribution License, which permits unrestricted use, distribution, and reproduction in any medium, provided the original work is properly cited. The publication of this article was funded by SCOAP³.

ESS will be a premier neutron source facility. Unprecedented neutron beam intensities are ensured by spallation reactions of a 5 MW, 2.0 GeV proton beam impinging on a tungsten target equipped with advanced moderators. The work presented here aims at investigating possibilities for installing an ultra cold neutron (UCN) source at the ESS. One consequence of using the recently proposed flat moderators is that they take up less space than the moderators originally foreseen and thus leave more freedom to design a UCN source, close to the spallation hotspot. One of the options studied is to place a large ^4He UCN source in a through-going tube which penetrates the shielding below the target. First calculations of neutron flux available for UCN production are given, along with heat-load estimates. It is estimated that the flux can give rise to a UCN production at a rate of up to $1.5 \cdot 10^8$ UCN/s. A production in this range potentially allows for a number of UCN experiments to be carried out at unprecedented precision, including, for example, quantum gravitational spectroscopy with UCNs which rely on high phase-space density.

1. Introduction

The fundamental physics community has expressed strong interest to investigate the possibility of installing source of ultra cold neutrons (UCNs) at the ESS. There are a number of different ways in which this could be realized. This paper focuses on the in-pile option, in particular the possibility that a UCN source could be hosted in a *through-going tube* that penetrates the monolith shielding as well as the outer and inner reflectors. This would allow the UCN converter to come as close as possible to the spallation region, thereby subject to the highest possible input neutron flux. In order not to conflict with the cold/thermal moderators at the ESS, the tube must pass under the lower moderator. The study presented here details the impact on the cold/thermal moderator performance inflicted by the introduction of a through-going tube and relates this to the location of the through-going tube. In addition first estimates of the possible UCN production rate are given.

2. Through-Going Tube in Baseline Design

The possibilities for installing a UCN moderator at the ESS strongly depend on the layout of the target-moderator-reflector. In Figure 1, the central parts of the target-moderator-reflector are shown according to the baseline design of the Technical Design Report [1]. In this scenario, voluminous parahydrogen moderators (two cylinders of 16 cm diameter, 13 cm high) are situated on each side of the target and thus close to the spallation neutron density hotspot. The introduction of a UCN moderator would have to stay clear of the two existing moderators, for example, by placing it in a through-going tube underneath the lower parahydrogen moderator. As the main focus of the ESS facility is providing cold and thermal neutrons, it is essential when altering the baseline design to monitor the performance impact on the cold/thermal neutrons available in the instruments beamlines. Therefore, a study was carried out monitoring the flux available for UCN moderation versus

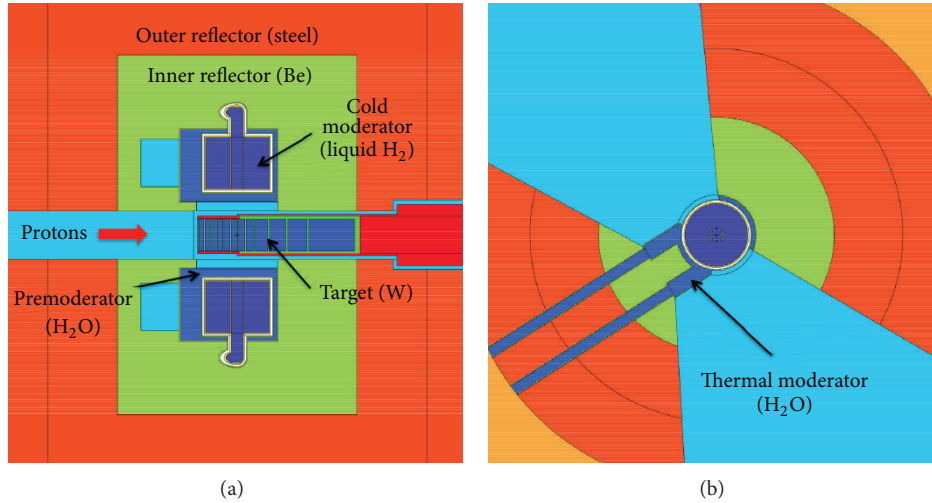


FIGURE 1: Vertical (a) and horizontal (b) cross-section of the target-moderator-reflector geometry in the Technical Design Report [1].

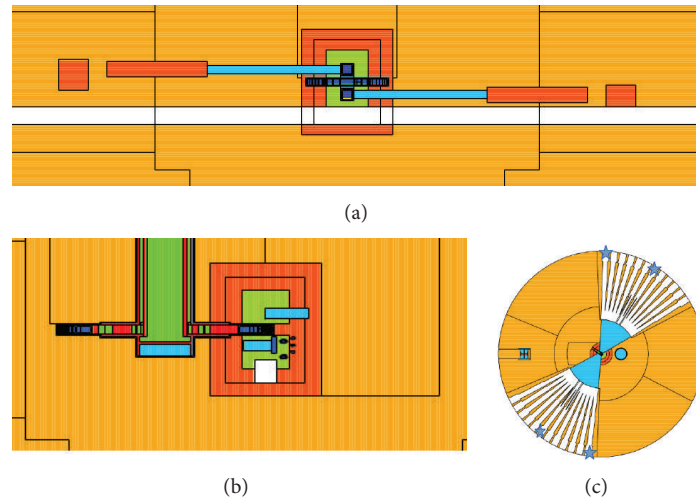


FIGURE 2: Geometry of the target, moderator, and reflector showing the UCN through-going tube (white areas in upper and lower left-hand inserts) placed at $y = -47.5$ cm (central), corresponding to the topmost of the studied geometries. The blue stars in the lower right-hand insert show the position of the lower point detectors. Note that the xz -plane (lower right-hand insert) is cut at $y = -18$ cm; wherefore the UCN tube is not visible.

the impact on neutron flux in the cold/thermal beamlines—for different vertical positions of the through-going tube.

3. Simulation Setup

Based on the baseline MCNPX [2, 3] model used for the neutronics calculations of the ESS Technical Design Report (TDR) [1], a $25 \text{ cm} \times 25 \text{ cm}$ tube is defined. To avoid the forward directed high energy shower particles from the proton beam impacting the target wheel, while obtaining maximal thermal flux, the tube is centered around and parallel to the x -axis (i.e., perpendicular to the proton beam). The tube is centered at $z = 0$ while the y coordinate (the “depth” under the proton beam) is left free and various possibilities are studied: $y \in [-47.5; -62.5]$ cm (central in tube) (the coordinate system used at the ESS is right-handed, with

the protons travelling along the z -axis, impacting the target in the origin; the y -axis is positive upwards (i.e., opposite gravity)). Figure 2 shows an example in which the void volume (the UCN through-going tube) replaces parts of the beryllium inner reflector (red) but more severely impacts the outer reflector (orange).

To measure the possible impact on cold/thermal beamlines, eight representative point detectors are placed in the beam-ports at the boundary of the target-moderator-reflector (TMR) plug, corresponding to the blue stars on the lower right insert of Figure 2.

4. Results

Comparing flux ratios between modified (i.e., including UCN tube) and baseline design in the three energy bins (cold,

TABLE 1: Heat-load on cryogenic ^4He and integrated cold/intermediate/thermal flux for the ESS implementation of Golub's UCN design discussed in the text and shown in Figure 4. The relative statistical uncertainties are $\sim 0.1\%$.

Heat-load [mW/cm ³]	Flux [0–5] meV [n/cm ² /s]	Flux [5–20] meV [n/cm ² /s]	Flux [20–100] meV [n/cm ² /s]
2.5	$3.8 \cdot 10^{12}$	$9.0 \cdot 10^{12}$	$1.8 \cdot 10^{12}$

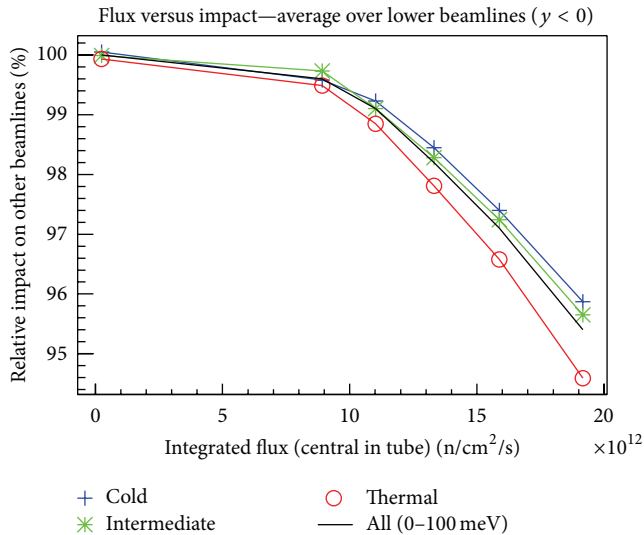


FIGURE 3: Relation between cold, intermediate, and thermal flux in the lower cold/thermal beamlines versus the flux available for UCN, central in the through-going tube. The black curve shows the (unweighted) average between the cold, intermediate, and thermal curves. Each point corresponds to a specific vertical position of the through-going tube.

intermediate, and thermal) shows that regardless of the position of through-going tube, the upper beamlines are unaffected.

Furthermore, the impact is approximately energy independent and does not fluctuate significantly between the four lower tally positions; therefore, the response of all lower tallies is collapsed to one average for each position of the through-going tube.

Finally, the relation between the impact in terms of relative decrease in available cold/thermal flux at the cold/thermal instruments versus the (central) flux available for UCN production is shown in Figure 3.

5. Discussion

There are several conclusions to be drawn for Figure 3. First, one can conclude that with proper design and carefully chosen distance from other moderators, a UCN moderator could be installed at the ESS without seriously impacting the performance of the scattering experiments. Unfortunately, one can also see from the figure that regardless of position under the lower parahydrogen moderator, the flux available for UCN production is very limited.

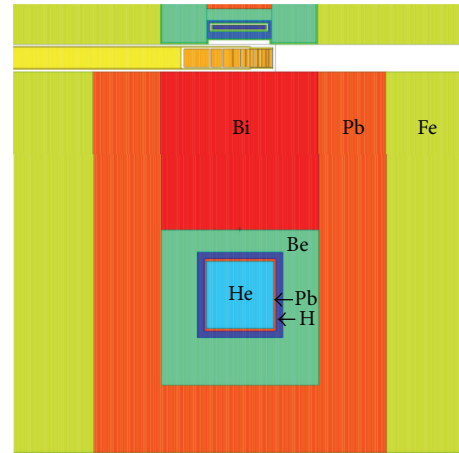


FIGURE 4: Assuming that all cold/thermal neutron scattering instruments can be served by a single flat moderator on top of the target wheel, a large ^4He source is installed below the target.

Despite these somewhat discouraging conclusions, there is some reason for hope. Simultaneously to the work presented here on through-going tube options, work is being carried out on the design of the cold moderators at the ESS. From the neutronics group of the ESS it is suggested to use flat moderator(s) for increased brightness [4, 5]. One feature of a flat moderator is that it is only viewed at a small area. Thus the amount of reflector “removed” per beamline is rather small, and the number of beamlines viewing a single moderator can be increased with respect to setup outlined in the TDR. In fact all the 22 foreseen instruments at the ESS can view one single flat moderator, with insignificant performance loss. Even in the case where two flat moderators of different heights will be installed, the reduced height of the moderator could allow for the installation of a second moderator below the target at a position favourable in terms of neutron flux (see Figure 3). In principle this reopens opportunity for installing a moderator below the target of a completely different type than the upper flat parahydrogen moderator.

One possibility would be to install a large ^4He moderator close to the spallation target, as initially suggested by Golub and colleagues more than 30 years ago [6]. Figure 4 shows an implementation of a UCN source inspired from this early work.

From this design, the heat-loads and fluxes shown in Table 1 are obtained from a MCNPX simulation of the geometry shown in Figure 4.

In [7] Golub and coauthors provide a scheme for calculating maximum UCN production, given an incoming

cold/thermal spectrum and integrated flux. Inserting the values of Table 1 and the observed spectrum, one arrives at a total maximal UCN production rate in $30\text{ cm} \times 30\text{ cm} \times 30\text{ cm}$ ^4He to be $1.5 \cdot 10^8$ UCN/s. It should be stressed that this is the maximum production rate, and it does not take into account any of the challenges confronted when attempting to store, extract or handle the UCN's.

Conflict of Interests

The authors declare that there is no conflict of interests regarding the publication of this paper.

Acknowledgment

This work has received financial support from CRISP (the Cluster of Research Infrastructures for Synergies in Physics). CRISP is cofunded by the partners and the European Commission under the 7th Framework Programme Grant Agreement no. 283745.

References

- [1] "The MCNPX Monte Carlo radiation transport code," ESS Technical Design Report ESS-doc-274, 2013.
- [2] L. S. Waters, G. W. McKinney, J. W. Durkee et al., "The MCNPX Monte Carlo radiation transport code," in *Proceedings of the Hadronic Shower Simulation Workshop*, vol. 896 of *AIP Conference Proceedings*, pp. 81–90, September 2006.
- [3] X-5 Monte Carlo Team, "MCNP—A General Monte Carlo N-Particle Transport Code," Version 5. LA-UR-03-1987.
- [4] F. Mezei, L. Zanini, A. Takibayev et al., "Low dimensional neutron moderators for enhanced source brightness," *Journal of Neutron Research*, vol. 17, pp. 101–105, 2014.
- [5] K. Batkov, A. Takibayev, L. Zanini, and F. Mezei, "Unperturbed moderator brightness in pulsed neutron sources," *Nuclear Instruments and Methods in Physics Research A: Accelerators, Spectrometers, Detectors and Associated Equipment*, vol. 729, pp. 500–505, 2013.
- [6] R. Golub, K. Böning, and H. Weber, *Ultra-Cold Neutrons at the SNQ Spallation Source*, TUM-E21/SNQ-UCN/81-4, 1981.
- [7] R. Golub, D. J. Richardson, and S. K. Lamoreaux, *Ultra-Cold Neutrons*, Taylor & Francis, London, UK, 1991.